UNIVERSITÀ DI PARMA

UNIVERSITA' DEGLI STUDI DI PARMA

Dottorato di Ricerca in Ingegneria Industriale

XXXI ciclo

Inverse Heat Transfer Approach for Heat Exchanger Characterization

Course coordinator:

Chiar.mo Prof. GIANNI ROYER CARFAGNI

Advisor:

Chiar.ma Prof.ssa SARA RAINIERI

Co-Advisor:

Prof. CARLOS J.S. ALVES

Prof. FABIO BOZZOLI

Chiar.mo Prof. MARCELO J. COLAÇO

Ph.D. candidate:

Ing. ANDREA MOCERINO

Academic years: 2015-2018

"How often have I said to you that when you have eliminated the impossible, whatever remains, however improbable, must be the truth?"

Sherlock Holmes

"In the sign of the four" (1890)

I certify that I have read this dissertation and that, in my opinion, it is fully adequate in scope and quality as a dissertation for the degree of European Doctor of Philosophy.

Prof.ssa SARA RAINIERI

(Principal advisor)

I certify that I have read this dissertation and that, in my opinion, it is fully adequate in scope and quality as a dissertation for the degree of European Doctor of Philosophy.

Prof. FABIO BOZZOLI

(Co-advisor)

I certify that I have read this dissertation and that, in my opinion, it is fully adequate in scope and quality as a dissertation for the degree of European Doctor of Philosophy.

Prof. MARCELO J. COLACO

(Co-advisor)

I certify that I have read this dissertation and that, in my opinion, it is fully adequate in scope and quality as a dissertation for the degree of European Doctor of Philosophy.

Prof. CARLOS J. S. ALVES

(Co-advisor)

I certify that I have read this dissertation and that, in my opinion, it is fully adequate in scope and quality as a dissertation for the degree of European Doctor of Philosophy.

Prof. GIANNI ROYER CARFAGNI

(Course coordinator)

Preface

Inverse Heat Transfer Problems (IHTP) use measurements for the estimation of unknown quantities appearing in the analysis of physical problems in thermal engineering. For example, inverse problems related to the heat conduction usually have to deal with the estimation of an unknown boundary heat flux, by using temperature measurements taken on a different boundary. Therefore, while in the classical direct heat conduction problem the cause (boundary heat flux) is given and the effect (temperature field in the body) is determined, the inverse problem involves the estimation of the cause from the knowledge of the effect.

The aim of this thesis is to present and test new methodologies able to solve the inverse heat transfer problem, in order to characterize some type of heat transfer devices. In particular, three original estimation procedures are developed, tested on virtual experiments and applied to different experimental data:

- a new method based on the Iterative Reweighted Least Square approach, is proposed for the estimation of the average thermal performances of a tube in tube heat exchanger. After its verification, the method was experimentally employed for the characterization of bio-inspired wall corrugate tubes developed in collaboration with the Denmark Technical University (DTU);
- an original improvement of Singular Valued Decomposition approach concerned the 2D local estimation of the convective heat transfer coefficient, is developed. After its verification, the method was experimentally employed for the local estimation of

the convective heat transfer coefficient in coiled tube, technology already developed and investigated at the University of Parma;

- an novel method, based on the Reciprocity Functional gap, concerned the 2D local estimation of the convective heat transfer coefficient at the internal boundary of a 2D annuls domain, is developed. After its verification, the method was experimentally employed for the local estimation of the convective heat transfer coefficient in coiled tube.

Finally, due to the complex fluid-wall interaction, a 3D zero order Tikhonov regularization scheme is implemented. After its numerical verification, the algorithm was employed for the local estimation of the convective heat transfer coefficient in an original test rig. The experimental setup consists of a straight tube fitted with a butterfly-shaped insert device. The same procedure, was applied for the local estimation of the convective heat transfer coefficient in an original test rig. The experimental setup consists of a straight cross-helix wall corrugated tube.

In order to give an overview on the content of the present work, a brief description of each chapter is given:

Chapter 1

The aim of this chapter is to give a general introduction to the common heat exchangers configuration. Their classifications, together with some typical applications are also provided. The governing equation related to the forced convection are briefly introduced and discussed, together with their dimensionless analysis. Finally, the common heat transfer enhancement techniques are presented.

Chapter 2

The scope of the present chapter is mainly related to the definition of the Direct and Inverse Problem in Heat Transfer. A simple example is introduced in order to show the ill-conditioning of the inverse problem and how it could affect the estimated solution. Finally, classifications and application to different fields are presented.

Chapter 3

The aim of the present chapter is to introduce the common solution techniques, both for the parameter and for the function estimation problems. In particular, two different problems are

stated and their common solution strategies are introduced. Finally, a brief discussion on the stopping criteria is provided.

Chapter 4

In this chapter, new solution strategies related to the problems stated in the previous chapter are developed. In particular, a new methodology based on the Iterative Re-weighted Least Square approach is used also as a solution strategy for the inverse estimation of the average thermal performances of heat exchangers. For what concern the function estimation, two different approaches are adopted to locally inverse estimate the thermal performances of the heat exchangers: an upgrade of the Truncated Singular Value Decomposition, here called Gaussian Filtered Singular Valued Decomposition, and an upgrade of the here called Numerical Reciprocity Functional, defined as Filtered Reciprocity Functional are presented.

Chapter 5

This chapter is devoted to the validation and comparison of three new solution strategies presented in *Chapter 4* with some of the common estimation algorithm presented in *Chapter 3*. The comparison is performed using virtual experiments in order to compare the reconstructed signal with the exact one. Moreover, in order to make a robust comparison, the reconstruction capabilities were tested using synthetic temperature measurements spoiled with different noise level.

Chapter 6

The aim of this chapter is related to the application of the estimation procedures used in *Chapter 5* to four different experiments. In particular, the estimation concerned the identification of the average performances of a double corrugated pipe and the identification of the local convective heat transfer coefficients in coiled tube as well as in straight tube fitted with a butterfly-shaped turbulator and a straight cross-corrugate wall tube.

The present thesis produced the following scientific publications:
Bozzoli2016, Bozzoli2016a, Bozzoli2017a, Bozzoli2017b, Bozzoli2018, Bozzoli2018a, Bozzoli2018b, Mocerino2018

Parma (Italy),
31/08/2018

Contents

Nomenclature

Acronyms

AEA	Alternating Elliptical Axis
ART	Algebraic Reconstruction Technique
BCG	Bi-Conjugate Gradient
BEM	Boundary element method
CG	Conjugate gradient
DE	Differential evolution
DFP	Davidon-Fletcher-Powell
DOE	Design Of Experiment
DSVD	Damped Singular Value Decomposition
FDM	Finite Difference Method
FEM	Finite Element Method
FRF	Filtered Reciprocity Functional
FVM	Finite Volume Method
GA	Genetic algorithm
GCV	Generalized Cross validation approach
GFSVD	Gaussian Filtered Singular Value Decomposition
IHTP	Inverse Heat Transfer Problem
IHCP	Inverse Heat Conduction Problem
IRLS	Iterative Reweighted Least Square
LM	Levenberg-Marquardt
NLS	Non-negative Least Square
NM	Nelder-Mead
NR	Newton-Raphson method
NRF	Numerical Reciprocity Functional
PSO	Particle Swarm Optimization
QN	Quasi-Newton method
RF	Reciprocity Functional
SA	Simulated Aneling
SCGM	Simplified Conjugate Gradient Method
SD	Steepest Descent method

SIRT	Simultaneous Iterative Reconstruction Technique
SLM	Selective Laser Melting
SQP	Sequential Quadratic Programming
SVD	Singular Value Decomposition
TM	Tikhonov regularization method
TSVD	Truncated Singular Value Decomposition
ULS	Unconstrained Least Square
WLS	Weighted Least Square

List of figures

List of tables

Chapter 1

Heat exchangers

1.1 Introduction

A heat exchanger is a device used to transfer thermal energy between two or more fluids in thermal contact, having different temperature. In heat exchanger, usually, there is no interaction with the exterior of the system (e.g. exchange of thermal energy, mechanical energy, chemical reactions, etc.). A heat exchanger consists of heat transfer elements such as a core or matrix containing the heat transfer surface, and fluid distribution elements such as headers, manifolds, tanks, etc. Usually, there are no moving parts in a heat exchanger; however, there are exceptions, such as a rotary regenerative or a scraped surface heat exchanger. The heat transfer surface in direct contact with fluids and through which heat is transferred by conduction. That portion of the surface that is in direct contact with both the hot and cold fluids and transfers heat between them, it is usually referred as *primary* or *direct surface*. To increase the heat transfer area, appendages could be added to the primary surface constituting a *secondary*, or *indirect surface*. These extended surface elements are usually referred as fins. Thus, heat is conducted through the fin to the surrounding fluid by convection or radiation. As a result, the addition of fins to the primary surface reduces the

thermal resistance on that side and thereby increases the total heat transfer that could be exchanged by the fluids under the same temperature difference. Fins, that could be added also for structural purposes, may form flow passages increasing the heat transfer capabilities by increasing the fluid mixing.

Typical application involve heating or cooling fluid stream, recover or reject heat, sterilize, pasteurize, fractionate, distil, concentrate, crystallize, control a process, etc. In the majority of the construction configurations, fluids are separated by a wall and they are referred as *indirect heat exchanger* or simply *regenerators*. On the other hand, if the fluids are mixed together directly exchanging heat, they are referred as *direct transfer heat exchanger* or simply *recuperators*. Common examples of heat exchangers are shell-and-tube exchangers, automobile radiators, condensers, evaporators, air preheater, cooling tower, etc. If no phase change occurs in any of the fluids, the heat exchanger is referred as *sensible heat exchanger*. There could be either internal thermal energy source (e.g. electric heater, nuclear fuel elements, etc.) or chemical reactions (e.g. boiler, fired heaters, fluidized-bed exchanger). The interaction with the exterior of the system, could be done also by exchanging work such as in the scraped surface heat exchanger, agitated vessels, stirred tank reactors, etc. In the indirect heat exchanger, the heat is exchanged by conduction through the solid domain, however in the heat pipe exchanger, the fluid remove the heat from the hot side by a combination of evaporation, condensation and conduction of the working fluid inside the heat pipe. A detail classification of the heat exchanger was done by Shah in (*Shah1981*).

1.2 Classifications and applications

The exchangers can be classified in different ways. As suggested by Shah (*Shah2003*) it is possible to categorize the heat exchanger devices according to the:

- heat transfer processes
- number of fluids
- heat transfer surface area/volume ratio
- construction type
- flow arrangements
- heat transfer mechanisms.

A brief discussion related to the each class is here listed:

CLASSIFICATION ACCORDING TO TRANSFER PROCESS

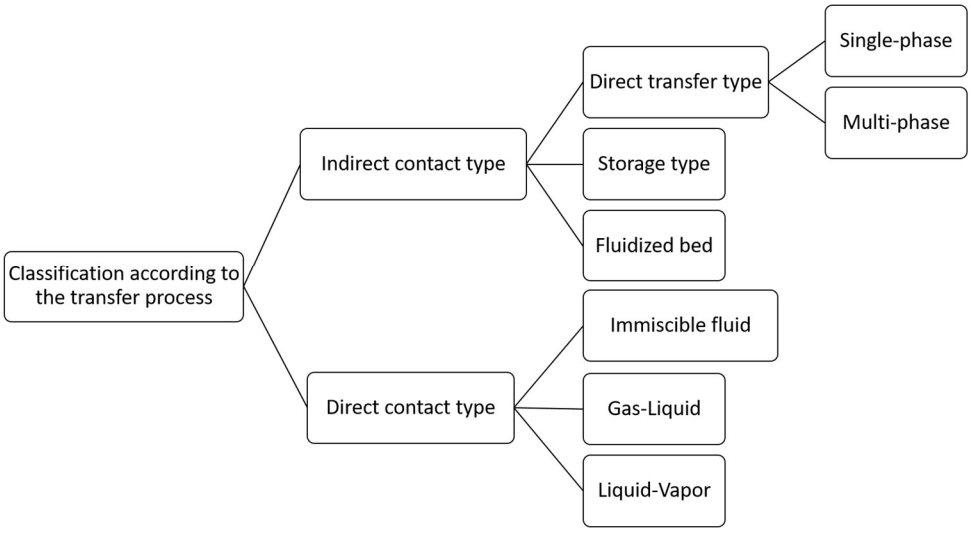

Figure 1.1: Heat exchanger: classification according to the transfer process

Indirect contact heat exchanger

This type of heat exchanger, the working fluids are divided by a wall and the heat is exchanged mainly by conduction. In general there is no moving parts, they are designed as a recuperator and are usually named *surface heat exchanger*. They can be classified as:

- direct-transfer type;
- storage type;
- fluidized-bed exchanger.

More in detail:

Direct-transfer type

In this category the heat is directly transferred from the hot fluid to the cold one. There could be more than two fluids and common examples are: tubular, plate and extended surface heat exchanger. Those devices are designed as a recuperator despite that term is not commonly used in the process industry for the shell-and-tube heat exchanger and plate heat exchanger. This category of device could be subdivided into *prime surface heat exchanger* and *extended surface heat exchanger*. The difference is that in the prime surface heat exchanger, no appendages to the surface could be used such as fins, while they could be used in the second category.

Storage type exchanger

In a storage type exchanger, both fluids flow alternatively pass through the same flow passages, and hence heat transfer is intermittent. The heat transfer surface (or flow passages) is generally cellular in structure and is referred to as a matrix or it is a porous

solid material, referred to as a packed bed. When hot gas flows over the heat transfer surface (through flow passages), the thermal energy from the hot gas is stored in the matrix wall, and thus the hot gas is being cooled during the matrix heating period. As cold gas flows through the same passages later (i.e., during the matrix cooling period), the matrix wall gives up thermal energy, which is absorbed by the cold fluid. Thus, heat is not transferred continuously through the wall as in a direct-transfer type exchanger (recuperator), but the corresponding thermal energy is alternately stored and released by the matrix wall. This storage type heat exchanger is also referred to as a regenerative heat exchanger, or simply as a regenerator.

Fluidized-bed heat exchanger

In a fluidized-bed heat exchanger, one side of a two-fluid exchanger is immersed in a bed of finely divided solid material, such as a tube bundle immersed in a bed of sand or coal particles. If the upward fluid velocity on the bed side is low, the solid particles will remain fixed in position in the bed and the fluid will flow through the interstices of the bed. If the upward fluid velocity is high, the solid particles will be moved away with the fluid. At a ‘‘proper’’ value of the fluid velocity, the upward drag force is slightly higher than the weight of the bed particles. This result in a solid particles floating with an increase in bed volume, which behaves as a liquid. This characteristic of the bed is referred to as a fluidized condition, characterized by a constant fluid pressure drop through the bed, which is independent to the flow rate, that strongly mixing of the solid particles. This results in a uniform temperature for the total bed (gas and particles) with an apparent thermal conductivity of the solid particles as infinity. Chemical reaction is common on the fluidized side in many process applications, such as the coal combustion fluidized beds. The common applications of the fluidized-bed heat exchanger are drying, mixing, adsorption, reactor engineering, coal combustion, and waste heat recovery.

Direct contact heat exchanger

In this category of heat exchangers, the working fluids are in contact an usually there is mass transfer in addition to the heat transfer. Usually, in this type of devices, at least one of the working fluid change phase, therefore the latent heat released represent a significant portion of the total transferred energy. Compared to the indirect contact heat exchanger, this type of devices does not have problems of fouling (since there is no separation walls), the construction is cheaper and the achievable heat transfer rate is very high. This family of heat exchanger can also be classified as: *immiscible fluid, gas-liquid* and *liquid-vapour exchanger*.

Immiscible fluid heat exchanger

In this type of heat exchanger, two immiscible fluid streams are brought into direct contact. These fluids may be single-phase fluids, or they may involve vaporization or condensation (e.g. condensation of organic vapors and oil vapors with water or air).

Gas-liquid heat exchanger

In this type of exchanger, one fluid is a gas, while the other is a low-pressure liquid. The fluid still be able to be separable after the heat is exchanged. In this devices the majority of the heat transferred is due to the phase change of the liquid fluid that is removed with the gas fluid after the heat transfer is ended. Typical applications are cooling tower with forced or natural convection. Other applications are the air-conditioning spray chamber, spray drier, spray tower, and spray pond.

Liquid-liquid heat exchanger

In this type is usually applied to steam flows. In particular, steam is partially or fully condensed using cooling water (or water is heated with waste steam) through direct contact in the exchanger. Non-condensables, residual steam and hot water are the outlet heat exchanger. Common examples are desuperheaters and open feedwater heaters (also known as deaeraters) in power plants.

CLASSIFICATION ACCORDING TO NUMBER OF FLUIDS

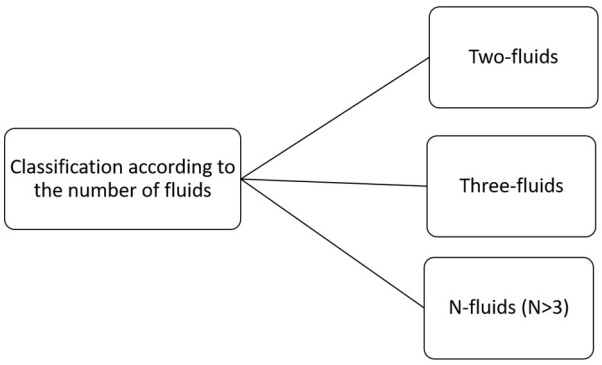

Figure 1.2: Heat exchanger: classification according to the number of fluids

Most processes of heating, cooling, heat recovery, and heat rejection involve the heat transfer between two (or many) fluid. Two fluid heat exchangers are the most common configuration, but there are also three fluid heat exchangers such as in the cryogenics, solar and chemical processes (e.g., air separation systems, a helium–air separation unit, purification and liquefaction of hydrogen, ammonia gas synthesis). Heat exchangers with as many as 12 fluid

streams have been used in particular chemical process applications but its design theory is algebraically very complex.

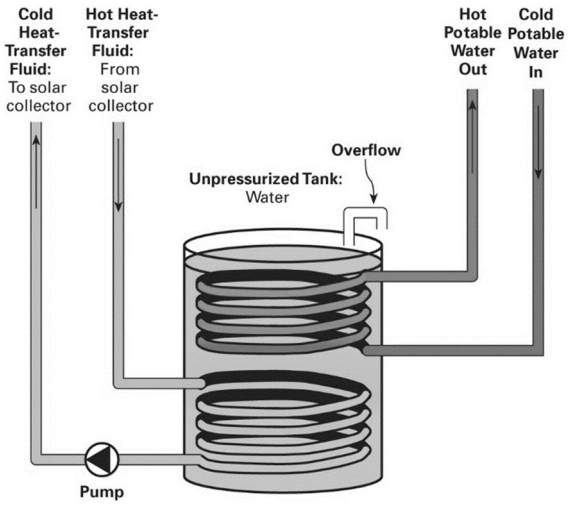

Figure 1.3: Three fluids heat exchanger for solar application

CLASSIFICATION ACCORDING TO SURFACE COMPACTNESS

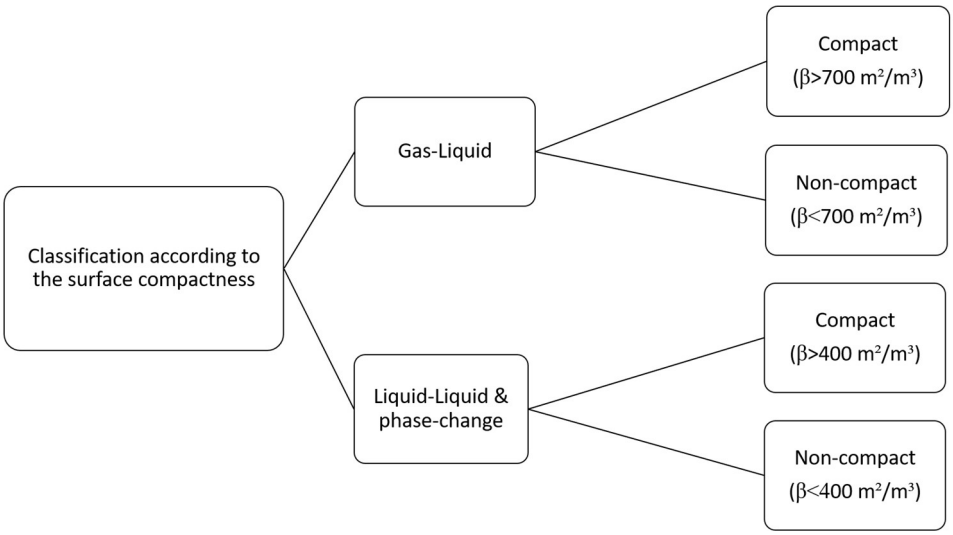

Figure 1.4: Heat exchanger: classification to the surface compactness

Compared to shell-and-tube exchangers, compact heat exchangers are characterized by a large heat transfer surface area per unit volume of the exchanger, resulting in reduced space, weight, support structure, footprint, energy requirements and cost. The motivation for using compact surface heat exchangers is to optimized a specific heat exchanger performance, $q/\Delta T_m$, within acceptably low mass and box volume constraints. The heat exchanger performance may be expressed as:

$$\frac{q}{\Delta T_m} = U\,A = U\,\beta_c\,V \tag{1.1}$$

where q is the heat transfer rate, ΔT_m is the true mean temperature difference, U is the overall heat transfer coefficient and β_c is the ratio between the exchanging area and the volume of the heat exchanger. The β_c coefficient can be arbitrarily defined on the cold or on the hot side. Anyway, it is clear that high β_c values minimize the exchanger volume V for a specified $q/\Delta T_m$.

Shah (*Shah1981*) proposed an empirical way to determine the type of heat exchanger that has to be used, as a function of the desired heat transfer surface area density or the hydraulic diameter of the heat exchanger, as shown in Figure (1.5).

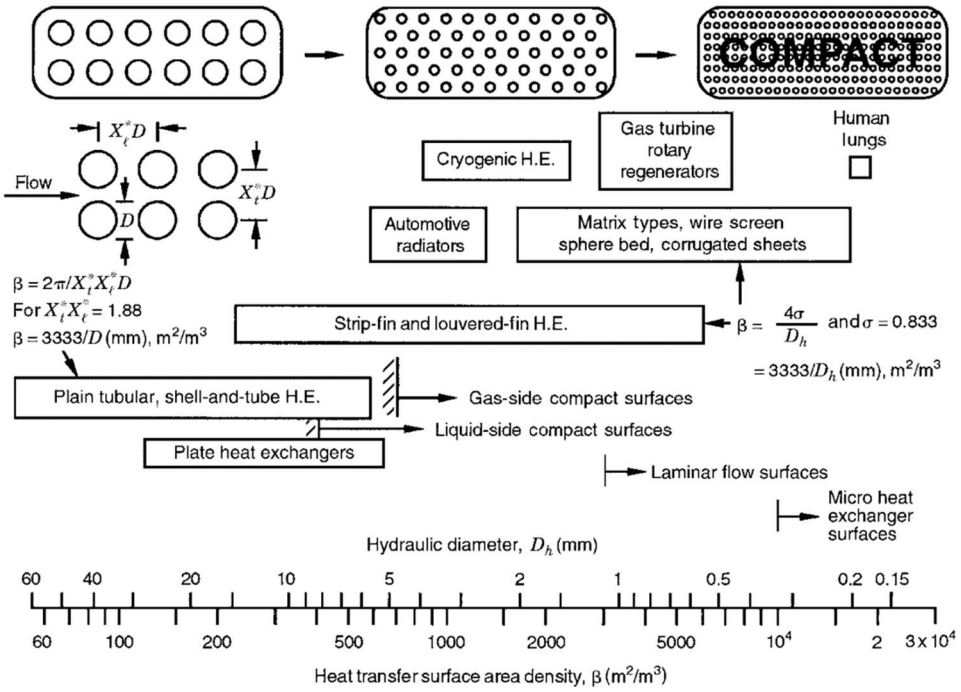

Figure 1.5: Heat transfer surface area density (*Shah1981*)

CLASSIFICATION ACCORDING TO CONSTRUCTION FEATURES

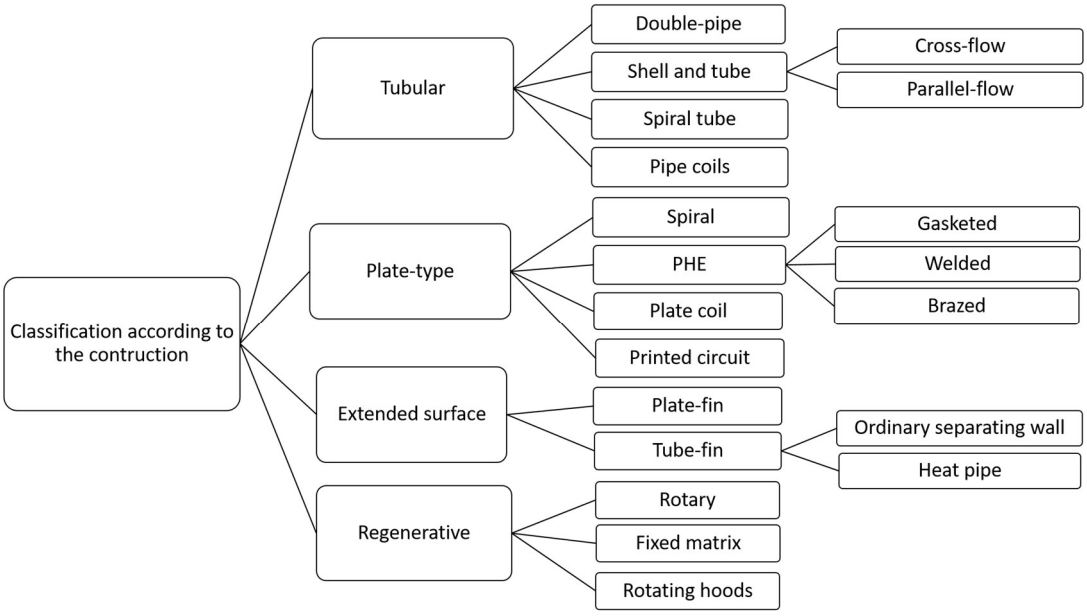

Figure 1.6: Heat exchanger: classification according to the construction features

Heat exchangers are frequently characterized by construction features. As it is possible to see in Figure (1.6), the four main construction types are:

- Tubular;
- Plate;
- Extended surface;
- Regenerative exchangers.

Heat exchangers with other constructions conformations are also available, such as scraped surface exchanger, tank heater, cooler cartridge exchanger, and many others (*Walker1990*).

Tubular heat exchanger

Tubular exchangers, which are schematically represented in Figure (1.7), are mechanically robust, therefore they can be designed for high relative pressures to the environment and high pressure differences between the fluids. Tubular exchangers are used primarily for liquid-to-liquid and liquid-to-phase change (condensing or evaporating) heat transfer applications. Nevertheless, these devices can also be used for gas-to-liquid and gas-to-gas heat transfer applications (e.g. high operating temperature and/or pressure, high fouling problem on at least one fluid side, etc.). These exchangers may be classified as shell-and-tube, tube-in-tube, and coiled tube exchangers. They are all prime surface exchangers except for exchangers having fins outside or inside the tubes.

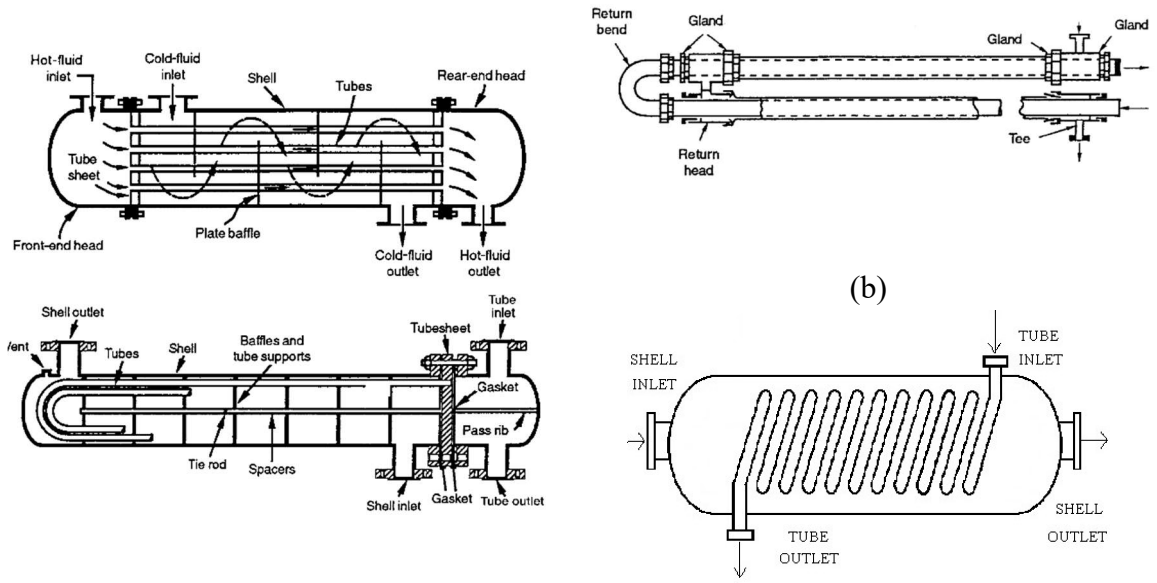

Figure 1.7: Tubular heat exchanger: (a) Shell-and-tube heat exchanger: (b) tube-in-tube heat exchanger and (c) coiled-in-shell heat exchangers (*Shah2003*)

Plate heat exchanger

Plate-type heat exchangers, shown in Figure (1.8), are usually prime surface built of thin plates. The plates are either smooth or have some form of corrugation, and they are either flat or wound in an exchanger. Generally, these exchangers cannot accommodate very high pressures or temperatures differences. Plate heat exchangers (PHEs) can be classified as gasketed (that can be welded or brazed on one or both fluid passages), spiral plate, lamella, and platecoil exchangers.

Usually plates heat exchanger are characterized by a heat transfer surface area bigger than in the tubular heat exchanger, thus increasing the heat transfer performances. This benefit is maximized keeping the chamber as thin as possible in order to maximize the volume of liquid in contact to the plate. Moreover, if small corrugation is added to the plate, it is possible to promote the transition to the turbulent flow. As compared to shell and tube heat exchangers, the temperature difference between the hot and cold side can be lower than in the shell and tube heat exchangers

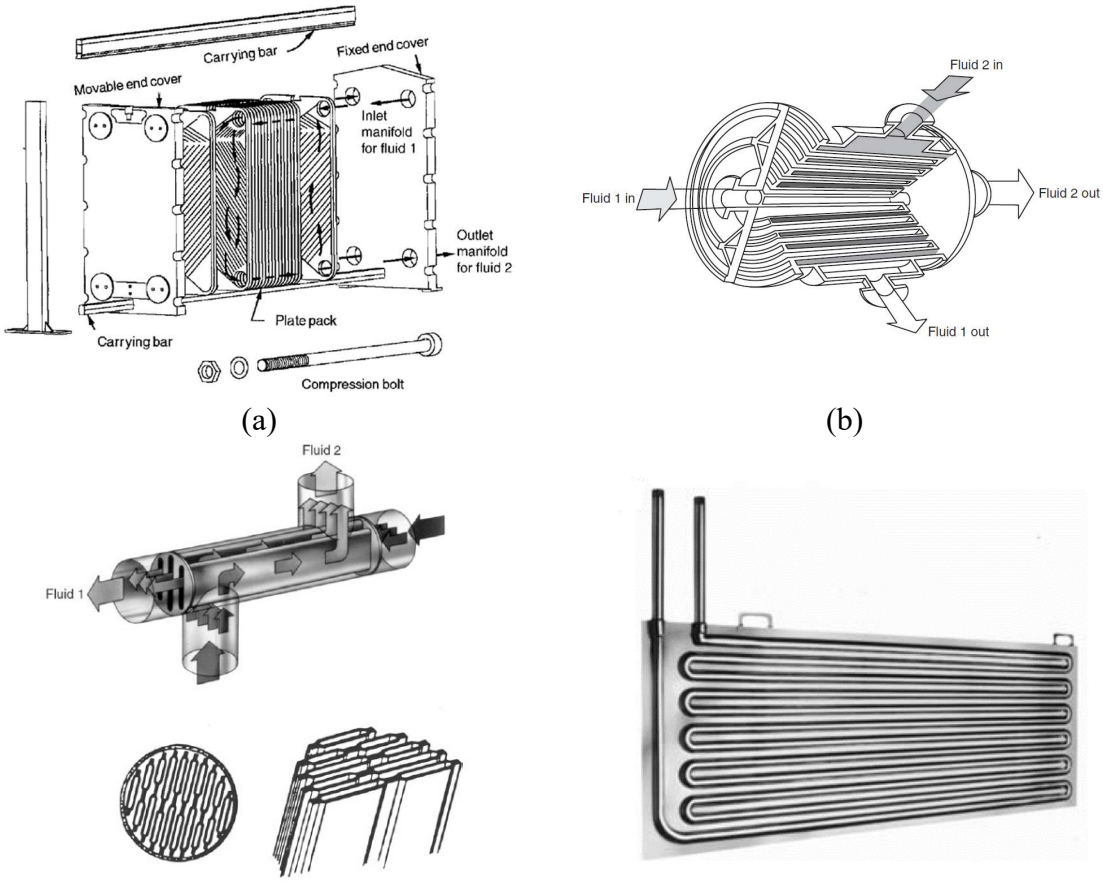

Figure 1.8: Plate heat exchanger: (a) gasketed: (b) spiral plate, (c) lamella and (d) plate coli heat exchangers (*Shah2003*)

Extended surface heat exchanger

Those devices differ from the previously described, since they are not prime surface heat exchanger. One of the most common methods to increase the surface area (and then exchanger compactness) is to add the extended surface , such as fins, to the heat transfer surface. The fins must be as dense as possible on one or both fluid sides, depending on the design requirement. Some of the most common types of extended surfaces are the plate-fin and tube-fin geometries (Figure (1.9)).

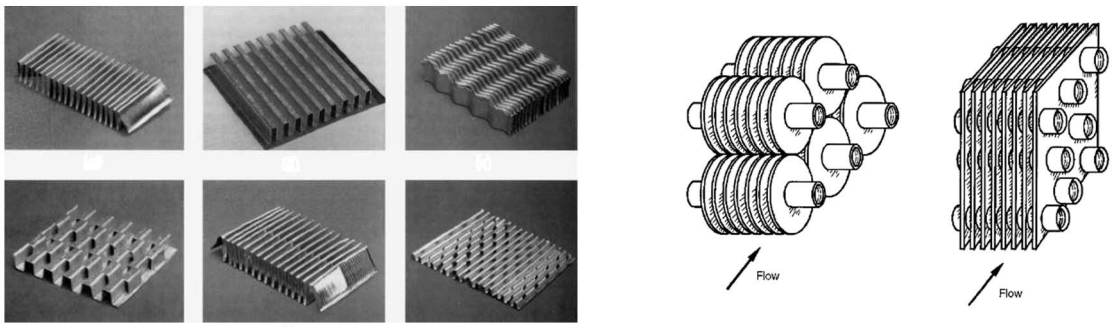

Figure 1.9: Extended surface heat exchanger: (a) plate-fin and (b) tube-fin heat exchanger (*Shah2003*)

Tube-fin heat exchanger can also be internally fined as well as internally-and-externally finned. One particular application of internally finned heat exchanger are the *heat pipes* (Figure (1.10)). Those devices are commonly used in the electronic equipment. They are based on the liquid-to-gas phase change thus they are able to remove a high quantity of heat from the hot device. There are a number of different ways to classify heat pipes, but perhaps the two most important categories are the variable-conductance heat pipes (those in which the magnitude and/or direction of the heat transfer can be controlled) and micro-heat pipes (those that are so small that the mechanisms controlling their operation are significantly different from those in more conventional heat pipes).

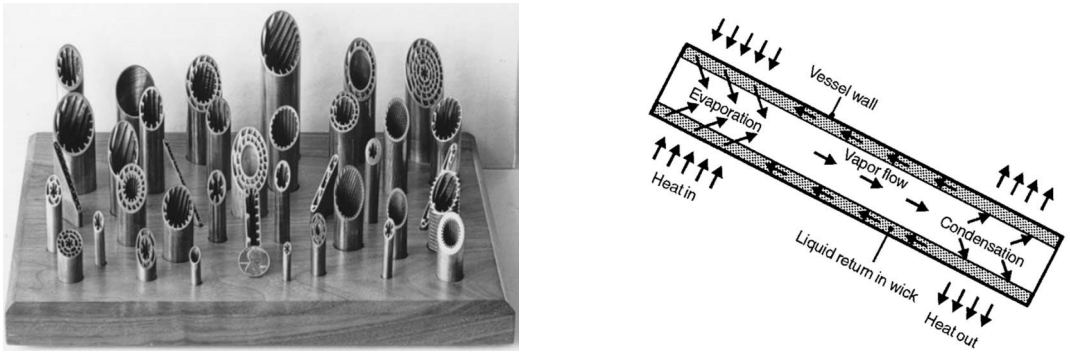

(a) (b)

Figure 1.10: Extended surface heat exchanger: (a) Internally finned tubes and (b) heat pipe heat exchanger (*Shah2003*)

Regenerator

Regenerators are a storage type heat exchanger and its exchanging surfaces are usually referred as a matrix of the regenerator. To have continuous operation, the matrix must be moved periodically into and out of the fixed streams of gases, as in a rotary regenerator.

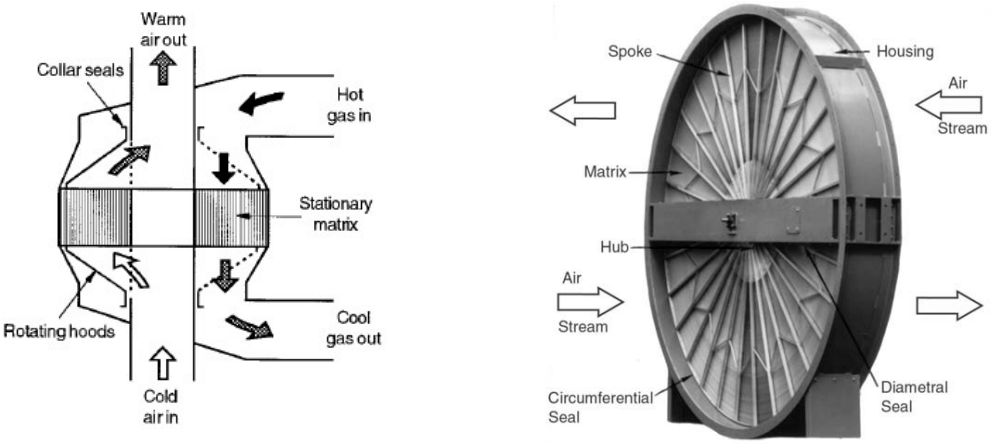

(a) (b)

Figure 1.11: Continuous matrix regenerator (*Shah2003*)

Another construction scheme state that the gas flows must be regulated by valves to and from the fixed matrices. This configuration is referred as a fixed matrix regenerator (Figure (1.11)).

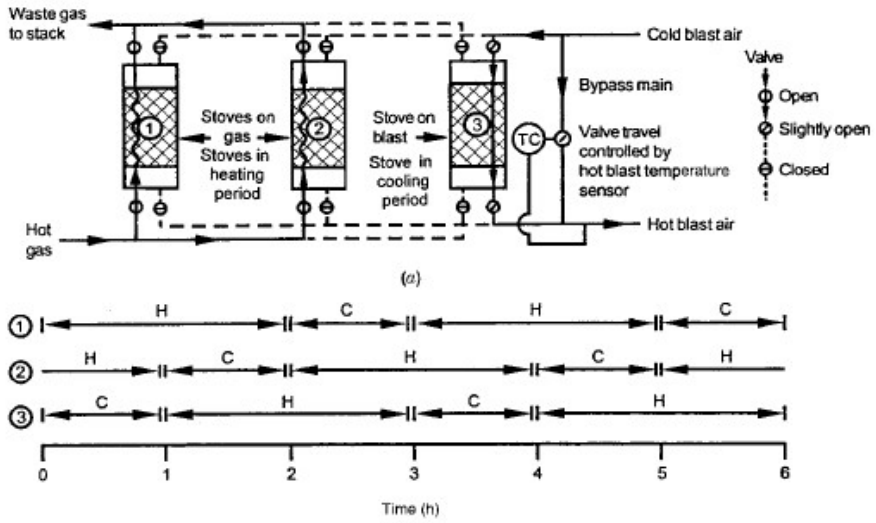

Figure 1.12: Intermittent three-stove fixed matrix regenerator: (a) plant configuration and (b) operating schedule (*Shah2003*)

CLASSIFICATION ACCORDING TO FLOW ARRANGEMENTS

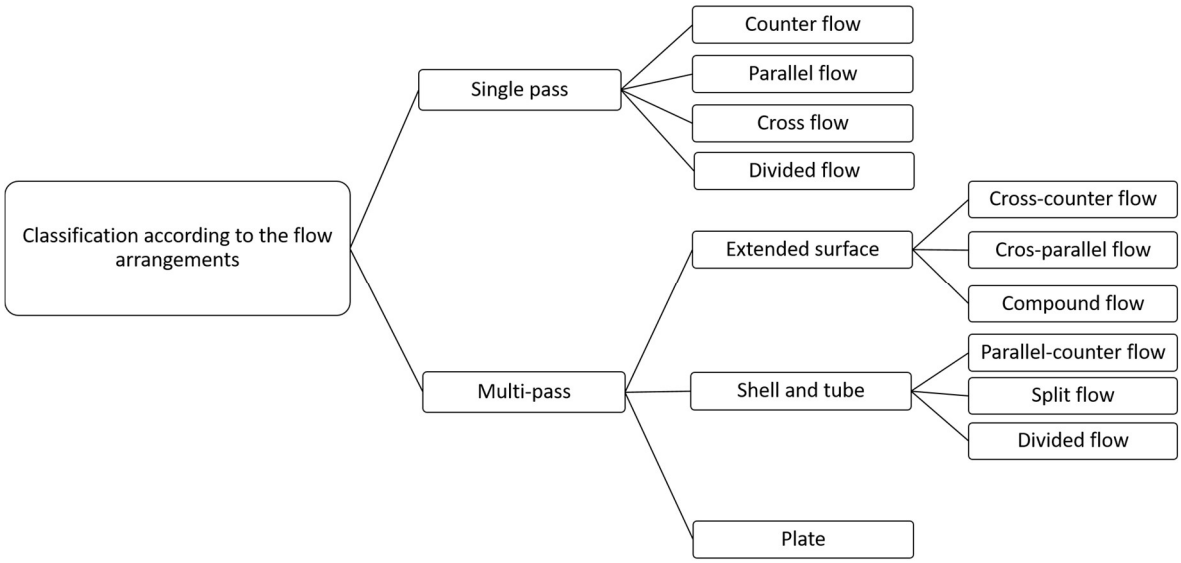

Figure 1.13: Heat exchanger: classification according to the flow arrangements

As it is possible to see in Figure (1.13), different choices of particular flow arrangement are available depending on the required exchanger effectiveness, available pressure drops, minimum and maximum velocities permitted, fluid flow paths, packaging envelopes, allowable thermal stresses, temperature levels, piping and plumbing considerations,

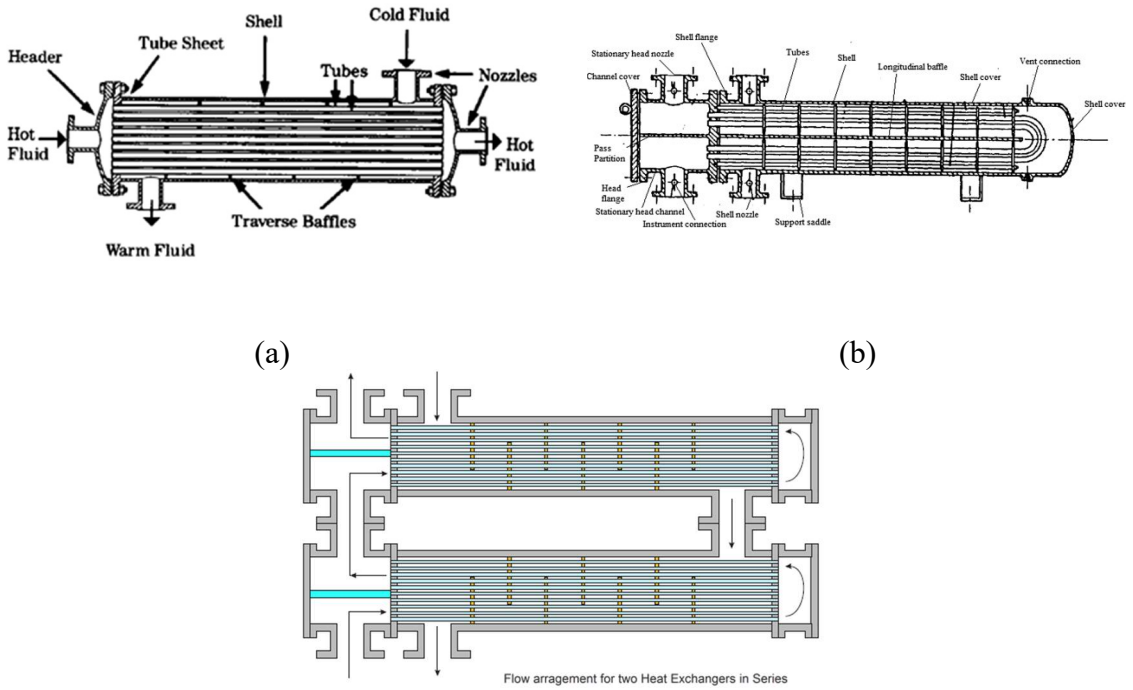

(a) (b)

(c)

Figure 1.14: Examples of multi passes shell and tube heat exchanger: (a) Single shell with single tube, (b) single shell with double tube and (c) double shell with double tube passes

or other design criteria. Fluid made one pass if it flows through the heat exchanger just one time. After the first pass, if the flow direction is reversed and fluid flows again through the heat exchanger, it is considered to have made a second pass that could be of equal or different size (Figure (1.14)). A *single pass unit* is defined as a heat exchanger in which both the fluids make one pass. Heat exchanger can be also subdivided according to the relative flow directions as: parallel, counter and cross flow if the flows are going in the same, opposite or orthogonal directions (Figure (1.15)).

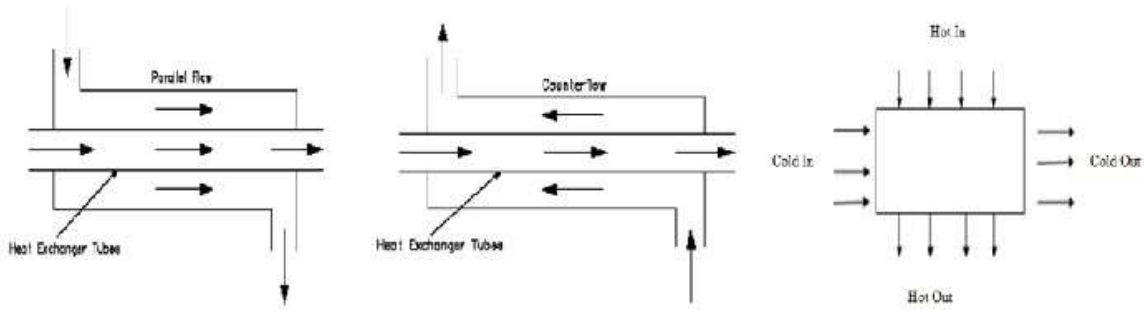

(a) (b) (c)

Figure 1.15: Different flows configurations: (a) parallel, (b) counter and (c) cross flows

CLASSIFICATION ACCORDING TO HEAT TRANSFER MECHANISM

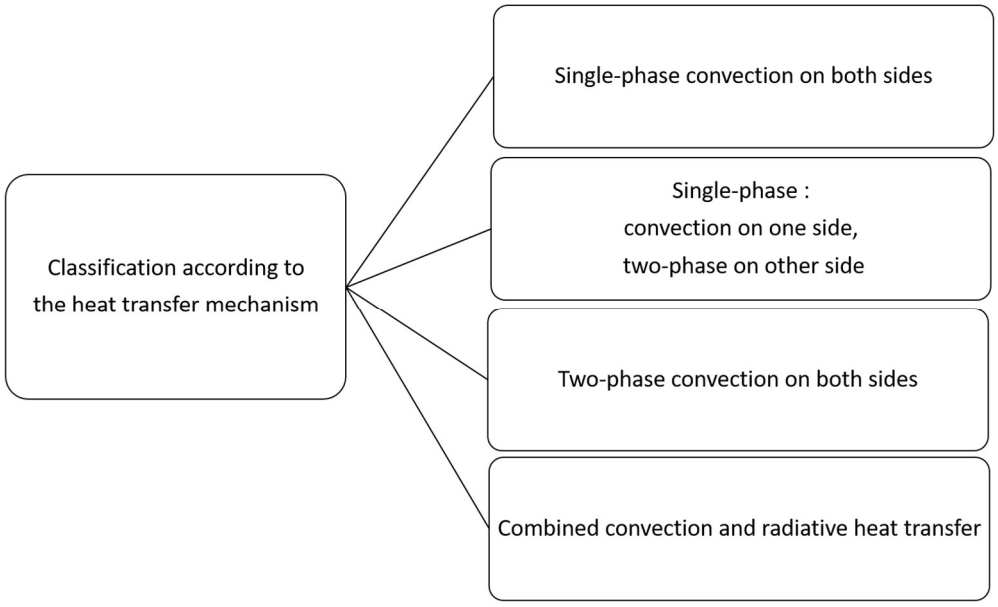

Figure 1.16: Heat exchanger: classification according to the heat transfer mechanism

The basic heat transfer mechanisms employed for transfer of thermal energy in indirect contact heat exchanger are: single-phase convection (that can be forced or natural), two-phase convection (e.g. condensation or evaporation), and combined convection and radiation heat transfer (Figure (1.16)). Any of these mechanisms individually or in combination can be active on each fluid side of the exchanger. Among all the possible application, usually single-phase convection on both sides occurs in: automotive radiators and passenger space heaters, regenerators, intercoolers, economizers, and so on. For what concern the single-phase convection on one side and two-phase convection on the other side occur in steam power plant condensers, automotive and process/power plant air-cooled condensers, gas or liquid heated evaporators, steam generators, humidifiers, dehumidifiers, and so on. The two-phase convection on both sides such as condensation on one side and evaporation on the other side, is common in air-conditioning evaporator. Radiant heat transfer combined with convective heat transfer plays a role in liquid metal heat exchangers and high-temperature waste heat recovery exchangers, while radiation heat transfer is a primary mode of transfer heat in fossil-fuel power plant boilers, steam generators, coal gasification plant exchangers, incinerators, and other fired heat exchangers.

1.3 Dimensional analysis

The governing heat transfer mechanism in the heat exchanger devices is the convection. Convection can be natural or forced, but it is in this second case that the convective heat transfer coefficient is higher. For this reason, it is of primary importance to study the set of differential equations that model the convection phenomena.

As already published literature (*Bejan1993*, *Incopera2002*), the system of differential equation that describe the heat transfer phenomenon in a general Cartesian coordinate system (x, y, z) for a Newtonian fluid in motion is composed by:

Continuity Equation:

$$\frac{D\rho}{Dt} + \rho \, div \, \boldsymbol{u} = 0 \tag{1.2}$$

Navier-stokes equations (or momentum conservation equations):

$$\rho \frac{Du}{Dt} = F_x - \frac{\partial p}{\partial x} + \frac{\partial}{\partial x}\left[\mu\left(2\frac{\partial u}{\partial x} - \frac{2}{3}\, div\, \boldsymbol{u}\right)\right] + \frac{\partial}{\partial y}\left[\mu\left(\frac{\partial u}{\partial y} + \frac{\partial v}{\partial x}\right)\right] + \frac{\partial}{\partial z}\left[\mu\left(\frac{\partial w}{\partial x} + \frac{\partial u}{\partial z}\right)\right]$$

$$\rho \frac{Dv}{Dt} = F_y - \frac{\partial p}{\partial y} + \frac{\partial}{\partial y}\left[\mu\left(2\frac{\partial v}{\partial y} - \frac{2}{3}\, div\, \boldsymbol{u}\right)\right] + \frac{\partial}{\partial z}\left[\mu\left(\frac{\partial v}{\partial z} + \frac{\partial w}{\partial y}\right)\right] + \frac{\partial}{\partial x}\left[\mu\left(\frac{\partial u}{\partial y} + \frac{\partial v}{\partial x}\right)\right] \tag{1.3}$$

$$\rho \frac{Dw}{Dt} = F_z - \frac{\partial p}{\partial z} + \frac{\partial}{\partial z}\left[\mu\left(2\frac{\partial w}{\partial z} - \frac{2}{3}\, div\, \boldsymbol{u}\right)\right] + \frac{\partial}{\partial x}\left[\mu\left(\frac{\partial w}{\partial x} + \frac{\partial u}{\partial z}\right)\right] + \frac{\partial}{\partial y}\left[\mu\left(\frac{\partial v}{\partial z} + \frac{\partial w}{\partial y}\right)\right]$$

Energy balance:

$$\rho \frac{De_i}{Dt} + p \, div \, \boldsymbol{u} = \, -div(\lambda \nabla T) + q_g + \mu \, \phi \tag{1.4}$$

where:

- ρ is the density of the fluid $[kg/m^3]$;
- $\boldsymbol{u}$ is the velocity vector of the fluid of components $\boldsymbol{u} = [u, v, w]$ along the x, y, z axes $[m/s]$;
- p is the fluid pressure $[Pa]$;
- μ is the local fluid dynamic viscosity $[Pa\ s]$;
- λ is the fluid thermal conductivity $[W/(m\ K)\ ]$;
- q_g is the internal heat generation rate per unit volume $[W/m^3]$;
- F_x, F_y, F_z are the components of the body force $\boldsymbol{F}$ along the x, y, z axes $[N]$
- ϕ is the dissipation function $[kg/(m\ s^3)\ ]$

- e_i is the specific internal energy $\left[\frac{J}{kg}\right]$
- $\frac{D}{Dt}$ is the total derivative defined as: $\frac{D}{Dt} = \frac{\partial}{\partial t} + u\frac{\partial}{\partial x} + v\frac{\partial}{\partial y} + w\frac{\partial}{\partial z}$

The dissipation function ϕ represent the rate at which the kinetic energy is irreversibly converted into thermal energy due to the viscous effects in the fluid. It is possible to show (*Bejan1993*) that, the dissipation function is expressed as:

$$\phi = 2\left[\left(\frac{\partial u}{\partial x}\right)^2 + \left(\frac{\partial v}{\partial y}\right)^2 + \left(\frac{\partial w}{\partial z}\right)^2\right] - \frac{2}{3}\ div^2\boldsymbol{u} + \left(\frac{\partial u}{\partial y} + \frac{\partial v}{\partial x}\right)^2 + \left(\frac{\partial v}{\partial z} + \frac{\partial w}{\partial y}\right)^2 + \left(\frac{\partial w}{\partial x} + \frac{\partial u}{\partial z}\right)^2 \tag{1.5}$$

Assuming the material to be homogeneous and isotropic, together with the Boussinesq's approximation, which states that the density variation in the fluid is not significant except for the buoyancy forces, it is possible to rewrite the continuity equation (Equation (1.2)) as follows:

$$div\ \boldsymbol{u} = 0 \tag{1.6}$$

Since it was already assumed the material to be homogeneous and isotropic, it is possible to re-write the Navier-Stokes equation (Equation (1.2)) in the vectorial form:

$$\rho\frac{D\boldsymbol{u}}{Dt} = \boldsymbol{F} - \nabla p + \mu\,\nabla^2\,\boldsymbol{u}$$

Under the assumption that the only force field applied to the fluid is the gravitational field, together with the Boussinesq's approximation considering the following temperature dependence for the density function:

$$\rho = \rho_\infty[1 - \beta\ (T - T_\infty)]$$

where ρ_∞ and T_∞ represent respectively the density and the temperature reference, while β is the thermal expansion coefficient defined as follows:

$$\beta = \frac{1}{\rho}\left(\frac{\partial \rho}{\partial T}\right)_{p=cost}$$

It is possible to write the vectorial Navier-Stokes equation as follows:

$$\rho \frac{D\boldsymbol{u}}{Dt} = \rho\, \beta\, (T - T_\infty)\boldsymbol{g} - \nabla p + \mu\, \nabla^2\, \boldsymbol{u} \tag{1.7}$$

It has to be pointed out that in many the cases the natural convection term, has the same or even higher magnitude compared to the forced convection term (e.g. natural convection heat exchangers or compound heat exchangers).

From the definition of enthalpy $e_i = h - \frac{p}{\rho}$, assuming the fluid to be ideal together with Equation (1.6) and the already assumed hypothesis of homogeneous and isotropic material, it is possible to re-write the energy equation (Equation (1.4)) as follows:

$$\rho\, c_p \frac{DT}{Dt} = \lambda \nabla^2 T + q_g \tag{1.8}$$

Since the heat exchangers coming from the same family are similar one to each other, it is possible the write the Equations (1.6-1.8) in a more general form using the dimensionless quantities appearing in the equation after the definition of some reference variables (*Cocchi1990*). A fundament of the dimensional analysis is the Buckingham theorem which states that any physical law can be expressed in terms of dimensionless parameters and that the number of these needed parameters is given by the difference between the independent variables and the fundamental physical quantities (Mass [M], Length [L], Time [T], Temperature [Θ], Amount of substance [N], Electric current [I], Luminous intensity [J]). A necessary condition for the use of this method is to consider physical situation geometrically similar in order to employ the same dimensional characteristic. In the case of flow in ducts the characteristic dimension is represented by the hydraulic diameter D_h. The principal dimensionless groups are:

Reynolds Number

This dimensionless group represents the ratio between the inertial and viscous forces. It is expressed as follows:

$$Re = \frac{W D_h}{\nu} = \frac{\rho W D_h}{\mu} \tag{1.9}$$

where W is the fluid average velocity on the duct's cross section expressed as $W = \frac{1}{A_c}\int_{A_c}(\boldsymbol{u}\cdot\boldsymbol{n})dA_c$ while D_h is the hydraulic diameter, $D_h = 4\frac{A_c}{\Gamma}$, assuming Γ to be the length of the perimeter of the cross section. The Reynolds number is used to define the motion regime of the fluid and, in the case of internal flow, the following classification is available:

- $Re \leq 2300$ the flow remains laminar since the viscous forces are sufficiently high to prevent the amplification of those small noise and distortion present in each stream;
- $2300 < Re < 10000$ it is a zone of transition in which viscous effects become less important compared to the inertial forces and the flow distortions are amplified;
- $Re > 10000$ the motion becomes chaotic and the flow regime is turbulent.

Prandtl Number

The Prandtl number expresses the ratio between the terms that represent the contribution due to the momentum transport and the one due to the energy transport respectively:

$$Pr = \frac{\nu}{\alpha} = \frac{\mu c_p}{\lambda} \tag{1.10}$$

where α is the fluid thermal diffusivity. The Prandtl number is a characteristic of the fluid and doesn't depend, as it happens for other dimensionless groups, from the regime of motion.

Nusselt Number

The Nusselt number is a dimensionless group widely used in the study of convection problems as it is the only one that contains the convection coefficient, necessary for the determination of heat exchanged by convection. The Nusselt number is defined as follows:

$$Nu = \frac{hD_h}{\lambda} \tag{1.11}$$

where the convective heat transfer coefficient h, in case of flow in confined space, it is given by :

$$h = \frac{q}{(T_s - T_b)} \tag{1.12}$$

where T_s is the surface temperature of the heat exchanger while T_b is the bulk temperature of the fluid defined as:

$$T_b = \frac{\int_{A_c} \rho c_p T \boldsymbol{u} \cdot \boldsymbol{n}\, dA_c}{\int_{A_c} \rho c_p \boldsymbol{u} \cdot \boldsymbol{n}\, dA_c} \tag{1.13}$$

It has to be highlighted that, if the thermal properties of the fluid can be assumed constant, the definition of the bulk temperature becomes:

$$T_b = \frac{\int_{A_c} T \boldsymbol{u} \cdot \boldsymbol{n}\, dA_c}{W\, A_c} \tag{1.14}$$

Grashof Number

The Grashof Number represents the ratio between the buoyancy forces and the viscous forces and it is used in cases of natural or mixed convection:

$$Gr = \frac{g\beta \Delta T D_h^3}{\nu^2} \tag{1.15}$$

In case of uniform heat flux a modified version of Grashof number can be defined as

$$Gr_q = Gr\, Nu = \frac{g\beta q D_h^3}{\nu^2 \lambda} \tag{1.16}$$

Before starting to see how the main dimensionless groups appear into the differential equations of convection it's necessary to define some dimensionless variables :

$$\boldsymbol{u}^* = \frac{\boldsymbol{u}}{W}; \quad p^* = \frac{p}{p_\infty}; \quad T^* = \frac{T - T_\infty}{T_s - T_\infty}; \quad z^* = \frac{z}{D_h}; \quad t^* = t\frac{W}{D_h} \tag{1.17}$$

where p_∞ is a reference values of pressure.

In the same fashion, it is possible to write the following dimensionless operators:

$$\nabla^* = \nabla\, D_h; \quad div^* = div\, D_h; \quad \nabla^{*2} = \nabla^2\, D_h^2 \tag{1.18}$$

Appling these dimensionless definitions to the continuity equation (Equation (1.6)), it is possible to write it in the dimensionless form:

$$div^* \boldsymbol{u}^* = 0 \tag{1.19}$$

In the same fashion, it is possible to write the Navier-Stokes equation (Equation (1.7)), generalized with the natural convection term in the dimensionless form:

$$\frac{D\boldsymbol{u}^*}{Dt^*} = -\nabla^* p^* - \frac{Gr}{Re^2} T^* grad^* z^* + \frac{1}{Re} \nabla^{*2} \boldsymbol{u}^* \tag{1.20}$$

Similarly to what already done, it is possible to write the energy equation defined by Equation (1.8) in a dimensionless form:

$$\frac{DT^*}{Dt^*} = \frac{1}{Re\ Pr} \nabla^{*2}\ T^* \tag{1.21}$$

1.4 Convective heat transfer enhancement

Among the heat transfer field, one of the most important research argument is related to the heat transfer enhancement techniques. This aspect becomes of particular interest in the industrial applications in which the thermal processing of high viscous fluids is required, such as the food, chemical, pharmaceutical and cosmetics industry. In fact, in these conditions, the fluid flow regime is necessary laminar, therefore the heat transfer efficiency of the heat exchanger is inevitably penalized. For this reason, engineers have been striving to increase the heat transfer coefficient, reducing at the same time the pumping power requirements. J.P. Joule in his studies dating back to 1861 (*Bergles1998*) was one of the first researcher that tried to increase the heat transfer coefficient in a condensing steam flow. In particular, he studied different experimental setups in order to understand the effect the many parameters on the heat transfer rate. Among all of these experiments, Joule investigated the influence of bended wire inserts introduced into the water flow of a refrigerator, acting as a water agitator. Today this research argument is attracting a renewed interest in the process industry due to the increase of the energy and raw materials cost. This new interest is witnessed by a huge amount of scientific papers and by the growing numbers of registered patents related to heat transfer enhancement technology or devices. These techniques essentially reduce the thermal resistance by increasing the heat transfer coefficients with or without the increase of the heat transfer surface. The benefits that can derive are, for instance, the reduction of the size of the heat exchanger, that means costs reduction, the decrease of the temperature difference at which they work, that means a reduction of the thermal stress for the product, or the increase of the thermal power exchanged. This appears clear from the general heat transfer rate equation for a two fluid heat exchanger:

$$Q = U\,S\,\Delta T \tag{1.22}$$

where $U\ [W/m^2K]$ is the overall heat transfer coefficient, $\Delta T\ [K]$ is an appropriate temperature difference and $S\ [m^2]$ is the heat transfer area.

Usually, the techniques that are able to increase the heat transfer can be divided into *active techniques* that require an external power input (e.g. mechanical aid, electrostatic fields) and *passive techniques* that do not require an external power except the increment of the pumping power requirement (*Bergles1998*). In order to evaluate the performance of heat transfer and enhanced heat transfer surfaces, several numbers of performance criteria have been developed (*Ylmaz2001*, *Zimparov2001*). However, it is not so easy to establish the performance of heat exchangers since it is influenced by many different factors that can be also conflicting. Among these factors there are the costs (investment and operating), the safety, the pumping power, the area reduction, the heat duty increase, the pressure losses, the compact fabrication, etc. Taking into account these items, many performance evaluation criteria have been suggested in literature for evaluating the heat transfer enhancement techniques. Yilmaz proposed a classification based on (*Yilmaz2011*) the:

- comparison of the surface or volume of a heat exchanger under constant heat power, flow rates and hydraulic losses;
- comparison of the heat power with constant surface or volume, flow rates and hydraulic losses;
- comparison of the hydraulic losses under constant surface or volume, heat power and flow rates;
- evaluation of the economical accounting;
- evaluation of the energetic efficiency;
- evaluation based of the second law criteria.

ACTIVE TECHNIQUES

Within this category the most common applications are related to mechanical aids, vibrations, electrostatic fields and injections (*Bergles1998*; *Webb1994*).

Mechanical aids

Among the mechanical actions used as a technique for increasing the convection heat transfer, one common application is the scraped surfaces heat exchanger. In particular, those devices are widely used for the treatment of viscous fluids in the process industry. Reviews of the most widely used correlations are reported by Härröd (*Härröd1986*), Abichandani (*Abichandani1987*) and Skelland (*Skelland1958*). An interesting application related to the determination of heat transfer performance of SSHE (Scraped Surface Heat Exchangers) was presented by Rainieri (*Rainieri2004*). In particular the authors analyzed both synthetic and experimental data acquired on a coaxial SSHE pilot plant, especially designed for treating highly viscous fluid food enabling the estimation of an heat transfer correlation, expressing the Nusselt number as a function of the relevant dimensionless parameters.

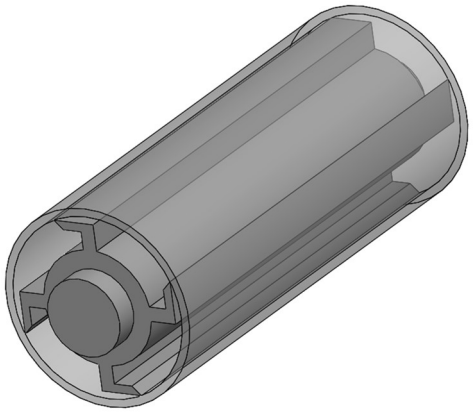

Figure 1.17: Scrapped surface heat exchanger scheme

A simple sketch of the apparatus used in their investigations is reported in Figure (1.17). Another kind of techniques that mechanically increase the heat transfer performance are the *rotating surfaces*. Those devices are commonly present in rotating electrical machines, in the rotor blades of gas turbines and in many other devices normally used in the industrial field. However, they can be also used with the purpose of increasing the heat transfer rate (*Bergles1998*). McElhincy (*McElhincy1977*) performed an experimental analysis of heat transfer from a condensing steam on the outside of a horizontal rotating tube. For rotations up to 40rev/min the cooling-side coefficient was slightly improved whereas at lower rotational speeds a significant deterioration of the cooling side coefficient was observed.

Mori (*Mori1967*) investigated the forced convective heat transfer in a straight rotating pipe around a parallel axis with a large angular velocity, while Miyazaki (*Miyazaki1971*) performed the analysis of the combined free and forced convective heat transfer of fluid flow in a rotating curved circular tube for the fully developed flow under a constant wall heat flux boundary condition.

Vibrations

The processes of heat transport can be strongly influenced by vibrations. In analysing the relationship between the heat transfer mechanism and the presence of vibratory phenomena, it is necessary to distinguish between wall vibrations and vibrations propagated into the fluid flow.

Surface Vibration

A fundamental element in the enhancement of the heat transfer is the control of fluid motion in the proximity of the wall. An efficient solution to increase heat transfer is to promote a renewal of the fluid that is near the wall. The main effects expected by a periodic movement of the surfaces in contact with the fluid are fluid mixing and boundary layer disruption. A possible way to realize it, consists in using movable walls at the location where heat transfer takes place. On the other hand wall deformation brings with itself some disadvantages, such as for example structural problems and noise. The easiest method to study the interaction between the heat transfer and the surface vibrations is to make the surface vibrate mechanically normally using an electrodynamics actuator. Usually, the frequencies used are below 1000 Hz since its has to be achieved an adequate oscillation amplitude. Normally, sufficiently intense vibrations lead to an increase of the heat transfer, but in certain situations, reductions of both the local and average Nusselt number have also been determined. The geometry commonly used for this type of heat transfer enhancement technique is the horizontal heated cylinder vibrating both horizontally and vertically (*Bergles1998*). Another possible solution is the oscillation of a flexible blade constituting a piezoelectric fan that produces the motion of the surrounding fluid (*Acikalin2004*). A positive element of this technique is that the piezoelectric fan can have very small dimensions permitting to reach the objective of compactness. Normally they are employed to promote the local motion of a fluid nearby a stagnant fluid area, increasing heat transfer in a hot spot, and so reducing local temperature.

Fluid vibrations

Sometimes it can happen that due to the large mass of the structure of the heat exchanger it is not possible or it is difficult to vibrate the surface. Thus, it is necessary to consider alternative techniques in which the vibration is transmitted directly to the fluid. The generators used for this kind of applications are of different types ranging from mechanical flow interrupter to the piezoelectric transducer. Using this methodology of transmitting vibration to the fluids it is possible to work in a frequencies range between 1 and 106 Hz. This solution is, however, certainly much more complex than that in which the vibrations involve the surfaces since it is much more difficult to define the vibrational variables and to describe the link between the heat transfer enhancement and vibration. Some studies related to the effects of sound fields on heat transfer from an horizontal cylinders to air, have been carried out by Fand (*Fand1961*). In particular, the authors performed an experimental study showing that the heat transfer from an heated cylinder is increased by a thermoacoustic streaming. Moreover, they proposed an empirical equation in order to find the convective heat transfer coefficient in case of an heated horizontal cylinder in the presence of horizontal transverse sound fields.

Electrostatic and magnetic fields

The electrostatic fields are applied in different ways in dielectric fluids (Figure (1.18)). In general, the electrostatic fields can be addressed to generate a greater mixing of the fluid and are particularly effective in increasing the heat transfer coefficients in the case of natural convection. One possible configuration is the one of a hot wire within a concentric tube maintained at a high voltage relative to the wire. The heat transfer coefficient can be significantly increased if a sufficient electric power is supplied. Interesting results were obtained also for laminar flows in forced convection: an increase of 100% was observed by applying voltages of the order of magnitude of 10kV with oil as working fluid (*Newton1977*).

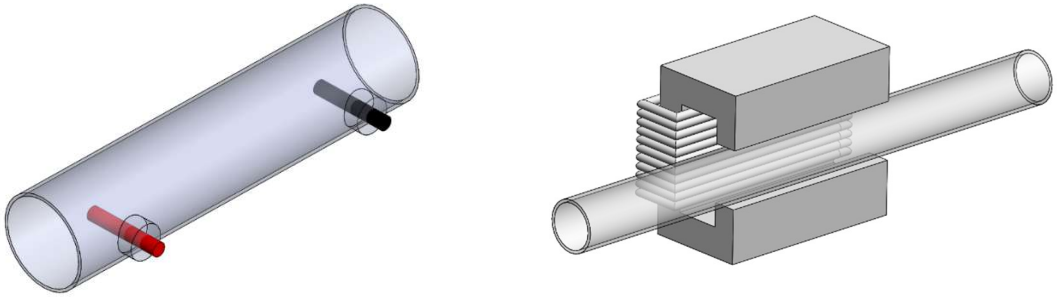

(a) (b)

Figure 1.18: Active heat transfer enhancement technique: (a) electrostatic and (b) magnetostatic techniques

Jet impingement

Injection is used in many industrial applications, as for example cooling of electronic devices, and it is based on the projection of a fluid at high speed towards a surface, increasing the convective heat transfer coefficient. The increment of the removed heat transfer rate is due to the breaking of the boundary layer together with the simultaneous mixing of the fluid in the proximity of the surface. The final effect is a significant increment of the convective heat transfer coefficient close to the stagnation region where the jets impinge on the plate. On the other hand, using this enhancement techniques the heat transfer augmentation decrease rapidly moving away from the impact zone. The elements that influence the convective heat transfer coefficient are in particular the nozzle geometry, nozzle-to-plate distance, jet Reynolds number, heat flux, velocity profiles and turbulence intensity (*Leal2013*). Normally this technique employs multiple jets to heat or cool extensively and uniformly the surface (*Oyakawa2009*). In absence of interaction between the jets, the increasing of heat transfer is comparable to the one obtained with the singular jet. The results are slightly different if there is interactions between the jets (interaction that it could happen before or after the impingement on the surface). If the interaction happens before the impingement on the plate, it can make the jet less powerful consequently reducing the heat transfer performance compared to the one without interactions. On the contrary, if the interaction between the jets happens after the impingement on the surface, it could rise a fountain flow that on one side enters the core of the closer jets reducing the heat transfer, but on the other side promotes a turbulence that increases the convective heat transfer coefficient producing global benefit effect (*Weigand2011*).

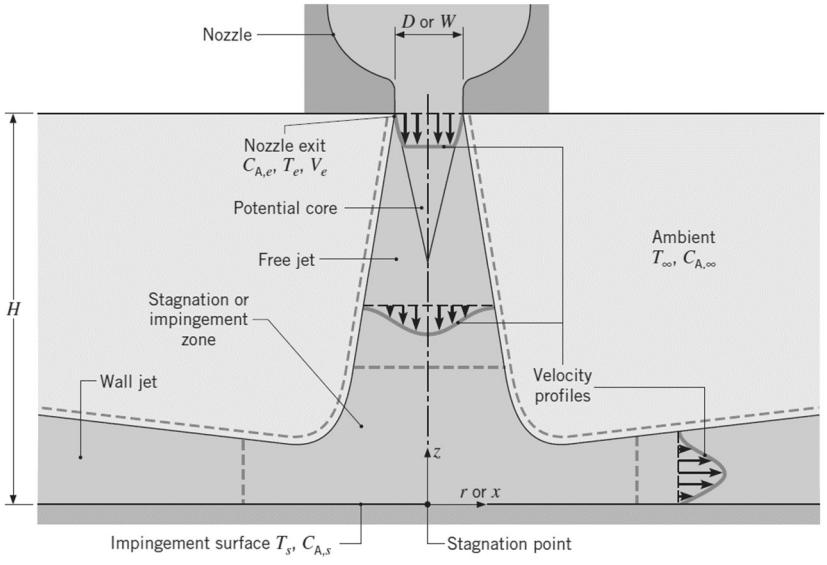

Figure 1.19: Jet impingement scheme (*Incoprera2002*)

Injection and aspiration

The increase in heat transfer performance can be also achieved by injecting gas through the porous surfaces of a heat exchanger. The injection of gas produces a shaking similar to that obtained in nucleated boiling, increasing the heat transfer rate up to 500% (*Gose1957*). An experimental study verified the hydrodynamic similarity between boiling and air bubbling inside a porous media (*Kudirka1965*); in particular, the author analysed the air injection within porous tubes in which ethylene glycol flowed; the results showed a parallelism within the two phenomena for gas-injection at low moderate bubbling rates. It was found out also an increase of convective heat transfer coefficient up to 130% compared to the one obtained in the absence of gas injection. Practical applications, however, are not very common due to the difficulty of inserting and removing the gas from the fluid. Even the suction is a technique difficult to use, especially for the insertion of the aspiration apparatus inside the ducts.

Figure 1.20: Example of flow injection: external and x-ray view of a gas turbine blade (*Incoprera2002*)

PASSIVE TECHNIQUES

The passive techniques for the enhancement of convective heat transfer are based on changes induced on the fluid flow through a proper conformation of the surface, such as curvature of the walls or surfaces roughness or corrugation or through the insertion of devices in the main flow direction or by means of additives (*Webb1994, Bergles1998*). The passive techniques are of great interest for industrial applications, since they do not require any external power except the increase of the pumping power. Those techniques are very common in industrial applications since they can be mounted after the commissioning, in already working plants, without any substantial modification to the plant and (especially) to its auxiliary systems. Finally, the manufacturing processes used to realize the passive heat transfer enhancement techniques are nowadays a consolidated technology.

Treated or coated surfaces

Those devices consist in surfaces that have a slight superficial alteration or a thin coating. These coatings can be either metallic or non-metallic and also continuous or discontinuous. They permit to significantly augment the heat transfer coefficient and are mainly used in applications that involve boiling and condensation (e.g. the use of Teflon as non-wetting coating in order to promote dropwise condensation (*Webb 1994*)). An estimation technique of the local heat transfer coefficient, based on the solution of the two-dimensional inverse heat conduction problem, has been adopted by Rainieri et al. (*Rainieri2009*). The authors investigated the effect of the surface wettability on the two-phase convective heat transfer in a dehumidifying process restoring the convective heat transfer coefficient distribution on aluminium plates coated with a hydrophobic oleic film.

Rough or corrugated surfaces

This typology of geometrical conformation of the heat exchanger is one of the first techniques used with the specific aim of producing an increase of the heat transfer by forced convection. They can be produced in different configurations and they can be integrated in the wall or obtained by placing a roughness adjacent to the surface. There are many industrial processes that could build the corrugation such as: moulding, casting and welding. The increase of the heat transfer rate promoted by this technique is also related to the appearing of a fin effect and the slightly increase of the heat transfer surface. Nevertheless, the advantages in terms of heat transfer are mainly due to the creation of turbulent motions and remixing of the fluid. In fact, in corrugated wall tubes, the most important effects are related to the macroscopic mixing of the fluid, activated by the destabilization of the flow which leads to the early transition from the laminar to the turbulent regime. Moreover, the interruption of the boundary layer locally increases the temperature gradient in the proximity of the wall with consequent beneficial effects on the convective heat transfer coefficient (*Rainieri1996*, *Rainieri2002*). This technique is primarily used for single-phase processes and are schematically showed in Figure (1.21). It is obvious that these typologies of heat transfer enhancement techniques increase also the pressure drop through the heat exchanger (*Ali 2001*). The increase of the heat transfer in the case of laminar regime obtained in this way is particularly important for applications that involve chemical and food industries, where the convective heat transfer coefficient is often confined within the intrinsic limit of the laminar flow regime. Furthermore, compared to the insert devices the advantage of the corrugated surfaces is to have no obstructions in the flow

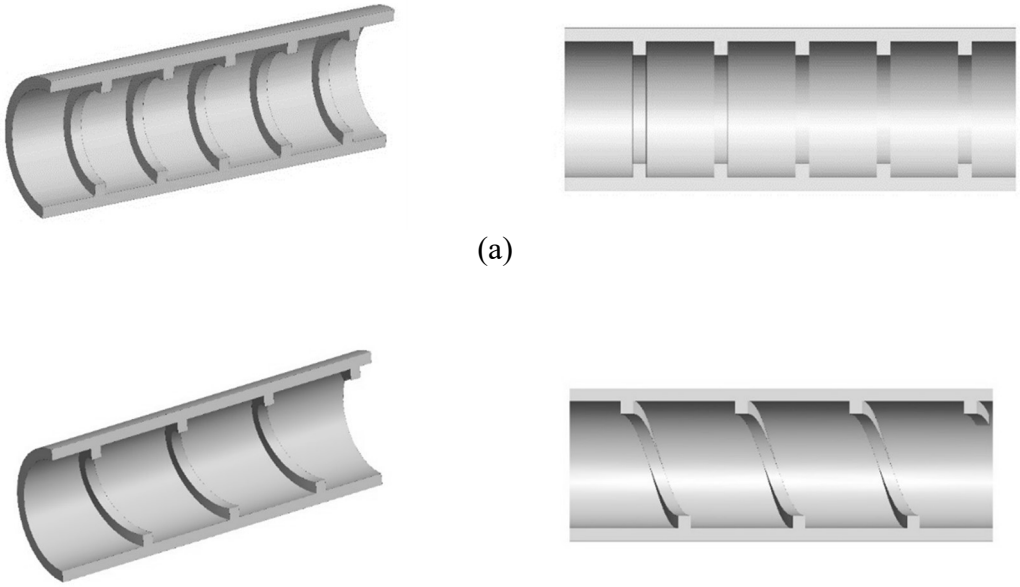

(a)

(b)

Figure 1.21: Corrugated surfaces (a) Transverse ribs (b) Helical ribs

path, and therefore they can also be used for fluids with solid suspensions or fibres avoiding the stream blockage risk (*Bergles1998*).

Extended surfaces

They are more commonly known as finned surfaces and they are characterized by a significant increase of the heat transfer surface. Flat fins are very common in heat exchangers since they are easy to be produced. Nevertheless, recent studies have led to change their shape with the purpose of increasing the heat transfer coefficients not only by expanding the surface area, but by also modifying the flow distribution. In particular, when there is the necessity to obtain heat exchangers with high surface area-to-volume ratio, the fins represent a very useful solution enabling the realization of more compact models. Many different possible geometrical configurations can be produced, as it is possible to see in Figure (1.22).

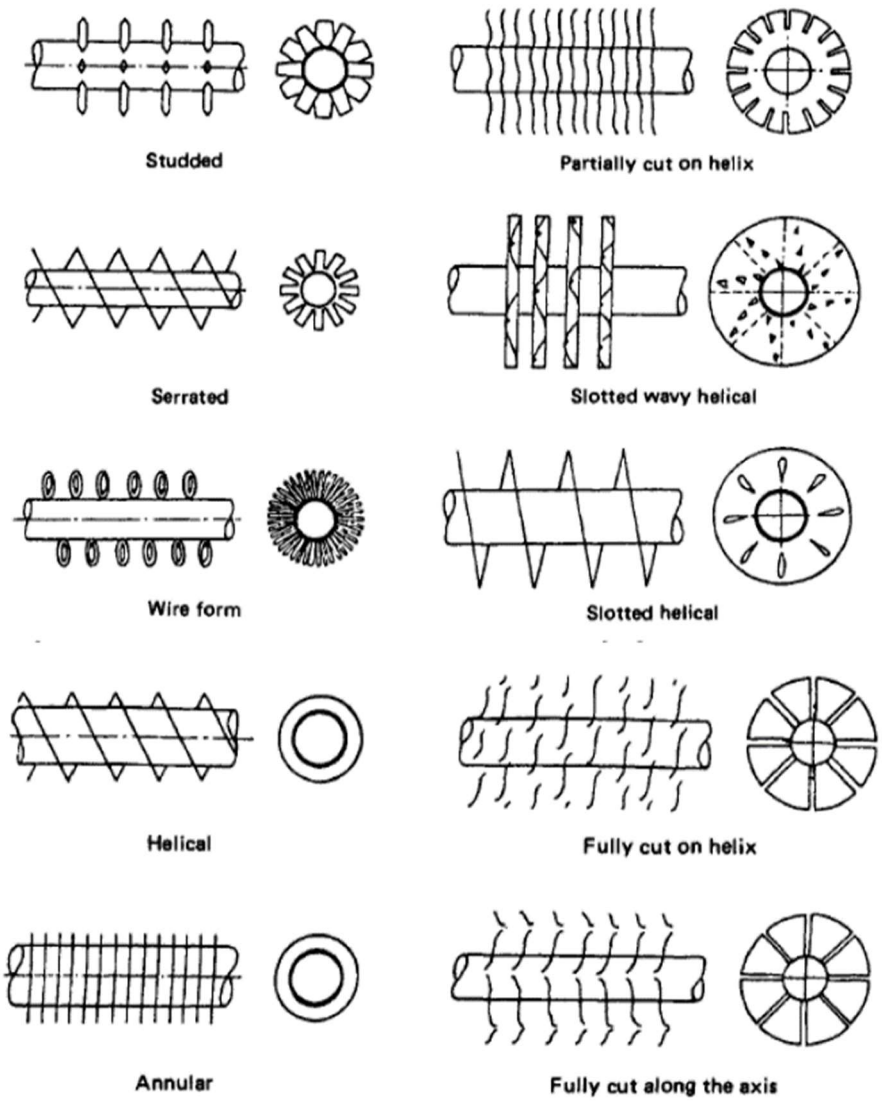

Figure 1.22: Extended surface typologies (*Shah2003*)

Inserts devices

They are elements that are positioned in the flow passage with the aim of increasing the heat transfer rate. The main reasons related to the heat transfer augmentation are the effect of fluid blockage, partitioning the onset of secondary flows that simultaneously promotes the mixing, reducing the boundary layer thickness. In literature, there are many typologies as well as configurations of insert devices but the most used devices are the displacement devices, wired coils and twisted tape. The effect related to the insertion of those devices is the reduction of the hydraulic diameter and the consequent enhancement of pressure drop and of viscous effect. It also produces an increase of flow velocity and sometimes promotes the onset of secondary swirl flows that increase the fluid mixing, yielding to an augmentation of heat transfer coefficient (*Dewan2004*).

Displaced enhancement devices

Using those devices the heated surface is left substantially unaltered, since the fluid flow path changes due to the presence of the insert in the flow stream thus increasing the energy transport phenomena. In the majority of cases the results obtained are interesting only for laminar flow regimes since the pressure drop becomes too high in the turbulent flow regime. The most used devices are metal grids, disks, cones, static mixers, crowns and balls. Promvonge (*Promvonge2008*) verified with an experimental study the effectiveness of the use of conical rings as displaced enhancement devices. In particular, different elements were inserted in the tube under test, as it is possible to see in Figure (1.23). The performances of the inserts were evaluated in terms of heat transfer enhancement and friction factor using different types of conical rings together with different aspect ratios and in different configurations (converging, diverging and converging-diverging conical rings).

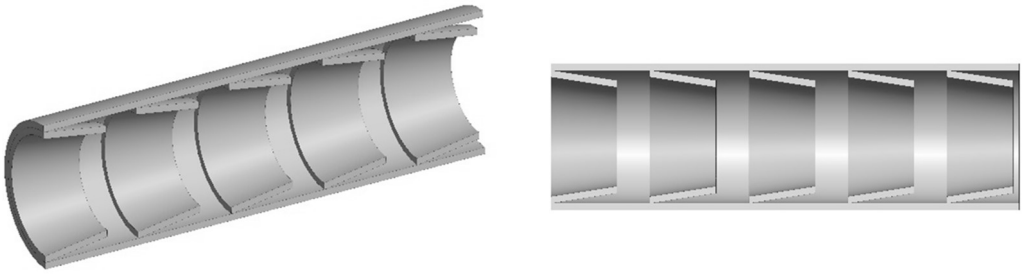

Figure 1.23: Conical rings insert device

The results show that both the ring to tube diameter ratio and the disposition of the conical rings influence the heat transfer. Moreover, the author found out that the best configuration, from the heat transfer point of view, is the diverging one. That configuration permitted to obtain an increment of heat transfer in terms of Nusselt number of about 330%. The converging and the converging-diverging configuration were also tested, and the author found that also those configurations are very effective since they reach an increasing of the Nusselt number of about 200% and 240%, respectively. It has to be pointed out that the usage of conical rings as a passive heat transfer enhancement techniques also increase the friction factor, as observed by Jadoaa (*Jadoaa2011*) that proposed to perforate the surface of the cone in order to reduce its pressure drop. His results showed that there were improvements both in terms of average Nusselt number and of friction factor compared to the case of non-perforated cones.

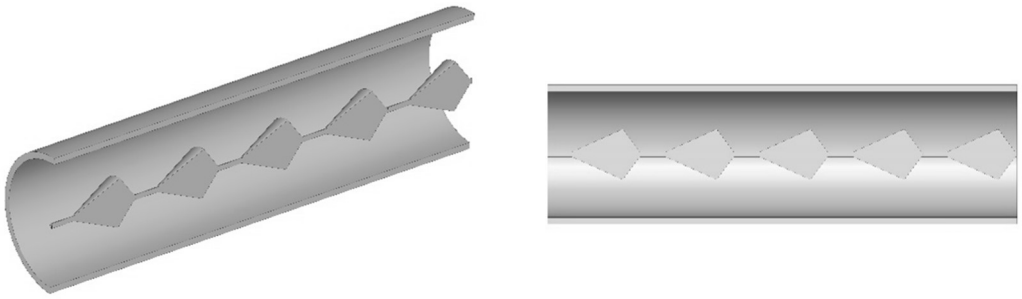

Figure 1.24: Diamond-shaped insert device

Eiamsa-ard (*Eiamsa-ard2010*) analysed another type of displacement devices based on a diamond-shaped turbolators in tandem arrangements inside a tube in a fully developed air flow filed.

The authors also proposed correlations for the Nusselt number and friction factor in order to evaluate the effects of using this type of devices on the heat transfer and pressure losses. Other interesting geometries were studied by Sununu (*Sununu1970*) Genetti (*Genetti1973*) using the *Keniks*® static mixer. This type of mixer is formed by several segments of metallic ribbon wrapped 360°, each of which is rotated 90° with respect to the previous one. In the experimental tests high-viscosity oil was used and an increment of about 150% was observed in terms of heat transfer rate together with a friction factor increment of 900%. Another type of mixer frequently encountered in literature is the *Sulzer mixer.* This device, usually used in turbulent flow applications, was experimentally studied by Van der Meer (*VanDerMeer1978*) using silicone oils as a working fluid. The authors observed an increment of 400% in terms of heat transfer. Unfortunately, for these devices, do not exist equations and relationships that can predict the average Nusselt number since there are so many geometries, which can be even not similar one to each other.

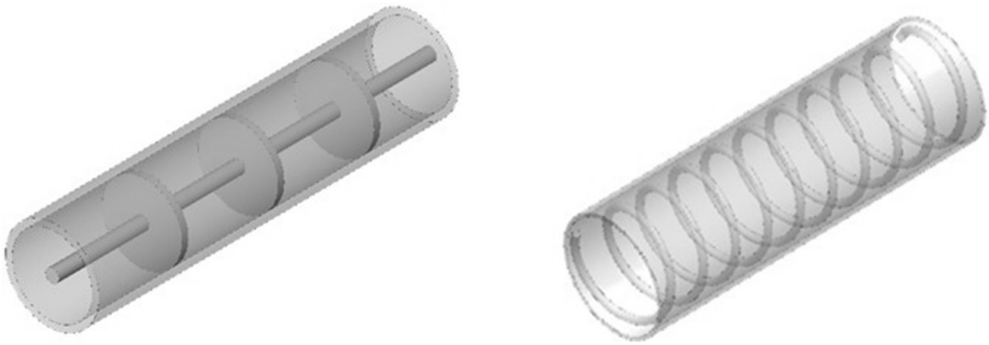

(a) (b)

Figure 1.25: Displacement devices: (a) disc and (b) wire coil

- *Swirl flow devices*

  Swirl flow devices are all those devices that are able to increase the heat transfer coefficient by generating a swirl flow (or a secondary flow motion) into the flow stream. There are a lot of different typology of devices within this family such as: twisted-tape inserts, inlet vortex generators, wire coils and axial core inserts with a screw-type winding (*Webb1994*). Date (*Date1972*) numerically investigated the heat transfer enhancement in laminar regime using viscous fluid under a uniform wall heat flux boundary condition. The authors simplified the flow conditions by considering negligible tape thickness, but considering the twist and fin effects related to this particular device. The same test case was experimentally investigated by Hong (*Hong1976*), who considered a laminar flow of water and Ethylene Glycol in an electrically heated metal tube with two twisted tapes inserted into the tube.

  The results showed an increment of the heat transfer in terms of Nusselt number up to nine times the ones obtained with the empty tube. Manglik (*Manglik1993*) proposed empirical correlations for the Nusselt number and friction factor, identifying a dimensionless swirl parameter.

  Wire coil inserts produces an heat transfer enhancement caused by the promotion to the turbulence regime.

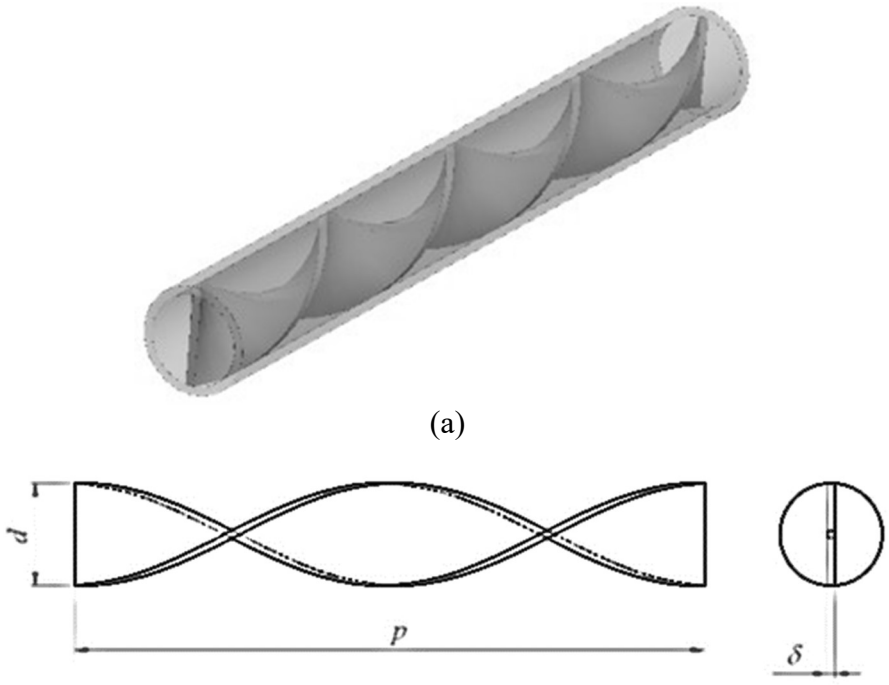

(a)

(b)

Figure 1.26: Twisted tape insert device

They also acts as roughness elements mixing the flow and producing secondary flow due to the generation of an helicoidal flow at the periphery (superimposed on the main axial flow).

Garcia (*Garcia2007*) performed a study of the flow mechanisms in tubes with wire coils using hydrogen bubble visualization and PIV techniques. The authors observed that at low Reynolds number (Re < 400) the flow in those type of tubes is similar to the flow in smooth pipes. In the Reynolds number range 400 < Re < 700 a recirculating flow appeared in short pitch wire coil, accelerating the transition to turbulence regime depending on wire coil pitch in the Reynolds range between 700 < Re < 1000.

Curved surfeces

Among the entire possible curved surface configuration, one common configuration in industrial plans are the coiled tubes. Those devices are a widely used passive heat transfer enhancement technique; they are usually employed in heat recovery processes, in air conditioning and refrigeration systems, in chemical reactors and food industry in general. The effectiveness of wall curvature is because it gives origin to centrifugal forces that induce a local maxima in the velocity distribution that locally increases the temperature gradients at the wall thus maximizing the heat transfer rate (*Naphon2006*). This solution, which often produces a swirl or helical type flow, appears very interesting also in the conditions in which the flow persists in the laminar regime (*Rainieri2011*).

Figure 1.27: Coiled tube heat exchanger

Additives for liquids

Different types of additive (*Webb1994*) could be inserted into the fluid flow in order to increase the heat transfer rate such as: solid particles, gas bubbles (for single-phase flow) and liquid traces (for boiling systems).

Solid particles for single-phase flows

Studies on the subject have been carried out by Watkins (*Watkins1976*) analysing the case of suspensions of polystyrene particles in a forced laminar flow of oil determining a maximum increase of the heat transfer of 40%.

Gas bubbles for single-phase flows

Tamari (*Tamari1976*) in their studies found out increases up to 400% of the average heat transfer coefficient value in case of air injected into water or Ethylene Glycol flows.

Additives for gas

The additives that could be used in a gas flow in order to increase the heat transfer coefficients could be solid or liquid. Dilute gas-solid suspensions are used as working fluids for gas turbines and nuclear reactors systems. The solid particles with a range of dimensions going from microns to millimeters are dispersed in the gas flow increasing the heat capacity of the mixture and facilitating the transport of enthalpy close to the heat transfer surface.

COMPOUND TECHNIQUES

Within this category there are all the possible combination or interaction of two or more different passive or active techniques. Compound techniques, are a promising tool for further enhancing the performances of thermal apparatuses, since the heat transfer coefficients are expected to be higher than any of the several techniques acting alone (*Kuppan2000*). Zimparov (Zimparov2002) presented an interesting article on compound technique based on corrugation wall and twisted tape inserts; in particular, the author experimentally investigated the heat transfer and the pressure drop in spirally corrugated tubes combined with five twisted-tape inserts in the Reynolds number range $4 \cdot 10^3$-$6 \cdot 10^4$. The authors observed higher heat transfer coefficients and friction factor than those of the smooth tube under the same operating condition. Promvonge (*Promvonge2008a*) experimentally studied the thermal augmentation in circular tube fitted with twisted tape and wire coil turbolators. The wire coil was inside the tube and the twisted tapes were inserted into the wire coil to create a swirl flow along the tube wall. The authors observed that the combined use of wire

coils and twisted tapes permitted to obtain double increase respect to their use alone (within the Reynolds number range investigated). Promvonge (*Promvonge2007*) experimentally investigated the heat transfer enhancement in a circular tube fitted with conical nozzles together with a snail swirl generator at the inlet of the tube to provide swirling flow. The fluid was subjected to a uniform wall heat flux boundary condition and the authors observed an increment of 316% over the plain, bigger than those obtainable with their use alone (278% for conical nozzle and 206% for the snail).

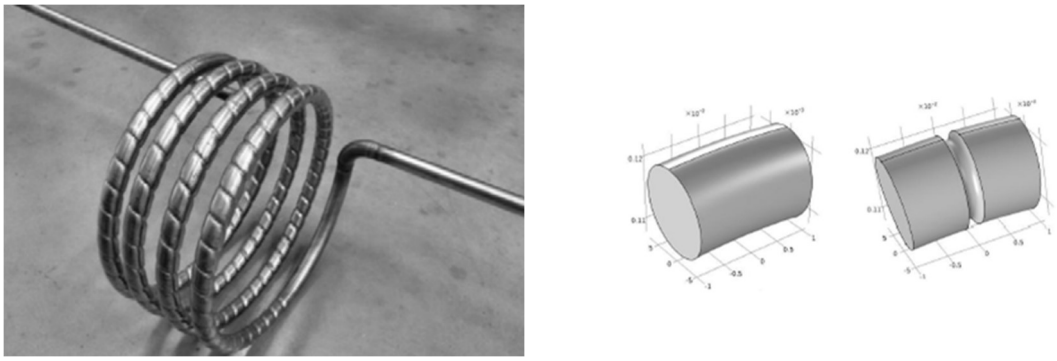

(a) (b)

Figure 1.28: Example of compound convective heat transfer enhancement: (a) experimental apparatus and (b) computational domain

Chapter 2

Inverse Heat Transfer Problems

2.1 Introduction

Inverse Heat Transfer Problems (IHTP) deal with estimation of unknown quantities appearing in the analysis of physical problems in thermal engineering by using temperature or flow measurements.

The standard heat transfer problems, usually known as *direct problems*, concerns the determination of the effect starting from the causes (e.g. the computation of a temperature field in a body starting from the boundary heat flux conditions). On the other hand, the inverse problems involve the estimation of the causes (e.g. boundary heat flux) from the measurement of their effect (*Ozisik 2000*). The impossibility to determine the exact solution is emphasized by the usage of the word "estimation". This impossibility is related to the presence of errors in the measurements that affect the accuracy of the reconstruction (*Beck1985*).

In recent years, the interest in the theory and application of the Inverse Heat Conduction Problems has significantly grown, covering almost every branch of science and engineering:

mechanical, aerospace, chemical, nuclear, medicine, ect. with different targets and applications.

In a more general way, the inverse approach has to be used when the established classical method for the direct estimation and measure of the unknown parameter is not possible. This necessity could be derived from the absence of the instrumentation able to measure the unknown parameter, the impossibility to directly measure it or the direct measurement of the parameter would not provide the desired degree of accuracy.

Among all the applications previously introduced, the one that played the main role in the development of solution techniques for the IHTP was the space program in late 50's and early 60's. For example, the aerodynamic heating of the space capsule during the re-entry in atmosphere is so high that the surface temperature of the thermal shield could not be directly measured with temperature sensors. For this reason, the temperature sensors were installed behind the thermal shield while the external wall temperature of the shield was recovered by inverse analysis. By using the same reconstruction strategies it was possible to estimate the thermophysical properties of the shield during the operating condition as well as the heat flux at the wall subjected to high heating due to the air friction during the re-entry procedure.

It has to be pointed out the mathematical difficulties in the solution of the IHTP. From the mathematical point of view, inverse problems belong to a class of problem called *ill-posed problems* (*Alifanov1977, Hadamard1923, Tikhonov1977, Beck1997, Alifanov1994, Beck1985, Tikhonov1963*), while direct heat transfer problems belong to a class called w*ell-posed problem*. The concept of well-posed problem, that was originally stated by *Hadamard (Hadamard1923)*, require that the solution has to satisfy three conditions:

- The solutions must exist;
- The solution must be unique;
- The solution must be stable under small changes to the input data (e.g. stability condition).

The concept of ill-posed problem (*Hadamard1923*) is breafly exposed in Figure (2.1). Looking at the upper part of the figure, it is possible to see that in a direct problem, which is well-posed, high perturbation of the input parameters does not affect much the image: this is the case of the parameters *A* and their image *A'* or the parameters *B* and their images *B'*.

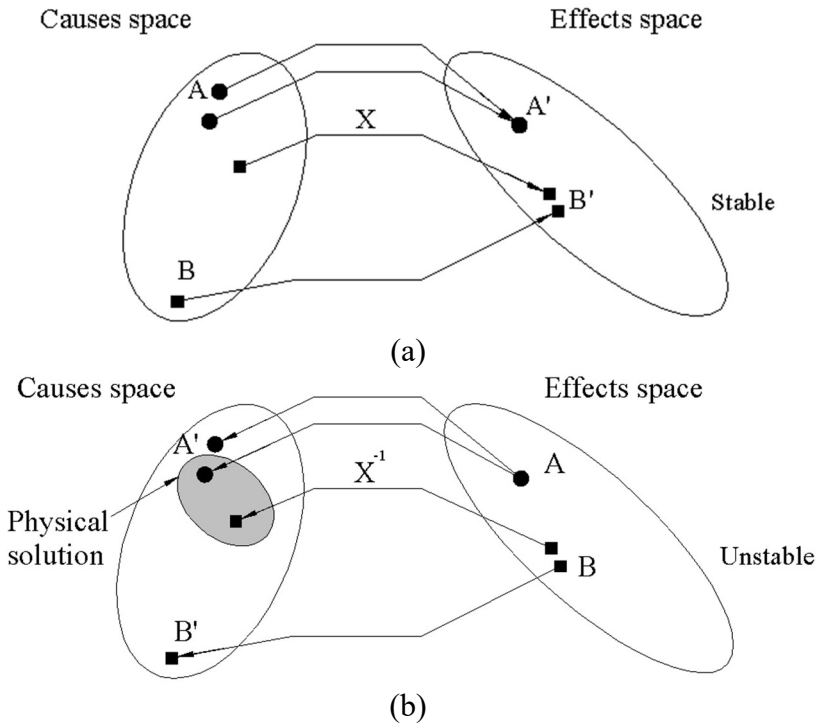

Figure 2.1: Graphical interpretation of the Hadamard ill-posed problem concept (a) Direct problem and (b) Inverse problem

For what concerned in the lower part of the Figure (2.1), it is possible to see that in the inverse formulation, the non-uniqueness and the instability of the parameters that has to be estimated could dramatically affect their reconstruction. In order to avoid this issue, some hypothesis on the physical solution have to be done in order to restrict the possible set of solution selecting one particular solution that is "*more correct*" than the other.

For a long time it was thought that the Hadamard criteria were strictly necessary in order to inverse problems, otherwise the results would be meaningless or would not have practical importance.

This barrier was removed by Tikhonov (*Tikhonov1977, Tikhonov1963, Tikhonov1975*), who developed a direct regularization procedure, Alifanov (*Alifanov1977, Alifanov1994, Alifanov1974, Alifanov1981, Alifanov1985a, Alifanov1978a, Alifanov1983, Alifanov1985b, Alifanov1978b, Alifanov1979, Alifanov1980, Alifanov1985c, Alifanov1995*) who developed an iterative regularization procedure, and Beck (*Beck1985, Beck1962*), who developed the function estimation approach.

The exact solution of an inverse heat transfer problems is impossible to be achieved, for this reason its estimated solution, generally involve the reformulation of the inverse problem as an approximate well-posed problem. In some of those methods, the solution of the inverse heat transfer problem is obtained using the *Least Squares Approach*.

Unfortunately, using this approach, the noise contained in the measurements, would corrupt the reconstruction, yielding to a meaningless solution. *Tikhonov* (*Tikhonov1963*), saw the possibility to upgrade the simple *Least Square Approach*, adding a penalty function, which plays the role of a damping factor, mitigating the disruptive effect of the noise present in the measurements.

In the *Iterative Regularization Approach,* the estimated solution is sequentially improved until it becomes stable with respect to the errors in the input data.

Giedt (*Giedt195*), who investigated the heat transfer at the inner surface of a gun barrel, presented one of the earliest discussion on the inverse thermal problems while *Stolz* (*Stolz1960*) presented one of the earliest numerical solution of the Inverse Heat Conduction Problem (IHCP).

Due to the extraordinary diffusion of high performance computers, the solution of the inverse heat transfer problem is now becoming attractive, also from the industrial point of view. This concerns especially industries characterized by a high-energy consumption that may be reduced by a better understanding of the physical phenomena that govern the installed heat exchanger. Many practical applications are reported by Beck (*Beck1977, Bozzoli2018*), especially related to the estimation of thermophysical properties of materials. Nevertheless, interesting researches were conducted in the control of the solid-liquid interface during the solidification (*Zabras1995*), boundary heat flux estimation inside pipe (*Huang1992, Bozzoli2017b*), estimation of the interface conductance between periodically contacting surfaces (*Orlande1993*), estimation of heat release during friction of two solids (*Alifanov1994*), estimation of local heat transfer coefficient (*Bozzoli2013, Bozzoli2014a, Bozzoli2014b, Bozzoli2016, Bozzoli2017a, Mocerino2018*), estimation of boundary shapes of solid domains (*Dulikravich1996*) and many others.

2.2 Mathematical concept

In order to better understand the physical significance of the inverse problem, consider a very simple example: 1D transient heat conduction problem in a semi-infinite solid heated by a sinusoidal surface heat flux of frequency ω. The problem is mathematically described by the following system of partial differential equation and schematically represented in Figure (2.2):

$$\frac{\partial}{\partial x}\left(k\frac{\partial T}{\partial x}\right) = \rho c_p \frac{\partial T}{\partial t} \qquad \text{in } x > 0 \qquad \text{for } t > 0 \qquad (2.1.1)$$

$$-k\frac{\partial T}{\partial x} = q(t) = q_0 \cos(\omega t) \qquad \text{at } x = 0 \qquad \text{for } t > 0 \qquad (2.1.2)$$

$$T = T_0 \qquad \text{for } t = 0 \qquad \text{in } x > 0 \qquad (2.1.3)$$

If in the system of Equations (2.1) the only unknown term is the temperature distribution *T(x,t)* in the interior region of the solid as a function of time and position, this problem is well-posed and is called *direct problem*, since the unknowns are the effects (the temperature distribution) related to the known causes (the imposed time-dependent heat flux at *x=0*).
It is possible to look at the mathematical system described by the Equations (2.1.1-2.1.3) as a linear system represented by an application matrix, that given the causes (e.g. heat flux distribution), is able to determine the effects (e.g. the temperature filed).

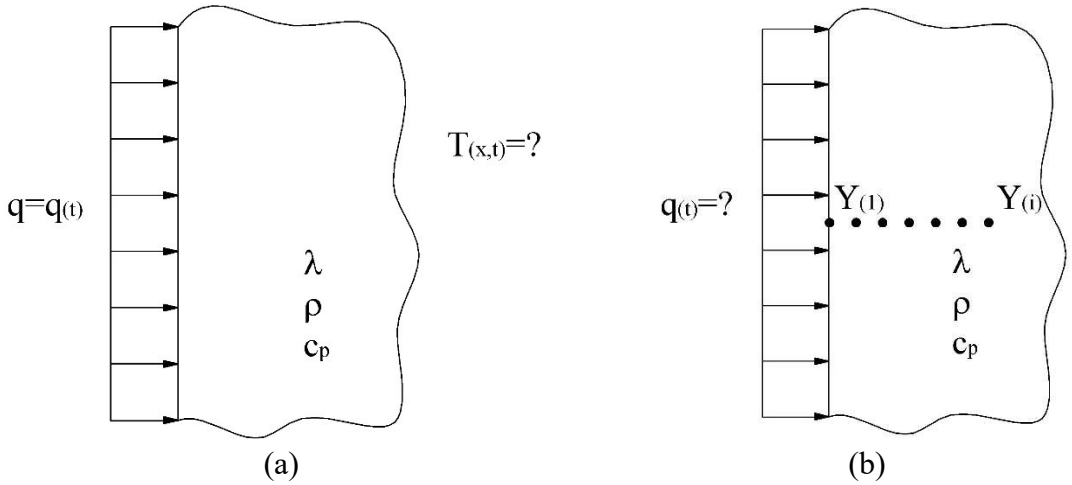

Figure 2.2: 1D transient heat conduction in a semi-infinity solid: (a) Direct problem and (b) Inverse problem

After a sufficient long time, the temperature solution also becomes periodic, yielding to:

$$T_{(x,t)} = T_0 + \sum_{\omega=1}^{N} \frac{q_0}{\lambda}\left(\frac{\alpha}{\omega}\right)^{1/2} \exp\left[-x\left(\frac{\omega}{2\alpha}\right)^{\frac{1}{2}}\right] \cos\left[\omega t - x\left(\frac{\omega}{2\alpha}\right)^{\frac{1}{2}} - \frac{\pi}{4}\right] \qquad (2.2)$$

where α and λ are, respectively, the thermal diffusivity and thermal conductivity of the material.

As it is possible to see from the Equation (2.2), the temperature response of the solid domain is lagged with respect to the imposed heat flux history. This lagging become more and more pronounced as far as the measurement point are located deeper inside the solid domain.

As it possible to see, due to the smoothness of the solution kernel (e.g. $\exp\left[-x\left(\frac{\omega}{2\alpha}\right)^{\frac{1}{2}}\right]$), small perturbations in the input parameter are not magnified in the calculation of the exact temperature distribution $T_{(x,t)}$. As it is possible to see in Table (2.1), a perturbation of 10% on the imposed heat flux, generate a perturbation on the local temperature of 4.2%.

Now, let us consider the same problem, but in this case, assume the imposed heat flux as unknown while all the other parameters are still known as an input data. In order to compensate the lack of information related to the unknown boundary condition, some extra-measurements were taken $T_{(x_{mes},t)} = Y_i$ at the interior point x_{mes} for different times $t_i = 1{:}\, t_f$ where t_f is the final time. Since the value of the boundary conditions is unknown, this new problem might be called an i*nverse problem* (Equations (2.3.1)-(2.3.4)).

$$\frac{\partial}{\partial x}\left(k\frac{\partial T}{\partial x}\right) = \rho c_p \frac{\partial T}{\partial t} \qquad \text{in } x > 0 \qquad \text{for } t > 0 \qquad (2.3.1)$$

$$-k\frac{\partial T}{\partial x} = q(t) = ? = unknown \qquad \text{at } x = 0 \qquad \text{for } t > 0 \qquad (2.3.2)$$

$$T = T_0 \qquad \text{for } t = 0 \qquad \text{in } x > 0 \qquad (2.3.3)$$

$$T_{(x_{meas},t)} = Y_i \qquad \text{at } x = x_{meas} \qquad \text{for } t > 0 \qquad (2.3.4)$$

Table 2.1: Problem stability

q_0	$\lambda\ [W/m\,K]$	$\alpha\ [m^2/s]$	$\omega\ [rad/s]$	$T_0\ [K]$	$T_{(0.8,\ 0.1)}\ [K]$
1000	15	10^{-5}	1	293.15	293.273
1100	15	10^{-5}	1	293.15	293.286

As previously observed, it is possible to look at the mathematical system described by the Equations (2.2.1-2.2.5) as a linear system represented by an application matrix, that given the effects (e.g. the temperature field), is able to estimate the causes (e.g. heat flux distribution). Due to the analytical solution of the direct problem, it is possible to simply invert the Equation (2.2) in order the get the estimation of the solution of the inverse problem:

$$q_0 = \left(T_{(x,t)} - T_0\right) \sum_{\omega=1}^{N} \frac{\lambda \exp\left[x\left(\frac{\omega}{2\alpha}\right)^{\frac{1}{2}}\right]}{\left(\frac{\alpha}{\omega}\right)^{\frac{1}{2}} \cos\left[\omega t - x\left(\frac{\omega}{2\alpha}\right)^{\frac{1}{2}} - \frac{\pi}{4}\right]} \tag{2.4}$$

and, using the same numerical example, it is possible to see that a perturbation of 4.2% on the relative temperature reading, yield to an error in the estimation of the unknown heat flux value q_0 of 10%. As suggested by Aster (*Aster2005*), this instability of the estimated solution of the inverse problem, is not only related to the noise presence in the measurements, but also to the smoothing that occurs in most of the forward problems and the corresponding roughening that occurs in estimating their inverse solution.

Related to the stability of the estimated inverse solution respect to the noise presence in the measurements, it is possible to calculate the maximum temperature oscillation at any location as setting the $\cos(\cdot)$ appearing in the Equation (2.2) equals to 1:

$$|\Delta T|_{(x)} = \frac{q_0}{\lambda}\left(\frac{\alpha}{\omega}\right)^{1/2} \exp\left[-x\left(\frac{\omega}{2\alpha}\right)^{\frac{1}{2}}\right] \tag{2.5}$$

It is easy to conclude that the maximum measured temperature difference must be greater than the measurements error; otherwise, it is impossible to distinguish if the measured temperature oscillation is due to the changing in the boundary heat flux or in the noise content in the temperature measurement.

As it is possible to see from Equation (2.5), as the frequency ω increases, the temperature difference decreases. Moreover, it has to be pointed out that the maximum temperature rise occur at $x = 0$:

$$|\Delta T|_{(x=0)} = \frac{q_0}{\lambda}\left(\frac{\alpha}{\omega}\right)^{1/2} \tag{2.6}$$

For any point inside the domain, it is possible to define the dimensionless temperature difference as:

$$\frac{|\Delta T|_{(x)}}{|\Delta T|_{(x=0)}} = \exp\left[-x\left(\frac{\omega}{2\alpha}\right)^{\frac{1}{2}}\right] \tag{2.7}$$

that highlights the sharply decrease of the temperature difference as far as the measurements are taken deeper in the solid domain. The last equation, also shows the high influence of the frequency; for example, assuming the smallest dimensionless measured temperature difference of 0.01, the sensors must be located until:

$$x < 4.6\left(\frac{\omega}{2\alpha}\right)^{1/2} \tag{2.8}$$

that, assuming the same material properties of Table 2.1, yields to: $x < 8.2\ [mm]$.

As it is possible to understand, it is fundamental the study of the sensitivity of the system with respect to the unknown variable, in order to build the most suitable experiment for its estimation. Usually this aspect goes under the *Design Of Experiments(DOE)* category (*Beck1977*) and it is strictly correlated to the estimation of the solution of the inverse problem; this occurs because in the design of experiments, it has to be find out the best experimental configuration that maximizes the sensitivity of the system to the parameter that has to be estimated.

Concluding, the main goal of the direct problem is the determination of the effects (e.g. temperature distribution) related to a specific causes (e.g. the heat flux distribution), while the main purpose of the inverse problem is to estimate the causes observing the effects at some specific locations. The concept was clearly explained by Ozisik (*Ozisik2000*): "*In the direct problem the causes are given, the effect is determined; whereas in the inverse problem the effects are given, the causes are estimated*".

The simple example presented in the previous paragraph is concerned to the Inverse Heat Conduction Problem (IHCP), but there are many others Inverse Heat Transfer Problems (IHTP) that could be related to: convection, radiation a mixed mode of heat transfer and many others. Moreover, it has to be observed that the considered example was related to the Boundary Inverse Heat Transfer Problem (BIHTP), but there are many other types of IHTP that could be related to the estimation of: Initial condition, energy generation, thermophysical properties and so on. A brief classification scheme is described in the next paragraph.

2.3 Classifications

The IHTP could be classified in many different way:

- Type of problem;
- Heat Transfer Mechanism;
- Dimensionality of the problem;
- Time dependency;
- Linear and non-linear inverse problem;
- Direct or iterative solution strategies;
- Parameter or function estimation;
- Direct problem solution strategy;
- Inverse problem solution strategy;

TYPE OF PROBLEM

The additional information that has to be extracted from a model, could be used to classify the inverse problems in three main groups:

- Control problem

  This type of inverse problem consists in finding the control law that satisfies an optimality criterion, usually called *cost function*. Commonly in these types of problems, the unknown control variable is the stimulus (e.g. the imposed heat flux distribution) while the feedback variable is the output of the model (e.g. the temperature distribution).

- System identification problem

  These particular types of inverse problems have to deal with the identification of the mathematical model of the system under test. It can be mainly related to two categories:

  - Model reduction

    The aim of this type of inverse problem is to identify a subset of equations that still are able to represent the physical model even if the detailed model was simplified. The use of a model that is too much simplified (e.g. the lamped parameter) can produce a systematic error that will affect the reconstruction quality diverging the prediction from the experimental observation and simulations. On the other hand, the choice of a too detailed model, with a high number of parameters, will significantly increase the computation cost to invert the model and will lead to an unstable solution because of the noise amplification. Due to the ill-posed nature of the inverse problem, usually is better a parsimonious model in terms of numbers of unknown parameters, but it is obvious that a balance between the measurement fidelity and the model simplification has to be found.

  - Experimental model identification

    Within the experimental model identification framework, the mathematical representation of the physical domain is assumed to be known, while the parameters inside the model are unknown. It has to be pointed out that the knowledge of the mathematical models as well as the physical meaning of the parameters inside the model, yields to a *white box* problem, while the experimental investigation of the model, that yields to a non-physical meaning of the parameter that are inside it, produce a *black box* model (there is no knowledge related to the physical meaning of the model and of its parameters).

- Inverse measurements problem

  In this type of inverse problem, the lack of information related to the unknown parameter, is overcome by adding some extra-measurements. Among this class of inverse problems, it is possible to find different applications:

  - Parameter estimation

    The parameter estimation is very common in the heat transfer field; in particular, the most common estimated parameters are the thermophysical properties of the material, such as thermal conductivity and specific heat capacity. It has to be

pointed out that it is possible to estimate the properties of both black, grey and withe box models; it is straightforward that the parameters in those three models have different meaning.

- Boundary values estimation

  Belong to this category all the problems that are dealing with the estimation of the location and the value of the stimulus. In the more general abstraction, the stimulus could be related to the entire volume, surface, line or point. It differs from the previous point since, in this case, the estimation concerns the imposed boundary condition (that could be different from one experiment to all the other) and not a property of the material (that is characteristic of that specific material).

- Initial state estimation

  This problem is closed to the boundary values problem, but in this case, the estimation is related to finding the initial value of the unknown variables and their evolution in time. It has to be highlighted that this type of estimation procedure could also require the estimation of the local unknown variables distribution, not only their evolution in the time domain.

- Shape reconstruction

  Usually the boundaries of the domain are fixed and known but in certain case, the shape of the domain or the location of an interface between two domains has to be found without its direct measurement (e.g. non accessible portion of the heat exchanger). This particular type of inverse problem requires the parametrization of the geometrical boundary of the problem in order to reconstruct it through inversion.

- Optimal design

  This approach can provide a methodology for a pertinent choice of inputs, location of measurements points, time observation window, etc. The choice of these design quantities can be made in order to maximize a criterion based on the sensitivity of the output observation to the unknown parameter.

HEAT TRANSFER MECHANISM

The classification of the inverse problems can be based on the governing heat transfer mechanism. In particular, it is possible to have:

- Inverse heat conduction problem:

  These types of problems are the most investigated. Due to the linearity of the problem with respect to many of the variables that could appear into the heat equation, which significantly reduce the computational time, most of the early studies on the inverse heat transfer problems concerned heat conduction. The application of the inverse analysis to problems involving convection and radiation is more recent, especially because they are not linear with respect to the imposed heat flux.
- Inverse heat convection problem:

  These problems are still under investigation. The estimation of their solution has a lot of practical applications but, unfortunately, they are nonlinear with respect to the convective heat transfer coefficient. Nowadays, the problem in bypassed by re-writing the inverse heat convection problem as a inverse heat conduction, for the estimation of the unknown heat flux, and then by the solution of one direct problem, the convective heat transfer coefficient could be estimated.
- Inverse heat surface radiation problem:

  Like the previews inverse problem types, the inverse heat surface radiation problem is could be nonlinear with respect the unknown variable. This issue was overcome by Alifanov (*Alifanov1994*) who showed how to linearize this problem respect to the unknown variables.
- Inverse hate transfer problem of mixed phenomena:

  This is the most general and varied group of the inverse heat transfer problems. Due to the high number of methodological difficulties, solution of this problems are not yet well developed (*Alifanov1994*).
- Inverse heat transfer problem of phase change materials:

  They are mainly related to the cast processing (*Zabras1988*), but there are many applications also related to the enhancement of the thermal performances of the thermal energy storage (e.g. melting wax).

DIMENSIONALITY OF THE PROBLEM

Inverse problems, like all the physical problems, can be also classified with respect to the dimensionality of the problem; therefore, it is possible to have 0D, 1D, 2D and 3D problems according to the physical dimension of the investigated problem. Obviously, from the historical point of view, the first inverse problem concerned the lamped parameter estimation (e.g. 0D) since the computation cost of this kind of problem is lower than all the others. It has to be pointed out that the model reduction based on both geometrical and physical consideration can reduce the computational cost significantly. This type of model reduction is based on physical observation of the geometrical domain under test and it is called *physical model reduction*.

TIME DEPENDENCY

Inverse problems can be classified with respect to the time-dependency of the problem. Therefore it is possible to have stationary or non-stationary inverse heat transfer problems. The stationary inverse heat transfer problems are characterized by properties that have the mean, variance and autocorrelation structure constant over time. Stationarity can be defined in precise mathematical terms, but from the practical point of view, the stationary regime is reached when the all the properties of the system (that could be the boundary condition, the physical equation or physical properties) do not change over time. On the other hand, the non-stationary inverse problem are characterized by the variation over time of at least one of the quantities (or its properties) appearing in the mathematical modelling of the phenomena.

LINEAR AND NON-LINEAR INVERSE PROBLEM

The possibility of the inverse problem to be linear with respect to the unknown variable is one of the most important aspects of the problem. This feature is strictly connected to the solution strategy chosen for the estimation of the solution. In particular, linear inverse problems are easier to be solved than the non-linear ones; for this reason, researchers started to study linear inverse problem. Moreover, if a problem is not linear, researchers try to linearize it in a small range of application. Besides the pedagogical importance of the linear problems, there are a lot of physical problem that are linear with respect to the parameters of interest. Nonlinear mathematical models arise when the parameters of interest have an inherently non-linear relationship to the observables ones. This situation commonly occurs,

for example, in electromagnetic field problems where we wish to relate geometric model parameters such as layer thicknesses to observed field properties.

As suggested by Beck (*Beck1977*), the practical way that could be followed in order to understand the linearity of a problem, respect to the parameters under test, is to calculate the sensitivity of the problem with respect to those parameters. If the problem is linear with respect to the parameters, then the sensitivity coefficients are bot function of the perturbated parameter, otherwise the problem is non-linear (*Beck1985*).

DIRECT AND ITERATIVE SOLUTION STRATEGIES

The solution strategy adopted in order to estimate the solution of the inverse problem could be another way to classify them; therefore it is possible to have direct or iterative solutions of inverse problems. The direct solution do not require any type of iterations, since they are able to obtain the solution in just one step. On the other hand, the iterative solution, require some iteration in order to get the best estimation of the unknown parameters. Usually, the iterative approach is used in non-linear inverse problem, since there is no direct connection between the effect and the causes; nevertheless the iterative techniques can also be applied to the linear inverse heat transfer problems solutions.

PARAMETER OR FUNCTION ESTIMATION

Inverse problems could also be divided into two classes: the parameter estimation and the function estimation. The distinction between the two techniques is different if it is stated by engineers or by mathematicians. Professor Lamm (*Lamm1999*) said: "M*athematicians generally think of function estimation as the determination of an infinity-dimensional function (not just a finite-dimensional discretization of a function, even though the dimension may be quite large). But, this is a theoretical concept, and when one goes to implement the theory, one typically resort to finite-dimensional approximation. This finite-dimensional approximation should converge to the infinite-dimensional function that is though*".

Due to the non-easy distinction between parameter estimation and function estimation, same aspects that are emphasized more in parameter estimation, than in function estimation are (*Woodbury2003*):

- A limited number of parameter are going to be estimated;
- Usually, problems are not so ill-posed, but they are usually non-linear with respect to the unknown parameters, even if the describing differential equations are linear;

- The parameters are usually referred to a physical properties of the material and not to external causes (e.g. the imposed heat flux);
- Parameter estimation analysis need to be coupled with the confidence intervals, otherwise the information is not complete;
- Parameter estimation requires a "good" modelling of the phenomena, in order to have a robust estimation of it properties;
- Parameter estimation requires a careful examination of the residual in order to check the adequacy of the mathematical model. Residual does not have trends that persist experiments after experiments (e.g. bias);
- The residual function (e.g. sum of squares or weighted sum of squares) has to be chosen according to the measurements error;
- Optimal experiment design is very important in order to have the best accuracy of the estimates.

On the other hand, some characteristic related to the function estimation, are:

- High number of parameter that has to be estimated;
- The problems are usually ill-posed; moreover, they can be also non-linear;
- Computational efficiency is crucial, especially in the calculation of the sensitivity parameters.

A classic example related to the parameter estimation, is the estimation of constant thermophysical properties, such as the thermal conductivity *k*. It has to be observed that, a function estimation problem could be reduced to parameter estimation problem if some informations related to the function that has to be estimated are available. For example, if the shape of the function that has to be estimated is known, then it is possible to reconstruct the information only estimating the coefficients appearing in its definition. Let's assume that the unknown heat flux distribution can be represented by the following polynomial equation:

$$f_{(t)} = P_1 + P_2 t + P_3 t^2 + \cdots + P_N t^{N-1} \tag{2.9}$$

or in a more general way:

$$f_{(t)} = \sum_{j=1}^{N} P_j C_j(t) \tag{2.10}$$

where P_j are the unknown coefficients while $C_j(t)$ are known trial function (e.g. sine and cosine, if the unknown function was approximated using the Fourier's series decomposition, or polynomial in complex form). It follows that, the function estimation approach, required to estimate the unknown polynomial heat flux distribution, could be reduced to a parameter estimation problem, in which the total number of unknown parameters has to be chosen in advance.

DIRECT PROBLEM SOLUTION STRATEGY

Many different solution strategies can be used in order to obtain the solution of the direct problem. In particular, the solution can be achieved by using exact or approximated methodologies. Among the exact solution strategies, it has to be pointed out the separation of variables, Laplace transform and the Duhamel's theorem. Usually, the analytical solution of the direct problem can be achieved only for simple cases, while the numerical formulation can be applied in more general applications. Like the analytical solution, the numerical one can be obtained in different ways, but the two most used approaches require the integral or the differential formulation of the mathematical model. Among the numerical solution schemes, it has to be pointed out the finite difference, finite element method, finite volume method, boundary element methods and finite control volume techniques. It has also to be highlighted that, in the literature, there are many other numerical solutions schemes that could also represent the numerical approximation of an analytical formulation (e.g. numerical formulation of the Duhamel's theorem).

INVERSE PROBLEM SOLUTION STRATEGY

In the more general case, the inverse problem can be a time dependent multi-dimensional problem and different solution strategies can be adopted in order to estimate the solution of the inverse problem. In particular, different strategies can be identified:

- Whole domain or sequential specification;
- Regularization methods;
- Trial function method;
- Filter method.

Let's go more into the detail.

Whole domain or sequential specification

In an inverse time dependent problem, the estimation of the unknown function can be achieved once the entire phenomena is concluded and the entire time and spatial measurement were acquired. This solution strategy is known as *whole domain estimation* and it is intrinsically a non-real time estimation, since all the information has to be acquired before all the unknown parameter could be estimated. On the other hand, if a moving window is applied to the incoming signal, which is assumed to be represented by a polynomial defined inside the window, it is possible to estimate the solution in a quasi-real time scheme. This solution strategy is known as *sequential function specification*, since window by window the unknown function distribution (the polynomial) has to be estimated.

Regularization methods

This approach is a modification of the *least square approach* in which a penalty function is added in order to dump the instability present in the estimated solution of the unknown function. The instability that usually characterize the estimated solution are non physical and related to the ill-posed nature of the inverse problems (unless special treatment of the instabilities is introduced). There are many different types of penalty functions and they are manly formulated as a whole domain estimator except for the case investigate by Beck (*Beck1984*) in which a sequential function specification approach was used in the regularization of the inverse heat conduction problem. Among the possible solution strategy for the linear inverse problem it has to be pointed out the: Ridge regression, damped least square, Tikhonov regularization, Alifanov regularization, maximum entropy regularization and many others. For what concerned the non-linear inverse problem, the algorithm proposed by Levenberg (*Levenberg1944*) and Marquardt (*Marquardt1963*) is frequently used.

Trial function method

This is a particular combination of the function specification with the regularization approach. Its formulation, given by Twomey (*Twomey1963*), require the minimization of a cost function that consists in a sum of squared criterion plus an addition a term that is a generalization of the regularization term, which consist of the difference between the unknown distribution and a predetermined “trial” function. The trial function can incorporate the prior information related to the shape of the expected heat flux or it could

be a simple function, such as a constant. Since the choice of the prior information is frequently subjective, different numerical experiments must be done in order to find a satisfactory distribution of the trial function. This approach could be used in the whole domain formulation as well as in the sequential function specification.

Filter method

It is possible to demonstrate that linear inverse heat conduction problem can be formulated as digital filter. This approach could be formulated as whole domain or as a function specification. It has to be pointed out that the approximation of the heat conduction problem, characteristic of this solution strategy, does not affect the validity of the approach. The digital filter approach is an important solution methodology (*Bozzoli2013*) since it is usually computationally more efficient than all the other techniques and it can run in a quasi-real time scheme. The digital filtering approach, also permits the simultaneously usage of different types of sensors reading in order to increase the reconstruction quality. Due to the utility of filtering techniques, there are numerous resources on their use in the physical sciences, engineering, and pure mathematics. For example, Gubbins (*Gubbins2004*) applied the Fourier filtering technique in order to understand the inverse theory in a geophysical context, while Kak (*Kak2001*) gave an extensive treatment of Fourier-based methods for tomographic imaging. This topic is also common in image processing: for example, Vogel (*Vogel2002*) discussed Fourier methods for image deblurring.

2.4 Applications

Modern complex materials have thermophysical properties strongly varying with temperature and position; for this reason, conventional methods based on the direct estimation of the thermophysical properties has become unsatisfactory. The same considerations are also valid for the industrial modern applications; usually, these applications require an accurate in situ estimation of thermophysical properties under actual operating conditions as well as estimation of the applied boundary condition.

Inverse problem techniques are also successfully used in the medical field, for the detection of skin and breast cancer as well as for the estimation of the thermal damage after laser ablation.

Related to the food industry, inverse heat transfer problems are successfully applied for the study of better thermal treatment of the foods as well as for the performance estimation of heat exchanger.

Inverse heat transfer problem approaches can provide satisfactory answers for the estimation of unknown quantities that are difficult (or impossible) to be measured. They can also provide information that could not be accessible due to physical restrictions; for this reason, the inverse problems formulation could be used to conduct experiments as close to the real conditions as possible.

There are a lot of possible applications of inverse problems, for this reason, the list here presented is not exhaustive but it contains the most common application in which the inverse heat transfer problems were successfully applied:

- Estimation of thermophysical properties;
- Estimation of radiation properties;
- Estimation of boundary conditions;
- Estimation of reaction function;
- Control and optimization;
- Estimation of boundary shapes of bodies;
- Non-direct sensor reading.

More in detail:

- Estimation of thermophysical properties

  The estimation of the thermophysical properties of materials is nowadays an extremely important topic, especially because engineered materials are becoming interesting and used in many industrial application.

  The estimation of temperature-dependent thermophysical properties has been generally treated as a parameter estimation problem. Dantas *et al.* (*Dantas1996*) applied the function estimation approach to the inverse problem of determining the temperature dependence of either, the volumetric heat capacity or the thermal conductivity. No information regarding the functional form of the unknown property were needed and the minimization of the cost function was performed in an infinite dimensional space of functions. The minimization algorithm used was the Conjugate Gradient Method with Adjoint Equation and the effects of sensor location on the inverse problem solution were also addressed through a sensitivity analysis framework. The accuracy of the presented solution strategy was examined by using transient simulated temperature measurements containing random errors. Such

simulated measured data were obtained from the solution of the direct problem, by considering six fictitious functionals form for the thermophysical properties. The chosen stopping criteria was the Morozov's discrepancy principle (*Morozov1984*). Results showed that the presented approach was able of recovering discontinues functions, which are the most difficult to be recovered by an inverse analysis.

A more practical application was presented by Jurkowski *et al.* (*Jurkowski1996*), who estimated the thermal conductivity of thermoplastics under moulding conditions characterized by a high pressure and temperature values. A specific apparatus was designed while a parameter estimation method was used for the experimental data processing. The research was based on the solution of a one-dimensional non-linear Inverse Heat Conduction Problem. The optimisation algorithm developed required the iterative evaluation of the cost function in order to solve the problem in an efficient and stable way. This new algorithm is a combination of the well-known Gauss (*Beck1977*), Levenberg (*Levenberg1994*) and Marquardt (*Marquardt1963*) algorithms of which the authors took the best feature of each one: speed (Gauss), stability (Levenberg) and convergence (Marquardt). The estimated results using this new algorithm were compared with each separated algorithm itself. They observed that the stability and convergence of the algorithm they developed was not related to the measurement noise. Moreover they observed that no convergence was reached using the Gauss method while the Levenberg algorithm reach the convergence very slowly compared with the Marquardt method that reached the convergence but to a wrong value. The same consideration related to the comparison between the Levenberg and Marquardt method was obtained by Davies *et al.* (*Davies1972*) and confirmed by Beck (*Beck1977*). Confidence intervals of the estimated parameters took into account errors both in the temperature measurements and in the model parameters, while the heat capacity was estimated from calorimetric measurements.

- Estimation of radiation properties

  The estimation of the radiation properties is becoming more and more interesting, especially because of the space industry, since in the deep space, the heat transfer could happen only through the radiation mechanism.

  One of the first works related to the inverse estimation of the radiation properties is by Li *et al.* (*Li1994*). The authors presented a methodology for the simultaneous estimation of the unknown temperature distribution and the diffuse surface

reflectivity in an absorbing, emitting, and isotropically scattering grey plane-parallel medium from the knowledge of the external radiation intensities. The inverse radiation problem was stated as an optimization problem in a finite-dimensional space and the conjugate gradient method of minimization was then used for its solution. The scheme was shown to be stable, insensitive to the initial guess and, in the absence of measurement errors, the estimated solution converged to the exact result. Moreover, the authors performed a sensitivity analysis respect to the unknown parameter. The inverse procedure was tested by using simulated measurement contaminated with different levels of noise on both the measurements of the radiation intensities of the two surfaces. With no measurement errors, the estimated solutions converged to the exact values. The estimation became more sensitive to the measurement errors as the optical thickness was increased.

Using the same minimization technique applied to the same cost function, Park *et al.* (*Park1999*) estimated the radiative parameter using the inverse framework with the simultaneous presence of radiation and conduction. They considered a parallelepiped enclosure in which the heat could be transferred via conduction and radiation. For the inverse solution, they measured the temperature in different location inside the enclosure and, using the conjugate gradient method suggested by Fletcher and Reeves (*Fletcher1964*), they were able to minimize the cost function consisting in the square root of the squared differences between the simulated and the measured temperatures. They used simulated measurements in order to study the feasibility of the problem and its accuracy. Since the temperature field is much more sensible to the absorption coefficient with respect to the scattering coefficient, its simultaneous estimation could not work unless the initial approximation was near to the exact value. In order to overcome this difficulty, the authors performed a two-stage estimation. In the first stage, they assumed to be known the less sensitive parameter (the scattering coefficient) and performed the optimization only on the most sensible parameter (the absorption coefficient), reaching its convergence. Once they got the estimated value, which was near to the exact one, they assumed it as known and started the optimization on the other variable (the scattering coefficient). Finally they performed the simultaneous estimation of both parameters, starting from their singular estimation.

Ertuk *et al*. (*Ertuk2001*) made a comparison of the performance, in terms of reconstruction quality, between three different types of algorithms: Conjugate

gradient (CG method), bi-conjugate gradient (BGC method) and truncated singular value decomposition (TSVD). The study concerned the reconstruction of the imposed boundary condition in a three-dimensional enclosure, that simulated a furnace. All the physical properties were assumed to be known as well as the geometry of the system. The authors observed that the bi-conjugate gradient method required more iterations that the conjugate gradient method. Moreover, they tried to compare the three methodologies using the same number of iteration and of singular values and iterations number for the TSVD, CG and BCG respectively. It has to be pointed out that this type of comparison is not exactly correct since the two quantities (number of singular values and number f iterations) have different physical meaning. Moreover, they showed the computational time required from all the three methodologies to perform the estimation, that is an interesting quantity, but is also interesting the number of times that the cost function was called. Finally they observed the loose of physical meaning, since for high noise level negative emissive powers were predicted. This situation is very common when we are dealing with an inverse problem; for this reason, bounded least square approaches were proposed in the past.

- Estimation of boundary conditions

  The estimation of the boundary conditions is one of the most important type of inverse problems. This type of problem has to deal with the reconstruction of unknown values of the boundary conditions.

  There are many applications related to the estimation of the boundary conditions, especially in the heat transfer enhancement field. Bozzoli *et al.* (*Bozzoli2013*) investigated optimal filtering of raw input data acquired by means of infrared thermographic technique in order to solve an inverse heat conduction problem. The authors tested their algorithm on both numerical and experimental data, showing the necessity of filtering the noise from the measurements in order to achieve a stable solution of the inverse problem. The experimental setup concerned the estimation of the heat source field on a thin conductive wall. The filtering technique approach was already successfully adopted in the literature with regard to the inverse heat conduction problem and it could be understood as a regularization method in the sense that it is based on computing the smoothest approximated solution consistent with the available data. The authors compared the effect of different filtering

techniques, namely the ideal low-pass, the Gaussian and the Wiener filter, focusing on the optimal choice of the cut-off frequency. The different filters were compared using synthetic 1-D periodic signal and then applied to the experimental temperature maps acquired on the rear surface of a copper thin plate on which two point heat sources were located. The authors observed that the particular shape of the transfer function that was derived by applying two consecutive Wiener windows, amplified the self-adaptive capacity of the filter by making it particularly suitable for de-noising thermal images by minimizing, at the same time, the undesired signal attenuation effect.

The same authors (*Bozzoli2014*) estimated the boundary conditions on the internal surface of a coiled tube. This device is often used as a heat transfer enhancement device since the presence of the Dean's vortices reduce the boundary layer, increasing the heat transfer capabilities of the device. This type of wall curvature is able to passively enhance the convective heat transfer and it is particularly effective in the thermal processing of highly viscous fluids. The highly uneven convective heat flux distribution along the circumferential coordinate, due to the presence of the secondary vortices, significantly impact the performance of the fluid thermal treatment. In their work, the authors estimated the local convective heat flux acquiring the temperature distribution maps on the external wall surface of the coil wall. Those measurements were used as an input data in order to solve the inverse heat conduction problem in the solid domain of the tube. The estimation procedure was based on the Tikhonov regularization technique, while the experimental campaign was particularly focused on the laminar regime. The authors concluded the local investigation in coiled tube, paying particular attention to the turbulent regime (*Bozzoli2017*) using the same solution strategy.

The inverse problem was successfully addressed by Hsu *et al.* (*Hsu2000*) for the estimation of the heat flux in a film condensation on a vertical surface. The inverse analysis was based on thickness readings, taken at several different points on the plate. The linear least square method was used in order to minimize the cost function that consisted in the mismatch between the measured and the simulated thickness of the condensed film layer. The methodology was tested using simulated measurements spoiled with different level of white noise with zero mean, in order to test the robustness of the approach. The authors observed that the algorithm

successfully deal with the estimation procedure, also with a few points of measurement.

- Estimation of reaction function

  The study of reaction-diffusion problems has several application, such as in chemical reactors analysis and in combustion processes. A vast amount of literature exists on the analysis and solution of linear inverse reaction problems. In the case of nonlinear inverse diffusion problem, the available works are mostly concerned with the estimation of temperature-dependent properties, such as thermal conductivity and heat capacity.

  One of the most interesting works concerning the estimation of reaction function was presented by Orlande et al. (*Orlande1994*). In this work the authors used a function estimation approach based on the conjugate gradient method with adjoint equation in order to estimate the unknown reaction function in a reaction-diffusion parabolic problem thorough the solution of an inverse problem. They assumed that no prior information was available on the functional form of the unknown quantity. Extra-temperature measurements were used in order to overcome the lack of information related to the unknown value of the boundary condition. Since the conjugate gradient method requires the solution of the direct, adjoint and sensitivity problems, the authors were able to identify the best position of the sensor in order to maximize its sensibility to the unknown parameter. The ability of the mathematical model to reconstruct the unknown function, was tested using synthetic data produce by numerical simulation. The robustness of the approach was then tested by spoiling the synthetic measurements with withe noise having zero mean. The results showed a good ability of the algorithm to estimate the reaction function using extra-temperature measurement also in the presence of noise in the temperature measurements.

  Related to the reaction function estimation, an interesting work was made by Brizaut *et al.* (*Brizuat1993*). The authors estimated the reaction function involved in a model of vulcanization of a thick piece of rubber. The reticulation kinetics was determined using different approaches, as for example: mechanical (rheometry), thermal (differential scanning calorimetry) or dielectric properties. The authors used the thermal reticulation model in order to estimate the reaction function. They tested the robustness of the algorithm using synthetic data spoiled with different levels of noise. Since the algorithm shown a good agreement between the estimated and the exact

solutions, the authors applied the algorithm also to experimental measurements. The only a priori information needed was the factorization of the temperature dependence; however, the kinetics that they obtained was the same obtained by other models, validating the mathematical model used. The authors concluded that the proposed method appear as a promising approach to construct new kinetic characterization equipment.

- Control and optimization

  Many problems of control can be understood as an inverse problem.

  One of the main researchers who applied the control theory to the inverse heat transfer problem was Zabaras. One of his main research topic was related to the control of the interface morphology during a solidification process in the presence of natural convection (*Zabaras1995*). In particular, the boundary heat flux was calculated such that a desired freezing front velocity and shape were obtained. A front tracking deforming finite element technique was employed in order to follow the solidification front. Moreover, a brief review of the front tracking deforming finite element technique for a general viscous incompressible material was presented. The minimization of the cost functional was performed by the conjugate gradient method via the solutions of the direct, sensitivity and adjoint problems. In particular, the inverse solidification design problem was decomposed into two independently solvable problems. The first of these problems was a direct convection problem in the liquid phase, while the second one is an inverse design problem in the solid phase that employs the interface heat fluxes calculated from the solution of the former problem. Finally, an example was presented for the solidification of a superheated incompressible liquid aluminium, where the effects of natural convection in the moving interface shape were controlled with a proper adjustment of the cooling boundary conditions.

  A similar project was investigated by Colaço *et al.* (*Colaço2006*), but in this work, the authors optimized the electrodes that control the magnetic field during the solidification process in the presence of natural convection, of a magnetic alloy, in order to control the solidification front. The work concerned the reduction and control the natural convection effects in a cavity filled with a molten material by applying an external magnetic field whose intensity and spatial distributions were obtained by the use of a hybrid optimizer, which incorporates automatic switching among several of

the most popular optimization modules: the Davidon-Fletcher-Powell (DFP) gradient method, a genetic algorithm (GA), the Nelder-Mead (NM) simplex method, quasi-Newton algorithm of Pshenichny-Danilin (LM), differential evolution (DE), and sequential quadratic programming (SQP). The solidification front shape, distribution of the charged particles in the accrued solid, and the amount of accrued solid phase in such processes can be influenced by an appropriate distribution and orientation of the electric field. The transient Navier-Stokes and Maxwell equations were discretized using the finite volume method in a generalized curvilinear non-orthogonal coordinate system. The inverse problem was formulated in order to find the electric boundary conditions in such a way that the temperature gradients along the horizontal direction were minimized. The optimization results have shown that it is possible to control the natural convection phenomena by using an externally applied electric field. This conceptually new approach to manufacturing could be used in creation of layered and functionally graded material objects.

Experimental application of the optimization interpretation of the inverse problem was also used in the determination of the best chemistry composition of a hard magnetic alloy (*Jha2016*). The generated candidate alloy compositions were examined for phase equilibria and associated magnetic properties using a thermodynamic database in the desired temperature range. These initial candidate alloys were manufactured, synthesized and tested for desired properties. Then, the experimentally obtained values of the properties were fitted with a multi-dimensional response surface. The desired properties were treated as objectives and were extremized simultaneously by utilizing a multiobjective optimization algorithm that optimized the concentrations of each of the alloying elements. A few of the best predicted Pareto optimal alloy compositions were then manufactured, synthesized and tested to evaluate their macroscopic properties. Several of these Pareto optimized alloys outperformed most of the candidate alloys on most of the objectives. A sensitivity analysis of each of the alloying elements was also performed to determine which of the alloying elements contributes the least to the desired macroscopic properties of the alloy. These elements can then be replaced with other candidate alloying elements such as not-so-rare earth elements.

- Estimation of boundary's shapes of bodies

  The inverse heat transfer problem was successfully solved also for the estimation of the boundary shapes of bodies.

  Among the scientific contribution from the scientific community, it has to be pointed out the work of Cheng (*Cheng2003*). In their paper, the authors presented a simplified conjugate gradient method for shape identification based on thermal data. The authors tested the reconstruction capabilities of the proposed algorithm using different simulated measurements. These test cases used three kinds of thermal data measured on the outer surface of a solid body, including temperature distribution, local heat flux distribution, and the overall heat transfer rate. Results show that for all test cases, the optimization process leads to acceptable accuracy for the objective functions of different forms. The authors made a very interesting work testing the algorithm capabilities in presence of different noise levels added to the measurements and with different initial guesses of the shape that had to be reconstruct. Moreover they performed the estimation using different measurement as well as using one type of measurement per time (e.g. only temperature, only heat flux, both of them, etc.).

  The identification of boundary's shape is more interesting in the structural mechanical application. In particular, Banks et al. (*Banks1990*) were able to identify structural flaws in a two-dimensional domain. For a thermal diffusion system with external boundary input, observations of the temperature on the surface were used in a least-squares approach. Parameter estimation techniques based on the 'method of mappings' were discussed and approximation schemes were developed based on a finite element Galerkin approach. Theoretical convergence results for both simulated noisy data and experimental data applied at the Nondestructive Measurement Science Branch at NASA Langley Research Center showed the ability of the methodology to identify flaws using thermal testing on structural materials.

  Another application related to the shape identification through thermal measurements, was done by Huang *et al.* (*Huang1995*). In particular, the authors estimated the solution of an inverse geometry heat conduction problem (shape identification problem) detecting the unknown irregular boundary in a two-dimensional domain. In order to solve the inverse problem, they used the Levenberg-Marquardt method (LM), for the minimization of the objective cost function,

comparing its results with the conjugate gradient method (CG). A sequence of forward steady-state heat conduction problems was solved, measuring the temperatures at different sensors locations. The authors observed that the conjugate gradient method was better than the Levenberg-Marquardt method since it: (i) needs very short computational time ; (ii) does not require a very accurate initial guess for the boundary shape ; and (iii) needs a few number of sensors. Finally, the effects of the measurement errors in the inverse solutions were discussed.

- Non-direct sensor reading

  This is a particular inverse problem application to the heat transfer field. Almost all the sensors are not able to directly measure the quantity that we are looking for. Let us consider a thermocouple. These are the most used sensors in thermometry, since they are small, cheap and accurate, if used with an understanding on their working mechanism. Thermocouple is a device that convert thermal energy into electrical energy. The first research related to this energy conversion was published by Seebeck (*Seebeck1823*), who observed that, when two different metals form a closed electrical circuit and their junctions are kept at different temperatures a current starts to pass inside the metals. The current flow generation depends on the material couple used and on the temperature difference between the two junctions. The Seebeck effect is actually the combination of two other phenomena: the Peltier effect (*Peltier1834*), which state that a temperature gradient in a solid generate an electromotive force within it, and the Thomson effect (*Thomson1848*), which state that the contact of two different metals generates an electromotive force. Usually the Thomson effect is negligible compared to the Peltier effect, if the thermocouple is properly designed. Since the thermal reading is related to the temperature difference between the two junction, we need to fix the temperature of one junction (called cold junction) in order to know the absolute temperature of the hot junction (used to probe the temperature in in the measurement point).

  The construction of the calibration curve that links the voltage measurement to the temperature of the hot junction is a typical parameter estimation problem in which we known the function (that could be an exponential function) and we would like to estimate its parameters.

Chapter 3

Solution techniques

3.1 Introduction

In the Inverse Heat Transfer Problem, many of the encountered difficulties are related to the non-stability of the solution, since small perturbations in the input data (e.g. noise contented in the temperatures measurements) could yields to a completely different estimated solution that has nothing to do with the physical system under study.
Since there are many different solution strategies that could be used in order to estimate the solution of the inverse problem, Beck (*Beck1979*) suggested a list of possible criteria useful to evaluate the different IHTP methods:

- the method should be stable with respect to measurement errors;
- the predicted quantity should be accurate if the measured data are of high accuracy;
- temperature measurements from one or more sensors should be permitted;
- the method should have a statistical basis and permit various statistical assumptions for the measurement errors;
- the method should not require the input data to be a priori smoothed;

- the method should be stable for small time steps or intervals, permitting to obtain an higher number of information and a better resolution of the time variation respect to those obtainable by large time steps;
- the method should not require continuous first derivatives of unknown functions. Furthermore, this method allows using functions containing significant discontinuities;
- the method should not be restricted to any fixed number of observations;
- the method should be able to consider complex physical situations, as composite solids, temperature variable properties, moving boundaries, combined modes of heat transfer, multi-dimensional problems and irregular geometries;
- a deep experience in mathematics should not be required in order to use the method;
- the computational cost should be moderate;
- the method should permit extensions to more than one unknown;
- the method should be easy to program.

3.2 Problems statement and solution techniques

Among all the possible problems that could arise in the heat transfer field, concerning a heat exchanger, two of the most interesting application are related to the estimation of the average and local performances of the heat transfer devices. The direct measurement of those two quantities is usually difficult, thus their estimation through the inverse heat transfer approach is required.

The present chapter is subdivided in two section: parameter estimation and function estimation. The subdivision is not related to the estimation capabilities of the inverse solution technique here proposed (some of the presented approaches could be used for both the parameter and the function estimation) while is related to the number of unknown variables that has to be estimated in order to characterize the heat exchanger. For this reason, two different problems are going to be introduced in order to define the practical application in which the IHTP was successfully applied. The same subdivision will be used in the next chapters for the presentation of the new solution methodologies (*Chapter 4*), their verification using synthetic data measurements (*Chapter 5*) and their application to experimental data sets (*Chapter 6*).

3.2.1 Parameter estimation

This category of inverse problem, usually have to deal with the estimation of a small/medium number of unknown parameters; for example, from the industrial point of view, it is interesting the estimation of the average performances of the heat transfer devices such as thermal, fluid dynamic and overall heat transfer efficiencies. Related to this aspect, it is possible to consider the physical problem, represented in Figure (3.1), which consists in a counter flow tube in tube heat exchanger.

The fluid that is passing through the system is assumed to be water in both the tube and shell side. Both the fluids are characterized by the thermal properties k, ρ and c_p which represent the thermal conductivity, density and specific heat, respectively. Those quantities are assumed varying with the temperature of the fluid. The temperatures at the inlet and outlet of both the tube and shell sides are assumed to be known as well as the two mass flow rates. The system is assumed to be in a steady state regime without exchanging energy with the environment. Therefore, it is possible to write:

$$Q = \dot{m}^T c_p^T (T_{in}^T - T_{out}^T) \tag{3.1.1}$$

$$Q = \dot{m}^S c_p^S \left(T_{in}^S - T_{out}^S\right) \tag{3.1.2}$$

where $\dot{m}$ and Q are the mass flow rate and the exchanged power, respectively.

Thus, the energy balance becomes:

$$\dot{m}^T c_p^T (T_{in}^T - T_{out}^T) = \dot{m}^S c_p^S \left(T_{in}^S - T_{out}^S\right) \tag{3.2}$$

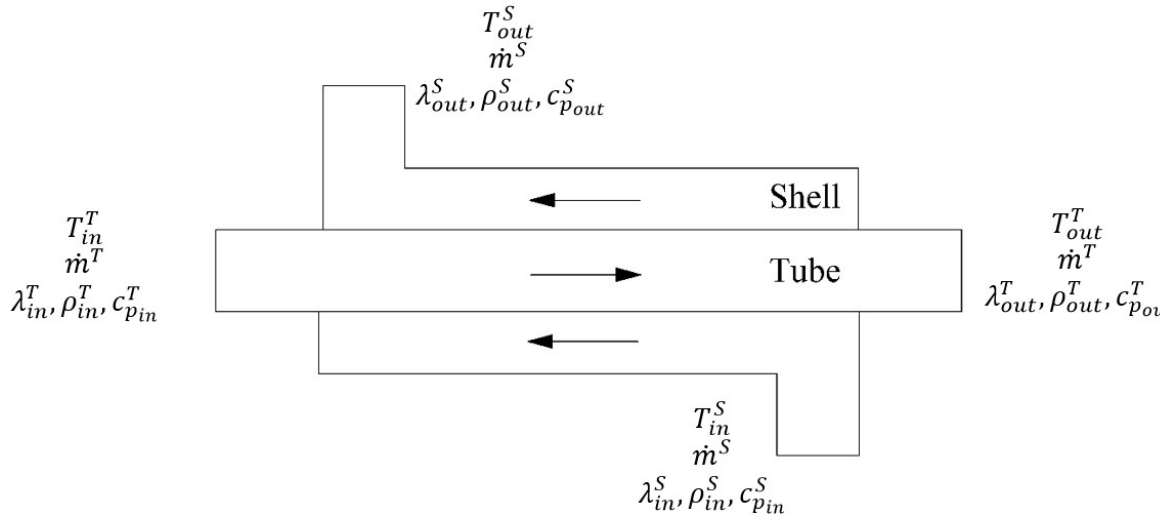

Figure 3.1: Parameter estimation: geometrical domain

The direct problem consist in the determination of the outlet temperate, knowing the input variables h^T and h^S. In order to generalize the shell and tube performances, it is possible to define:

$$Nu^T = Nu^T_{P_1,P_2,\ldots,P_N} \tag{3.3.1}$$

$$Nu^S = Nu^S_{P_1,P_2,\ldots,P_N} \tag{3.3.2}$$

where Nu is the Nusselt number at each side characterized by a set coefficients individual for heat exchanger. This type of mathematical approach is commonly used in the literature in order to describe the thermal characteristic of heat transfer devices (*Incoprera2002, Rainieri2004*) having water as a working fluid.

Usually, the coefficients α, β and h appearing in the equations (3.3.1)-(3.3.2) are unknown and since they can not be directly measured, their inverse estimation is required. In particular, the inverse problem have to deal with the estimation of both α and β coefficients related to the tube and shell side, knowing, at least, four temperature measurements, since the fourth one could be derived by the energy balance provided by the Equation (3.2). Since the problem is non-linear with respect to the unknown variables, the usage of non-linear optimization algorithm is required. The optimization procedure could be done using:

A) deterministic methods;
B) evolutionary and stochastic methods;
C) hybrid methods.

As suggested by Beck (*Beck1974*), since the problem is non-linear, its sensitivity matrix change each time a new information is added; for this reason it has to be recalculated for each solution step making the algorithm expensive from the computational point of view.

As already mentioned in the beginning of this section, the solution strategies proposed here could also be used in function estimation problems, but since they are coming from the optimization field in which the number of variables that has to be estimated is usually small, the estimation procedure listed above are here introduced in agreement with the final goal of the proposed problem.

A) *Deterministic methods*

These types of methods, usually applied to non-linear minimization problems, generally rely on establishing an iterative procedure, which, after a certain number of iterations, will hopefully converge to the minimum of the objective function. The iterative procedure can be written in the following general form (*Beck1977*):

$$\boldsymbol{P}^{k+1} = \boldsymbol{P}^{k} + \xi \boldsymbol{d}^{k} \tag{3.4}$$

where $\boldsymbol{P}$ is the vector of the design variables (e.g. α and β coefficients for the tube and the shell side), ξ is the search step size, $\boldsymbol{d}$ is the direction of descent and k is the number of iterations.

An iteration is acceptable if the value of the objective function at the iteration $k+1$ is lower than the value of the same objective function at the iteration k. It is possible to define the stationary point of the objective function as the point in which the gradient of the objective function is zero. It is straightforward that the optimization algorithm has to reach a stationary point in order to minimize the objective function. The convergence to the global minimum can be guaranteed only if it can be shown that the objective function has no other stationary point than the global minimum, but as suggested by Bard (*Bard1974*), this kind of optimization algorithms reach the local minimum in the valley in which the initial guess for the iterative procedure was located.

Here the Conjugate Gradient method (CG) and the Levenberg-Marquardt algorithm (LM) are going to be introduced but it has to be pointed out that exists many other deterministic optimization algorithms such as the Steepest Descent method (SD), the Newton-Raphson method (NR), the Quasi-Newton method (QN) (*Broyden1967*), etc.

Conjugate gradient method

The conjugate gradient method is an iterative algorithm used to regularized the estimated solution of both linear and non-linear inverse problems. This method improves the convergence rate of the steepest descent method by choosing directions of descent that are a linear combination of the gradient direction with the directions of the descent of the previous iterations. In this iterative procedure, at each iteration a suitable step size is considered along the descent direction in order to minimize the objective function. The descent direction is obtained as a linear combination of the negative

gradient direction at the current iteration with the direction of descent of the previous iteration (*Ozisik2000*). The iterative procedure of the Conjugate Gradient method for the solution of a general inverse heat transfer problem concerning the estimation of N unknown parameters P_j , $j = 1,2,3, \dots, N$, based on the minimization of the ordinary least square norm $\Pi(\boldsymbol{P})$ is written as follows:

$$\boldsymbol{P}^{k+1} = \boldsymbol{P}^k + \xi \boldsymbol{d}^k \tag{3.5}$$

where ξ^k is the search step size at each iteration k and $\boldsymbol{d}^k$ is the direction of descent, which can be expressed as follows:

$$\boldsymbol{d}^0 = -\nabla\Pi(\boldsymbol{P}^0) \tag{3.6.1}$$

$$\boldsymbol{d}^k = -\nabla\Pi(\boldsymbol{P}^0) + \gamma^k \boldsymbol{d}^{k-1} \tag{3.6.2}$$

Different version of the CG method can be found in literature depending on how the conjugation coefficient γ^k is computed (*Powell1977)*. For instance in the Polak-Ribiere (*Polak1971*) version it is computed as:

$$\gamma^0 = 0, \;\; k = 0$$

$$\gamma^k = \frac{\sum_{j=1}^{N}\{[\nabla\Pi(\boldsymbol{P}^k)]_j[\nabla\Pi(\boldsymbol{P}^k) - \nabla\Pi(\boldsymbol{P}^{k-1})]_j\}}{\sum_{j=1}^{N}[\nabla\Pi(\boldsymbol{P}^{k-1})]_j^2}, \qquad k = 1,2,3, \dots \tag{3.7}$$

while in the Fletcher-Reeves (*Fletcher1963, Fletcher1964, Fletcher2000*)it is written as:

$$\gamma^0 = 0, \;\; k = 0$$

$$\gamma^k = \frac{\sum_{j=1}^{N}[\nabla\Pi(\boldsymbol{P}^k)]_j^2}{\sum_{j=1}^{N}[\nabla\Pi(\boldsymbol{P}^{k-1})]_j^2}, \qquad k = 1,2,3, \dots \tag{3.8}$$

The search step size ξ^k can be found by minimizing the ordinary least square norm $\Pi(\boldsymbol{P}^{k+1})$ at the $k+1$ iteration with respect to the search step size ξ^k at the iteration k:

$$\min_{\xi^k} \nabla\Pi(\boldsymbol{P}^{k-1}) = \min_{\xi^k}[\boldsymbol{Y} - \boldsymbol{T}(\boldsymbol{P}^{k+1})]^T[\boldsymbol{Y} - \boldsymbol{T}(\boldsymbol{P}^{k+1})] \tag{3.9}$$

The procedure that avoids the minimum search goes beyond the present thesis, but the reader is referred to the works of Armijo (*Armijo1966*), Goldstein (*Goldstein1962*, *Goldstein1965*, *Goldstein1967*) and Wolfe (*Wolfe1969*, *Wolfe1971*) who proposed different criteria for the definition of the search step size.
By substituting Equation (3.5) into Equation (3.9):

$$\min_{\xi^k} \nabla\Pi(\boldsymbol{P}^{k-1}) = \min_{\xi^k}[\boldsymbol{Y} - \boldsymbol{T}(\boldsymbol{P}^k + \xi^k \boldsymbol{d}^k)]^T[\boldsymbol{Y} - \boldsymbol{T}(\boldsymbol{P}^k + \xi^k \boldsymbol{d}^k)] \tag{3.10}$$

By following a standard approach (*Bozzoli2011, Huang2005*) the temperature vector $\boldsymbol{T}(\boldsymbol{P}^k + \xi^k \boldsymbol{d}^k)$ can be linearized with Taylor series expansion. Rearranging and considering the sensitivity matrix $\boldsymbol{X}^k$ the search step size can be written as:

$$\xi^k = \frac{[\boldsymbol{X}^k \boldsymbol{d}^k]^T[\boldsymbol{T}(\boldsymbol{P}^k) - \boldsymbol{Y}]}{[\boldsymbol{X}^k \boldsymbol{d}^k]^T[\boldsymbol{X}^k \boldsymbol{d}^k]} \tag{3.11}$$

After calculating the gradient direction $\nabla\Pi(\boldsymbol{P}^k)$, the sensitivity matrix $\boldsymbol{X}^k$, the conjugation coefficient γ^k, and the search step size ξ^k, the iterative procedure expressed by Equation (3.5) can be implemented until a stopping criterion is reached one of the most used stopping criteria for this procedure is the discrepancy principle that states that the inverse problem solution is regarded to be sufficiently accurate when the difference between the estimated and the measured temperatures is close to the standard deviation of the measurements (*Morozov1984*). An adequate choice of the stopping criterion permits to reduce the oscillations that could appear in the inverse problem solution due to its ill-posed nature.

Levenberg-Marquardt algorithm

This technique is a powerful iterative technique that can be applied to the solution of a large variety of inverse problems (*Ozisik2000*). This method was firstly derived by Levenberg (*Levenberg1944*) by modifying the ordinary least square norm and later also by Marquardt (*Marquardt1963*) by using a different approach. The solution of a general inverse heat transfer problem concerning the estimation of N unknown parameters P_j at different time t_i, is based on the minimization of the ordinary least square norm:

$$\Pi(\boldsymbol{P}) = [\boldsymbol{Y} - \boldsymbol{T}(\boldsymbol{P})]^T[\boldsymbol{Y} - \boldsymbol{T}(\boldsymbol{P})] = \sum_{j=1}^{N} \left(Y_j - T_j(\boldsymbol{P})\right)^2 \tag{3.12}$$

where $\boldsymbol{P}$ is the vector of unknown parameters. To minimize it, it is necessary to have the derivatives of $\Pi(\boldsymbol{P})$ equal to zero:

$$\nabla\Pi(\boldsymbol{P}) = 2\left[-\frac{\partial \boldsymbol{T}^T(\boldsymbol{P})}{\partial \boldsymbol{P}}\right][\boldsymbol{Y} - \boldsymbol{T}(\boldsymbol{P})] = 0 \tag{3.13}$$

Where the transpose of the term $\frac{\partial \boldsymbol{T}^T(\boldsymbol{P})}{\partial \boldsymbol{P}}$ is the sensitivity matrix $\boldsymbol{X}(\boldsymbol{P})$:

$$\boldsymbol{X}(\boldsymbol{P}) = \left[-\frac{\partial \boldsymbol{T}^T(\boldsymbol{P})}{\partial \boldsymbol{P}}\right]^T = \begin{bmatrix} \frac{\partial T_1}{\partial P_1} & \cdots & \frac{\partial T_1}{\partial P_N} \\ \vdots & \ddots & \vdots \\ \frac{\partial T_i}{\partial P_1} & \cdots & \frac{\partial T_i}{\partial P_N} \end{bmatrix} \tag{3.14}$$

Therefore, Equation (3.13) can be written as:

$$2\boldsymbol{X}^{\boldsymbol{T}}(\boldsymbol{P})[\boldsymbol{Y} - \boldsymbol{T}(\boldsymbol{P})] = 0 \tag{3.15}$$

If the inverse problem is linear the sensitivity matrix is not a function of the unknown parameters and thus Equation (3.15), according to Beck (*Beck1977*), can be solved in explicit form for the vector of the unknown parameters $\boldsymbol{P}$:

$$\boldsymbol{P} = (\boldsymbol{X}^{\boldsymbol{T}}\boldsymbol{X})^{-1}\boldsymbol{X}^{\boldsymbol{T}}\boldsymbol{Y} \tag{3.16}$$

The situation is more complicated in case of non-linear problems where the sensitivity matrix depends on the unknown parameters vector. For this reason it is necessary to introduce an iterative procedure, obtained by linearizing the vector of estimated temperature $\boldsymbol{T}(\boldsymbol{P})$ with a Taylor series expansion around the current solution $\boldsymbol{P}^k$ at iteration k:

$$\boldsymbol{T}(\boldsymbol{P}) = \boldsymbol{T}(\boldsymbol{P}^k) + \boldsymbol{X}^k(\boldsymbol{P} - \boldsymbol{P}^k) \tag{3.17}$$

Substituting it in Equation (3.16) and rearranging the resulting expression according to Beck (*Beck1977*) it is possible to define the iterative procedure that is able to estimate the vector of unknown parameters:

$$\boldsymbol{P}^{k+1} = \boldsymbol{P}^{k} + \left[\left(\boldsymbol{X}^{\boldsymbol{k}}\right)^{T}\boldsymbol{X}^{k}\right]^{-1} (\boldsymbol{X}^{k})^{T} [\boldsymbol{Y} - \boldsymbol{T}(\boldsymbol{P}^{k})] \quad (3.18)$$

Actually, the iterative procedure based on this equation is named *Gauss Method* (GM). It is possible to demonstrate that this algorithm suffers of instability if the inverse problem is ill-posed. For this reason Levenberg and Marquardt added a damping factor λ to Equation (3.18):

$$\boldsymbol{P}^{k+1} = \boldsymbol{P}^{k} + \left[\left(\boldsymbol{X}^{\boldsymbol{k}}\right)^{T}\boldsymbol{X}^{k} + \lambda\boldsymbol{\Omega}^{k}\right]^{-1} (\boldsymbol{X}^{k})^{T} [\boldsymbol{Y} - \boldsymbol{T}(\boldsymbol{P}^{k})] \quad (3.19)$$

where λ is a scalar factor and $\boldsymbol{\Omega}$ is a diagonal matrix often expressed as $diag[(\boldsymbol{X}^{k})^{T}\boldsymbol{X}^{K}]^{-1}$ even if there are many other possible formulation (e.g. the identity matrix).

Here the positive parameter λ is adjusted during the course of the algorithm to ensure the convergence. One important reason for using a positive value of λ is that the $\lambda\boldsymbol{\Omega}$ term ensures that the matrix is non-singular.

B) *Evolutionary and stochastic methods*

The CG method and the LM algorithm are deterministic approaches that use the gradient of the objective function in order to find the direction of descent to the global minimum. On the other hand, evolutionary algorithms (*Deb2002*), such as genetic algorithm (*Goldberg1989*), differential evolution (*Storn1996*), simulated aneling (*Corana1987, Goffe1994*), ant colony (*Dorigo2004*) and particle swarm (*Kennedy1995, Kennedy1999*) do not rely, in general, on strong mathematical basis. Those estimation methodologies try to mimic the nature in order to find the minimum of the objective function, by selecting, in a fashionable and organized way, the points where such function is going to be computed (*Colaço2006*).

Here the popular Genetic Algorithm method (GA) and the Particle Swarm Optimization method (PSO) are going to be introduced but it has to be pointed out that exists many other deterministic optimization algorithms such as the Simulated Aneling (SA) and Differential Evolution (DE) (*Colaço2006*).

Genetic algorithm

Genetic algorithms are heuristic global optimization methods that are based on the process of natural selection. In particular the algorithm tries to increase the quality of the population, generation after generation, by exchanging genetic information between the members of the population, in what is referred to as the crossover operation. If the crossover produces members with higher quality than the parents, then they will be used to populate the next generation (*Goldberg1989, Deb2002*), otherwise they will be discharged. The basic genetic algorithm works iteratively with a collection (or population) of potential solutions to the minimization problem. At each iteration (or generation), three operators are applied to the entire population of designs: selection, crossover, and mutation. For the operators to be effective, each potential solution (or design) must be represented as a collection of finite parameters (or genes) referred as chromosome. It has to be pointed out that, each design must have a unique sequence of genes. The genes themselves are often encoded as binary strings although they can be represented as real numbers. The length of the binary string determines how precisely the value, also know as the allele of the gene, is represented.

The optimization process based on the genetic algorithm methods begins with an initial population of random designs in which each gene is generated by randomly extracted 0's and 1's. The objective function is evaluated for each design in the population and a fitness value, which corresponds to the value of the objective function for that design, is assigned to each chromosome. In the case of minimization, a higher fitness is assigned to designs with lower values of the objective function. Next, each member of the population is evaluated for reproduction, based on its fitness. The selection operator randomly chooses pairs of individuals from the population and the ones with higher fitness will mate and produce offspring. Once a mating pair is selected, the crossover operator is applied offspring are generated by combining the genes from the parent designs in a stochastic manner. For example in the uniform crossover scheme, it is possible to obtain any combination of the two parent's chromosomes assigning a random number between 0 and 1 to each bit in each gene. If a number greater than 0.5 is generated then that bit is replaced by the corresponding bit in the gene from the other parent. If it is less than 0.5, the original bit in the gene remains unchanged. This process is repeated for the entire chromosome for each of the parents. When complete, two offspring are generated, which may replace the parents in the population. The mutation process follows next. Each bit in each gene in the design is subjected to a chance for a

change from 0 to 1, or vice-versa (also known as the mutation probability, which is usually small). This introduces additional randomness into the process, which helps to avoid local minima. Completion of the mutation process signals the end of a design cycle. Many cycles are usually needed before the method converges to an optimum design.

Particle swarm

This optimization methodology was created by Kennedy J. and Eberhart R. (*Kennedy1995, Kennedy1999, Naka2001, Eberhart2001*) as an alternative to the Genetic Algorithm method. This method, based on the observation of the social behaviour of various species, tries to equilibrate the individuality and sociability of the individuals in order to locate the optimum of interest. The original idea of Kennedy and Eberhard came from the observation of birds looking for nesting places. In particular, when the individuality is increased, the search for alternative places for nesting is also increased (if the individuality becomes too high, the individual might never finds the best place) while if the sociability is increased, the individual learns more from its neighbours experience, reaching a compromise for the nest location (if the sociability becomes too high, all the individuals might converge to the first minima found, which is possibly a local minima).

In this method, the iterative procedure is given by:

$$P_i^{k+1} = P_i^k + v_i^{k+1} \tag{3.20}$$

where

$$v_i^{k+1} = \alpha v_i^k + \beta\, r_{1,i}\left(P_i^* - P_i^k\right) + \beta\, r_{2,i}\left(P_g^* - P_i^k\right), \quad 0 < \alpha < 1 \;\; and \;\; 1 < \beta < 2 \tag{3.21}$$

P_i is the $i-th$ parameter that has to be estimated of the vector $\boldsymbol{P}$ and v_i is its velocity, $r_{1,i}$ and $r_{2,i}$ are two random number with uniform distribution between 0 and 1, while $P_i^*$and P_g^* are the best values found for the parameter P_i and of the entire population, respectively.

In Equation (3.21), the second term on the right hand side represents the individuality while the third term represents the sociability. The first term on the right-hand side

represents the inertia of the particles and, in general, must be decreased as the iterative process runs. In this equation, the vector P_i^* represents the best value ever found for the $i-th$ component vector of parameters P_i during the iterative process. Thus, the individuality term involves the comparison between the current value of the $i-th$ individual P_i with its best value in the past. The vector P_g^* is the best value ever found for the entire population of parameters (not only the $i-th$ individual). Thus the sociability term compares P_i with the best value of the entire population in the past.

C) *Hybrid methods*

The Hybrid methods are a combination of the deterministic and the evolutionary/stochastic methods in which the advantages of each one of them are used. Those methods usually employ an evolutionary/stochastic method in order to identify the region where the global minimum is located and then switches to a deterministic method to get closer to the exact point faster. The core of the algorithm is the heuristic method, which does almost the entire optimization task. When some percentile of the population find a minima, the algorithm switches to the deterministic optimization method. If there is an improvement of the objective function, the algorithm returns to the heuristic method, meaning that some other region is more prone to have a global minimum. If there is no improvement of the objective function, the global minimum is reached. Finally, the algorithm returns again to the heuristic method in order to check if there are any changes in the minimum location and the entire procedure is repeated in order to test the robustness of the result. More involved Hybrid Methods, dealing with the application of other deterministic and stochastic methods, can be found in references (*Colaço2003a, Colaço2003b, Colaço2003c, Colaço2004, Dulikravich2003a, Dulikravich2003b, Dulikravich2003c, Dulikravich2004*).

3.2.2 Function estimation

This category of inverse problem, usually have to deal with the estimation of a large amount of unknown parameters; for example, from the industrial point of view, it is interesting the estimation of the local convective heat flux distribution (e.g. food treatment, heat removal from electrical devices, etc.). Related to this aspect, it is possible to consider the physical problem, represented in Figure (3.2), which consists in a cross-section of a circular duct with internal radius r_{int} and external radius r_{ext}. The thermal conductivity of the material, k, is assumed to be constant and uniform such as the environmental temperature T_{env} and the bulk temperature T_b of the fluid that flows inside the tube. Both the external and internal surfaces are subjected to Robin's boundary condition: there is a prescribed convective heat transfer coefficient distribution h_{int} at the inner surface Γ_{int} of the pipe, while the exterior surface Γ_{ext} is subjected to an overall convective heat transfer coefficient h_{ext}. The domain Ω is also subjected to an internal heat generation per unit of volume q_g.

The equations that describe the physical problem are listed below:

$$\nabla^2 T = -\frac{q_G}{K} \quad \text{in } \Omega \tag{3.22.1}$$

$$-K\left.\frac{\partial T}{\partial \mathbf{n}}\right|_{\Gamma_{int}} = h_{int}(T - T_b) \quad \text{on } \Gamma_{\text{int}} \tag{3.22.2}$$

$$-K\left.\frac{\partial T}{\partial \mathbf{n}}\right|_{\Gamma_{ext}} = h_{ext}(T - T_{env}) \quad \text{on } \Gamma_{\text{ext}} \tag{3.22.3}$$

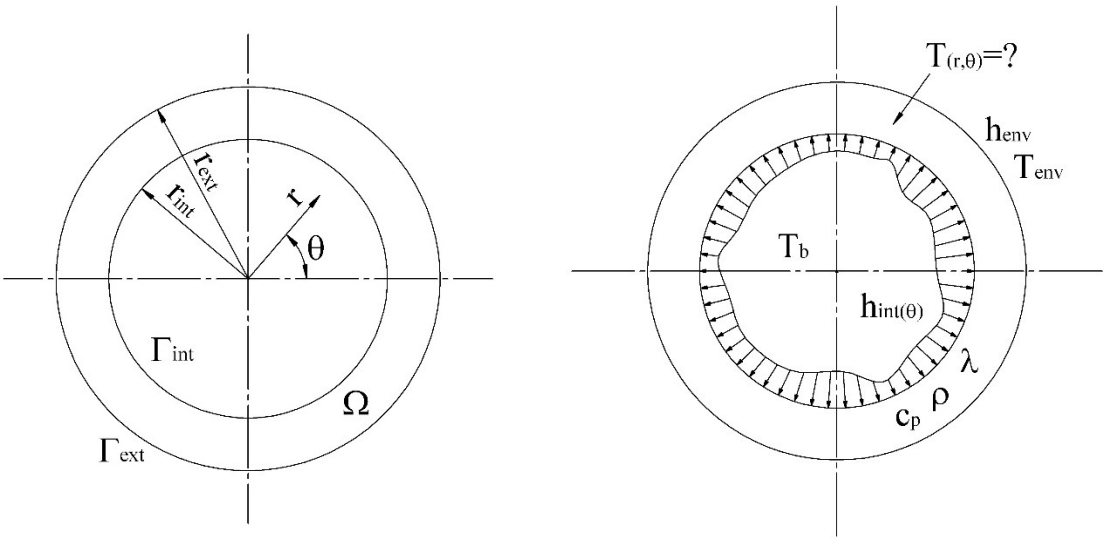

(a) (b)

Figure 3.2: Function estimation: (a) Geometrical domain and (b) direct problem boundary conditions schemes

The direct problem presented in equations (3.22.1)-(3.22.3) concerns the determination of the temperature field T within the Ω domain given the distribution of the convective heat transfer coefficient on both the internal and external surfaces. As it is possible to see, from the system of Equations (3.22) the direct problem is linear respect to the unknown variable T, while the inverse problem related to the estimation of the convective heat flux distribution is not linear in the unknown variable h_{int}. This unwanted behaviour could be overcome by formulating an auxiliary problem in which the internal surface is subjected to an imposed heat flux distribution:

$$\nabla^2 T = -\frac{q_G}{K} \quad \text{in } \Omega \tag{3.23.1}$$

$$-k\frac{\partial T}{\partial \mathbf{n}}\Big|_{\Gamma_{int}} = q(\theta) \quad \text{on } \Gamma_{\text{int}} \tag{3.23.2}$$

$$-k\frac{\partial T}{\partial \mathbf{n}}\Big|_{\Gamma_{ext}} = h_{ext}(Y - T_{env}) \quad \text{on } \Gamma_{\text{ext}} \tag{3.23.3}$$

where Y are some extra temperature measurements taken at the external surface Γ_{ext} by means of the thermographic camera.

In this way, the system of Equation (3.23) becomes linear with respect to the imposed heat flux and the convective heat flux distribution could be calculated, once the heat flux estimation is performed, as:

$$h_{int}(\theta) = \frac{q(\theta)}{\left(T_{wall}(\theta)|_{\Gamma_{int}} - T_b\right) A_{int}} \tag{3.24}$$

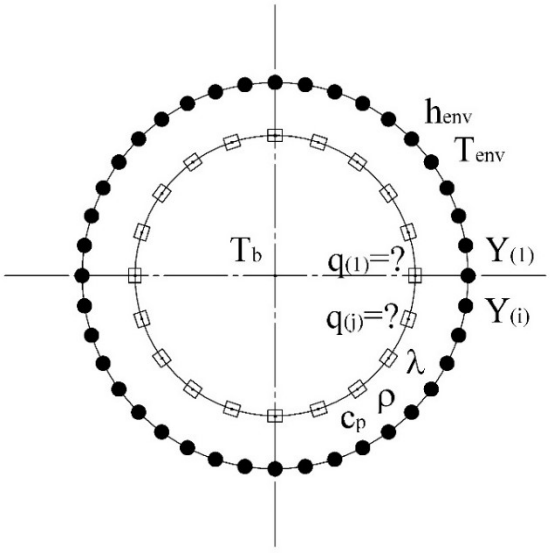

Figure 3.3: Function estimation: Inverse Heat Condition Problem boundary conditions scheme

As already mentioned in the previous chapter, the linearity of the problem is an interesting property since it allows solving the problem in an easy way, avoiding the usage of iterative procedure that are cost-expensive in terms of computational requirement.
As suggested by Beck (*Beck1985*) and Dennis (*Dennis2013*), since the problem is linear with respect to the heat flux $q(x)$, it can be written in the discrete domain as follows:

$$\boldsymbol{T} = \boldsymbol{X}\boldsymbol{q} + \boldsymbol{T}_{\boldsymbol{q}=\boldsymbol{0}} \tag{3.25}$$

where $\boldsymbol{T}$ is the estimated temperature on the sampling position (e.g. in all the entire), $\boldsymbol{X}$ is the sensitivity matrix, $\boldsymbol{q}$ is the imposed heat flux distribution and $\boldsymbol{T}_{q=0}$ is the estimated temperature on the sampling position if no heat flux is applied on the boundary at Γ_{int}. The homogeneous term $\mathbf{T}_{\mathrm{q=0}}$ has to take care about the forcing term (e.g. internal heat source, imposed potential boundary conditions, etc.): it represents the response of the system if no heat flux $\boldsymbol{q}$ is imposed highlighting the effect of the forcing term. The sensitivity matrix is the linear application that links the heat flux at each discretization point m, to the measured temperature at any location n. It can be calculated analytically or numerically (e.g. Finite Difference Method (FDM), Finite Element Method (FEM), Finite Volume Method (FVM), Boundary Element Method (BEM), etc.). Each column of the sensitivity matrix represents the response of the system after a perturbation of one of the discretizing parameter is applied. It follows that the sensitivity matrix has a number of columns that is equal to the discretising number of parameters and a number of rows that is equal to the number of sensors used to measure the effect of the perturbation. It follows that the quantities present in the Equation (3.25) are given by:

$$\boldsymbol{T}^{\boldsymbol{T}} = [T_1, T_2, T_3, \dots T_n, \dots, T_i] \tag{3.26}$$

$$\boldsymbol{q}^{\boldsymbol{T}} = [q_1, q_2, q_3, \dots q_m, \dots, q_j] \tag{3.27}$$

$$\boldsymbol{X}^{\boldsymbol{T}} = \begin{bmatrix} \partial T_1/\partial q_1 & \partial T_2/\partial q_1 & \cdots & \partial T_n/\partial q_1 & \cdots & \partial T_i/\partial q_1 \\ \partial T_1/\partial q_2 & \partial T_2/\partial q_2 & \cdots & \partial T_n/\partial q_2 & \cdots & \partial T_i/\partial q_2 \\ \vdots & \vdots & & & & \vdots \\ \partial T_1/\partial q_{\mathrm{m}} & \partial T_2/\partial q_{\mathrm{m}} & & \partial T_n/\partial q_m & & \partial T_i/\partial q_m \\ \vdots & \vdots & & & & \vdots \\ \partial T_1/\partial q_j & \partial T_2/\partial q_j & \dots & \dots & & \partial T_i/\partial q_j \end{bmatrix} \tag{3.28}$$

where i is the total number of sensors while j is the total number of discretizing parameters.

It has to be highlighted that in the heat transfer field, the systems are usually overdetermined. Thus, the number of equations is much larger than the number of parameters (e.g. $i > j$).
It has to be pointed out that the sensitivity matrix represents the temperature responses of the system after the perturbation of the imposed heat flux is applied, while the homogeneous term take care of the imposed forcing boundary condition. For this reason it is possible to conclude that sensitivity matrix $\boldsymbol{X}$ has to be calculated each time the geometry of the heat exchanger changes, while the homogeneous term $\boldsymbol{T}_{q=0}$ has also to be calculated each time the boundary conditions value, change.
For the point of view of the linear algebra, if the final goal of the Inverse Heat Conduction Problem is the estimation of the heat flux distribution, it is possible to invert the linear system of Equation (3.25) to get:

$$\boldsymbol{q} = \boldsymbol{X}^{-1}\left(\boldsymbol{Y} - \boldsymbol{T}_{\boldsymbol{q=0}}\right) \tag{3.29}$$

where $\boldsymbol{Y}^T = [Y_1, Y_2, Y_3, \dots, Y_m, \dots, Y_j]$ is the vector of the discrete thermal measurements. In this case, the linear system of equation defined in Equation (3.29) links the effects (e.g. the discrete temperature measurements $\boldsymbol{Y}$), to the causes (e.g. the heat flux distribution $\boldsymbol{q}$). It has to be pointed out, that usually the sensitivity matrix $\boldsymbol{X}$ is not square, thus its direct inversion is not possible.
For this reason, is often used the pseudo-inverse of the sensitivity matrix that yields to the following formulation of the heat flux distribution:

$$\boldsymbol{q} = (\boldsymbol{X}^{\boldsymbol{T}}\,\boldsymbol{X})^{-1}\,\boldsymbol{X}^{\boldsymbol{T}}\left(\boldsymbol{Y} - \boldsymbol{T}_{\boldsymbol{q=0}}\right) \tag{3.30}$$

As suggested by many researchers (*Bozzoli2013*), the presence of noise in the measurement $\boldsymbol{Y}$ can completely damage the estimation of the unknown imposed heat flux; for this reason, the estimated solution has to be regularized. Among all the solution strategies, it has to be pointed out the:

A) Least Square Problem;
B) Singular Value Decomposition;
C) Tikhonov regularization method;
D) Reciprocity functional.

A) *Unconstrained Least Squares:*

From the historical point of view, the first solutions estimation was done by using the *Least Square Approach*; there are many different types of Least Square Approaches, but the first developed one was the *Unconstrained Least Square*.

Using this methodology the temperature measurements are forced to match the estimated temperature given by Equation (3.25) by tuning the imposed heat flux from Equation (3.30).

It is possible to write the linear system of Equation (3.25) in terms of relative temperature, as follows:

$$\boldsymbol{T_{rel} = T - T_{q=0} = Xq} \tag{3.31}$$

As suggested by Aster (*Aster2005*), for a full rank application matrix $\boldsymbol{X}$, it is frequently the case that no solution $\boldsymbol{q}$ is able to exactly satisfy the Equation (3.30). This happens because the dimension of the range of $\boldsymbol{X}$ is smaller than the total number of observation j and a noisy data vector can easily lie outside of the range of $\boldsymbol{X}$. A useful approximation of the solution of the inverse problem $\boldsymbol{q}$ could be find by minimizing the mismatch between the temperature measurements $\boldsymbol{Y}$ and the estimated temperature in the same locations $\boldsymbol{T}$, obtained by the linear application (e.g. sensitivity matrix) $\boldsymbol{X}$ (Eq.(3.25)). Therefore, the residual vector, which is the objective function of the approach, is defined as:

$$\boldsymbol{r = Y - \left(Xq + T_{q=0}\right)} \tag{3.32}$$

One common model to measure the misfit is the 2-norm of the residual:

$$\boldsymbol{q_{restored} = \min_{q} \left\| Y - \left(Xq + T_{q=0}\right) \right\|_2} \tag{3.33}$$

It is possible to demonstrate that the solution provided by the minimization problem introduced by the Equation (3.33) is equal to the once obtained in Equation (3.30) by making some simple observation.

Under the assumption that the standard deviation of the measurements is a known parameter, another useful indicator of the misfit between the measurement and their estimated value is the *chi-square statistic*:

$$\boldsymbol{\chi^2} = \sum \frac{\left[\boldsymbol{Y} - \left(\boldsymbol{Xq} + \boldsymbol{T_{q=0}}\right)\right]^{\mathbf{2}}}{\sigma^2} \tag{3.34}$$

where σ is the standard deviation of the measurement.

The *Unconstrained Least Square approach* (*ULS*), is of particular interest since it turns out to be statistically the most likely solution, if the data errors are normally distributed (e.g. assumption that has to be proven, but at the same time, is also the most common situation.). If the errors in the measurements are not Gaussian distributed or the mathematical model has a different form respect to what was introduced in Equation (3.29), there are many other different model that can be used in order to properly measure the misfit. For example, if the error are distributed with a double-side exponential distribution:

$$f(x) = \frac{1}{2\sigma} e^{-\frac{1|x-\mu|}{\sigma}} \tag{3.35}$$

where μ is the mean value of the measure. It is possible to demonstrate that the L_1 regression represents the maximum likelihood interpretation for data sets with this error distribution typology. Moreover, it is possible to demonstrate that the L_1 regression is more robust to the presence of outliers than the L_2 regression previously introduced.

$$\boldsymbol{q_{restored}} = \mathbf{min}_{\boldsymbol{q}} \left\| \boldsymbol{Y} - \left(\boldsymbol{Xq} + \boldsymbol{T_{q=0}}\right) \right\|_{\mathbf{1}} \tag{3.36}$$

It has to be pointed out that data sets characterized by a noisy distribution given by Equation (3.35) are not commonly encountered in engineering applications. Nevertheless, the solution provided by Equation (3.36) has to be considered rather than the solution provided by the Equation (3.33) if there is reason to suspect the presence of outliers (even if most of the measurement are normally distributed). The more robustness of the $\|\cdot\|_1$ compared to the $\|\cdot\|_2$ in presence of outliers, is because the $\|\cdot\|_1$ solution does not square each of the terms in the misfit measure, as $\|\cdot\|_2$ does. An

interesting example that compare the L_1 and the L_2 norm is provided by Aster (*Aster2005*).

Weighted Least Square:

In this approach, in order to reduce the high sensibility of the inverse problem to the noise, a penalty term related to the standard deviation of the noise is added. It is usually assumed that the response data is of equal quality and, therefore, has constant variance. If this assumption is violated, the reconstruction quality will be corrupted by data of poor quality. To improve the reconstruction quality, it is possible to use the W*eighted Least-Squares approach.* This approach is similar to the unconstrained least squares approach, but in this case, an additional scale factor (the weight) is included in the process. The weights determine how much each response value influences the final parameter estimates. A high-quality data point influences the fit more than a low-quality data point. Weighting the data is recommended if the weights are known, or if there is justification that they follow a particular form. In particular, the reconstructed heat flux is penalized by the introduction of the diagonal matrix W, in which the diagonal terms represent the variance of the measurements in the data set:

$$w_i = 1/\sigma_i^2 \tag{3.37}$$

where σ_i is the standard deviation of the i-th parameter that has to be estimated.
The restored heat flux distribution is estimated by simply extending the Equation (3.30):

$$\boldsymbol{q_{restored}} = (\boldsymbol{X^T\, W\, X})^{-1}\, \boldsymbol{X^T\, W}\left(\boldsymbol{Y - T_{q=0}}\right) \tag{3.38}$$

As it is possible to see, if the parameters that have to be estimated are of the same type, the weighting factor acts as a scaling factor, avoiding modification to the shape of the reconstructed signal. On the other hand, if the estimated parameters are of different type, the weighting factor may have different values yielding to different reconstructed signal. The standard deviation of the measurements is not the only parameter that could be used in order to assign the weights in a weighted least square approach. There are many other different strategies in order to establish the entity of weights, such as in the *Iterative Reweighted Least Square approach* (*IRLS*). Using this approach, the weights consist in

the residual vector defined by the Equation (3.32). The iterative algorithm start with a classical ULS method to determine the starting residual vector $\boldsymbol{r}_0$:

$$\boldsymbol{r_0} = \boldsymbol{Y} - \left(\boldsymbol{X q}_{ULS} + \boldsymbol{T_{q=0}}\right) \tag{3.39}$$

Then the weighting matrix is build such as:

$$w_i = 1/\left|\mathrm{r}_{0_i}\right| \tag{3.40}$$

It is straight forward that if the residual becomes zero, the procedure fails. For this reason, when the residual goes below a certain tolerance ϵ, the weight factor is fixed to:

$$w_i = 1/|\epsilon| \tag{3.41}$$

Once the weighting matrix is build, it is possible to proceed with the estimation of the unknown heat flux distribution:

$$\boldsymbol{q_1} = \left(\boldsymbol{X^T W_{r_0} X}\right)^{-1} \boldsymbol{X^T W_{r_0}} \left(\boldsymbol{Y - T_{q=0}}\right) \tag{3.42}$$

and the procedure can be repeated, calculating the new residual vector, weighting matrix, heat flux estimation and so on so forth.

The procedure has to be repeated until the algorithm converge. A typical stopping criteria is:

$$\frac{\|q_k - q_{k-1}\|_2}{1 + \|q_k\|_2} < \tau \tag{3.43}$$

where τ is a tolerance value defined by the researcher.

It is possible to demonstrate that this approach converge to a L_1 norm minimizing scheme.

Bounded Least Square:

Bound constraint methods allow using a priori knowledge related to the permissible range of parameter values. In many physical applications there are physical bounds connected to the physical meaning of the parameters that are going to be estimated.

There are different types of bound that can be applied to the more general ULS. One of the most common constraint is related to the estimation of positive define function. This particular case of the ULS, is called *Non-negative Least Square approach* (NLS). In particular, the solution is subjected to an extra-constrain defined as:

$$min \, \|\boldsymbol{Xq} - \boldsymbol{T}_{rel}\|_2 \qquad \boldsymbol{q} \geq 0 \tag{3.44}$$

where $\boldsymbol{q} > 0$ means that all the values of the reconstructed heat flux has to be positive defined. The non-negative least square approach was originally developed by Lawson (*Lawson1995*); the same authors were also able the generalize the approach for a general lower and upper limited bounded problem. It has to be pointed out, that a general bound constraint condition could be applied to the Tikhonov regularization scheme (*Stark*1995).

It is obvious that this approach can only be used when the defined constrains are in agreement with the phenomena under investigation. The usage of this approach is in agreement with the general concept that adding new information related to problem increases the reconstruction quality of the inverse solution.

B) *Singular Value Decomposition:*

A better estimation of the inverse problem can be achieved by using the *Singular Valued Decomposition* (*SVD*). In particular the sensitivity matrix X can be decomposed into three matrices as follows:

$$\boldsymbol{X} = \boldsymbol{U}\boldsymbol{\Sigma}\boldsymbol{V}^T = \sum_{i=1}^{n} u_i \sigma_i v_i^T \tag{3.45}$$

where $\boldsymbol{U} = [u_1, u_2, \dots, u_n]$ and $\boldsymbol{V} = [v_1, v_2, \dots, v_m]$ are matrices with orthogonal columns that represent a basis in the *data space,* R^n and a basis in the *model space,* R^m respectively.

The diagonal matrix $\boldsymbol{\Sigma}$ containing the singular values.

$$\boldsymbol{\Sigma} = diag(\sigma_1, \sigma_2, \dots, \sigma_n) \tag{3.46}$$

The Singular Values contained in the Σ matrix are non negative and they appear in a decreasing order:

$$\sigma_1 \geq \sigma_2 \geq \cdots \geq \sigma_n \tag{3.47}$$

It has to be pointed out that some singular value may be zero. Therefore, assuming that the first p singular values are non-zero, it is possible to write the matrix that contains the singular values as:

$$\boldsymbol{\Sigma} = \begin{bmatrix} \boldsymbol{\sigma}_p & 0 \\ 0 & 0 \end{bmatrix} \tag{3.48}$$

where $\boldsymbol{\sigma}_p$ is a p x p diagonal matrix containing the first p non-zero singular values. Therefore, it is possible to write the Equation (3.47) as:

$$\boldsymbol{X} = \boldsymbol{U}\boldsymbol{\Sigma}\boldsymbol{V}^T = \left[\boldsymbol{U}_p, \boldsymbol{U}_0\right] \begin{bmatrix} \boldsymbol{\sigma}_p & 0 \\ 0 & 0 \end{bmatrix} \left[\boldsymbol{V}_p, \boldsymbol{V}_0\right]^T \tag{3.49}$$

where $\boldsymbol{U}_p$ and $\boldsymbol{V}_p$denotes the first p column of $\boldsymbol{U}$ and $\boldsymbol{V}$ respectively, while $\boldsymbol{U}_0$ and $\boldsymbol{V}_0$denotes the last $m - p$ column of $\boldsymbol{U}$ and $n - p$ column of $\boldsymbol{V}$ respectively. It has to be observed that $\boldsymbol{U}_0$ and $\boldsymbol{V}_0$, which are the column of the matrices $\boldsymbol{U}$ and $\boldsymbol{V}$, will be multiplied by the null vectors of the $\boldsymbol{\Sigma}$ matrix. Thus they will not participate in the reconstruction of the signal, reducing the space dimension of the possible solution. It has to be observed that $\boldsymbol{U}_0$ and $\boldsymbol{V}_0$ constitute a orthonormal base of the null space $\boldsymbol{X}^T$as well as the orthonormal bases $\boldsymbol{U}_p$ and $\boldsymbol{V}_p$. Due to this observation, it is possible to write the last expression in a more compact form:

$$\boldsymbol{X} = \boldsymbol{U}_p \boldsymbol{\Sigma}_\mathrm{p} \boldsymbol{V}_p^T \tag{3.50}$$

Based on this decomposition, it is possible to write the linear system of Equation (3.31), as:

$$\boldsymbol{T_{rel}} = \boldsymbol{X}\boldsymbol{q} = \mathbf{U}_\mathrm{p}\left(\boldsymbol{\Sigma}_p \boldsymbol{V}_p^T\, \mathbf{q}\right) = \sum_{\boldsymbol{i=1}}^{\boldsymbol{p}} u_i \sigma_i v_i q_i \tag{3.51}$$

The SVD can be used in order to compute the generalized inversion of a matrix in the Moore-Penrose [*Moore1920, Penrose1955*] sense:

$$\boldsymbol{X}^{-1} = \boldsymbol{V}_p \boldsymbol{\Sigma}_{\mathrm{p}}^{-\mathbf{1}} \boldsymbol{U}_p^T \tag{3.52}$$

It is possible to demonstrate that the pseudo-inverse of a matrix in the Moore-Penrose sense always exist; this is not true for the generalized inverse matrix $(\boldsymbol{X}^T \boldsymbol{X})^{-1}$ if $\boldsymbol{X}$ is not a full rank matrix.

Based on the singular value decomposition, it is possible to estimate the solution of the inverse problem as:

$$\boldsymbol{q}_{restored} = \mathbf{X}^{-1}\left(\boldsymbol{Y} - \boldsymbol{T}_{q=0}\right) = \boldsymbol{V}_p\left(\boldsymbol{\Sigma}_{\mathrm{p}}^{-1} \boldsymbol{U}_p^T \boldsymbol{Y}\right) = \sum_{i=1}^{n} \frac{u_i^T}{\sigma_i} v_i \ \left(\boldsymbol{Y} - \boldsymbol{T}_{q=0}\right) \tag{3.53}$$

Aster (*Aster2005*) showed that the estimation based on the SVD is both least square solution and a minimum length solution.

As already mention, singular values could be vary small; therefore it is useful to examine their range of values. In particular, small singular value cause a generalized inverse solution to be extremely sensible to the noise present in the measurements. It has to be pointed out, that the distinction between extremely small and zero singular values is a difficult task. As it is possible to see form the Equation (3.53), small singular values can give a very large coefficient in the model space $\boldsymbol{V}$ thus this basis vector can dominate the solution making the answer useless. A measure of the instability of the solution is the *condition number*:

$$cond(\boldsymbol{X}) = \frac{\sigma_1}{\sigma_k} \tag{3.54}$$

where k is the minimum number between the total number of unknown parameters and the total number of measurements.

The condition number is a property of the linear application and can be computed in the design phase of the experiment, before any data are collected.

Filtered Singular Value Decomposition

In order to stabilize the reconstructed solution with respect to the noise, many different penalty functions were introduced in the literature (*Bozzoli2017b*), being the most adopted the Truncated Singular Value Decomposition (TSVD) or the Damped Singular Value Decomposition (DSVD).

In the Truncated Singular Value Decomposition, the smallest Singular Values are neglected at some singular value $p' < p$ in order to increase the well-posedness of the inverse matrix. One way to decide when the matrix has to be truncated is to use the *discrepancy principle*. Using this approach, the truncation parameter p' is the one that satisfies the following inequality:

$$\left\| \boldsymbol{X}_{p'}^{-1} \boldsymbol{q} - \boldsymbol{Y} \right\| \leq \sigma \tag{3.55}$$

where, $\boldsymbol{X}_{p'}^{-1}$ is the truncated pseudo-inverse of order $p' \neq p$ and σ is the standard deviation of the measurements. The final solution can be written as:

$$\boldsymbol{q}_{restored} = \boldsymbol{V}\boldsymbol{\Sigma}_{\mathrm{p}'}^{-1}\boldsymbol{U}^T\,\boldsymbol{Y} = \sum_{i=1}^{p'} \frac{u_i^T}{\sigma_i} v_i f_i\;\boldsymbol{Y} \tag{3.56}$$

where f_i is a filter function defined as:

$$f_i = \begin{cases} 0\,, & \sigma_i > \sigma_{p'} \\ 1\,, & \sigma_i \leq \sigma_{p'} \end{cases} \tag{3.57}$$

where $\sigma_1 > \sigma_{p'} > \sigma_p$ is the regularization parameter.

In the Damped Singular Value Decomposition (DSVD), the filter function is continuously defined in terms of singular value and is given by:

$$f_i = \frac{\sigma_i}{\sigma_i + \sigma_{p'}} \tag{3.58}$$

The penalization of the smallest singular values of the diagonal matrix $\boldsymbol{\Sigma}$ goes under the category of the *regularization technique*. Those techniques, reduce the space solution assuming as valid only the possible solution characterized by a regular shape. This

restriction is physically justified, since the nature of the physical problem is continuous (e.g. it is not possible to have a heat flux defined by a step function, since this required an infinity energy).

It has to be pointed out that, the application of a window filter (TSVD) implies that all the information after the cut-off frequency can not be used. On the other hand, smoothing the singular value (DSVD) allows using more singular values than in the TSVD, thus it is possible to add more information to the inverse problem and then increase the reconstruction quality.

C) *Tikhonov regularization:*

All the techniques previously described are effected by a high sensibility to the noise present in the measurement. For this reason, a regularization technique is required. These regularization techniques are a modification of the least square approach, in particular adding a penalty term, which plays the role of a damping factor, which is added to the objective function that has to be minimized. One of the most common regularization schemes is the Tikhonov (TM). This approach is also known as ridge regression, Tikhonov-Miller method, Phillips-Twomey method, etc.

Starting from the SVD approach, it is possible to derive the Tikhonov regularization technique, which is a solution strategy that is able to give greater weight to larger singular values in the SVD and at the same time, less weight to small singular values.

In the Tikhonov regularization technique, the goal is to select among all the possible solution characterized by $\left\|\boldsymbol{Y}-\left(\boldsymbol{Xq}+\boldsymbol{T}_{q=0}\right)\right\|_2 \leq \delta$ the one that minimize the $\|\boldsymbol{q}\|_2$. The reason to select the minimum norm of the imposed heat flux is that this should ensure the presence of high oscillating heat flux values that are supposed to be not physical. It has to be pointed out that $\|\boldsymbol{q}\|_2$ represents the measure of the variability of the unknown heat flux distribution $\boldsymbol{q}$. The problem can be stated, using the Lagrange multipliers in a damped least square problem as:

$$\min\left\|\boldsymbol{Y}-\left(\boldsymbol{Xq}+\boldsymbol{T}_{\boldsymbol{q=0}}\right)\right\|_2^2+\lambda^2\|\boldsymbol{qL}\|_2^2 \quad \lambda>0 \tag{3.59}$$

where $\|\cdot\|_2^2$ stands for the square of the two-norm, λ is the unknown regularization parameter and $\boldsymbol{L}$ is the identity matrix:

$$\boldsymbol{L} = \begin{bmatrix} \mathbf{1} & & \mathbf{0} \\ & \ddots & \\ \mathbf{0} & & \mathbf{1} \end{bmatrix} \tag{3.60}$$

The Tikhonov regularization procedure, based on $\boldsymbol{L} = \boldsymbol{I}$ is called *zero-order Tikhonov regularization*, since the $\boldsymbol{L}$ matrix could be understand as the zero order discrete derivative of the unknown heat flux distribution $\boldsymbol{q}$.

The minimization of the objective function reported in Equation (3.59) require an optimal balance between the reconstruction fidelity to the data and the stability of the solution that could be done by properly tuning the regularization parameter λ. There are many different ways that can be used in order to estimate the regularization parameter λ, such as the: *L-curve*, *Morozov's discrepancy principle*, *generalized cross-validation*, *etc*. A brief discussion related to this aspect is addressed in the next paragraph.

It is possible to write the problem defined in Equation (3.59) in the following way:

$$\min \left\| \begin{bmatrix} \boldsymbol{X} \\ \lambda \boldsymbol{L} \end{bmatrix} \boldsymbol{q} - \begin{bmatrix} \boldsymbol{Y} - \boldsymbol{T}_{q=0} \\ 0 \end{bmatrix} \right\|_2^2 \quad \lambda > 0 \tag{3.61}$$

As long as λ is a non-zero coefficient, the problem defined by the Equation (3.61) can be solved by the method of the normal equations as follows:

$$[\boldsymbol{X}^T \quad \lambda \boldsymbol{L}] \begin{bmatrix} \boldsymbol{X} \\ \lambda \boldsymbol{L} \end{bmatrix} \mathbf{q} = [\boldsymbol{X}^T \quad \lambda \boldsymbol{L}] \begin{bmatrix} \boldsymbol{Y} - \boldsymbol{T}_{q=0} \\ 0 \end{bmatrix} \quad \lambda > 0 \tag{3.62}$$

which yield to:

$$(\boldsymbol{X}^T \boldsymbol{X} + \lambda^2 \boldsymbol{L}) \boldsymbol{q} = \boldsymbol{X}^T \left(\boldsymbol{Y} - \boldsymbol{T}_{q=0} \right) \quad \lambda > 0 \tag{3.63}$$

It is possible to demonstrate that the solution of the last system of equation is given by:

$$\boldsymbol{q}_\lambda = (\boldsymbol{X}^T\boldsymbol{X} + \lambda^2\boldsymbol{L}^T\boldsymbol{L})^{-1}\boldsymbol{X}^T\left(\boldsymbol{Y} - \boldsymbol{T}_{\boldsymbol{q}=\boldsymbol{0}}\right) \tag{3.62}$$

$$= \sum_{i=1}^{k} \frac{s_i^2}{s_i^2 + \lambda^2}\frac{u_i^T}{\sigma_i}v_i \ \left(\boldsymbol{Y} - \boldsymbol{T}_{q=0}\right)$$

$$= \sum_{i=1}^{k} f_i \ \frac{u_i^T}{\sigma_i}v_i \ \left(\boldsymbol{Y} - \boldsymbol{T}_{q=0}\right)$$

As it is possible to see, the solution kernel is the same as what was already shown for the SVD approach, except for the term $f_i = \frac{s_i^2}{s_i^2+\lambda^2}$, which represents the filter factor of the Tikhonov regularization scheme.

The same considerations, related to the regularization parameter and provided during the discussion of the Filtered SVD, are still valid; in particular, some of the common schemes usually used in order to find the regularization parameter will be discussed in the next paragraph.

It is possible to assume in the Tikhonov regularization scheme different $\boldsymbol{L}$ matrices in order to measure the variability of $\boldsymbol{q}$. For example it is possible to use the first or second order discrete derivative, which are define as:

$$\boldsymbol{L_1} = \begin{bmatrix} \mathbf{1} & \mathbf{-1} & & & \mathbf{0} \\ & \ddots & \ddots & & \\ & & \ddots & \ddots & \\ & & & \ddots & \mathbf{-1} \\ \mathbf{0} & & & & \mathbf{1} \end{bmatrix} \tag{3.63.1}$$

$$\boldsymbol{L_2} = \begin{bmatrix} \mathbf{-2} & \mathbf{1} & & & \mathbf{0} \\ \mathbf{1} & \ddots & \ddots & & \\ & \ddots & \ddots & \ddots & \\ & & \ddots & \ddots & \mathbf{1} \\ \mathbf{0} & & & \mathbf{1} & \mathbf{-2} \end{bmatrix} \tag{3.63.2}$$

It has to be observed that, if the unknown heat flux distribution is not one-dimensional, it is better to approximate the discrete derivative with the finite-difference approximation of the Laplacian operator.

It has to be highlight that, many other $\boldsymbol{L}$ matrices could be used instead of $\boldsymbol{L_0}, \boldsymbol{L_1}$ and $\boldsymbol{L_2}$ (*Hansen2008)*. Related to this aspect, Hansen (*Hansen2008*) provided a very interesting example on the effect of the discrete smoothing norm. Moreover, the author pointed out the requirement of using the $\|\cdot\|_1$ in order to increase the reconstruction accuracy related to the discontinuous function (*Dahl2010*).

To extend the zero-order Tikhonov regularization to higher order regularization, it is necessary to use the Generalized Singular Value Decomposition (GSVD) which is the extension of the SVD approach for higher order regularization schemes.

D) Reciprocity functional:

This particular solution technique needs low computational resources since it avoids the calculation of the sensitivity matrix $\boldsymbol{X}$. Two important works by Andrieux (*Andrieux1993, Andrieux1996*) showed the concept and use of reciprocity functional. This approach is based on Betti's theorem, also known as *Maxwell-Betti reciprocal work theorem*. The theorem states that for a linear elastic structure subject to two sets of forces P and Q, the work done by the force P through the displacements produced by the force Q is equal to the work done by the force Q through the displacements produced by the force P. Starting from the research provided by Andrieux, other studies based on the reciprocity functional began to emerge in different areas. Delbary (*Delbary2008*) developed a qualitative method for breast cancer detection by combining the reciprocity functional method with the linear sampling method. Colaço (*Colaço2013*) estimated the spatial variation of the thermal contact conductance by using a reciprocity functional approach with the method of fundamental solutions and non-intrusive temperature measurements. Shifrin (*Shifrin2010*) developed a method for identifying small defects in an anisotropic elastic body based on the reciprocity functional method. Other studies, regarding the estimation of the thermal contact conductance through the reciprocity functional, using non-intrusive measures, can be found in (*Colaço2013*, *Colaço2015a*).

Recently, Colaço et al. (*Colaço2015*) presented a methodology, based on the reciprocity functional approach, to estimate internal convective heat transfer coefficients in ducts, using only data available at an exterior boundary and the solutions of two auxiliary problems that depends only on the system geometry. By this approach, here referred as Numerically integrated Reciprocity Function (NRF) method, the two auxiliary problems are solved numerically and the unknown function can be estimated solving a linear system, where the solution vector is composed of integrals of the measured boundary data.

Given the domain Ω represented in Figure (3.2) it is possible to estimate the local convective heat flux coefficient distribution, by defining two auxiliary problem, as suggested by Colaço (*Colaço2015*). The first auxiliary problem concerns the estimation of the unknown local internal heat flux distribution; in particular, the following well-posed auxiliary problem, given by the Equations (3.64.1)–(3.64.3) can be introduced:

$$\nabla^2 G_k = 0 \quad \text{in } \Omega \tag{3.64.1}$$

$$\left.\frac{\partial G_k}{\partial \mathbf{n}}\right|_{\Gamma_{\text{int}}} = 0 \quad \text{on } \Gamma_{int} \tag{3.64.2}$$

$$G_k = \psi_k \quad \text{on } \Gamma_{ext} \tag{3.64.3}$$

where ψ_k is a set of orthogonal functions, which, for a 2D case, can be written as a standard orthonormal Fourier's basis (3.65.1)-(3.65.3):

$$\psi_k = \frac{1}{\sqrt{r_{ext}}\sqrt{2\pi}} \quad \text{for } k = 1 \tag{3.65.1}$$

$$\psi_k = \frac{1}{\sqrt{r_{ext}}\sqrt{\pi}} \cos\left(\frac{k}{2}\theta\right) \quad \text{for } k = 2,4,6, \dots N-1 \tag{3.65.2}$$

$$\psi_k = \frac{1}{\sqrt{r_{ext}}\sqrt{\pi}} \sin\left(\frac{k-1}{2}\theta\right) \quad \text{for } k = 3,5,7, \dots N \tag{3.65.3}$$

where θ is the angular coordinate.

The Betti's theorem allows identifying flaws in materials, but it could be extended to the heat transfer flied considering a continuous and homogeneous medium Ω, subjected to two different potential fields both in equilibrium: the imposed heat flux $\boldsymbol{q}$ and an auxiliary unknown potential filed ψ that allows using the Betti's formulation. Therefore, it is possible to define the reciprocity functional as:

$$\begin{aligned} R_{G,k} &= \int_{\Gamma_{\text{ext}}} \left(\psi_k \frac{\partial T}{\partial \mathbf{n}} - \boldsymbol{Y} \frac{\partial G_k}{\partial \mathbf{n}}\right) \mathrm{d}\Gamma_{\text{ext}} \\ &= \int_{\Gamma_{\text{ext}}} \left[-\psi_k \frac{h_{env}(T - T_{env})}{K} - \boldsymbol{Y} \frac{\partial G_k}{\partial \mathbf{n}}\right] \mathrm{d}\Gamma_{\text{ext}} \end{aligned} \tag{3.66}$$

where h_{env} and T_{env} are the constant and uniform convective heat flux coefficient with the environment and the temperature of the environment, respectively, while K is the thermal conductivity of the solid domain Ω and $\boldsymbol{n}$ is its normal derivative at the external surface Γ_{ext}. It is possible to define the integral of the internal heat source as:

$$Q_{G,k} = \int_{\Omega} \left(G_k \frac{q_g}{K}\right) \mathrm{d}\Omega \tag{3.67}$$

where q_g is the constant and uniform heat flux generation.

As suggested by Colaço (*Colaço2015*), it is possible to write the following identity:

$$\int_{\Gamma_{\text{int}}} \left(G_k \frac{\partial T}{\partial \mathbf{n}} \right) \mathrm{d}\Gamma_{int} = -R_{G,k} - Q_{G,k} \tag{3.68}$$

Using the orthonormal basis defined in Equations (3.65.1)-(3.65.3) and defining γ_k as the trace of the solution G_k on Γ_{int} , the last expression can be manipulated in order to get:

$$-R_{G,k} - Q_{G,k} = \int_{\Gamma_{\text{int}}} \left(G_k \frac{\partial T}{\partial \mathbf{n}} \right) \mathrm{d}\Gamma_{int} = \int_{\Gamma_{\text{int}}} \left(\gamma_k \frac{\partial T}{\partial \mathbf{n}} \right) \mathrm{d}\Gamma_{int} \tag{3.69}$$

The normal derivative of the temperature on the internal surface can be approximated by using the induced basis $\gamma_1, \dots, \gamma_N$ as follows:

$$\left. \frac{\partial T}{\partial \mathbf{n}} \right|_{\Gamma_{\text{int}}} = \alpha_1 \gamma_1 + \cdots + \alpha_N \gamma_N \tag{3.70}$$

Truncating the expansion with N terms, the system of Equations (3.69) is reduced to the following linear system

$$\sum_{k=1}^{N} \int_{\Gamma_{\text{int}}} (\gamma_k \alpha_j \gamma_j) \, \mathrm{d}\Gamma_{int} = \sum_{k=1}^{N} \int_{\Gamma_{\text{int}}} (\gamma_k \gamma_j) \alpha_j \, \mathrm{d}\Gamma_{int} = -\mathbf{R_G} - \mathbf{Q_G} \tag{3.71}$$

$$\text{for } j = 1,2,3, \dots, N$$

Equation (3.71) can be written in matrix form as:

$$\mathbf{M}\, \boldsymbol{\alpha} = -\mathbf{R_G} - \mathbf{Q_G} \tag{3.72}$$

Since the trace of the solution $\gamma_1, \dots, \gamma_N$ are linearly independent, the system in invertible, therefore the α_j coefficients can be found as:

$$\boldsymbol{\alpha} = \mathbf{M}^{-1}(-\mathbf{R_G} - \mathbf{Q_G}) \tag{3.73}$$

Finally, the estimation of $\partial T/\partial \boldsymbol{n}|\Gamma_{int}$ is obtained by simply using the expansion presented in Equation (3.70).

The auxiliary problem presented in Equations (3.64.1)-(3.64.3) can be solved by using different approaches such as: finite difference, finite element, boundary element, method of fundamental solutions, etc.

As already mentioned, in order to estimate the local convective heat flux distribution, it is necessary to introduce two auxiliary direct problems in which the first one concerned the estimation of the internal heat flux distribution. The second auxiliary problem is related to the estimation of the internal wall temperature distribution; in particular, as suggested by Colaço (*Colaço2015*), the following auxiliary problem, has to be solved in order to obtain $T|_{\Gamma_{int}}$:

$$\nabla^2 F_k = 0 \quad \text{in } \Omega \tag{3.74.1}$$

$$F_k = 0 \quad \text{on } \Gamma_{\text{int}} \tag{3.74.2}$$

$$F_k = \psi_k \quad \text{on } \Gamma_{\text{ext}} \tag{3.74.3}$$

This problem is well posed and, for simplicity, the same basis defined in the first auxiliary problem by the Equations (3.65.1)-(3.65.3) could be used. Following the same procedure, it is possible to define the second reciprocity functional and the integral of the heat generation terms as:

$$R_{F,k} = \int_{\Gamma_{\text{ext}}} \left(\psi_k \frac{\partial T}{\partial \mathbf{n}} - Y \frac{\partial F_k}{\partial \mathbf{n}} \right) \mathrm{d}\Gamma_{\text{ext}} \tag{3.75}$$

$$= \int_{\Gamma_{ext}} \left[-\psi_k \frac{h_{\text{env}}(T - T_{\text{env}})}{K} - Y \frac{\partial F_k}{\partial \mathbf{n}} \right] \mathrm{d}\Gamma_{\text{ext}}$$

$$Q_{F,k} = \int_{\Omega} \left(F_k \frac{q_g}{K} \right) \mathrm{d}\Omega \tag{3.76}$$

In the same fashion, it is possible to define the following identity:

$$\int_{\Gamma_{\text{int}}} \left(T \frac{\partial F_k}{\partial \mathbf{n}} \right) \mathrm{d}\Gamma_{\text{int}} = R_{F,k} + Q_{F,k} \tag{3.77}$$

Using the orthonormal basis defined in Equations (3.65.1)-(3.65.3) and defining the ξ as the trace of the solution F_k on Γ_{int}, the last expression can be manipulated in order to get:

$$R_{F,k} + Q_{F,k} = \int_{\Gamma_{\text{int}}} \left(T \frac{\partial F_k}{\partial \mathbf{n}} \right) \mathrm{d}\Gamma_{\text{int}} = \int_{\Gamma_{\text{int}}} (\xi_k T)\, \mathrm{d}\Gamma_{int} \tag{3.78}$$

The temperature on the internal surface can be approximated by using the induced basis $\xi_1, \dots, \xi_N$ as follows:

$$T|_{\Gamma_{\text{int}}} = \beta_1 \xi_1 + \cdots + \beta_N \xi_N \tag{3.79}$$

Truncating the expansion with N terms, the system of equations (3.78) is reduced to:

$$\sum_{k=1}^{N} \int_{\Gamma_{\text{int}}} (\xi_k \boldsymbol{\beta_j} \xi_j)\, \mathrm{d}\Gamma_{int} = \sum_{k=1}^{N} \int_{\Gamma_{\text{int}}} (\xi_k \xi_j) \boldsymbol{\beta_j}\, \mathrm{d}\Gamma_{int} = -\boldsymbol{R}_{F,k} - \boldsymbol{Q}_{F,k} \quad \text{for } j = 1,2,3, \dots, N \tag{3.80}$$

which can be written in the following matrix form:

$$\mathbf{N}\,\boldsymbol{\beta} = -\mathbf{R}_{\boldsymbol{F}} - \mathbf{Q}_{\boldsymbol{F}} \tag{3.81}$$

The system is invertible since $\xi_1, \dots, \xi_N$ are linearly independent, therefore Equation (3.79) is easily solved having the β_j coefficient as unknown:

$$\boldsymbol{\beta} = \mathbf{N}^{-1}(-\mathbf{R}_{\boldsymbol{F}} - \mathbf{Q}_{\boldsymbol{F}}) \tag{3.82}$$

Finally, the estimation of the internal wall temperature $T|_{\Gamma_{int}}$ is obtained simply by using the expansion presented in equation (3.70).

Once the heat flux (Equation (3.70)) and temperature (Equation (3.82)) distributions are known at the internal boundary Γ_{int}, it is possible to estimate the convective heat transfer coefficient distribution as suggested form the Equation (3.24).

As already mentioned for the first auxiliary problem, there are many different approaches that could be used in order to determine the solution of the direct auxiliary problem. In the next chapter the *Classical Integral Transform Technique* (CITT) will be used.

3.3 Stopping criteria

There are many different criteria that could be used in order to choose the regularization parameter. Among all it has to be pointed out the *L-curve method* and the *Morozov's discrepancy principle*, but there are many other approaches such as the *Generalized Cross Validation* (GCV) and the *Fixed-point method* that could be used.

L-curve method

The L-curve method is the easiest methodology that could be used in order to identify the regularization parameter λ. This approach is based on graphically finding the best balance between the data misfit and the solution regularity (Figure (3.4)).

In order to deal with this problem, the measure of the regularity of the solution $\|\boldsymbol{q_\lambda}\|_2^2$ has to be plotted as a function of the data misfit $\left\|\boldsymbol{X q_\lambda} - \left(\boldsymbol{Y} - \boldsymbol{T}_{q=0}\right)\right\|_2^2$. When these two quantities are plotted in a log-log scale, the graph often takes a characteristic L shape but multiple notch could arise if the inverse problem is severely ill-posed. The L-shape of the chart happens because $\|\boldsymbol{q_\lambda}\|_2^2$ is a strictly decreasing function of λ while $\left\|\boldsymbol{X q_\lambda} - \left(\boldsymbol{Y} - \boldsymbol{T}_{q=0}\right)\right\|_2^2$ is a strictly increasing function of λ. The sharpness of the notch varies from problem to problem but it is frequently well-defined.

Hansen (*Hansen1992, Hansen1993, Hansen1999*) provided a very good analysis related to the formulation and application of the L-curve criterion for both the Tikhonov and the SVD regularization schemes. He also observed the curvature of the L-curve and provided an automatic algorithm for the identification of the notch.

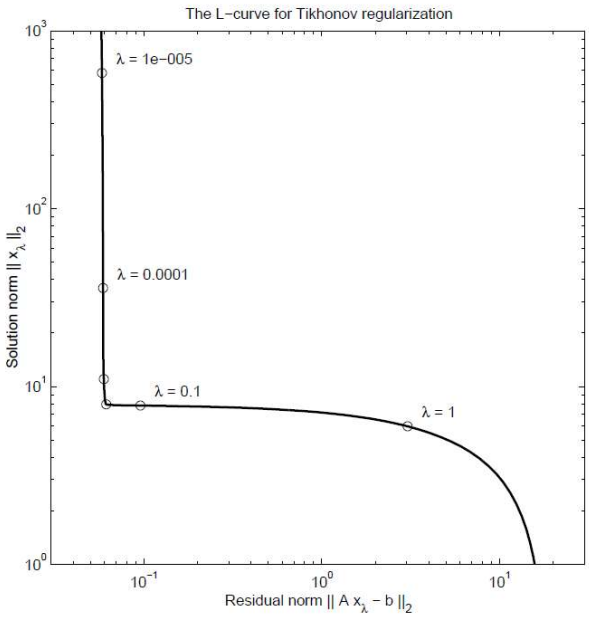

Figure 3.4: Example of a L-curve (*Hansen1999*)

Morozov's discrepancy principle

The importance of the choice of the regularization parameter was widely analysed in the literature. In particular, Hansen (*Hansen1999*) performed a survey on the Tikhonov regularization parameter choice. From the qualitative point of view, adopting large regularization parameters means that the solution will be extremely stable and smooth, prejudicing the data fitting, while adopting a very small regularization parameter will estimate a solution that perfectly fits the data but that is completely unstable. The effect of different criteria was already investigated by Bazàn (*Bazàn2009*), but is the Morozov's discrepancy principle that, from a practical point of view, could suggest one of the feasible values of λ.

In particular, the Morozov's discrepancy principle affirms that the regularization parameter has to be the smallest parameter that satisfy the following inequality:

$$\frac{\left\| \boldsymbol{Y} - \left(\boldsymbol{X}\boldsymbol{q}_{\lambda} - \boldsymbol{T}_{q=0} \right) \right\|_2}{\left\| \sqrt{N} \right\|} \approx \sigma \tag{3.83}$$

where σ is the expected standard deviation of the measurement.

According to this criterion, the solution of the inverse problem is assumed to be satisfactorily accurate when the difference between the simulated $\left(\boldsymbol{X}\boldsymbol{q}_{\lambda} - \boldsymbol{T}_{q=0} \right)$ and measured $\boldsymbol{Y}$ temperature distributions, is close to the standard deviation of the raw data, σ.

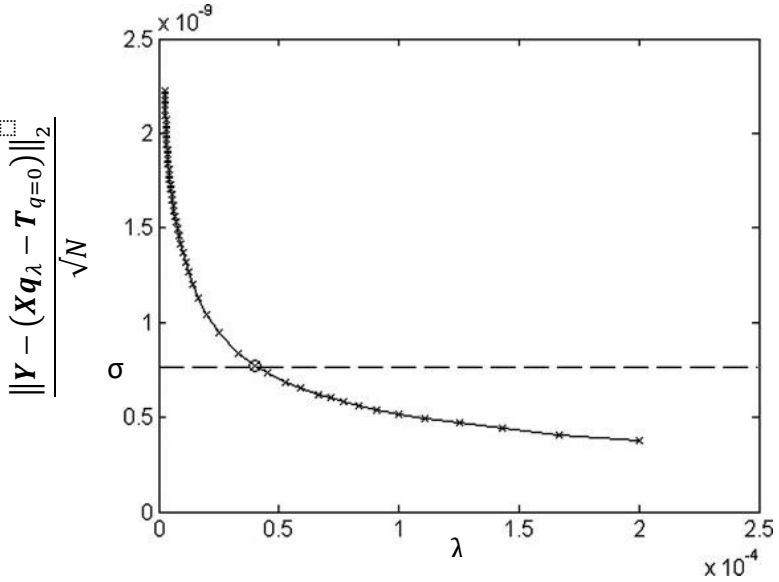

Figure 3.5: Example of discrepancy principle

This could be interpreted also as that there is no more information that could be extracted from the signal once it is only noise.

Fixed-point

The fixed point of a function is an element of the function's domain that is mapped onto itself by the function. Application of the fixed-point method requires the computation of the solution semi-norm and the corresponding residual norm, and it selects the parameter that minimises the product of these norms subjected to the minimum distance from the origin as a function of the regularisation parameter. Like the L-curve, the reason to use this algorithm is that the sought minimiser corresponds to a good balance between the size of these norms. Algorithmically, the regularisation parameter chosen by the fixed-point method is the limit value of the sequence:

$$\lambda_{k+1}^{*} = \phi(\lambda_k^{*}) = \frac{\left\|\boldsymbol{Y} - \left(\boldsymbol{X}\boldsymbol{q}_\lambda - \boldsymbol{T}_{q=0}\right)\right\|_2}{\|\boldsymbol{L}_{\boldsymbol{d}}\boldsymbol{q}\|}, \quad k = 0,1,2,\ldots \tag{3.84}$$

In order to ensure the convergence of the fixed point sequence, the invariance and the contractivity of the sequence has to be guarantee, but this particular aspect goes beyond the scope of the present thesis.

The value for the regularisation parameter can also be visually represented as a fixed-point of the curve $\phi(\lambda^{*})$.

In practice, the sequence converges very quickly, and the computed regularisation parameter yields to solutions with accuracy comparable to that of the L-curve method, but it is more robust and computationally less expensive (*Bazán2008, Bazán2009*).

The regularised solution $\boldsymbol{q}_{\lambda^*}$ is computed efficiently by means of the GSVD of the matrix pair $[\boldsymbol{X}, \boldsymbol{L}]$, which simplifies the implementation of the fixed-point algorithm according to Bazàn (*Bazán2008*).

The fixed-point method, like the L-curve approach, does not require a priori knowledge of the noise level.

Chapter 4

New methodologies

4.1 Introduction

As already mentioned in the previous chapter, the new methodologies proposed here are subdivided in two groups: parameter estimation and function estimation. The subdivision is not related to the estimation capabilities of the inverse solution technique (some of the presented approaches could be used for both the parameter and the function estimation), but it is related to the number of unknown variables that has to be estimated in order to characterized the heat exchanger in each specific application introduced in *Chapter 3*.

4.2 Parameter estimation

Among all the possible technique coming from the optimization research field that could be used for a parameter estimation, one common algorithm is the non-linear fit based on the IRLS method.

This particular estimation procedure was applied to the estimation of the α, β and γ coefficients appearing in the common Nusselt number formulation (*Incopera2005, Rainieri2004*):

$$Nu = \alpha \, Re^{\beta} Pr^{\gamma} \tag{4.1}$$

The Nusselt number function defined in Equation (4.1) is based on the assumption that the heat transfer mechanism is governed by the single-phase forced convection. If evaporation or condensation occurs, then other terms drive the heat transfer mechanism (e.g. vapour quality, heat flux, and pressure).

The approach is based on the minimization of the objective function defined as:

$$r = \left\| U_{exp} - U_{pred} \right\|_2 \tag{4.2}$$

where U_{exp} and U_{pred} are respectively the experimental and the predicted global heat transfer coefficient.

In a general industrial application, it is common to have a shell and tube heat exchanger in which could pass different fluids. Therefore, it is interesting the estimation of the interaction with the system of both the fluid that is passing thorough the shell and the fluid that is passing through the tube. Hence, a six parameter optimization procedure is required in order to retrieve the α, β and γ coefficients for both the tube and the shell side needed for the definition of the Nusselt number function (Equation (4.1)).

For any double flow heat exchanger in a steady state condition, characterized by a perfect thermal insulation from the environment, in which is negligible the heat conduction in the flow direction, it is possible to determine the average overall heat transfer coefficient U for the inner heat transfer surface area A_i as follows:

$$U = \frac{Q}{A_i \Delta T_{ml}} \tag{4.3}$$

where ΔT_{ml} is the logarithmic mean temperature difference while Q is the exchanged heat flow rate.

The exchanged heat flow rate could be determined by the energy balance:

$$Q = \dot{m}^t c_p^t (T_{in}^t - T_{out}^t) = \dot{m}^s c_p^s (T_{in}^s - T_{out}^s) \tag{4.4}$$

where $\dot{m}$ and c_p are the mass flow rate and the specific heat capacity, respectively, while $\cdot^t$ and $\cdot^s$ stay for the tube and the shell side, respectively

Due to the electrical analogy, it is possible to define the overall heat transfer coefficient as a summation of thermal resistances as follows:

$$\frac{1}{UA_i} = \frac{1}{h_i A_i} + R_w + \frac{1}{h_o A_o} \tag{4.5}$$

where h_i and h_o are the internal and external convective heat transfer coefficient respectively, while A_i and A_o are the internal and the external heat exchanger surface areas, respectively.

Due to the quasi-cylindrical configuration characteristic of a tube side heat exchanger, the thermal resistance of the wall R_w could be approximated as:

$$R_w = \frac{\ln\left(\frac{D_o}{D_i}\right)}{2\pi K_w L} \tag{4.6}$$

where D_0 and D_i are the external and internal hydraulic diameters of the tube, respectively, while K_w and L are the thermal conductivity and the length of the tube that is exchanging heat, respectively. Thus it is possible to assume the thermal resistance of the wall to be known, for a given heat exchanger configuration, under a given operating condition.

Assuming that the internal diameter of the tube is known, as well as the characteristic length, it is possible to define the internal Nusselt number coefficient as:

$$Nu_i = \frac{h_i D_i}{K} \tag{4.7}$$

where K is the thermal conductivity of the fluid that is passing inside the tube.

The convective heat transfer coefficients h_o and h_i appearing in the Equation (4.5) are unknown. Moreover, their values are difficult to be determined also because they change for

each application. Therefore, they can be estimated, with a suitable accuracy, by adopting a parameter estimation technique under an inverse data processing problem methodology (*Beck1977*). This implies that the following cost function has to be minimised:

$$r_{(\alpha^t,\beta^t,\gamma^t,\alpha^s,\beta^s,\gamma^s)} = \sum_{j=1}^{M}\left(U_{exp,j} - U_{pred,j}\right)^2 \qquad (4.8)$$

where M is the total number of measurements made by varying both the Reynolds number at the shell and the tube side Re^s and Re^t, respectively, and the working fluid (represented by the Prandtl number) at the both tube Pr^t and the shell Pr^s.

It is possible to write the Equation (4.5), highlighting the effect of the unknown parameters:

$$U_{pred} = A_i\left(\frac{D_i}{A_i\lambda^t\alpha^t(Re^t)^{\beta^t}(Pr^t)^{\gamma^t}} + R_w + \frac{D_i}{A_o\lambda^s\alpha^s(Re^s)^{\beta^s}(Pr^s)^{\gamma^s}}\right)^{-1} \qquad (4.9)$$

The optimization algorithm will find the best set of unknown parameters that are able to minimise the cost function defined by the Equation (4.8), giving also their confidence intervals.

4.3 Function Estimation

Two new solution strategies for the function estimation procedure were developed for the solution of the ICHP. The main goal of this type of problem is the estimation of the internal heat flux distribution, given some external extra-measurements of the solid body temperature.

The first solution technique is an upgrade of the Singular Value Decomposition, in which a new filter function based on the Gaussian distribution was applied in order to overcome some of the limitation related to the TSVD.

The second solution scheme is based on the RF and, due to its analytical formulation, it was developed for the two-dimensional annular domain.

4.3.1 Gaussian Filtered Singular Value Decomposition

The regularization approach for the unconstrained linear least square problem proposed here, improves the classical methods based on the singular value decomposition approach by employing the Gaussian filter. This kind of filter has been proved to be effective in several applications related to noise suppression with regards to inverse problems (*Bozzoli2013*).

In the classical SVD approach, the inverse matrix is approximated by the Moore-Penrose pseudo inverse. In order to increase the stability of the reconstructed signal, the solution space is even reduced by truncating the singular values used in the approximation of the inverse matrix (TSVD). Although this technique is very effective, some authors have proposed improvements in order to overcome some of its acknowledged limitations.

In particular, TSVD approach is not conservative when the signal to be estimated is characterised by a wide-spectrum. Ekstrom (*Ekstrom1974*), suggested a modified approach called DSVD that damps the small singular values instead of neglecting them, in order to increase the reconstruction quality of the signal. Therefore, while the TSVD approach filters the singular value series by a sharp ideal high-pass filter, the damped SVD smooths the singular value series by a first-order filter. The idea behind this type of approach is that singular values near by the cut-off frequency of the ideal high-pass filter (TSVD) could add more information than instability during the reconstruction procedure, increasing the quality of the estimated solution.

An upgrade to the DSVD can be done simply by changing the filter factor, since it is the function that describe the way in which the singular values are dumped.

As already shown in the *Chapter 3* (Equation 3.67), it is possible to write the estimated solution given by the filtered SDV as the product of a filter function f_i times the SVD expansion. In particular, a Gaussian function distribution is adopted, since its properties to smooth noisy data has been successfully experimented also in the image quality enhancement within graphics software (*Murio1993*).

The Gaussian filter factor assumes the following expression:

$$f_i = e^{-\frac{1}{2}\left(\frac{\lambda}{\sigma_i}\right)^2} \tag{4.11}$$

where λ is the regularization parameter that should be adequately chosen. The application of a Gaussian factor has the effect of reducing large $1/\sigma_i$ values in order to overcome the ill-posedness of the problem.

This approach, as well as the TSVD, DSVD and Tikhonov regularization methodologies, is based on the idea that the singular values appearing in the **Σ** matrix of the SVD expansion has to be damped as far as the noise inside the measurement increase, in order to retrieve a smooth estimated solution (properties that are required, due to the continuous behaviour of the nature).

The filter factor of the investigated approaches are listed below:

Table 4.1: Filter factor summary

TSVD	$f_i = \begin{cases} 0, & for\ \sigma_i > \lambda \\ 1, & for\ \sigma_i \leq \lambda \end{cases}$	(4.12.1)
DSVD	$f_i = \frac{\sigma_i}{\sigma_i + \lambda}$	(4.12.2)
GFSVD	$f_i = e^{-\frac{1}{2}\left(\frac{\lambda}{\sigma_i}\right)^2}$	(4.12.3)
TM	$f_i = \frac{\sigma_i^2}{\sigma_i^2 + \lambda^2}$	(4.12.4)

The shape of the four considered filter functions is reported in Figure (4.1), where the cut-off value σ_c, which is the frequency at which the filter function in equal to $\sqrt{2}$, is introduced according to the classical definition (*Bozzoli2013*).

As it is possible to see, the trend at which the singular values are pushed to zero as far as their values increase is different for each filter form.

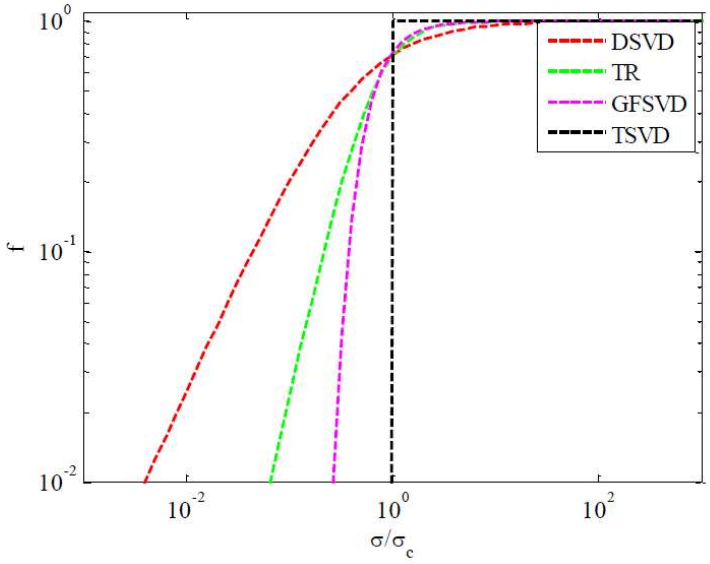

Figure 4.1: Filter functions

Once the heat flux is estimated according to equation (3.56), the internal wall temperature of the tube T_{int} can be estimated by solving the direct auxiliary problem defined by the linear system of equations (3.23).

Under the assumption that the bulk temperature is known, it is possible to determine the convective heat transfer coefficient as:

$$h_{int} = \frac{q}{A_{int}\,(T_{int} - T_b)} \tag{4.13}$$

where A_{int} is the internal wall surface area.

It has to be pointed out that, the computational requirement of the GFSVD is comparable with the ones of TSVD and DSVD methods since all the solution strategies require the filtering of the singular value coefficients. For this reason, the comparison has to be performed in terms of reconstruction capabilities instead of computational requirements.

4.3.2 Filtered Reciprocity Functional

The new methodology here presented, starts from the findings of Colaço (*Colaço2013, Colaço2015*) with the aim of overcome the limit of the numerical solution of the auxiliary problems by means of the Classical Integral Transform Technique (CITT), a well-known analytical method (*Ozisik1993)* used for the solution of the Partial Differential Equations system. In this way, thanks to a fully analytical approach, it is possible to understand how the RF approach deals with the noise content in the experimental data and therefore the regularization factor can be tuned in order to improve the robustness of the approach. The new solution methodology, named Filtered Reciprocity Functional (FRF), is fully demonstrated in *Appendix 2*, numerically verified in *Chapter 5* and experimentally validated in *Chapter 6*.

DETERMINING THE NORMAL DERIVATIVE OF THE TEMPERATURE AT THE INTERNAL BOUNDARY $\partial T/\partial \boldsymbol{n}$*:*

As suggested by Colaço (*Colaço2015*), the following well-posed auxiliary problem, already introduce in *Chapter 3* and here reminded, can be used in order to obtain $\left.\frac{\partial T}{\partial \boldsymbol{n}}\right|_{\Gamma_{int}}$:

$$\nabla^2 G_k = 0 \quad \text{in } \Omega \tag{4.14.1}$$

$$\left.\frac{\partial G_k}{\partial \mathbf{n}}\right|_{\Gamma_{\text{int}}} = 0 \quad \text{on } \Gamma_{int} \tag{4.14.2}$$

$$G_k = \psi_k \quad \text{on } \Gamma_{ext} \tag{4.14.3}$$

where ψ_k is a set of orthogonal functions, which, for a 2D case, can be written as a standard orthonormal Fourier's basis (4.15.1)-(4.15.3):

$$\psi_k = \frac{1}{\sqrt{r_{ext}}\sqrt{2\pi}} \quad \text{for } k = 1 \tag{4.15.1}$$

$$\psi_k = \frac{1}{\sqrt{r_{ext}}\sqrt{\pi}} \cos\left(\frac{k}{2}\theta\right) \quad \text{for } k = 2,4,6,\dots N-1 \tag{4.15.2}$$

$$\psi_k = \frac{1}{\sqrt{r_{ext}}\sqrt{\pi}} \sin\left(\frac{k-1}{2}\theta\right) \quad \text{for } k = 3,5,7,\dots N \tag{4.15.3}$$

Defining the reciprocity functional and the integral of the internal heat source, respectively, as follows

$$R_{G,k} = \int_{\Gamma_{\text{ext}}} \left(\psi_k \frac{\partial T}{\partial \mathbf{n}} - Y \frac{\partial G_k}{\partial \mathbf{n}}\right) \mathrm{d}\Gamma_{\text{ext}} \tag{4.16}$$

$$= \int_{\Gamma_{\text{ext}}} \left[-\psi_k \frac{h_{env}(T - T_{env})}{K} - Y \frac{\partial G_k}{\partial \mathbf{n}}\right] \mathrm{d}\Gamma_{\text{ext}}$$

$$Q_{G,k} = \int_{\Omega} \left(G_k \frac{q_g}{K}\right) \mathrm{d}\Omega \tag{4.17}$$

it is possible to write the following identity:

$$\int_{\Gamma_{\text{int}}} \left(G_k \frac{\partial T}{\partial \mathbf{n}}\right) \mathrm{d}\Gamma_{int} = -R_{G,k} - Q_{G,k} \tag{4.18}$$

More details about the equation above can be found in Colaço (*Colaço2015)*.
Using the orthonormal basis defined in Equations (4.15.1)-(4.15.3), and defining γ_k as the trace of the solution G_k on Γ_{int}, the last expression can be manipulated in order to get:

$$-R_{G,k} - Q_{G,k} = \int_{\Gamma_{\text{int}}} \left(G_k \frac{\partial T}{\partial \mathbf{n}}\right) \mathrm{d}\Gamma_{int} = \int_{\Gamma_{\text{int}}} \left(\gamma_k \frac{\partial T}{\partial \mathbf{n}}\right) \mathrm{d}\Gamma_{int} \tag{4.19}$$

The normal derivative of the temperature on the internal surface can be approximated by using the induced basis $\gamma_1, \dots, \gamma_N$ as follows:

$$\left.\frac{\partial T}{\partial \mathbf{n}}\right|_{\Gamma_{\text{int}}} = \alpha_1\gamma_1 + \cdots + \alpha_N\gamma_N \tag{4.20}$$

Therefore, truncating the expansion with N terms, the system of equations (4.19) is reduced to the following linear system

$$\sum_{k=1}^{N}\int_{\Gamma_{\text{int}}}\left(\gamma_k\alpha_j\gamma_j\right)\mathrm{d}\Gamma_{int} = \sum_{k=1}^{N}\int_{\Gamma_{\text{int}}}\left(\gamma_k\gamma_j\right)\alpha_j\,\mathrm{d}\Gamma_{int} = -\mathbf{R_G} - \mathbf{Q_G} \quad \text{for } j = 1,2,3,\dots,N \tag{4.21}$$

Equation (4.21) can be written in matrix form as:

$$\mathbf{M}\,\boldsymbol{\alpha} = -\mathbf{R_G} - \mathbf{Q_G} \tag{4.22}$$

The system is invertible since $\gamma_1, \dots, \gamma_N$ are linearly independent and therefore the α_j coefficients can be found as:

$$\boldsymbol{\alpha} = \mathbf{M}^{-1}(-\mathbf{R_G} - \mathbf{Q_G}) \tag{4.23}$$

After that, the estimation of $\left.\frac{\partial T}{\partial \boldsymbol{n}}\right|_{\Gamma_{int}}$ is obtained by simply using the expansion presented in Equation (4.20).

The auxiliary problem presented in equations (4.14.1)-(4.14.3) is then solved analytically by using the Classical Integral Transform Technique (*Ozisik1993*). Initially, equation (4.14.1) is expressed in the cylindrical coordinate system:

$$\frac{\partial^2 G_k}{\partial r^2} + \frac{1}{r}\frac{\partial G_k}{\partial r} + \frac{1}{r^2}\frac{\partial^2 G_k}{\partial \theta^2} = 0 \tag{4.24}$$

Then, defining the integral transform as

$$\overline{G_{k,\nu}} \equiv \overline{G_k}(r,\nu) = \int_{\theta=0}^{2\pi} G_k(r,\theta')\cos[\nu(\theta-\theta')]\,\mathrm{d}\theta' \tag{4.25}$$

and the inversion formula as

$$G_k \equiv G_k(r,\theta) = \frac{1}{2\pi}\bar{G}_k(r,\nu=0) + \sum_{\nu=1}^{\infty}\frac{1}{\pi}\bar{G}_k(r,\nu) \tag{4.26}$$

Equation (4.24), multiplied by $\cos[\nu(\theta-\theta')]$and integrated, becomes:

$$\frac{\mathrm{d}^2\overline{G_{k,\nu}}}{\mathrm{d}r^2} + \frac{1}{r}\frac{\mathrm{d}\overline{G_{k,\nu}}}{\mathrm{d}r} + \frac{1}{r^2}\nu^2\overline{G_{k,\nu}} = 0 \tag{4.27}$$

With the same procedure, Equation (4.14.2), which expresses the boundary condition imposed on the internal boundary Γ_{int}, result to get:

$$\frac{\mathrm{d}\overline{G_{k,\nu}}}{\mathrm{d}r} = 0 \tag{4.28}$$

and the external boundary condition can be re-written as follows:

$$\overline{G_{k,\nu}} = \overline{\psi_{k,\nu}} \tag{4.29}$$

where $\overline{\psi_{k,\nu}}$ is the transformation of the potential imposed in the first auxiliary problem given by Equation (4.14.3):

$$\overline{\psi_{k,\nu}} = \int_{\theta'=0}^{2\pi}\psi_k\cos[\nu(\theta-\theta')]\,\mathrm{d}\theta' \tag{4.30}$$

Using the above equations, the transformed first auxiliary problem is finally obtained as:

$$\frac{\mathrm{d}^2\overline{G_{k,\nu}}}{\mathrm{d}r^2}+\frac{1}{r}\frac{\mathrm{d}\overline{G_{k,\nu}}}{\mathrm{d}r}+\frac{1}{r^2}\nu^2\overline{G_{k,\nu}}=0 \quad \text{in } \Omega \tag{4.31.1}$$

$$\left.\frac{\mathrm{d}\overline{G_{k,\nu}}}{\mathrm{d}r}\right|_{\Gamma_{\mathrm{int}}}=0 \quad \text{on } \Gamma_{int} \tag{4.31.2}$$

$$\overline{G_{k,\nu}}=\overline{\psi_{k,\nu}} \quad \text{on } \Gamma_{ext} \tag{4.31.3}$$

whose solution can be found as:

$$\overline{G_{k,\nu}}=\overline{\psi_{k,\nu}}\cosh\left\{\nu\left[\ln\left(\frac{r_{int}}{r}\right)\right]\right\}\operatorname{sech}\left\{\nu\left[\ln\left(\frac{r_{int}}{r_{ext}}\right)\right]\right\} \tag{4.32}$$

In order to obtain the solution of the first auxiliary problem, the above equation has to be inverted using the definition given by Equation (4.26):

$$G_k=\frac{1}{2\pi}\overline{\psi_{k,\nu=0}}+\sum_{\nu=1}^{\infty}\frac{1}{\pi}\overline{\psi_{k,\nu}}\cosh\left\{\nu\left[\ln\left(\frac{r_{\mathrm{int}}}{r}\right)\right]\right\}\operatorname{sech}\left\{\nu\left[\ln\left(\frac{r_{\mathrm{int}}}{r_{\mathrm{ext}}}\right)\right]\right\} \tag{4.33}$$

The measurements $\boldsymbol{Y}$ are decomposed by the Fourier series expansion, in order to take advantage of the harmonic decomposition of the Classical Integral Transform Technique:

$$\boldsymbol{Y}(\theta)=\frac{a_0}{2}+\sum_{\nu=1}^{N}[a_\nu\cos(\nu\theta)+b_\nu\sin(\nu\theta)] \tag{4.34}$$

where $a_i$and b_i are real numbers and ν is an integer number.

Thanks to this, it is possible to distinguish between the signal and the noise. In almost every practical situation (*Bozzoli2013*), the signal content is mainly present at low frequencies, while noise is present over the whole spectrum.

This approach, whose details are reported in the *Appendix 1*, enables to conveniently express the terms of Equation (4.22) in the following way:

The main advantage of the analytical solution of the reciprocity functional consist in the diagonal form that characterized the matrix of the inner products $\boldsymbol{M}$. This behaviour is due to the proper choice of the ψ basis appearing in the definition of the auxiliary problem that are orthogonal to the eigenfunctions appearing in the solution of the auxiliary problem provided by the CITT.

$$\boldsymbol{\alpha} = \begin{bmatrix} \alpha_{v=1} \\ \alpha_{v=2} \\ \vdots \\ \alpha_{v=v} \end{bmatrix} \tag{4.35}$$

$$\mathbf{R_G} = -\sqrt{\pi r_{ext}} \begin{bmatrix} \sqrt{2}\dfrac{h_{env}}{K}(a_0 - T_{env}) \\ \left\{\dfrac{h_{env}}{K} - \tanh\left[\ln\left(\dfrac{r_{int}}{r_{ext}}\right)\right]\dfrac{1}{r_{ext}}\right\} & a_1 \\ \left\{\dfrac{h_{env}}{K} - \tanh\left[\ln\left(\dfrac{r_{int}}{r_{ext}}\right)\right]\dfrac{1}{r_{ext}}\right\} & b_1 \\ \left\{\dfrac{h_{env}}{K} - \tanh\left[2\ln\left(\dfrac{r_{int}}{r_{ext}}\right)\right]\dfrac{2}{r_{ext}}\right\} & a_2 \\ \left\{\dfrac{h_{env}}{K} - \tanh\left[2\ln\left(\dfrac{r_{int}}{r_{ext}}\right)\right]\dfrac{2}{r_{ext}}\right\} & b_2 \\ \vdots \\ \left\{\dfrac{h_{env}}{K} - \tanh\left[v\ln\left(\dfrac{r_{int}}{r_{ext}}\right)\right]\dfrac{v}{r_{ext}}\right\} & a_v \\ \left\{\dfrac{h_{env}}{K} - \tanh\left[v\ln\left(\dfrac{r_{int}}{r_{ext}}\right)\right]\dfrac{v}{r_{ext}}\right\} & b_v \end{bmatrix} \tag{4.36}$$

$$\mathbf{Q_G} = \begin{bmatrix} \dfrac{q_g}{K}\sqrt{\dfrac{\pi}{2r_{ext}}}(r_{ext}^2 - r_{int}^2) \\ 0 \\ \vdots \\ 0 \end{bmatrix} \tag{4.37}$$

$$\mathbf{M} = \frac{r_{int}}{r_{ext}} \begin{bmatrix} 1 & & & & & & 0 \\ & \operatorname{sech}^2\left[1\ln\left(\frac{r_{int}}{r_{ext}}\right)\right] & & & & & \\ & & \operatorname{sech}^2\left[1\ln\left(\frac{r_{int}}{r_{ext}}\right)\right] & & & & \\ & & & \operatorname{sech}^2\left[2\ln\left(\frac{r_{int}}{r_{ext}}\right)\right] & & & \\ & & & & \operatorname{sech}^2\left[2\ln\left(\frac{r_{int}}{r_{ext}}\right)\right] & & \\ & & & & & \ddots & \\ & & & & & & \operatorname{sech}^2\left[v\ln\left(\frac{r_{int}}{r_{ext}}\right)\right] \\ 0 & & & & & & \operatorname{sech}^2\left[v\ln\left(\frac{r_{int}}{r_{ext}}\right)\right] \end{bmatrix} \tag{4.38}$$

$$\boldsymbol{\gamma} = \frac{1}{\sqrt{\pi r_{ext}}} \begin{bmatrix} \frac{1}{\sqrt{2}} \\ \cos(1\,\theta)\,\mathrm{sech}\left[1 \ln\left(\frac{r_{int}}{r_{ext}}\right)\right] \\ \sin(1\,\theta)\,\mathrm{sech}\left[1 \ln\left(\frac{r_{int}}{r_{ext}}\right)\right] \\ \cos(2\,\theta)\,\mathrm{sech}\left[2 \ln\left(\frac{r_{int}}{r_{ext}}\right)\right] \\ \sin(2\,\theta)\,\mathrm{sech}\left[2 \ln\left(\frac{r_{int}}{r_{ext}}\right)\right] \\ \vdots \\ \cos(\nu\,\theta)\,\mathrm{sech}\left[\nu \ln\left(\frac{r_{int}}{r_{ext}}\right)\right] \\ \sin(\nu\,\theta)\,\mathrm{sech}\left[\nu \ln\left(\frac{r_{int}}{r_{ext}}\right)\right] \end{bmatrix} \tag{4.39}$$

The values of α_j coefficient, which are the goal of the first auxiliary problem, are easily obtained from a mathematical point of view by Equation (4.23). Due to the ill-posed nature of the problem and the presence of the noise in the measurement vector $\boldsymbol{Y} = [y_1, y_2, \dots, y_n]$, the inversion of the matrix $\boldsymbol{M}$ has to be approached by inverse problem solution techniques in order to find a realistic estimation of the unknown heat flux.

Since the matrix $\boldsymbol{M}$ is diagonal, its inverse can be easily determined as follows:

$$\mathbf{M}^{-1} = \frac{r_{ext}}{r_{int}} \begin{bmatrix} 1 & & & & & & & 0 \\ & \frac{1}{\mathrm{sech}^2\left[1 \ln\left(\frac{r_{int}}{r_{ext}}\right)\right]} & & & & & & \\ & & \frac{1}{\mathrm{sech}^2\left[1 \ln\left(\frac{r_{int}}{r_{ext}}\right)\right]} & & & & & \\ & & & \frac{1}{\mathrm{sech}^2\left[2 \ln\left(\frac{r_{int}}{r_{ext}}\right)\right]} & & & & \\ & & & & \frac{1}{\mathrm{sech}^2\left[2 \ln\left(\frac{r_{int}}{r_{ext}}\right)\right]} & & & \\ & & & & & \ddots & & \\ & & & & & & \frac{1}{\mathrm{sech}^2\left[\nu \ln\left(\frac{r_{int}}{r_{ext}}\right)\right]} & \\ 0 & & & & & & & \frac{1}{\mathrm{sech}^2\left[\nu \ln\left(\frac{r_{int}}{r_{ext}}\right)\right]} \end{bmatrix} \tag{4.40}$$

The analytical expression achieved clearly highlights the destructive effect of the noise on the reconstruction of the α_j coefficient: the values of $\boldsymbol{M}^{-1}$ matrix components, following the $1/\,\mathrm{sech}^2[\nu \ln(r_{int}/r_{ext})]$ function, increase with the number of the harmonic. For this reason, these terms work as operators that amplifies the high frequency components of $\boldsymbol{R_G}$ more than the low ones of a given input data set $\boldsymbol{Y}$. In Figure (4.3), the values of $\boldsymbol{M}^{-1}$ components are plotted for a representative ratio $r_{int}/r_{ext} = 0.9$ as a function of the harmonic order.

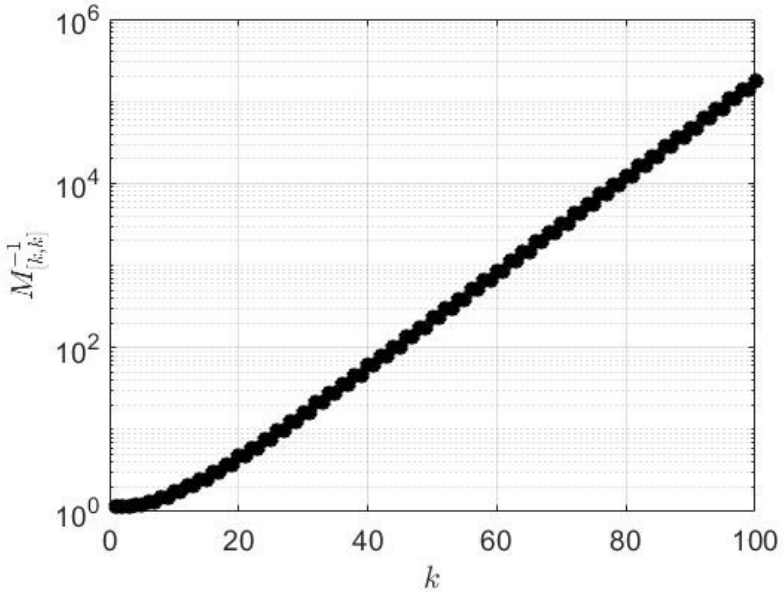

Figure 4.2: Diagonal elements of the $\boldsymbol{M^{-1}}$ matrix for a representative value $r_{int}/r_{ext} = 0.9$

For cases where both the signal and the noise have frequency components equally distributed over the spectrum of interest, the $\boldsymbol{M^{-1}}$ matrix does not deteriorate the signal content in comparison to the original data. Unfortunately, in almost all practical situations, the signal has frequency components concentrated in the low frequency range of the spectrum, while the spectral components of noise is expected to be uniformly distributed over the entire frequency domain, (*Bozzoli2013*). Therefore the $\boldsymbol{M^{-1}}$ operator makes very difficult the extraction of some useful information from the $\boldsymbol{R_G}$ vector. For this reason, some regularization technique is needed.

In the present work this problem is tackled by conveniently truncating the $\boldsymbol{M^{-1}}$ matrix, considering only the first ν harmonics as suggested by Bozzoli (*Bozzoli2013*) in an analogous inverse problem. The number of harmonics to keep is chosen by the classical discrepancy principle, originally formulated by Morozov (*Morozov1984*). More efficient approaches in terms of computational costs are available, but since this aspect is related to the stopping criteria and not to the methodology itself, more studies are needed in order investigate the effect of the criteria adopted.

DETERMINING THE INTERNAL WALL TEMPERATURE $T|_{\Gamma_{int}}$:

As suggested by Colaço (*Colaço2015*), the following auxiliary problem, already introduce in *Chapter 3* and here reminded, can be used in order to obtain $T|_{\Gamma_{int}}$:

$$\nabla^2 F_k = 0 \quad \text{in } \Omega \tag{4.41.1}$$
$$F_k = 0 \quad \text{on } \Gamma_{\text{int}} \tag{4.41.2}$$
$$F_k = \psi_k \quad \text{on } \Gamma_{\text{ext}} \tag{4.41.3}$$

This problem is well posed and, for simplicity, we used the same basis defined in the first auxiliary problem, equations (4.15.1)-(4.15.3). Following the same steps used in the first auxiliary problem, the second reciprocity functional and the integral of the heat generation terms can be defined as:

$$R_{F,k} = \int_{\Gamma_{\text{ext}}} \left(\psi_k \frac{\partial T}{\partial \mathbf{n}} - Y \frac{\partial F_k}{\partial \mathbf{n}}\right) \mathrm{d}\Gamma_{\text{ext}} = \int_{\Gamma_{ext}} \left[-\psi_k \frac{h_{\text{env}}(T - T_{\text{env}})}{K} - Y \frac{\partial F_k}{\partial \mathbf{n}}\right] \mathrm{d}\Gamma_{\text{ext}} \tag{4.42}$$

$$Q_{G,k} = \int_{\Omega} \left(F_k \frac{q_g}{K}\right) \mathrm{d}\Omega \tag{4.43}$$

Therefore, it is possible to write the following expression:

$$\int_{\Gamma_{\text{int}}} \left(T \frac{\partial F_k}{\partial \mathbf{n}}\right) \mathrm{d}\Gamma_{\text{int}} = R_{F,k} + Q_{F,k} \tag{4.44}$$

Using the orthonormal basis defined in equations (4.15.1)-(4.15.3) and defining ξ as the trace of the solution F_k on Γ_{int}, the last expression can be manipulated in order to get:

$$R_{F,k} + Q_{F,k} = \int_{\Gamma_{\text{int}}} \left(T \frac{\partial F_k}{\partial \mathbf{n}}\right) \mathrm{d}\Gamma_{\text{int}} = \int_{\Gamma_{\text{int}}} (\xi_k T) \, \mathrm{d}\Gamma_{int} \tag{4.45}$$

The temperature on the internal surface can be approximated by using the induced basis $\xi_1, \dots, \xi_N$ as follows:

$$T|_{\Gamma_{\text{int}}} = \beta_1 \xi_1 + \cdots + \beta_N \xi_N \tag{4.46}$$

Therefore, truncating the expansion with N terms, the system of Equations (4.45) is reduced to the following linear system (4.47):

$$\sum_{k=1}^{N} \int_{\Gamma_{\text{int}}} \left(\xi_k \boldsymbol{\beta_j} \xi_j\right) \mathrm{d}\Gamma_{int} = \sum_{k=1}^{N} \int_{\Gamma_{\text{int}}} \left(\xi_k \xi_j\right) \boldsymbol{\beta_j} \, \mathrm{d}\Gamma_{int} = -\boldsymbol{R}_{F,k} - \boldsymbol{Q}_{F,k} \quad \text{for } j = 1,2,3, \dots, N \tag{4.47}$$

which can be written in the following matrix form:

$$\mathbf{N}\,\boldsymbol{\beta} = -\mathbf{R}_{\boldsymbol{F}} - \mathbf{Q}_{\boldsymbol{F}} \tag{4.48}$$

The system is invertible since $\xi_1, \dots, \xi_N$ are linearly independent. Equation (4.47) is easy to solve having the β_j coefficient as unknown:

$$\boldsymbol{\beta} = \mathbf{N}^{-1}(-\mathbf{R}_{\boldsymbol{F}} - \mathbf{Q}_{\boldsymbol{F}}) \tag{4.49}$$

After that, the estimate of $T|_{\Gamma_{\text{int}}}$ is obtained simply by using the expansion presented in equation (4.46).

Analogously to the approach adopted in the previous problem, the second auxiliary problem, presented in equations (4.41.1)-(4.41.3), is solved analytically by using the Classical Integral Transform Technique. For 2D problems, it is possible to write the Laplacian defined in equation (4.41.1) as:

$$\frac{\partial^2 F_k}{\partial r^2} + \frac{1}{r}\frac{\partial F_k}{\partial r} + \frac{1}{r^2}\frac{\partial^2 F_k}{\partial \theta^2} = 0 \tag{4.50}$$

Defining the integral transform as:

$$\overline{F_{k,\nu}} \equiv \overline{F_k}(r,\nu) = \int_{\theta=0}^{2\pi} F_k(r,\theta') \cos[\nu(\theta-\theta')]\, \mathrm{d}\theta' \tag{4.51}$$

and the inversion formula as (4.52):

$$F_k \equiv F_k(r,\theta) = \frac{1}{2\pi}\bar{F}_k(r,\nu=0) + \sum_{\nu=1}^{\infty}\frac{1}{\pi}\bar{F}_k(r,\nu) \tag{4.52}$$

it is possible to transform equation (4.50) as follows:

$$\frac{\mathrm{d}^2\overline{F_{k,\nu}}}{\mathrm{d}r^2} + \frac{1}{r}\frac{\mathrm{d}\overline{F_{k,\nu}}}{\mathrm{d}r} + \frac{1}{r^2}\nu^2\overline{F_{k,\nu}} = 0 \tag{4.53}$$

By an analogous elaboration, the boundary condition imposed on the internal boundary Γ_{int}, Equation (4.41.2), results to get:

$$\overline{F_{k,\nu}} = 0 \tag{4.54}$$

In the same way, the external boundary condition can be rewritten as:

$$\overline{F_{k,\nu}} = \overline{\psi_{k,\nu}} \tag{4.55}$$

Where $\psi_{k,\nu}$ is the transformation of the potential imposed in the second auxiliary problem, Equation (4.41.3), according to the equation (4.30).
Using the above equations, the transformed second auxiliary problem is obtained as:

$$\nabla^2\overline{F_{k,\nu}} = 0 \quad \text{in } \Omega \tag{4.56.1}$$

$$\overline{F_{k,\nu}} = 0 \quad \text{on } \Gamma_{\text{int}} \tag{4.56.2}$$

$$\overline{F_{k,\nu}} = \overline{\psi_{k,\nu}} \quad \text{on } \Gamma_{\text{ext}} \tag{4.56.3}$$

whose solution is:

$$\overline{F_{k,\nu}} = \overline{\psi_{k,\nu}} \sinh\left\{\nu\left[\ln\left(\frac{r_{\text{int}}}{r}\right)\right]\right\} \operatorname{csch}\left\{\nu\left[\ln\left(\frac{r_{\text{int}}}{r_{\text{ext}}}\right)\right]\right\} \tag{4.57}$$

In order to obtain the solution of the second auxiliary problem, the above equation needs to be inverted using the definition given in the Equation (4.52):

$$F_k = \frac{1}{2\pi}\overline{\psi_{k,\nu=0}}\frac{\ln\left(\frac{r_{\text{int}}}{r}\right)}{\ln\left(\frac{r_{\text{int}}}{r_{\text{ext}}}\right)} + \sum_{\nu=1}^{\infty}\frac{1}{\pi}\overline{\psi_{k,\nu}}\sinh\left\{\nu\left[\ln\left(\frac{r_{\text{int}}}{r}\right)\right]\right\} \operatorname{csch}\left\{\nu\left[\ln\left(\frac{r_{\text{int}}}{r_{\text{ext}}}\right)\right]\right\} \tag{4.58}$$

Analogously to the previous problem, in order to take advantage of the harmonic decomposition of the Classical Integral Transform Technique and to obtain a fully analytical expression, it is useful to represent the measurements $\boldsymbol{Y}$ as a Fourier series expansion:

$$\boldsymbol{Y}(\theta) = \frac{a_0}{2} + \sum_{\nu=1}^{N}[a_\nu \cos(\nu\theta) + b_\nu \sin(\nu\theta)] \tag{4.59}$$

This approach, whose details are reported in *Appendix 1*, enables to conveniently express the terms of Equation (4.48) in the following way:

$$\boldsymbol{\beta} = \begin{bmatrix} \beta_{\nu=1} \\ \beta_{\nu=2} \\ \vdots \\ \beta_{\nu=\nu} \end{bmatrix} \tag{4.60}$$

$$\mathbf{R}_{\boldsymbol{F}} = -\sqrt{\pi r_{ext}}\begin{bmatrix} \sqrt{2}\dfrac{h_{env}}{K}\left\{\left[1-\dfrac{K}{h_{env}r_{ext}\ln\left(\frac{r_{int}}{r_{ext}}\right)}\right]a_0 - T_{env}\right\} \\ \left\{\dfrac{h_{env}}{K} - \operatorname{cotanh}\left[\ln\left(\frac{r_{int}}{r_{ext}}\right)\right]\dfrac{1}{r_{ext}}\right\} \quad a_1 \\ \left\{\dfrac{h_{env}}{K} - \operatorname{cotanh}\left[\ln\left(\frac{r_{int}}{r_{ext}}\right)\right]\dfrac{1}{r_{ext}}\right\} \quad b_1 \\ \left\{\dfrac{h_{env}}{K} - \operatorname{cotanh}\left[2\ln\left(\frac{r_{int}}{r_{ext}}\right)\right]\dfrac{2}{r_{ext}}\right\} \quad a_2 \\ \left\{\dfrac{h_{env}}{K} - \operatorname{cotanh}\left[2\ln\left(\frac{r_{int}}{r_{ext}}\right)\right]\dfrac{2}{r_{ext}}\right\} \quad b_2 \\ \vdots \\ \left\{\dfrac{h_{env}}{K} - \operatorname{cotanh}\left[\nu\ln\left(\frac{r_{int}}{r_{ext}}\right)\right]\dfrac{\nu}{r_{ext}}\right\} \quad a_\nu \\ \left\{\dfrac{h_{env}}{K} - \operatorname{cotanh}\left[\nu\ln\left(\frac{r_{int}}{r_{ext}}\right)\right]\dfrac{\nu}{r_{ext}}\right\} \quad b_\nu \end{bmatrix} \tag{4.61}$$

$$\mathbf{Q}_{\boldsymbol{F}} = \begin{bmatrix} \dfrac{q_g}{K}\sqrt{\dfrac{\pi}{2r_{ext}}}\left[r_{ext}^2 + \dfrac{1}{2}\dfrac{(r_{ext}^2 - r_{int}^2)}{\ln\left(\frac{r_{int}}{r_{ext}}\right)}\right] \\ 0 \\ \vdots \\ 0 \end{bmatrix} \tag{4.62}$$

$$\mathbf{N} = \frac{1}{r_{int}r_{ext}}\begin{bmatrix} \dfrac{1}{\ln^2\left(\frac{r_{int}}{r_{ext}}\right)} & & & & & & & 0 \\ & \operatorname{csch}^2\left[1\ln\left(\frac{r_{int}}{r_{ext}}\right)\right] & & & & & & \\ & & \operatorname{csch}^2\left[1\ln\left(\frac{r_{int}}{r_{ext}}\right)\right] & & & & & \\ & & & 2^2\operatorname{csch}^2\left[2\ln\left(\frac{r_{int}}{r_{ext}}\right)\right] & & & & \\ & & & & 2^2\operatorname{csch}^2\left[2\ln\left(\frac{r_{int}}{r_{ext}}\right)\right] & & & \\ & & & & & \ddots & & \\ & & & & & & \nu^2\operatorname{csch}^2\left[\nu\ln\left(\frac{r_{int}}{r_{ext}}\right)\right] & \\ 0 & & & & & & & \nu^2\operatorname{csch}^2\left[\nu\ln\left[\frac{r_{int}}{r_{ext}}\right]\right] \end{bmatrix} \tag{4.63}$$

$$\boldsymbol{\xi} = \frac{1}{\sqrt{\pi r_{ext}}}\begin{bmatrix} \frac{1}{\sqrt{2}}\frac{1}{\ln\left(\frac{r_{\mathrm{int}}}{r_{\mathrm{ext}}}\right) r_{\mathrm{int}}} \\ \frac{1}{r_{int}}\cos(1\,\theta)\,\mathrm{csch}\left[1\ln\left(\frac{r_{int}}{r_{ext}}\right)\right] \\ \frac{1}{r_{int}}\sin(1\,\theta)\,\mathrm{csch}\left[1\ln\left(\frac{r_{int}}{r_{ext}}\right)\right] \\ \frac{2}{r_{int}}\cos(2\,\theta)\,\mathrm{csch}\left[2\ln\left(\frac{r_{int}}{r_{ext}}\right)\right] \\ \frac{2}{r_{int}}\sin(2\,\theta)\,\mathrm{csch}\left[2\ln\left(\frac{r_{int}}{r_{ext}}\right)\right] \\ \vdots \\ \frac{\nu}{r_{int}}\cos(\nu\,\theta)\,\mathrm{csch}\left[\nu\ln\left(\frac{r_{int}}{r_{ext}}\right)\right] \\ \frac{\nu}{r_{int}}\sin(\nu\,\theta)\,\mathrm{csch}\left[\nu\ln\left(\frac{r_{int}}{r_{ext}}\right)\right] \end{bmatrix} \tag{4.64}$$

The values of β_j coefficients, which are the goal of the second auxiliary problem, are obtained from a mathematical point of view by Equation (4.49). Due to the ill-posed nature of the problem and the presence of the noise in the measurement vector $\boldsymbol{Y}$, the inversion of the matrix $\boldsymbol{N}$ has to be approached by inverse problem solution techniques in order to find a realistic estimation of the unknown heat flux.

The diagonal behaviour of the matrix of the inner product $\boldsymbol{N}$ allows us easily calculating its inverse as follow:

$$\mathbf{N^{-1}} = r_{int}r_{ext}\begin{bmatrix} \ln^2\left(\frac{r_{int}}{r_{ext}}\right) & & & & & & & 0 \\ & \frac{1}{\mathrm{csch}^2\left[1\ln\left(\frac{r_{int}}{r_{ext}}\right)\right]} & & & & & & \\ & & \frac{1}{\mathrm{csch}^2\left[1\ln\left(\frac{r_{int}}{r_{ext}}\right)\right]} & & & & & \\ & & & \frac{1}{2^2\mathrm{csch}^2\left[2\ln\left(\frac{r_{int}}{r_{ext}}\right)\right]} & & & & \\ & & & & \frac{1}{2^2\,\mathrm{csch}^2\left[2\ln\left(\frac{r_{int}}{r_{ext}}\right)\right]} & & & \\ & & & & & \ddots & & \\ & & & & & & \frac{1}{\nu^2\,\mathrm{csch}^2\left[\nu\ln\left(\frac{r_{int}}{r_{ext}}\right)\right]} & \\ 0 & & & & & & & \frac{1}{\nu^2\,\mathrm{csch}^2\left[\nu\ln\left[\frac{r_{int}}{r_{ext}}\right]\right]} \end{bmatrix} \tag{4.65}$$

This operator has many points in common with the operator defined in Equation (4.40) for the previous auxiliary problem. It means that, also in this case, the presence of noise has a

negative impact on the estimation of the β coefficients because the values of $\boldsymbol{N}^{-1}$ matrix components, following $1/\nu^2\,\mathrm{csch}^2[\nu\ln(r_{int}/r_{ext})]$ function, increase with the number of the harmonic. In Figure (4.4), the values of $\boldsymbol{N}^{-1}$ components are plotted for a representative ratio $r_{int}/r_{ext} = 0.9$ as a function of the harmonic order. Also in this case, the values of the diagonal terms of the $\boldsymbol{N}^{-1}$ matrix increase as the harmonic order increases; for this reason the matrix in regularized by the same approach that was already employed in the solution of the first auxiliary problem.

Finally it has to be pointed out that, comparing Figure (4.3) with Figure (4.4), there are more than 6 orders of magnitude between $\boldsymbol{M}^{-1}$ and $\boldsymbol{N}^{-1}$. Therefore, the estimation of the internal heat flux is a more delicate procedure compared to the estimation of the internal wall temperature.

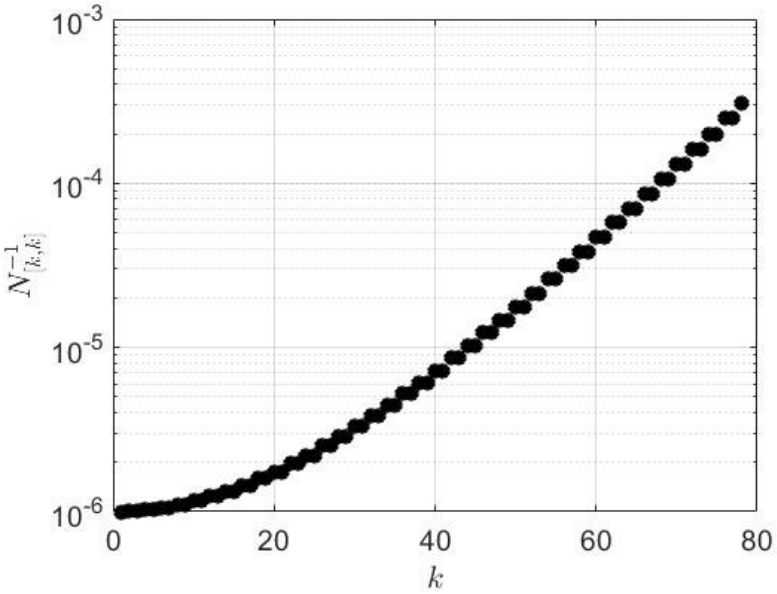

Figure 4.4: Diagonal elements of the $\boldsymbol{N}^{-1}$ matrix for a representative value $r_{int}/r_{ext} = 0.9$

It has to be pointed out that, the computational requirement of the FRF is comparable with the ones of TSVD and RF methods since all the solution strategies require the filtering of the singular value coefficients. For this reason, the comparison has to be performed in terms of reconstruction capabilities instead of computational requirements.

Chapter 5

Numerical verification

5.1 Introduction

Following the classification introduced in *Chapter 3*, the analysis of the new methodologies proposed in *Chapter 4* is subdivided in *Parameter estimation* and *Function estimation problem*. In particular, synthetic data produced by virtual experiments (e.g. numerical simulation) were performed in order to compare to the exact values, the reconstruction capabilities of the new estimation methodologies together with some of the common reconstruction algorithms presented in *Chapter 3*. In *Chapter 6* the new methodologies will be then employed for the estimation of the thermal performances in heat exchangers using real measurements.

5.1 Parameter estimation

The new proposed methodology is going to be tested within the Matlab® environment by adopting synthetic data. The physical problem considered in the present work, according to the conditions reported in the available literature (*Navickaite20018*), consists in a counter flow shell and tube heat exchanger characterized by tubes having internal diameter of $d_{int} = 0.005m$ and thickness of $t = 1mm$, while the shell has an internal diameter of $d_{she} = 0.0185m$. Water was assumed to be the working fluid in both the sides of the heat exchanger and its inlet temperature was assumed be constant and equal to $T_{in}^{T} = 323.15K$ and $T_{in}^{S} = 283.15K$ at the tube and the shell side respectively.

The thermal conductivity of the pipe $k = 250W/m\,K$ was assumed to be constant such as the environmental temperature $T_{env} = 283.15K$.

The boundary condition values together with the geometrical characterization of the heat exchanger are summarized in Table (5.1), while a representation of the geometrical domain, is shown in Figure (5.1).

As already mentioned in *Chapter 4,* the estimation procedure was applied to the estimation of the α and β coefficients appearing in the common Nusselt number formulation (*Incropera2005, Rainieri2004*) at both the shell and tube sides:

$$Nu = \alpha\, Re^{\beta} Pr^{\gamma} \tag{5.1}$$

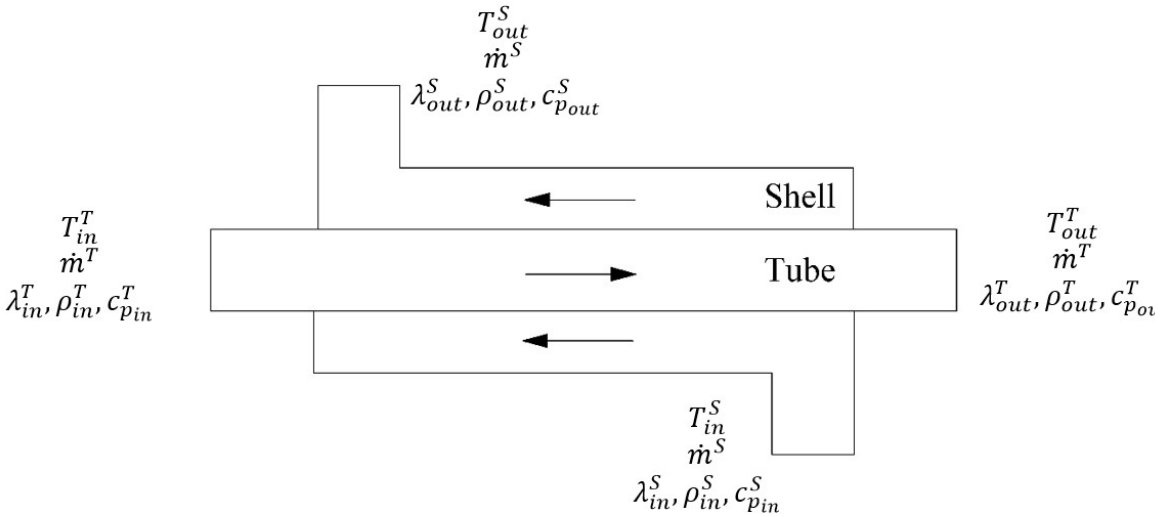

Figure 5.1: Parameter estimation: geometrical domain

Since the working fluid is supposed to be the same in all the working conditions, being the Prandtl number slightly dependent on the fluid temperature, there is no sensibility concerned the effect of the Prandtl number on the heat transfer mechanism, therefore Equation (4.1) could be simplify to the classical expression (*Incropera2005*):

$$Nu = \alpha \, Re^{\beta} Pr^{0.33} \tag{5.2}$$

which yields to a four parameters estimation procedure ($\alpha^T, \beta^T, \alpha^S$ and β^S).

The Nusselt number function defined in Equation (4.1) is based on the assumption that the heat transfer mechanism is governed by the single-phase forced convection since, if evaporation or condensation occurred, then other terms would drive the heat transfer mechanism (e.g. vapour quality, heat flux, and pressure).

The approach is based on the minimization of the objective function defined as:

$$r = \left\| U_{exp} - U_{pred} \right\|_2 \tag{5.3}$$

where U_{exp} and U_{pred} are respectively the experimental and the simulated global heat transfer coefficient.

The synthetic measurements were produced by analytically solving the energy balance; in particular, for any double flow heat exchanger in a steady state condition, perfectly thermally insulated from the environment in which the heat conduction in the flow direction is negligible, it is possible to write the energy balance as follows:

$$Q = \dot{m}^T c_p^T (T_{in}^T - T_{out}^T) = \dot{m}^S c_p^S \left(T_{out}^S - T_{in}^S\right) = U \, A_i \, \Delta T_{ml} \tag{5.4}$$

where ΔT_{ml} is the logarithmic mean temperature difference while Q is the exchanged heat flow rate, $\dot{m}$ and c_p are the mass flow rate and the specific heat capacity, respectively, while $\cdot^T$ and $\cdot^S$ stand for the tube and the shell side, respectively.

Table 5.1: Geometrical and boundary conditions parameters

Parameter	Tube	Shell
Internal diameter [m]	0.005	0.0185
Thickness of the tube [m]	0.001	0.0015
Thermal conductivity $[W/mK]$	250	15
Working fluid	Water	Water
Length [m]	0.25	0.25

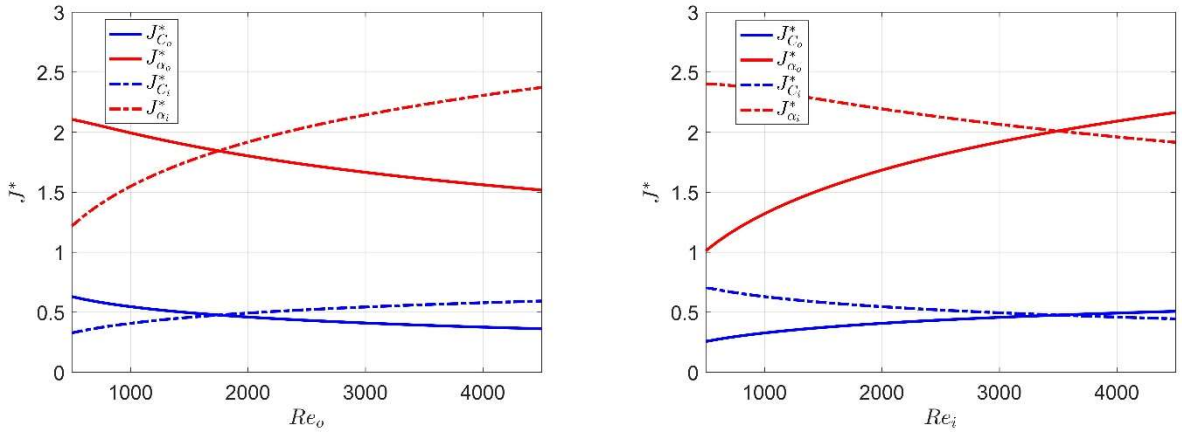

(a) (b)

Figure 5.2: Scaled sensitivity coefficient of the unknown parameter for the representative test case T1: (a) fixed tube Reynolds number (e.g.$Re^T = 1750$) and (b) fixed shell Reynolds number (e.g.$Re^S = 3500$)

Therefore, assuming the outlet temperature as the unknown variable of the direct problem, the solution of the last system of equations yield to:

$$T_{out}^T = T_{in}^T - \frac{Q}{\dot{m}^T c_p^T} \tag{5.5.1}$$

$$T_{out}^S = \frac{Q}{\dot{m}^S c_p^S} + T_{in}^S \tag{5.5.2}$$

$$Q = \frac{(B-1)\left(T_{in}^T - T_{in}^S\right)}{\frac{B}{m^T c_p^T} - \frac{1}{m^S c_p^S}} \tag{5.5.3}$$

where:

$$B = \exp\left(UA_i \frac{m^S c_p^S - m^T c_p^T}{m^S c_p^S m^T c_p^T}\right) \tag{5.6}$$

Due to the electrical analogy, it is possible to define the overall heat transfer coefficient as a summation of resistance as follows:

$$\frac{1}{UA_i} = \frac{1}{h_i A_i} + R_w + \frac{1}{h_o A_o} \tag{5.6}$$

where h_i and h_o are the internal and external convective heat transfer coefficients respectively, while A_i and A_o are the internal and the external heat exchanger surface areas, respectively.

Due to the quasi-cylindrical configuration characteristic of a tube side heat exchanger, the thermal resistance of the wall R_w can be approximated as:

$$R_w = \frac{\ln\left(\frac{d_{out}}{d_{int}}\right)}{2\pi k_w L} \tag{5.7}$$

where d_{0ut} and d_{int} are the external and internal diameter of the tube, respectively, while k_w and L are the thermal conductivity and the length of the tube that is exchanging heat, respectively. Thus it is possible to assume known the thermal resistance of the wall, for a given heat exchanger configuration, under a given operating condition.

Assuming the internal diameter of the tube as the characteristic length, it is possible to define the internal Nusselt number coefficient as:

$$Nu^T = \frac{h_i d_{int}}{k} = \alpha^T Re^{T\beta^T} Pr^{0.33} \tag{5.8.1}$$

$$Nu^S = \frac{h_o d_{int}}{k} = \alpha^S Re^{S\beta^S} Pr^{0.33} \tag{5.8.2}$$

where K is the thermal conductivity of the fluid.

Therefore, substituting Equations (5.6)-(5.8) into the system of Equations (5.5) and assuming the coefficients listed in Table (5.2) for three different test cases, the synthetic measurements that will be used in order to test the estimation capabilities of the methodology proposed here, can be generated.

It has to be pointed out that the thermal properties of the fluid were assumed to be constant and they were referred to the average bulk temperature between the inlet and outlet bulk temperature at each side.

It has to be highlighted that even if the heat transfer mechanism is influenced by the mass flow rate of the working fluids, in order to generalize the results, the correlations are proposed in terms of the Reynolds number. Related to this aspect, it was assumed:

$$Re^T = \frac{v^T d_{int}}{\nu^T} \tag{5.9.1}$$

$$Re^S = \frac{v^T (d_{int} - d_{shell})}{\nu^T} \tag{5.9.2}$$

where v is the average fluid velocity, while ν is the cinematic viscosity of the fluid, with average bulk temperature previously defined.

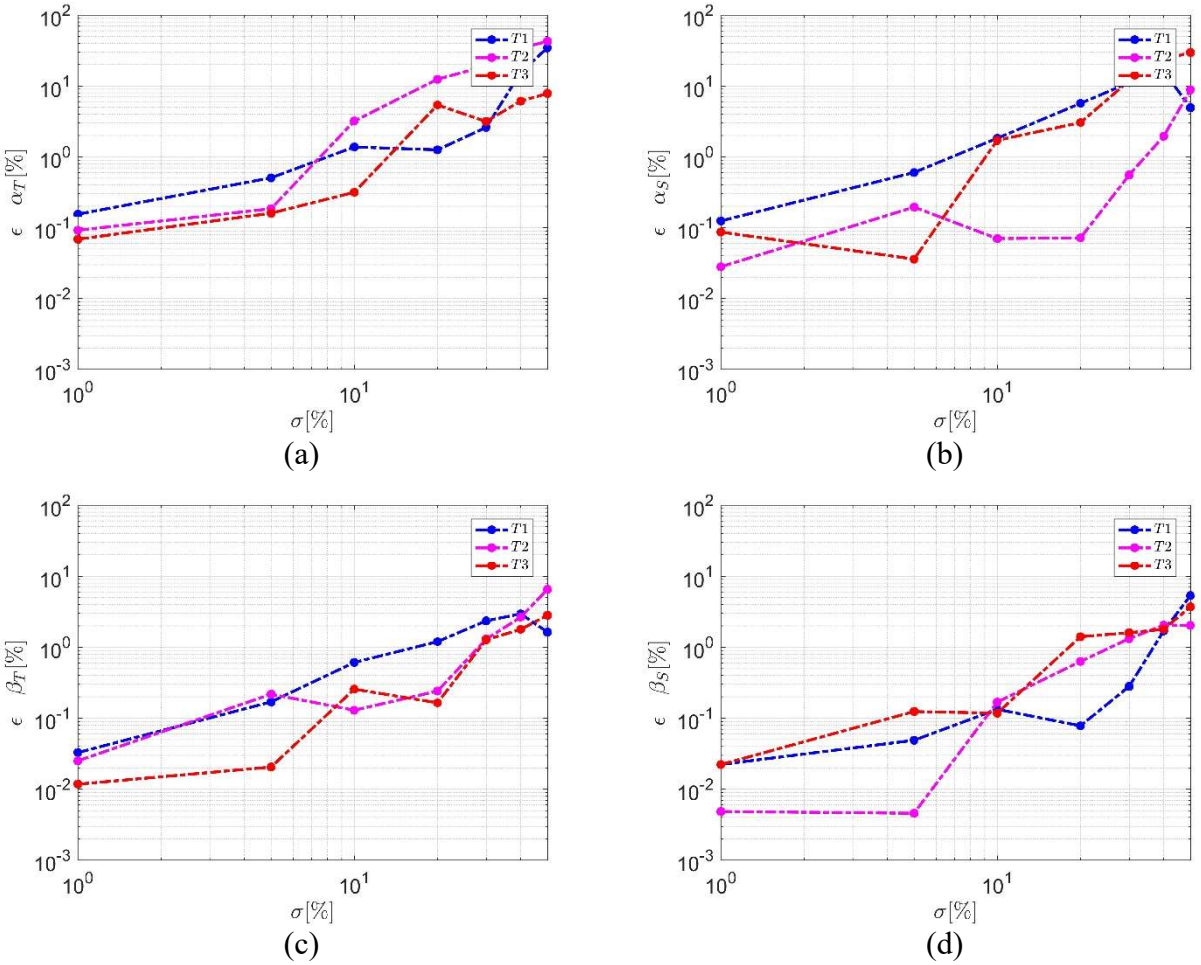

Figure 5.3: Relative error as a function of the noise level for the estimated coefficients: (a) α^T, (b) α^S, (c) β^T and (d) β^S

It has to be pointed out, that since the β coefficients play a small effect compared to the α coefficients in the overall heat transfer coefficient U, they were not modified during the analysis of the estimation capabilities of the method proposed here.

The parameters that correlate the response of system to the input parameters are the sensitivity coefficient. Since the magnitude of the sensitivity coefficients can be different for each parameter, the scaled sensitivity coefficient has to be defined according to (*Rainieri2014*):

$$J^*(P_j) = \frac{1}{U}\frac{\partial U}{\partial P_j}P_j \tag{5.10}$$

In order to perform a trustworthy comparison among the techniques, the synthetic measurement of the global heat transfer coefficient U were deliberately spoiled by random noise and then used as input data for all the mathematical inverse model.

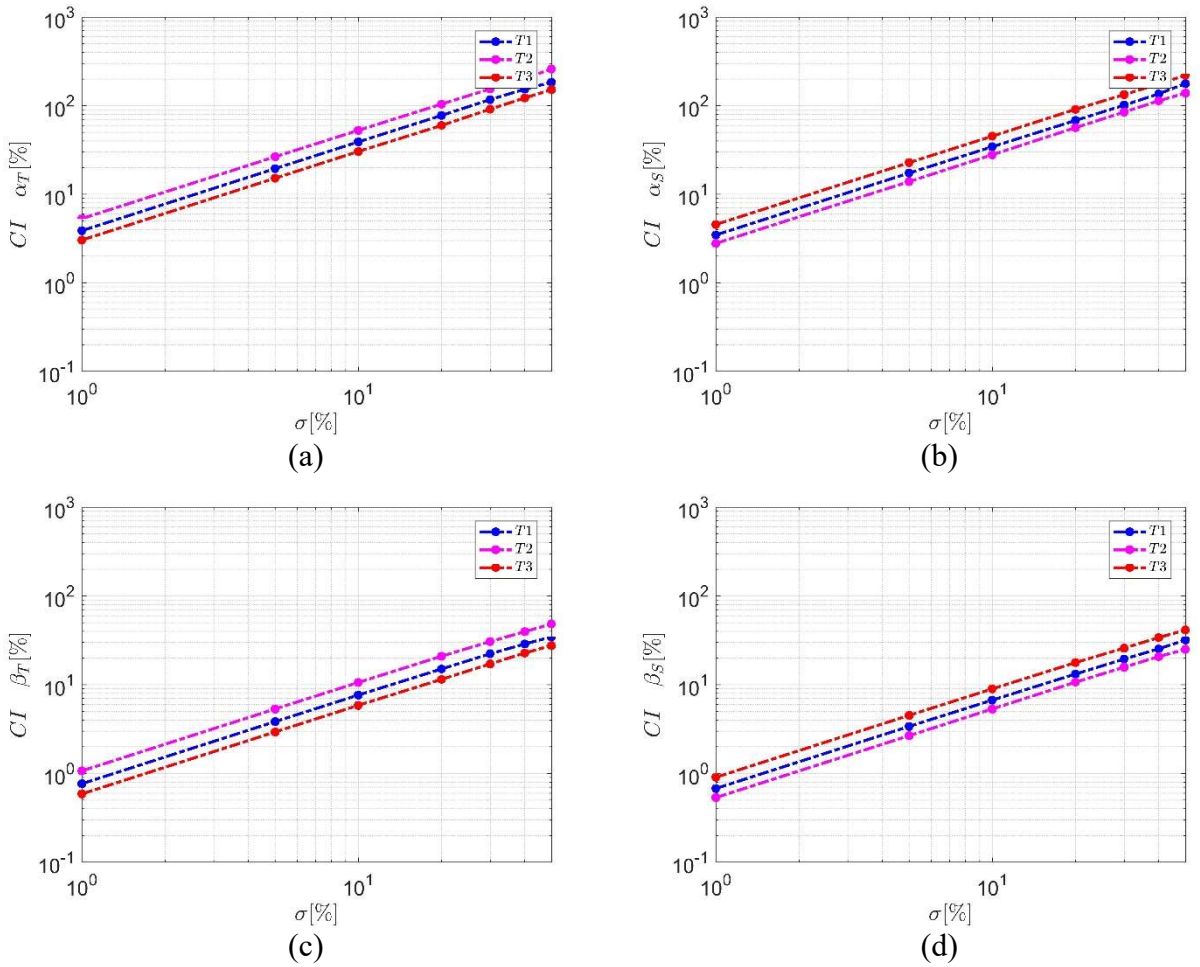

Figure 5.4: Confidence interval as a function of the noise level for the estimated coefficients: (a) α^T, (b) α^S, (c) β^T and (d) β^S

In particular, a Gaussian white noise characterized by a standard deviation ranging from $\sigma = 1\%$ to $\sigma = 50\%$ was introduced according to:

$$U = U_{exact}(1 + \sigma\epsilon) \tag{5.11}$$

where ϵ is a random Gaussian variable with zero mean and unit variance.

The estimation quality was measured by looking at different indexes. In particular, the relative errors of each estimated parameter were determined as follows:

$$\epsilon\ P_j = \frac{P_j - P_j^{exact}}{P_j^{exact}}\ 100 \tag{5.12}$$

Table 5.2: Test cases

Case:	α^T	β^T	α^S	β^S	Re^T	Re^S	$T^T_{inlet}\ [K]$	$T^S_{inlet}[K]$
T1	0.05	0.8	0.05	0.8	500÷4500	500÷4500	323.15	283.15
T2	0.1	0.8	0.05	0.8	500÷4500	500÷4500	323.15	283.15
T3	0.05	0.8	0.1	0.8	500÷4500	500÷4500	323.15	283.15

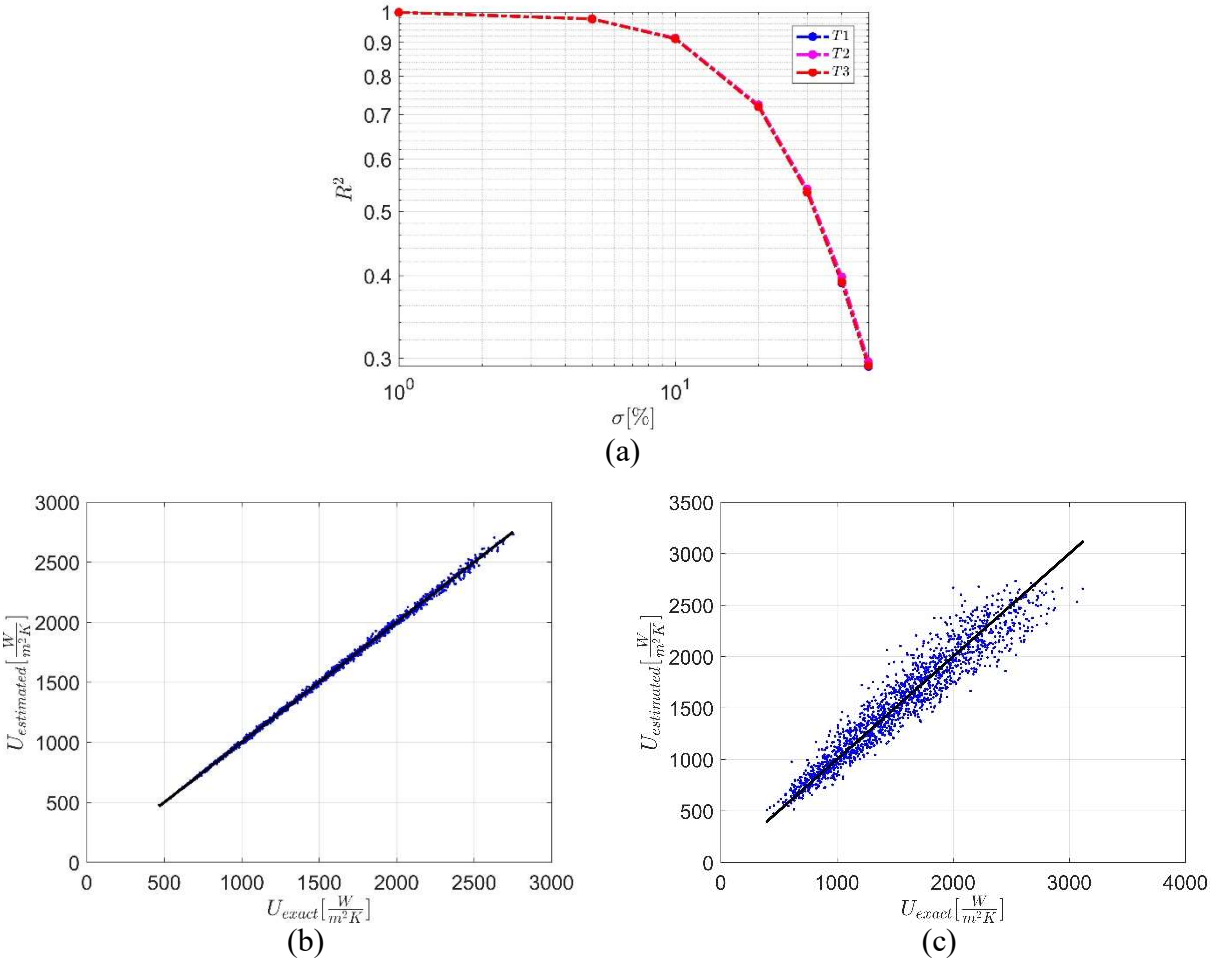

(a)

(b)

(c)

Figure 5.5: (a) R^2 index as a function of the noise level for the test cases here investigated, (b) Example of the correlation between the estimated and the measured global heat transfer coefficient for the test case T1 $\sigma = 1\%$ and (c) $\sigma = 10\%$

where P_j is the $j-th$ parameter that has to be estimated (e.g. $\alpha^T, \beta^T, \alpha^S$ and β^S).

More interesting than the relative error on each parameter, is the relative estimation error between the exact and the estimated Nusselt number correlation:

$$\epsilon\, Nu = \frac{\|Nu_{reconstructed} - Nu_{exact}\|_2}{\|Nu_{exact}\|_2} \tag{5.13}$$

Form the statistical point of view, the value of the estimated parameter, is an important aspect, but at the same time the confidence interval $CI\ P_j$ has to be considered.

The added noise depends intrinsically on the random sequence generated by Matlab®, thus the estimation procedure was repeated 300 times for different random noise sequences and an average value ϵ was calculated for each noise level for both Equation (5.12) and (5.13).

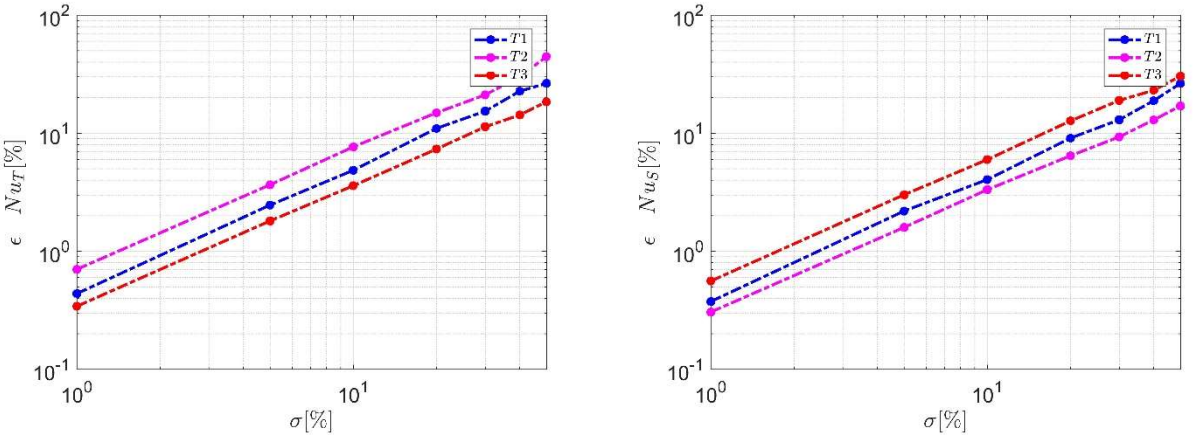

(a) (b)

Figure 5.6: Relative error on the estimated correlation as a function of the noise level at both the tube (a) and the shell (b) sides for the three test cases

It is well known that the estimation capabilities of the optimization algorithms strongly depends on the starting point, therefore, for all the estimation here performed, the starting point was assumed to be forthy percent lower than the exact set of coefficients.

As it is possible to see in Figure (5.2-a) the scaled sensitivity coefficient related to the unknown parameters at the shell side, for a fixed tube side Reynolds number, decreases as far as the shell side Reynolds number increases. This behaviour is justified by observing that, if the shell side Reynolds number increases, it is the thermal resistance at the tube side that governs the heat transfer phenomena. The opposite considerations are valid for the scaled sensitivity coefficient at the tube side.

The same considerations are valid for Figure (5.2-b) were the scaled sensitivity coefficients are plotted as function of the internal Reynolds number, for a fixed Reynolds number at the shell side.

Table 5.3: Estimation results for two representative noise level

Case:		α^T	β^T	α^S	β^S
Exact	T1	0.05	0.8	0.05	0.8
	T2	0.1	0.8	0.05	0.8
	T3	0.05	0.8	0.1	0.8
Starting point	T1	0.03	0.48	0.03	0.48
	T2	0.06	0.48	0.03	0.48
	T3	0.03	0.48	0.06	0.48
$\sigma = 1\%$	T1	0.0502±3.9%	0.7994±0.76%	0.0503±3.5%	0.7993±0.68%
	T2	0.0981±5.3%	0.8026±1.1%	0.0497±2.7%	0.8009±0.54%
	T3	0.0507±3.3%	0.7977±0.58%	0.0989±5.4%	0.8021±0.90%
$\sigma = 10\%$	T1	0.0564±38.7	0.7807±7.62	0.0404±34.8	0.8312±6.76
	T2	0.0827±52.5%	0.8284±10.6%	0.0511±27.9%	0.7961±5.3%
	T3	0.0444±30.6%	0.8185±5.9%	0.1096±45.1%	0.7833±9.0%

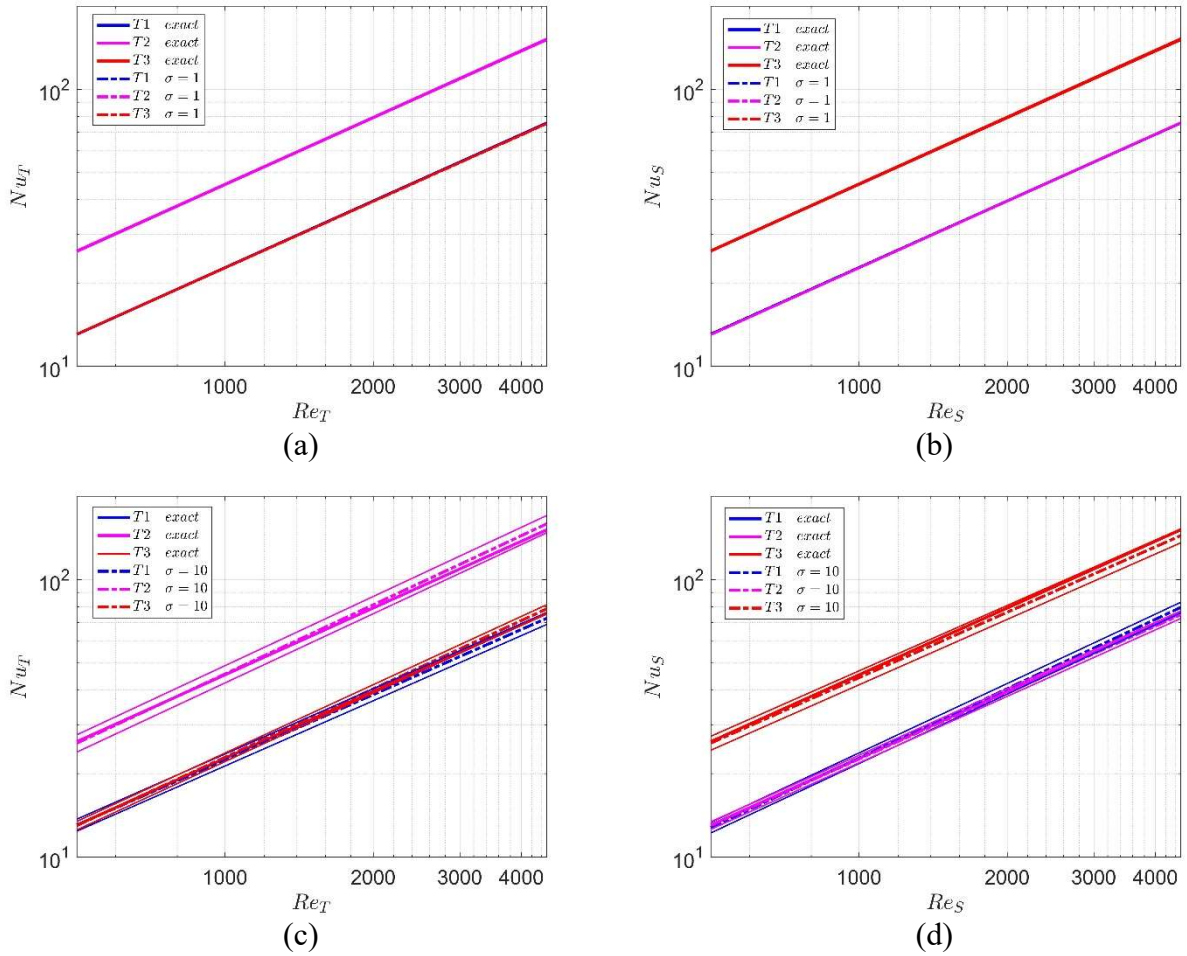

Figure 5.67 Nusselt number function at the tube side for two representative noise level (a) $\sigma = 1\%$ (c) $\sigma = 10\%$ and Nusselt number function at the shell side for two representative noise level (b) $\sigma = 1\%$ (d) $\sigma = 10\%$

As it is possible to see in Figure (5.3), even if the relative errors on each parameter were averaged on 300 different sets of measurements, they are not monotonically increasing as the noise contented in the measurements increases: this aspect suggest that the estimation algorithm is not perfectly stable.

From a statistical point of view, the value estimated from the optimization algorithm has to be presented with its confidence interval. As it is possible to see in Figure (5.4), the confidence interval of all the test cases here considered is monotonically increasing as far as the noise contented in the measurement is increasing.

This aspect suggest that even if the estimated parameter is very sensible to the set of noise randomly produced by the calculator, the estimation procedure is stable.

As it is possible to see in Figure (5.5-a) the coefficient of determination (R^2) is monotonically decreasing as far as the noise contented in the measurement is increasing: this behaviour is clearly understandable from the correlation graphs shown in Figures (5.5-b)-(5.5-c) for two different noise level, related to the test case *T1*. As it possible to see, the

correlation between the estimated solution and the measured one decreases as the noise contented in the measurement increases.

Since the main goal of the estimation approach is the identification of the correlation between the Nusselt and the Reynolds numbers, the relative error defined in Equation (5.13), is plotted in Figure (5.6) for both the tube and shell side. As already observed for the confidence interval, the relative error on the estimated Nusselt number correlation is monotonically increasing as the noise contented in the measurement increases, suggesting the stability of the estimation procedure.

The comparison between the estimated and the exact Nusselt number correlations, together with the confidence interval bands, are reported in Figure (5.7) for both the tube and the shell side for two representative noise levels (e.g. $\sigma = 1\%$ and $\sigma = 10\%$). As it is possible to see, the estimation procedure was able to estimate with a good accuracy the Nusselt number correlation, suggesting its application to a set of experimental data (*Chapter 6*).

It has to be pointed out that, for what concern the tube side, the test case *T3* is overlapped to the test case *T1* since those two sets of data share the same equation coefficients at the tube side. The same considerations are valid for the shell side where the test case *T2* is overlapped to the test case *T1*.

5.2 One dimensional function estimation

The 1D inverse problem here addressed, was stated in *Chapter 3* as a function estimation procedure, since the number of unknown variables is lerger than in the previous case. The estimated results, provided from the new methodologies formulated in *Chapter 4*, are compared with the estimated results coming from some of the common techniques presented in *Chapter 3*.

The new proposed methodologies are going to be compared within the Matlab® environment by adopting synthetic data. The finite element method implemented in Comsol Multiphysic® was used in order to generate the synthetic measurements (sampled at the external surface of the pipe) by imposing a known distribution of h_{int} at the internal wall surface of the tube. The physical problem considered in the present work, according to the conditions reported in the available literature (*Bozzoli2014a*, *Colaço2015*), consists in a cross-section of a circular duct with internal radius $r_{int} = 0.007m$ and external radius $r_{ext} = 0.008m$. The thermal conductivity of the pipe $k = 15W/m\,K$ was assumed to be constant such as the environmental temperature $T_{env} = 298.15K$ and the bulk temperature $T_b = 292.15$ of the fluid that flows inside the tube. The exterior surface Γ_{ext} of the tube was subjected to an overall convective heat transfer coefficient $h_{env} = 5W/m^2K$ with the environment and the domain Ω that was assumed to be homogeneous and isotropic, and subjected to an internal heat generation per unit of volume $q_g = 10^6W/m^3$.

A representation of the geometrical domain, together with the boundary conditions applied to both the direct and inverse problem is shown in Figure (5.8).

Since it is well known that the effectiveness of the estimated solution of the inverse problem depends on the shape of the function being estimated, different test cases were implemented in order to perform a robust comparison. The shapes of the internal convective heat transfer coefficients that were used as test functions are reported in Table (5.4). Test cases h1 and h2 are the classical step function with different amplitudes, chosen in order to test the limits of the estimation approaches, while case h3 and h4 are instead examples smooth functions. Moreover, test case h1-h3 and h2-h4 were assumed to have the same maximum h_{max}, minimum h_{min} and average h_{avg} values in order to make the comparison of different test functions more objective, minimizing the effect of the of the signal's amplitude.

Table 5.4: Test functions: internal convective heat transfer coefficient distribution

Case:	$h_{\text{int}}\left[\frac{\text{W}}{\text{m}^2\text{K}}\right]$:		$h_{\text{avg}}\left[\frac{\text{W}}{\text{m}^2\text{K}}\right]$:	$h_{\text{min}}\left[\frac{\text{W}}{\text{m}^2\text{K}}\right]$:	$h_{\text{max}}\left[\frac{\text{W}}{\text{m}^2\text{K}}\right]$:
	0	$-\pi < \theta < -\frac{2}{3}\pi$			
h1	600	$-\frac{2}{3}\pi < \theta < \frac{2}{3}\pi$	400	0	600
	0	$\frac{2}{3}\pi < \theta < \pi$			
	0	$-\pi < \theta < -\frac{2}{3}\pi$			
h2	6000	$-\frac{2}{3}\pi < \theta < \frac{2}{3}\pi$	4000	0	6000
	0	$\frac{2}{3}\pi < \theta < \pi$			
h3	$-600\frac{\theta^2}{\pi^2}+600$	$-\pi < \theta < \pi$	400	0	600
h4	$-6000\frac{\theta^2}{\pi^2}+6000$	$0 < \theta < 2\pi$	4000	0	6000

It is well known that the effectiveness of all regularization approaches strongly depends on the choice of a proper value of the regularization parameter (*Bazàn2012*, *Bozzoli2014a*). In the present analysis, to make the comparison between the considered regularization techniques more straightforward, the criterion provided by the discrepancy principle, originally formulated by Morozov (*Tikhonov1977*, *Beck1985*), was adopted for all the techniques.

In order to perform a trustworthy comparison among the techniques, the synthetic measurement temperatures Y were deliberately spoiled by random noise and then used as input data for all the mathematical models. In particular, a Gaussian white noise characterized by a standard deviation ranging from $\sigma = 0.01K$ to $\sigma = 5K$ was introduced according to:

$$Y = T_{exact}|_{\Gamma_{ext}} + \sigma\epsilon \tag{5.14}$$

where ϵ is a random Gaussian variable with zero mean and unit variance.

In order to perform a quantitative comparison among the three considered approaches, the global relative estimation error between the exact and the estimated internal heat transfer coefficient was calculated as a relative error in L2 norm:

$$E = \frac{\|\boldsymbol{h}_{reconstructed} - \boldsymbol{h}_{exact}\|_2}{\|\boldsymbol{h}_{exact}\|_2} \tag{5.15}$$

The added noise depends intrinsically on the random sequence generated by Matlab®, thus the estimation procedure was repeated 50 times for different random noise sequences and an average value E_{avg} as calculated for each noise level.

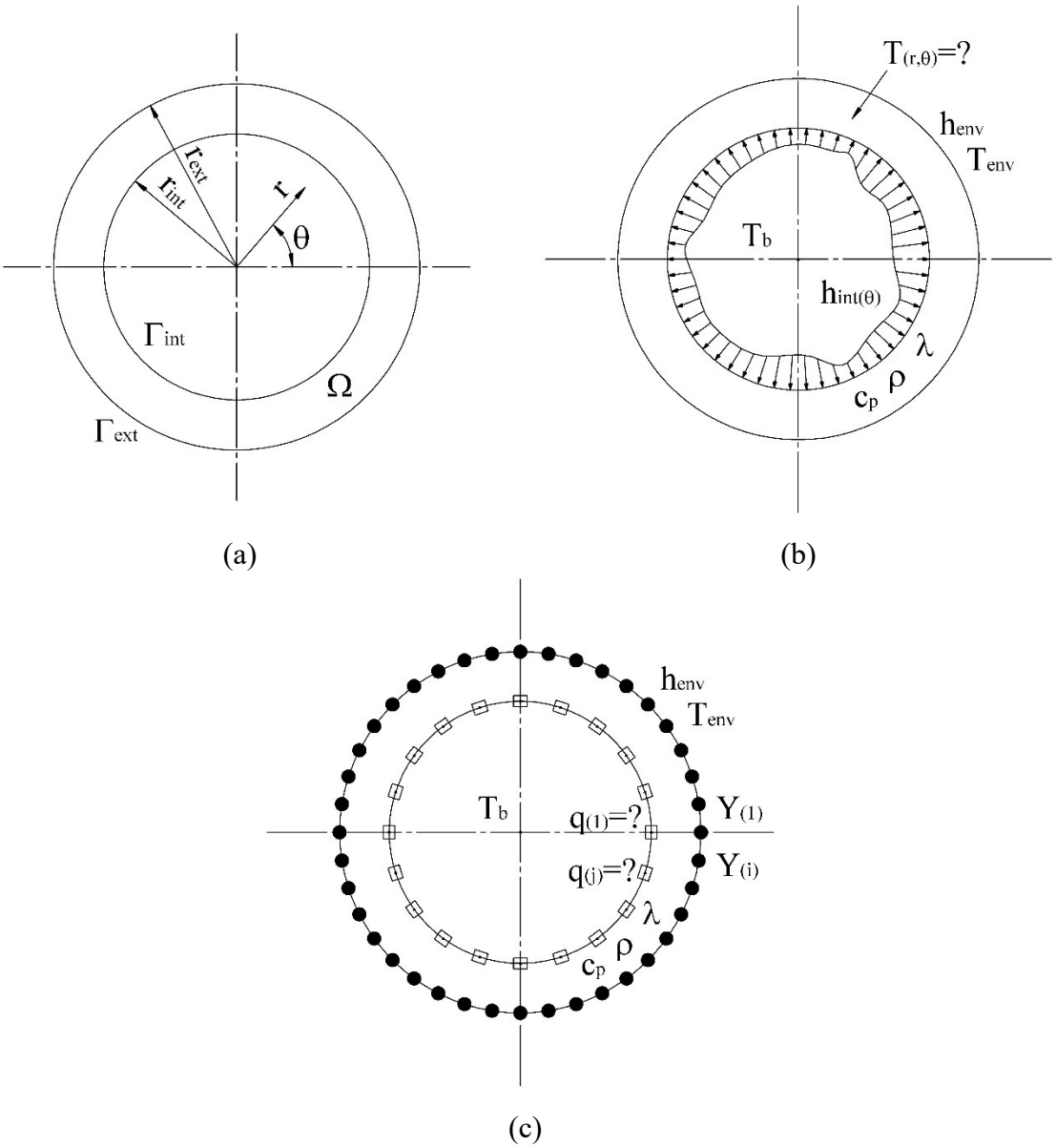

Figure 5.8: Function estimation: (a) Geometrical domain, (b) direct problem and (c) inverse problem boundary conditions schemes

5.2.1 Gaussian Filtered Singular Value Decomposition

Since this new proposed methodology is characterized by an smooth low pass filter function, its estimated results are going to be compared with the ones provided by its precursor TSVD and a common regularization scheme based on a smooth filter function, TM approach.

The reconstruction results related to the test function here analysed are shown in Figure (5.9)-(5.10), for two representative noise level (e.g. $\sigma = 0.1K$ and $\sigma = 1K$). As it is possible to see, the three estimation algorithms present different degrees of reconstruction accuracies, depending on the noise level and the test case considered.

In particular, the TSVD method suffer of ringing artefacts compare with the GFSVD and TM: this behaviour is due to the discontinue filter function, characteristic of the truncation methodologies. The instabilities of the estimated solution, that promotes the presence of the ringing artefacts are mitigated in the GFSVD and TM since the presence of damped high frequency harmonics compensate the lack of information typical of the truncation methodologies.

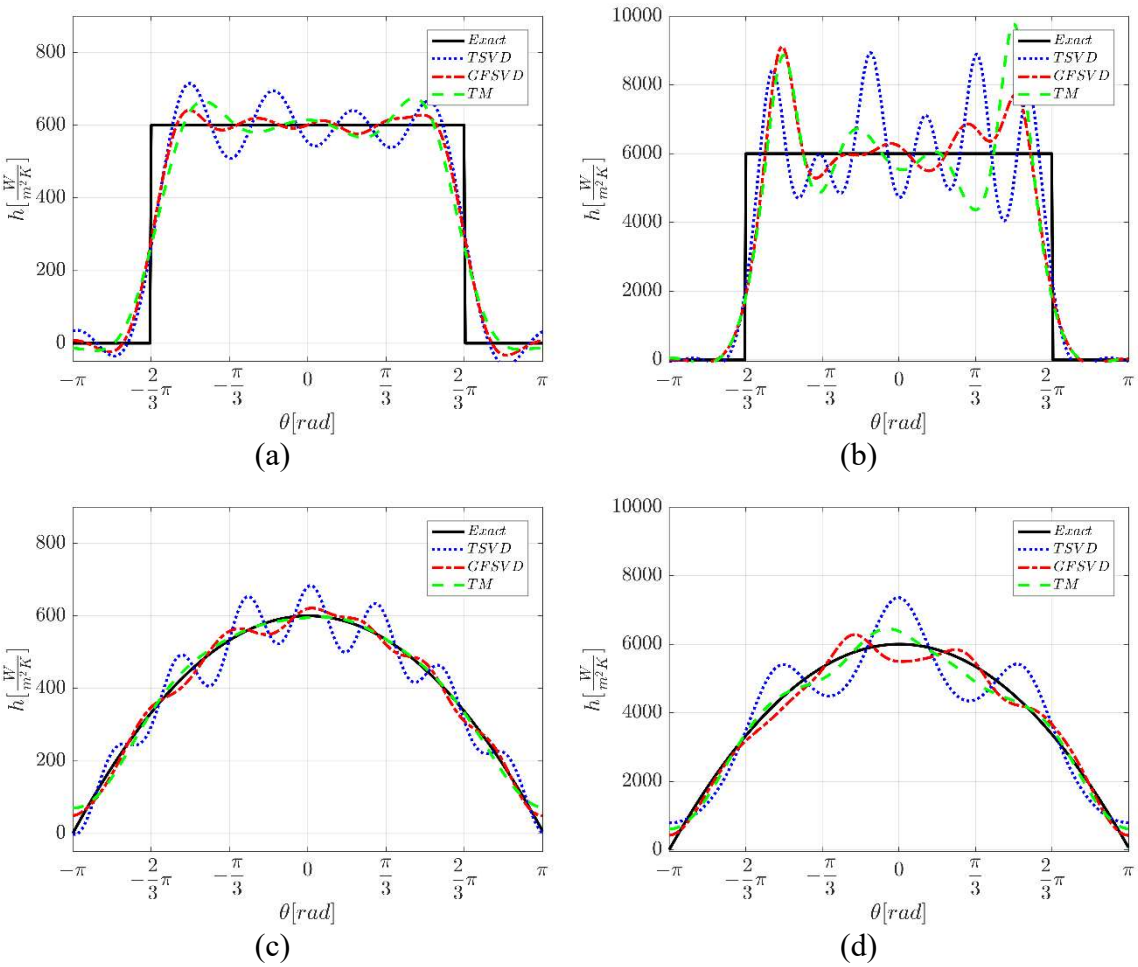

Figure 5.9: Reconstruction of the internal heat transfer coefficient for a) test case h1, b) test case h2, c) test case h3 and d) test case h4 ($\sigma = 0.1K$) (*Mocerino2018*)

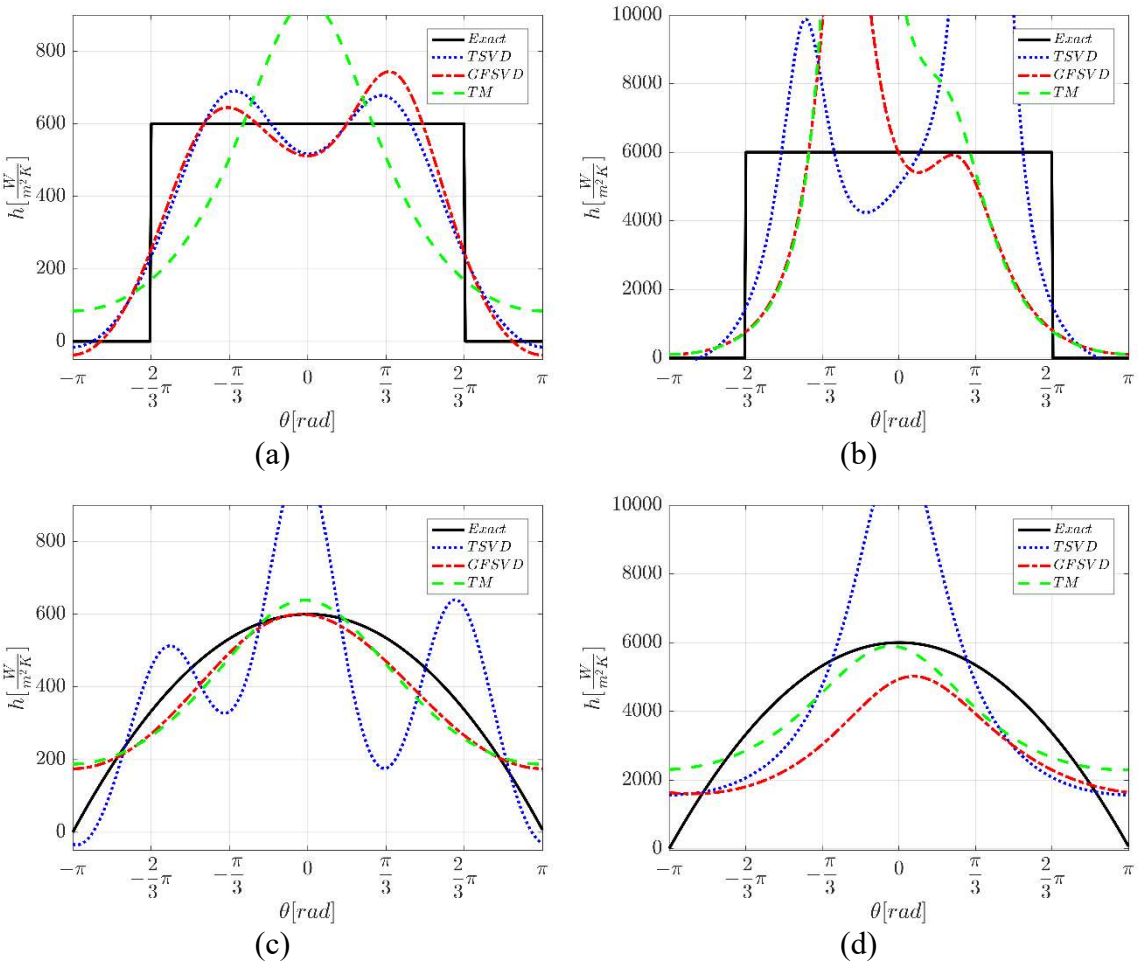

Figure 5.10: Reconstruction of the internal heat transfer coefficient for a) test case h1, b) test case h2, c) test case h and, d) test case h4 ($\sigma = 1K$) (*Mocerino2018*)

It has to be pointed out that for all the estimation procedures here addressed, the Morozov's discrepancy principle was adopted as a criterion for the determination of the regularization parameter.

As it is possible to see in Figure (5.11), this criterion was able to identify the regularization parameter for all the test functions used and listed in Table (5.4), since the residual between the estimated and the measured external wall temperatures are randomly distributed with zero mean and standard deviation equal to the once expected.

Figure (5.12) shows the Morozov's discrepancy principle of the three methodologies here investigated for a representative noise level $\sigma = 0.1K$.

As it is possible to see, for the TSVD and the GFSVD methodology, the standard deviation of the residuals between the measured and the estimated temperature at the external boundary monotonically decreases as far as the regularization parameter increase.

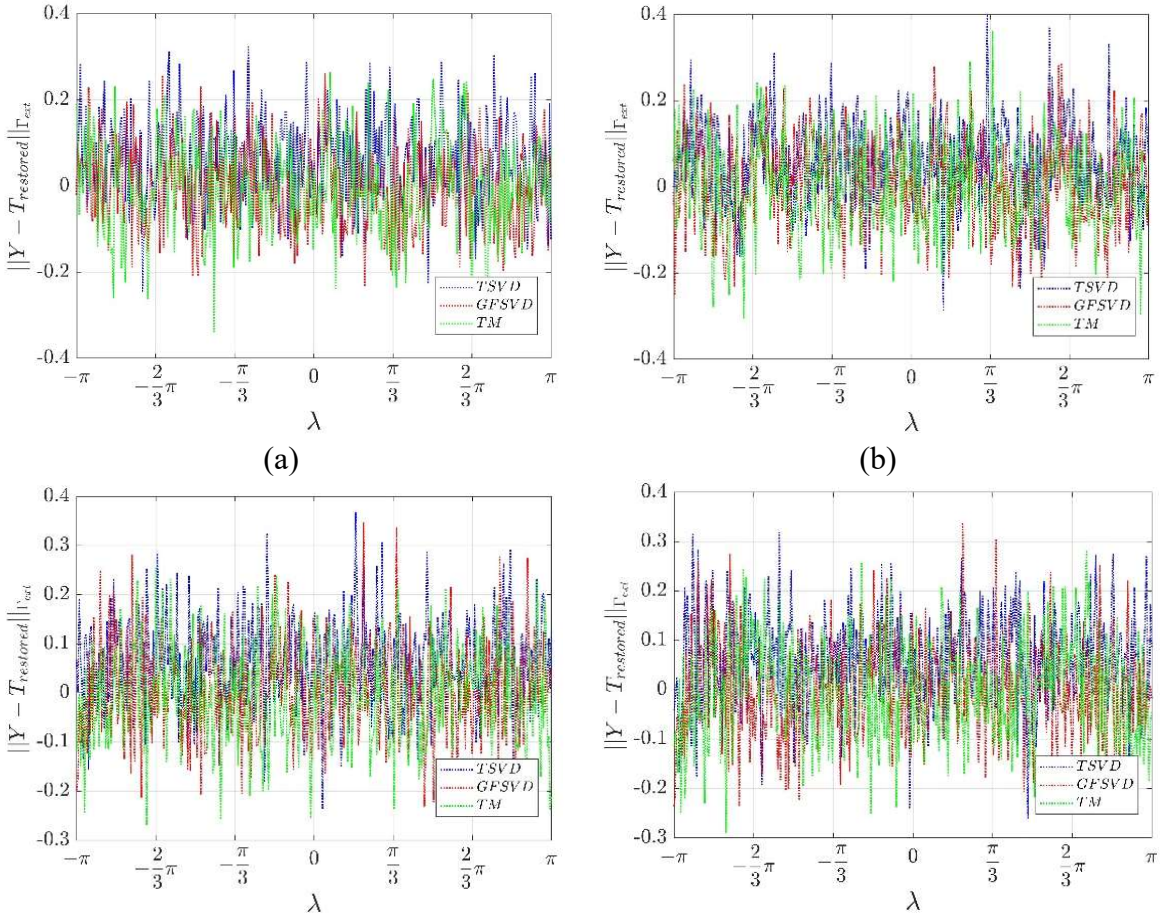

Figure 5.11: Residuals between the reconstructed and the measured external wall temperature for a representative noise level $\sigma = 0.1K$: (a) h1, (b) h2, (c) h3 and (d) h4

This behaviour is justified since incrementing the regularization parameter more information about the signal is preserved during the estimation procedure, thus reducing the misfit between the temperature estimation at the external boundary and the measured one. The opposite observation can be made for the TM method, since in this case the augmentation of the regularization parameter will produce an over-smoothed estimated solution, thus increasing the misfit between the temperature estimation at the external boundary and the measured one.

As highlighted by Figure (5.13), GFSVD method was able to estimate far better than the classical TSVD, which always shows the worst behaviour. Moreover, it estimation capabilities are comparable to the TM method, suggesting this approach to future application and development.

It has to be highlighted that the stopping criteria used affects the quality of the reconstruction as already shown by Bazàn (*Bazàn2012*), who compared the fixed-point criteria with the Morozov's discrepancy principle.

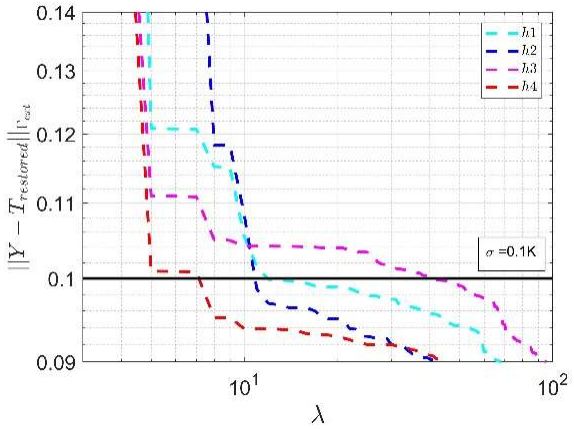

(a)

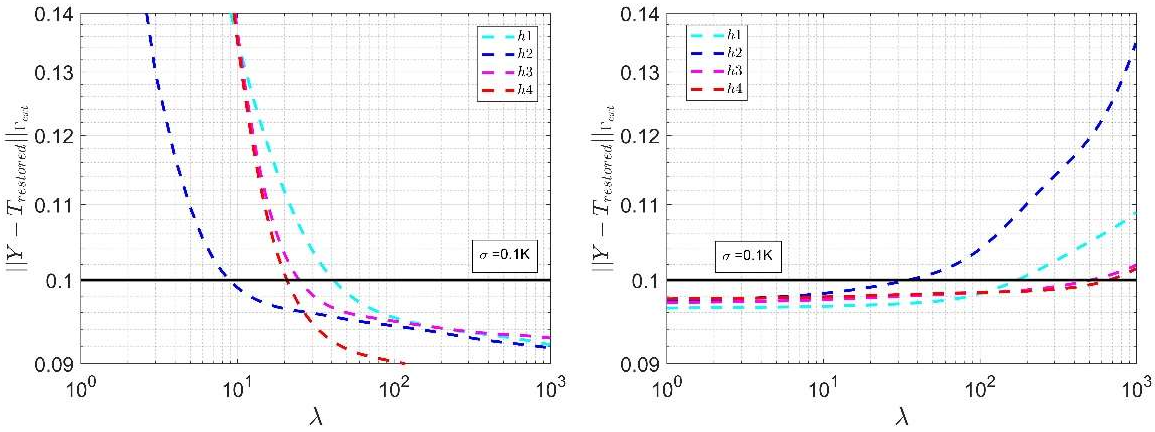

(b) (c)

Figure 5.12: Morozov's discrepancy principle for a representative noise level $\sigma = 0.1K$: (a) TSVD, (b) GFSVD and (c) TM

As observed in all inverse problems (*Beck1977*), the presence of the noise in the measurements corrupts the reconstruction of the unknown heat flux distribution. In almost every practical condition, the noise is uniformly distributed on the whole spectrum while the signal is almost always present in the lower harmonic orders.

Given the above observation, it is possible to conclude that the new regularization approach for the unconstrained linear least squares problem was able to successfully estimate the internal convective heat transfer coefficient. In particular, the numerical results here presented highlight the goodness of GFSVD and TM in solving this kind of inverse problem and the limits of TSVD that, although being probably the most widely used approach, suffers ringing artefacts in the reconstruction of the wanted information at low noise level.

GFSVD, thanks to the smooth penalty function added to the classical SVD approach, exhibited almost the same high-level performance as TM, providing an original point of view on the regularization techniques.

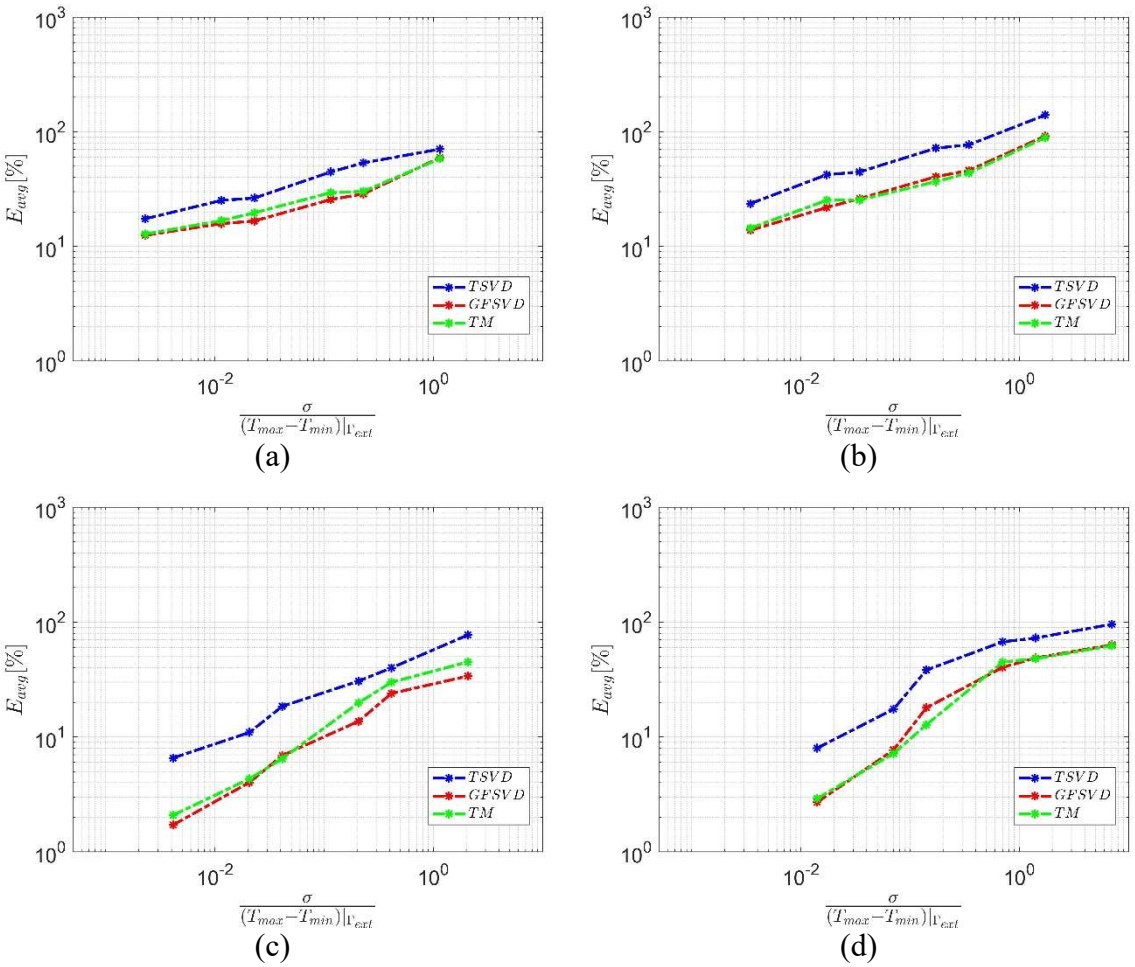

Figure 5.13: Average estimation error as a function of the dimensionless noise level for different test case: a) h1 b) h2 c)h3, and d) h4

4.3.2 Filtered Reciprocity Functional

Since this new proposed methodology is characterized by an ideal low pass filter function, its estimated results are going to be compared with the ones provided by its precursor NRF and the TSVD algorithm, a common regularization scheme based on the same filter function. The numerical data set used for the validation of the new methodology is the same that was adopted for the validation of the GFSVD.

The reconstruction results related to the test function here analysed are shown in Figure (5.14)-(5.15), for two representative noise level (e.g. $\sigma = 0.1K$ and $\sigma = 1K$). As it is possible to see, the three estimation algorithms present different degrees of reconstruction accuracies depending on the noise level and the test case considered. Moreover, it is possible to see that the reconstruction provided by FRF and TSVD are almost the same, while the once obtained from the NRF is less accurate. It has to be remarked that, the number of harmonics to keep is chosen by the classical discrepancy principle, originally formulated by Morozov (*Morozov1984*), in order to compare straightforwardly the three considered approaches.

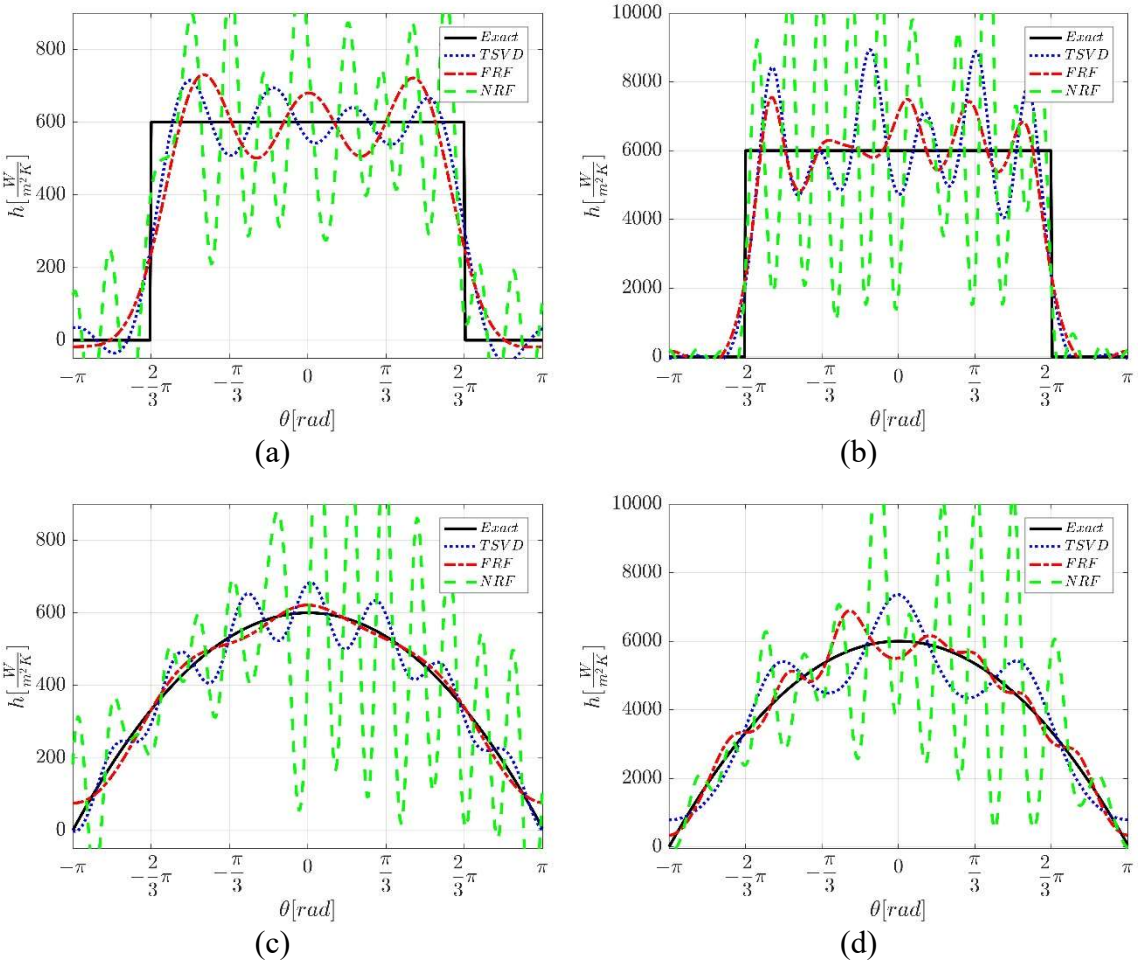

Figure 5.14: Reconstruction of the internal heat transfer coefficient for a) test case h1, b) test case h2, c) test case h3 and d) test case h4 (σ=0.1K)

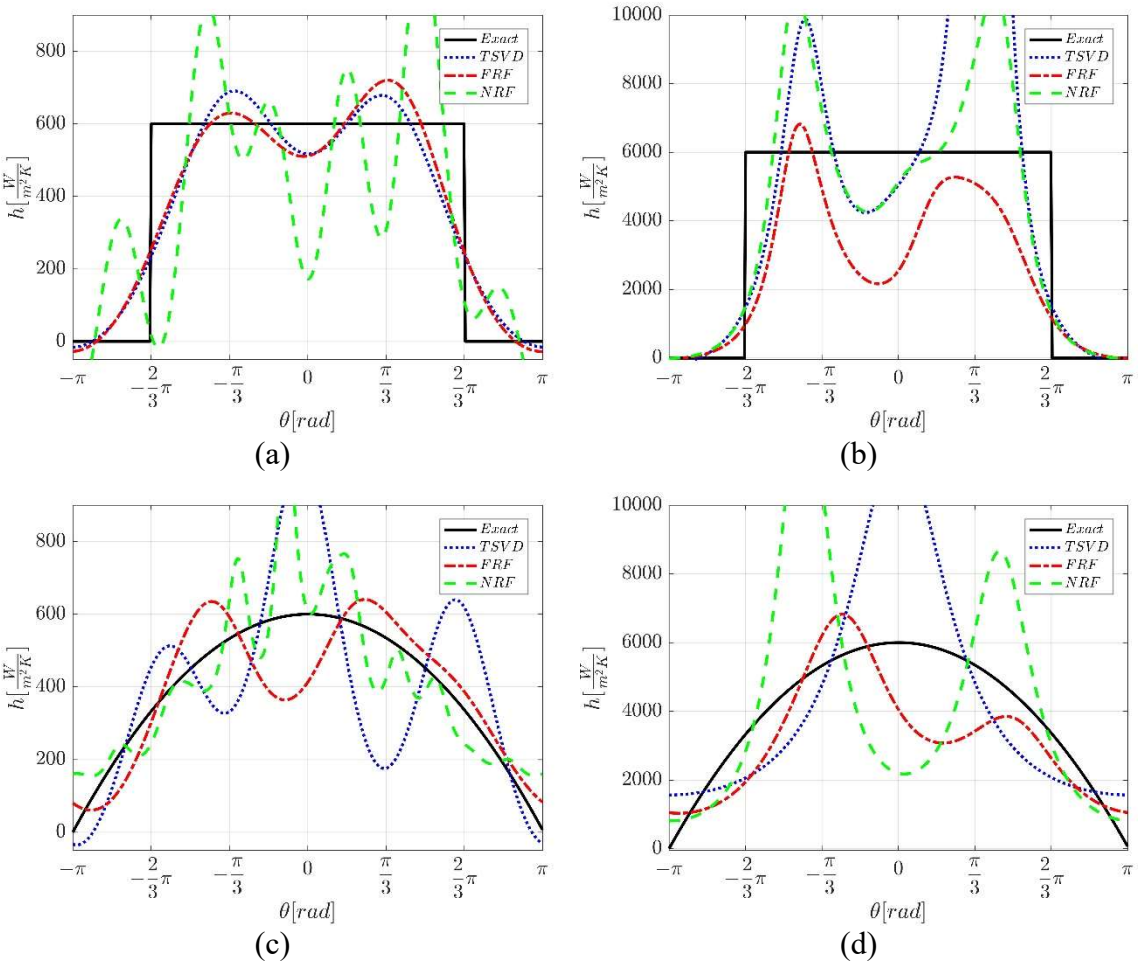

Figure 5.15: Reconstruction of the internal heat transfer coefficient for a) test case h1, b) test case h2, c) test case h and, d) test case h4 (σ=1K)

As suggested by Bazàn (*Bazàn*), the stopping criterion used affects the quality of the reconstruction; moreover, Colaço (*Colaço*) already showed that the reconstruction due the NFR could be better if a different stopping criterion is used.

Since the noise is uniformly distributed in all the frequencies, while the signal is almost present at low frequency, the worst reconstruction provided by the RFN compared to TSVD and FRF is due to its incapability to separate the signal form the noise, which means filter out the high harmonic frequencies.

Therefore, the noise content in the measurements is passed to the inversion algorithm which promotes instabilities in the estimated solution, yielding to high ringing artefact .

It has to be pointed out that for all the estimation procedure here addressed, the Morozov's discrepancy principle was adopted as a criterion for the determination of the regularization parameter.

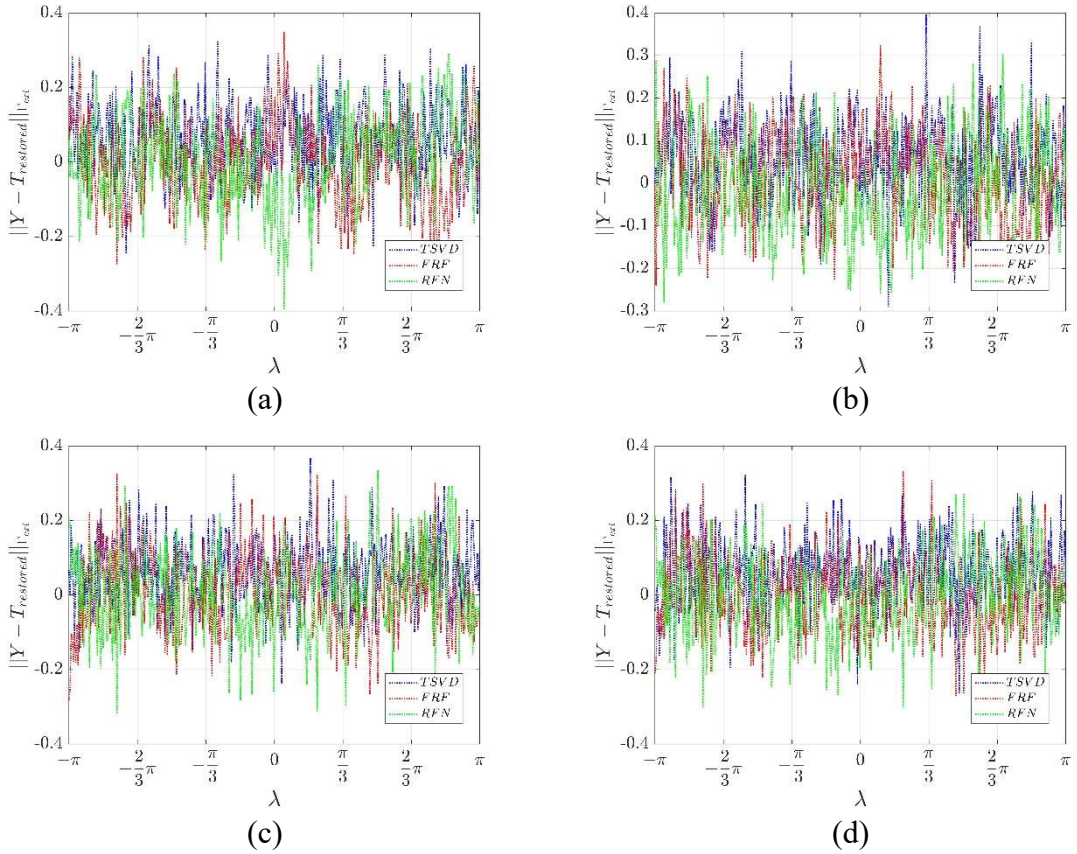

Figure 5.16: Residuals between the reconstructed and the measured external wall temperature for a representative noise level $\sigma = 0.1K$: (a) h1, (b) h2, (c) h3 and (d) h4

As it is possible to see in Figure (5.16), the criterion was able to identify the regularization parameter for all the test function used and listed in Table (5.4) since the residual between the estimated and the measured external wall temperature are randomly distributed with zero mean and standard deviation equal to the once expected.

Figure (5.17) shows the Morozov's discrepancy principle of the three methodologies here investigated for a representative noise level $\sigma = 0.1K$.

As it is possible to see, for all the methodologies here investigated, the standard deviation of the residuals between the measured and the estimated temperatures at the external boundary monotonically decrease as far as the regularization parameter increase.

This behaviour is justified since incrementing the regularization parameter more information about the signal are preserved during the estimation procedure, thus reducing the misfit between the temperature estimation at the external boundary and the measured one.

As highlighted by Figure (5.18), FRF estimates better than the classical RFN, which shows always the worst behaviour. Moreover, it estimation capabilities are comparable to the TSVD method, suggesting this approach to future application and development.

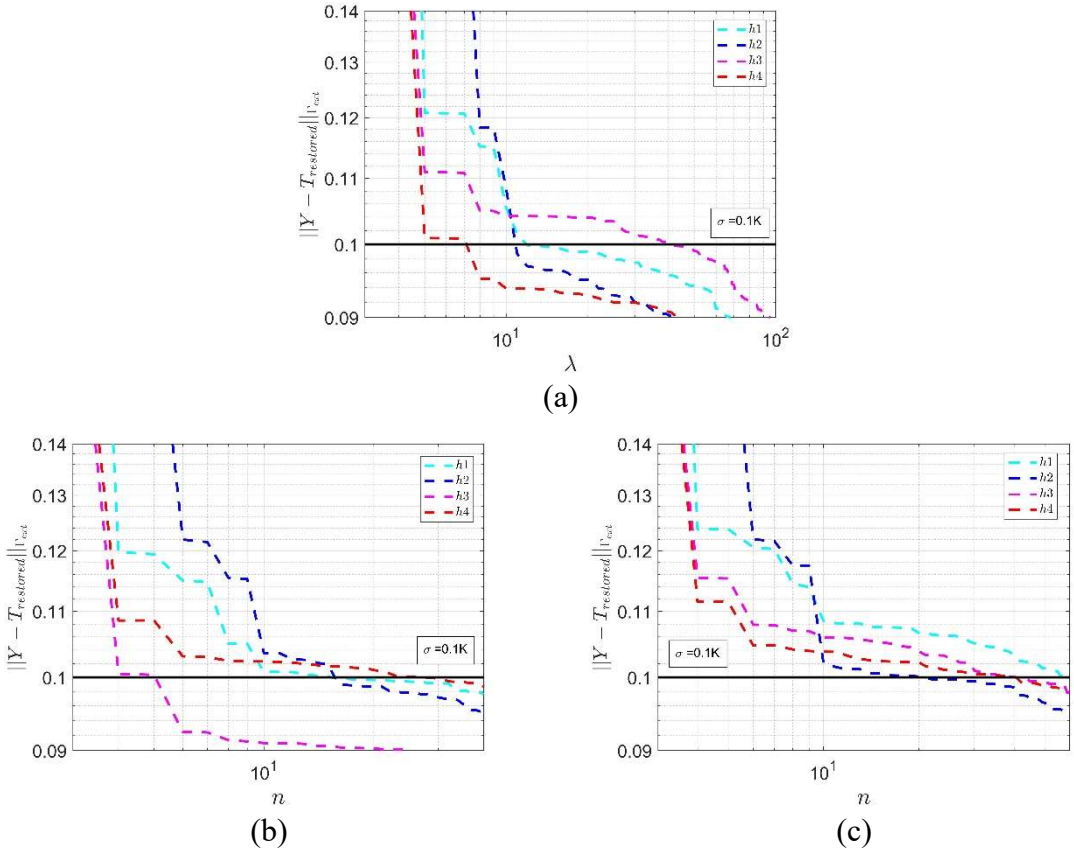

Figure 5.17: Morozov's discrepancy principle for a representative noise level $\sigma = 0.1K$: (a) TSVD, (b) FRF and (c) RFN

This means that the harmonic decomposition of the Classical Integral Transform Technique enables to efficiently remove the unwanted information from the measured data.

It has to be highlighted that the stopping criterion used affects the quality of the reconstruction as already shown by Bazàn (*Bazàn2012*) that compared the fixed-point criteria with the Morozov's discrepancy principle; moreover, Colaço (*Colaço2013*) already showed that the reconstruction due the NFR could be better if a different stopping criterion is used.

As already mentioned, in every practical condition, the noise is uniformly distributed on the whole spectrum while the signal is almost always present in the lower harmonic orders; under this statement, the magnification effect of the M^{-1} and N^{-1} matrices (*Chapter 4*), which increases as the harmonics order increase, requires the truncation of their diagonal elements. This kind of truncation can be performed according to the Morozov's discrepancy principle in the same fashion as it was already adopted for the TSVD approach.

This behaviour is clarified by Figure (5.19), which shows the reciprocity functional values for both the first and the second auxiliary problem as a function of the harmonic order, for the two representative test case h1 and h3.

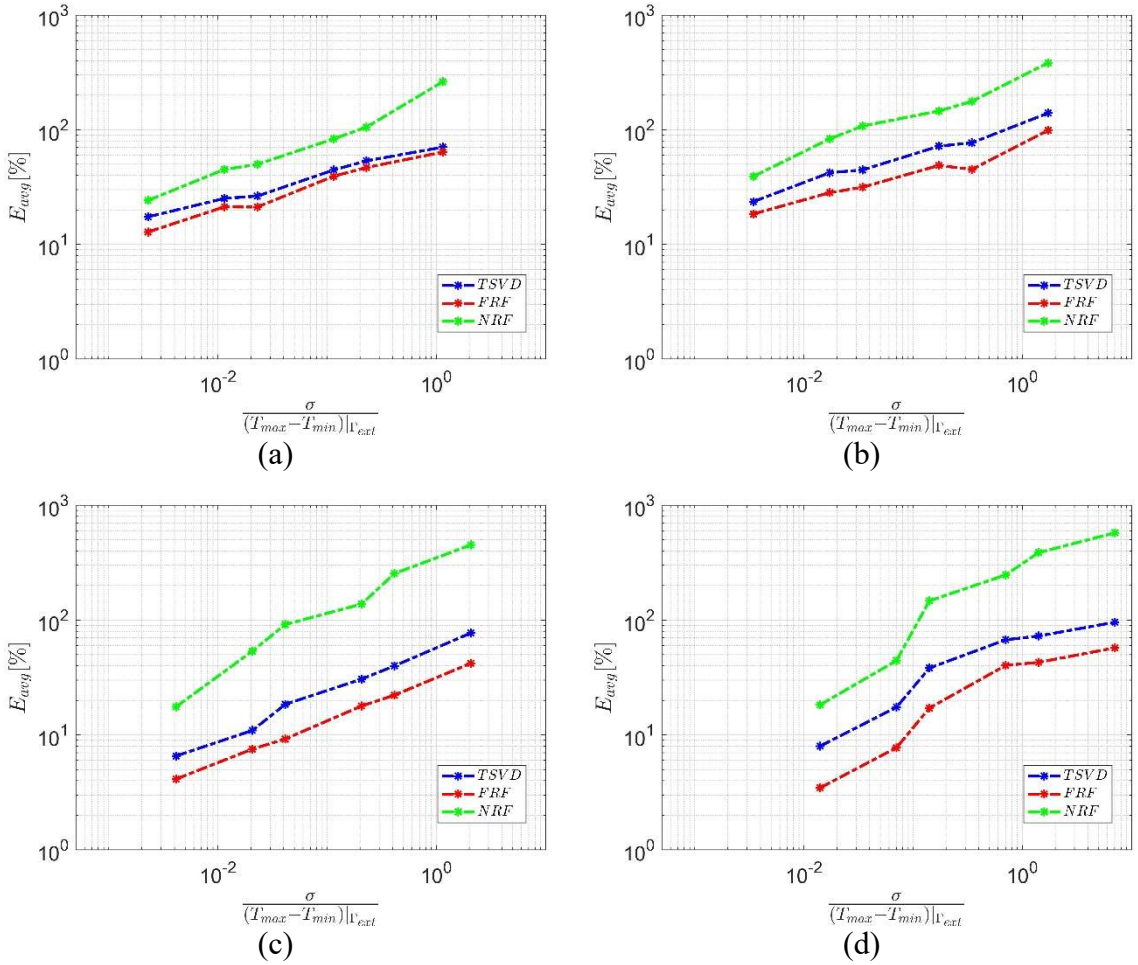

Figure 5.18: Average estimation error as a function of the dimensionless noise level for different test case: a) h1 b) h2 c)h3, and d) h4

In order to improve the readability of these plots, the reciprocity functionals are expressed in a more compact polar form, following the classical notation:

$$R_G^* = \sqrt[2]{{R_{G(k^*)}}^2 + {R_{G(k^*+1)}}^2}$$
$$R_F^* = \sqrt[2]{{R_{F(k^*)}}^2 + {R_{F(k^*+1)}}^2} \qquad (5.16)$$

where: $k^* = 2,4,6,\ldots,N-1$.

In all the graphs presented in Figure (5.19), the reciprocity functional of the noiseless signal (filled dot) is compared to the reciprocity functional of a representative set of white noise having standard deviation of $\sigma = 0.1K$ (empty dot), that were used to spoil the synthetic data. They confirm that, in the reciprocity functionals, the signal prevails for the lower harmonics, while the noise overcomes the signal for the higher harmonics.

Given the above results, it is possible to conclude that, the approach here developed was able to deals with the estimation of the local internal heat transfer coefficient in a convective heat

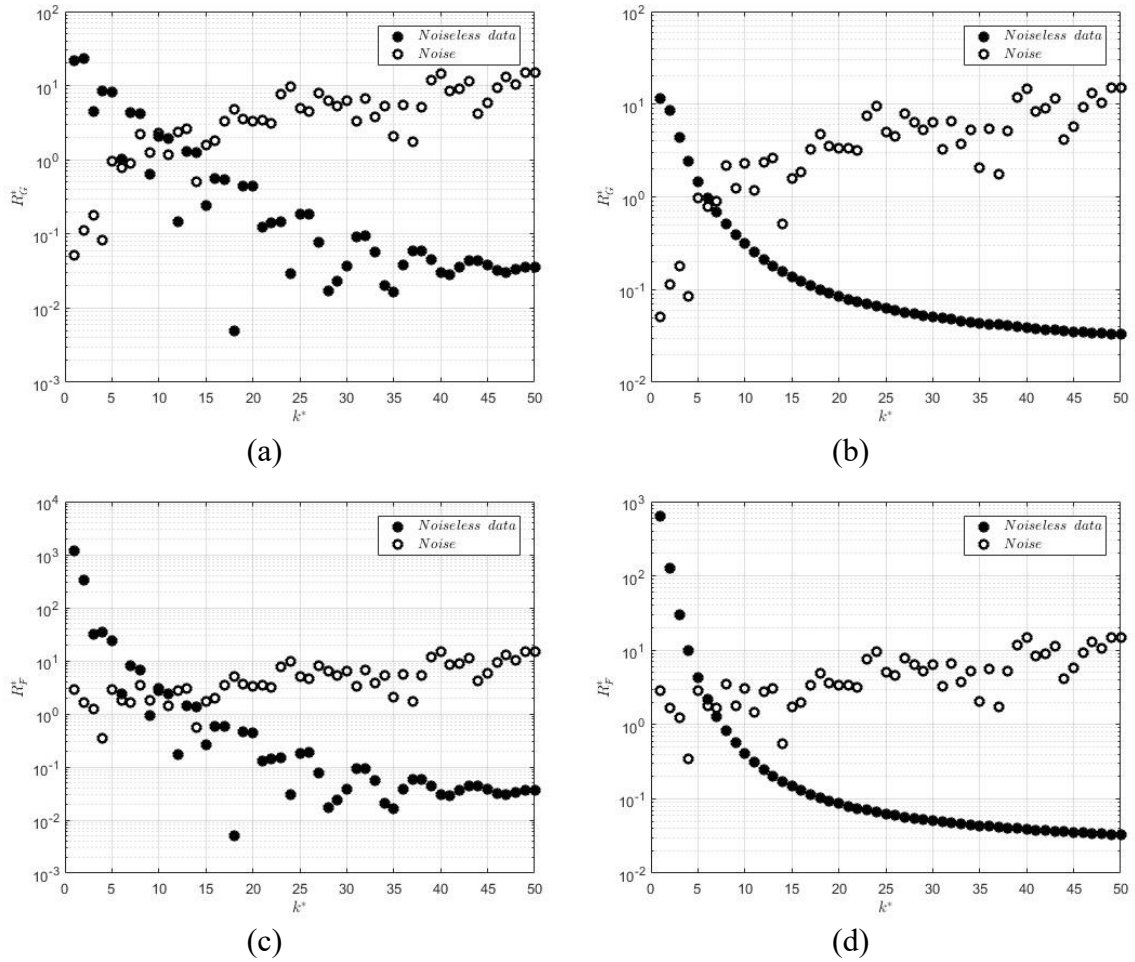

Figure 5.19: RG and RF for two representative test case: a) RG for test case h1 b) RG for test case h3 c) RF for test case h1 and d) RF for test case h3

transfer problem, given the external temperature measurements, by solving an Inverse Heat Conduction Problem.

The approach, named Filtered Reciprocity Functional approach, presents some practical advantages over the more classical inverse problem solution techniques since it is completely analytical and, for this reason, computationally inexpensive if compared to the NFR and TSVD approaches.

The application of FRF to the numerical measurements highlighted its effectiveness and robustness, suggesting the application to other challenging inverse problems. Moreover, the obtained formulation enables, from the theoretical point of view, to highlight the ill-posed nature of the inverse problem and, from the practical point of view to filter efficiently the noisy content thanks to the harmonic nature of CITT and the Fourier series expansion.

In the next chapter the methodologies here compared are going to be applied to a set of experimental measurements acquired by means of the thermographic camera.

5.2 Two dimensional function estimation

The 2D inverse problem here addressed concerns the estimation of the local thermal performances at the internal wall surface of tubes characterized by a circular cross-section. The methodology used is based on the Tikhonov regularization technique presented in *Chapter 3*. The inverse procedure is implemented in within the Matlab® environment by adopting synthetic data (sampled at the external surface of the pipe) generated by the finite element method implemented in Comsol Multiphysic® by imposing a known distribution of h_{int} at the internal wall surface of the tube. The physical problem considered in the present work, according to the conditions reported in the available literature (*Bozzoli2014a*, *Colaço2015*), consists in a piece of circular duct characterized by an internal radius $r_{int} = 0.007m$, external radius $r_{ext} = 0.008m$ and length $L = 0.016m$. The thermal conductivity of the pipe, $k = 15W/m\,K$, was assumed to be constant such as the environmental temperature, $T_{env} = 294.2K$, and the bulk temperature, $T_b = 291.9$, of the fluid that flows inside the tube. The exterior surface Γ_{ext} of the tube was subjected to an overall convective heat transfer resistance, $R_{env} = 0.2m^2K/W$, with the environment and the domain Ω, that was assumed to be homogeneous and isotropic, and subjected to an internal heat generation per unit of volume $q_g = 2.8\ 10^6 W/m^3$.

A representation of the geometrical domain, together with the boundary conditions applied in both the direct and inverse problem is show in Figure (5.20).

The direct problem could be stated as follows:

$$\nabla^2 T = -\frac{q_G}{k} \quad \text{in } \Omega \tag{5.17.1}$$

$$-k\left.\frac{\partial T}{\partial \mathbf{n}}\right|_{\Gamma_{int}} = h_{int}(\theta, z) \quad \text{on } \Gamma_{\text{int}} \tag{5.17.2}$$

$$-\mathrm{k}\left.\frac{\partial T}{\partial \mathbf{n}}\right|_{\Gamma_{ext}} = h_{ext}(T - T_{env}) \quad \text{on } \Gamma_{\text{ext}} \tag{5.17.3}$$

$$-k\left.\frac{\partial T}{\partial \mathbf{n}}\right|_{\Gamma_{int}} = 0 \quad \text{on } \Gamma_{top} \tag{5.17.4}$$

$$-k\left.\frac{\partial T}{\partial \mathbf{n}}\right|_{\Gamma_{int}} = 0 \quad \text{on } \Gamma_{bottom} \tag{5.17.5}$$

where h_{int} is the internal convective heat transfer coefficients used to produce the synthetic measurements which is defined as (*Bozzoli2016a*):

$$h_{int} = A + B \sin\left(\theta + 2\pi \frac{z}{p}\right) \tag{5.18}$$

where $p = 0.029m$ while A and B were chosen to be equal respectively to $400W/m^2K$ and $300W/m^2K$. A representation of the adopted internal heat flux distribution is shown in Figure (5.14) together with the produce noiseless temperature distribution.

The direct problem presented in Equations (5.17.1)-(5.17.5) concerns the determination of the temperature field T within the Ω domain given the distribution of the convective heat transfer coefficient on both the internal and external surfaces. As it is possible to see, from the system of Equations (5.17), the direct problem is linear with respect to the unknown variable T, while the inverse problem related to the estimation of the convective heat flux distribution is not linear in the unknown variable h_{int}, since the internal wall temperature of the duct could not be directly measured. This unwanted behaviour could be overcome formulating an auxiliary problem in which the internal surface is subjected to an imposed heat flux distribution:

$$\nabla^2 T = -\frac{q_G}{k} \quad \text{in } \Omega \tag{5.18.1}$$

$$-k \left.\frac{\partial T}{\partial \mathbf{n}}\right|_{\Gamma_{int}} = q_{int}(\theta, z) \quad \text{on } \Gamma_{\text{int}} \tag{5.18.2}$$

$$-k \left.\frac{\partial T}{\partial \mathbf{n}}\right|_{\Gamma_{ext}} = h_{ext}(Y - T_{env}) \quad \text{on } \Gamma_{\text{ext}} \tag{5.18.3}$$

$$-k \left.\frac{\partial T}{\partial \mathbf{n}}\right|_{\Gamma_{int}} = 0 \quad \text{on } \Gamma_{top} \tag{5.18.4}$$

$$-k \left.\frac{\partial T}{\partial \mathbf{n}}\right|_{\Gamma_{int}} = 0 \quad \text{on } \Gamma_{bottom} \tag{5.18.5}$$

where Y are some extra temperature measurements taken at the external surface Γ_{ext} by means of a thermographic camera, while $\boldsymbol{q}(\theta)$ is the unknown boundary condition that has to be estimated.

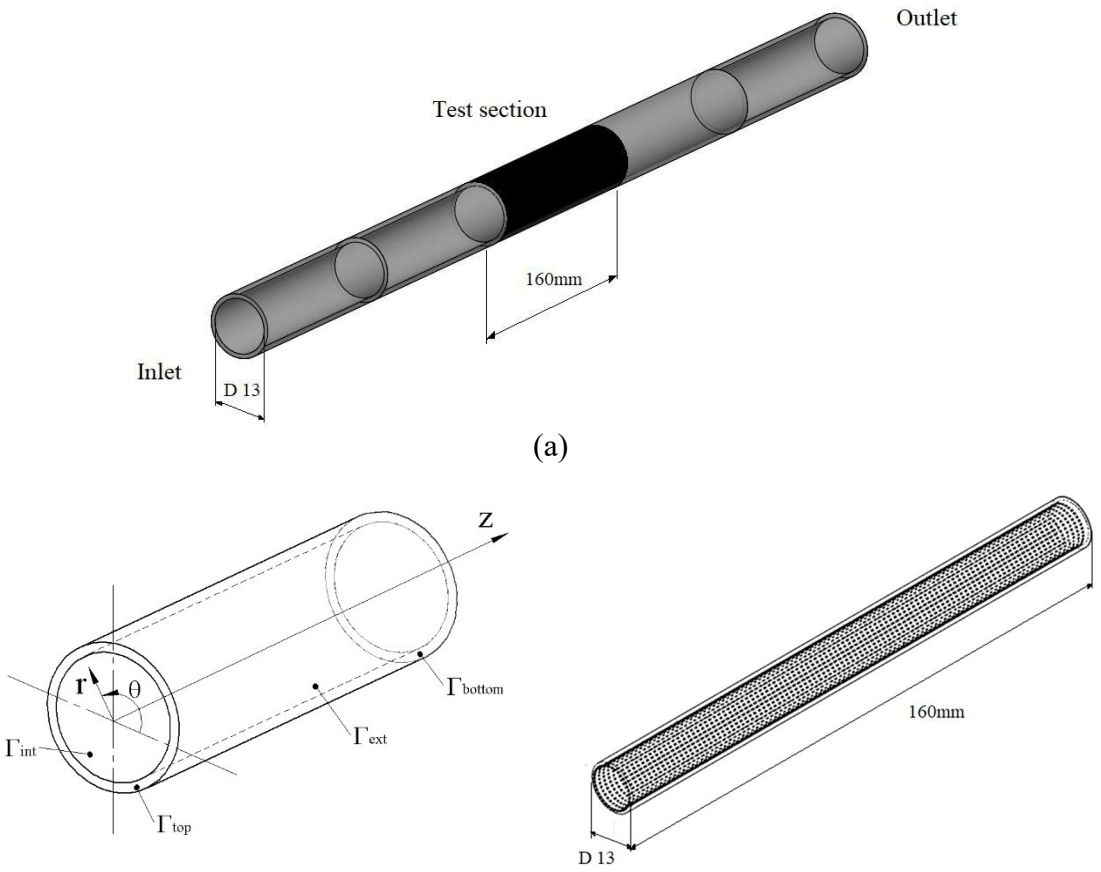

Figure 5.20: Function estimation: (a) Geometrical domain, (b) coordinate system and (c) internal heat flux discretization scheme

In this way, the system of Equation (5.18) becomes linear with respect to the imposed heat flux and the convective heat flux distribution can be calculated, once the heat flux estimation is performed, as:

$$h_{int}(\theta) = \frac{q(\theta)}{\left(T_{wall}(\theta)|_{\Gamma_{int}} - T_b\right) A_{int}} \tag{5.19}$$

As already mentioned in the previous chapter, the linearity of the system is an interesting property, since it allows to solve the problem in an easy way, avoiding the usage of iterative procedures that are cost-expensive in terms of computational requirement.

As suggested by Beck (*Beck1985*) and Dennis (*Dennis2013*), since the problem is linear with respect to the heat flux $q(x)$, it can be written in the discrete domain as follows:

$$\boldsymbol{T} = \boldsymbol{X}\boldsymbol{q} + \boldsymbol{T}_{\boldsymbol{q}=\boldsymbol{0}} \tag{5.20}$$

where $\boldsymbol{T}$ is the estimated temperature on the sampling position (e.g. in all the entire), $\boldsymbol{X}$ is the sensitivity matrix, $\boldsymbol{q}$ is the imposed heat flux distribution and $\boldsymbol{T}_{q=0}$ is the estimated temperature on the sampling position if no heat flux is applied on the boundary at Γ_{int}. The homogeneous term $\mathbf{T}_{\mathrm{q=0}}$ has to take care about the forcing term (e.g. internal heat source, imposed potential boundary conditions, etc.): it represents the response of the system if no heat flux $\boldsymbol{q}$ is imposed, highlighting the effect of the forcing term. It follows that the quantities present in the Equation (5.20) are given by:

$$\boldsymbol{T^T} = [T_1, T_2, T_3, \dots T_n, \dots, T_i] \tag{5.21}$$

$$\boldsymbol{q^T} = [q_1, q_2, q_3, \dots q_m, \dots, q_j] \tag{5.22}$$

$$\boldsymbol{X^T} = \begin{bmatrix} \partial T_1/\partial q_1 & \partial T_2/\partial q_1 & \cdots & \partial T_n/\partial q_1 & \cdots & \partial T_i/\partial q_1 \\ \partial T_1/\partial q_2 & \partial T_2/\partial q_2 & \cdots & \partial T_n/\partial q_2 & \cdots & \partial T_i/\partial q_2 \\ \vdots & \vdots & & & & \vdots \\ \partial T_1/\partial q_{\mathrm{m}} & \partial T_2/\partial q_{\mathrm{m}} & & \partial T_n/\partial q_m & & \partial T_i/\partial q_m \\ \vdots & \vdots & & & & \vdots \\ \partial T_1/\partial q_j & \partial T_2/\partial q_j & \dots & \dots & & \partial T_i/\partial q_j \end{bmatrix} \tag{5.23}$$

where i is the total number of sensors while j is the total number of discretizing parameters. The problem can be stated using the Lagrange multipliers in a damped least square problem:

$$\min\left\|\boldsymbol{Y} - \left(\boldsymbol{Xq} + \boldsymbol{T_{q=0}}\right)\right\|_2^2 + \lambda^2\|\boldsymbol{qL}\|_2^2 \quad \lambda > 0 \tag{5.24}$$

where $\|\cdot\|_2^2$ stands for the square of the two-norm, λ is the unknown regularization parameter and $\boldsymbol{L}$, for the zero order Tikhonov regularization, is the identity matrix:

$$\boldsymbol{L} = \begin{bmatrix} 1 & & 0 \\ & \ddots & \\ 0 & & 1 \end{bmatrix} \tag{5.25}$$

As long as λ is a non-zeros coefficient, the problem defined by the Equation (5.24) can be solved by the method of the normal equations as follows:

$$(\boldsymbol{X}^T\boldsymbol{X} + \lambda^2\boldsymbol{L})\boldsymbol{q} = \boldsymbol{X^T}\left(\boldsymbol{Y} - \boldsymbol{T}_{q=0}\right) \quad \lambda > 0 \tag{5.65}$$

which yields to the estimated internal wall heat flux:

$$\boldsymbol{q}_{\lambda} = (\boldsymbol{X}^T\boldsymbol{X} + \lambda^2\boldsymbol{L}^T\boldsymbol{L})^{-1}\boldsymbol{X}^T\left(\boldsymbol{Y} - \boldsymbol{T}_{\boldsymbol{q}=\boldsymbol{0}}\right) \tag{5.27}$$

It has to be pointed out that since the boundary conditions adopted on the top and on the bottom of the pipe are not the ones that better model the phenomenon, it was necessary to extend the module under investigation two times before and two times after the test section, as shown in Figure (5.20).

It has to be pointed out that, the unknown heat flux distribution was discretized in order to have the same pitch in both the circumferential and axial coordinate: in particular, it was discretised in 360 values along the θ coordinate and 1310 values along the z coordinate.

This configuration allowed using the same regularization parameter in both directions, giving the same weight to the filter function. The same discretization was adopted for the temperature measurements available at the external surface, after the image processing procedure.

It is well known that the effectiveness of all regularization approaches strongly depends on the choice of a proper value of the regularization parameter (*Bazàn2012*, *Bozzoli2014a*).

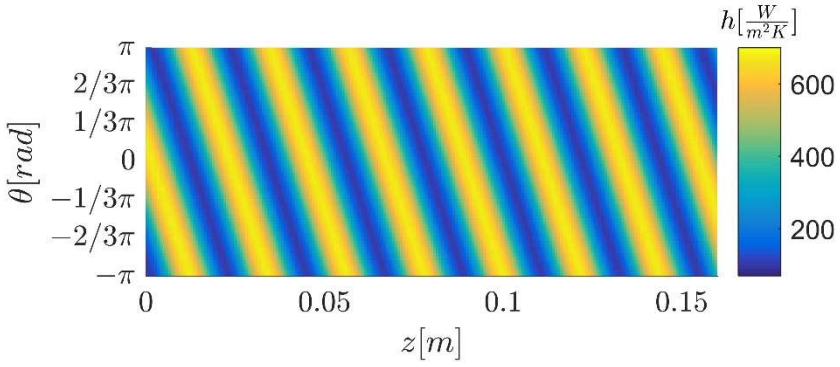

(a)

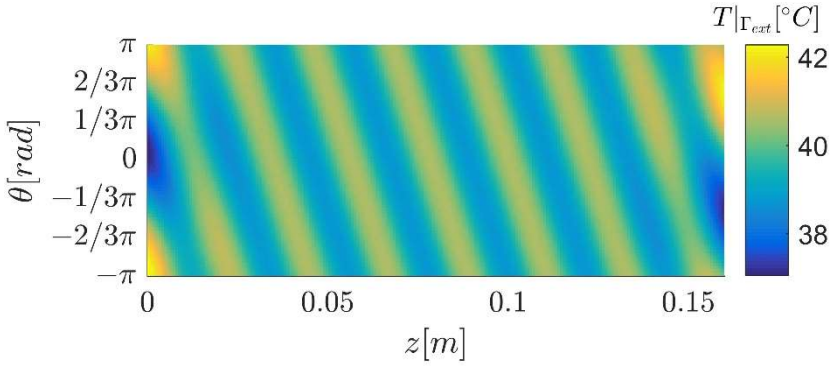

(b)

Figure 5.21: Function estimation: (a) internal convective heat transfer coefficient and (b) simulated temperature distribution

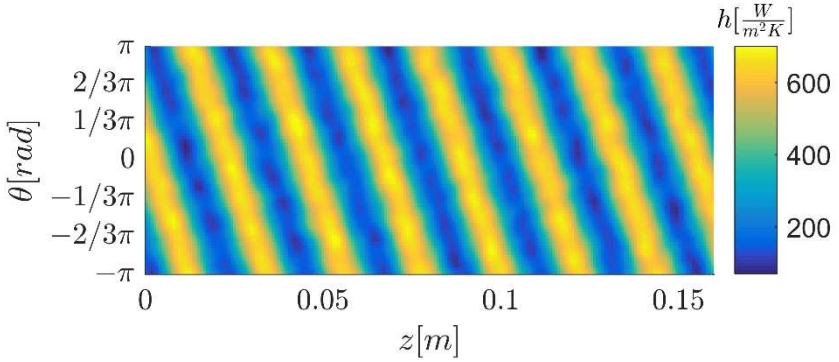

(a)

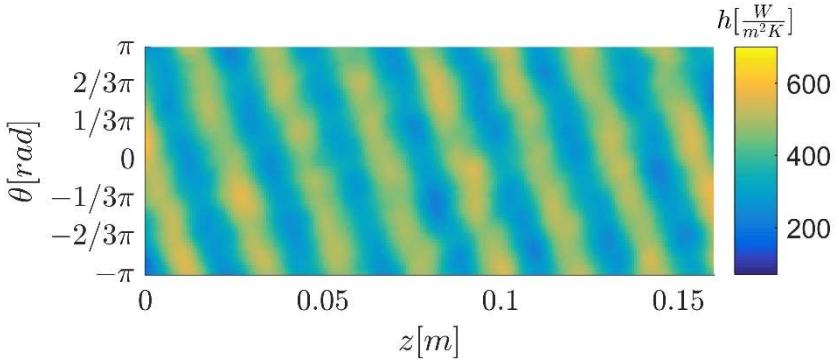

(b)

Figure 5.22: Function estimation: internal convective heat transfer coefficient for two representative noise level (a) $\sigma = 0.1K$ and (b) $\sigma = 1K$

In the present analysis, to make the comparison between the considered regularization techniques more straightforward, the criterion provided by the discrepancy principle, originally formulated by Morozov (*Tikhonov1977*, *Beck1985*), was adopted for all the techniques.

In order to test the estimation capabilities of the methodology adopted, the synthetic measurement temperatures Y were deliberately spoiled by random noise and then used as input data for all the mathematical models. In particular, a Gaussian white noise characterized by a standard deviation ranging from $\sigma = 0.01K$ to $\sigma = 5K$ was introduced according to:

$$Y = T_{exact}|_{\Gamma_{ext}} + \sigma\epsilon \tag{5.28}$$

where ϵ is a random Gaussian variable with zero mean and unit variance.

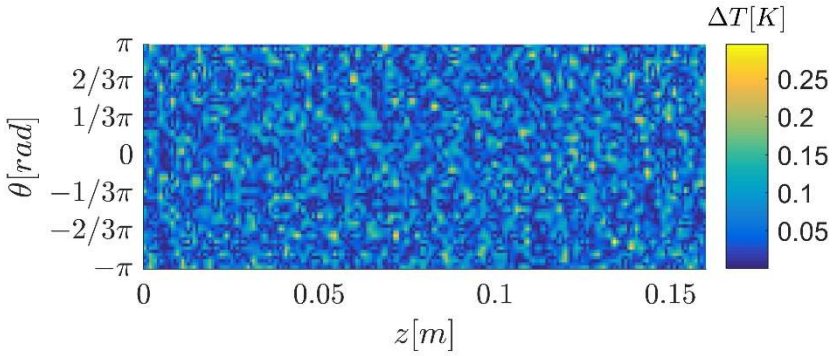

(a)

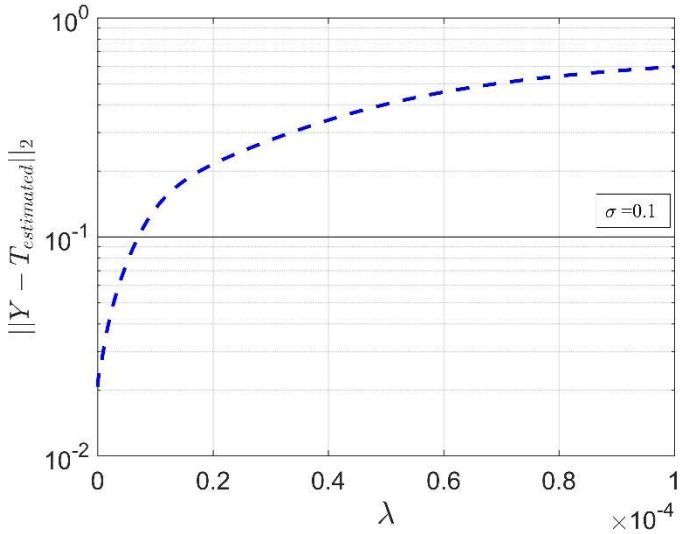

(b)

Figure 5.23: (a) Residual between the estimated and the reconstructed external wall temperature and (b) Morozov's discrepancy principle, for a representative test case $\sigma = 0.1K$

In order to give a quantitative indication of the estimation capabilities of the methodology adopted, the global relative estimation error between the exact and the estimated internal heat transfer coefficient was calculated as:

$$E = \frac{\|\boldsymbol{h}_{reconstructed} - \boldsymbol{h}_{exact}\|_2}{\|\boldsymbol{h}_{exact}\|_2} \tag{5.29}$$

The added noise depends intrinsically on the random sequence generated by Matlab®, thus the estimation procedure was repeated 50 times for different random noise sequences and an average value E_{avg} was calculated for each noise level.

The results of the local estimation of the heat transfer coefficient are reported in Figure (5.22). As it is possible to see, the reconstruction related to two different noise levels ($\sigma = 0.1K$ and $\sigma = 1K$) suffer of small ringing artefact.

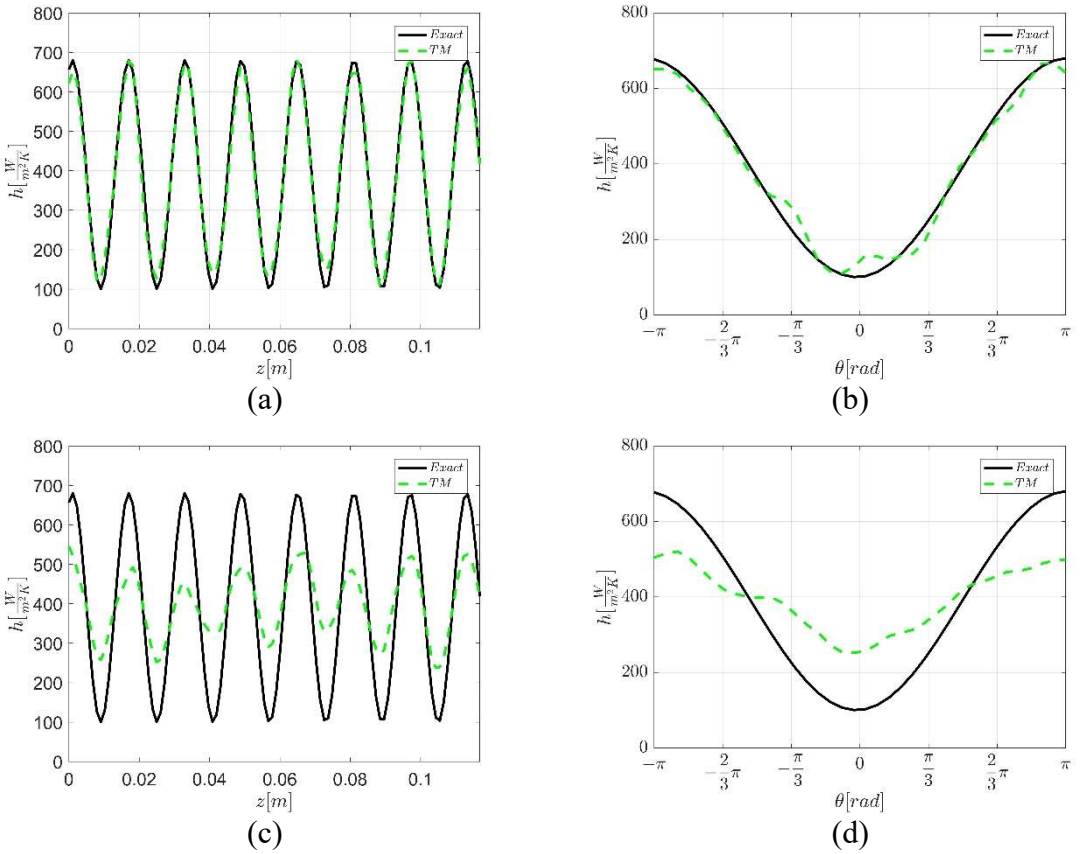

Figure 5.24: (a) longitudinal and (b) circumferential convective heat transfer coefficient distribution for a representative test case $\sigma = 0.1K$ and (c) and (d) for $\sigma = 1K$

It has to be pointed out that the Morozov's discrepancy principle was able to estimate the regularization parameter that has to be adopted, in all the noise levels here presented. This aspect is confirmed by the random behaviour of the residuals between the measured and the estimated external wall temperature profiles shown in Figure (5.23) for a representative noise level $\sigma = 0.1K$.

As it is possible to see, the standard deviation of the residuals between the measured and the estimated temperature at the external boundary, monotonically increases as far as the regularization parameter increases.

This behaviour is justified, since the increment of the regularization parameter will produce an over-smoothed estimated solution, thus increasing the misfit between the temperature estimation at the external boundary and the measured one.

In order to better understand the reconstruction capabilities of the TM here implemented, the comparison between the reconstructed and the imposed convective heat transfer coefficient is reported in Figure (5.24) for two representative noise levels. As it is possible to see, in both the longitudinal and circumferential directions, the algorithm was able to restore the internal convective heat transfer coefficient stating form the external temperature

measurements. It has to be pointed out that, as far as the noise level inside the measurements increase, the reconstructed signal becomes smoother and smoother, since a higher regularization is required in order to respect the Morozov's discrepancy principle.

As observed in all inverse problems (*Beck1977*), the presence of the noise in the measurements corrupts the reconstruction of the unknown convective heat transfer coefficient. The average estimating performances of the proposed method are reported in Figure (5.25).

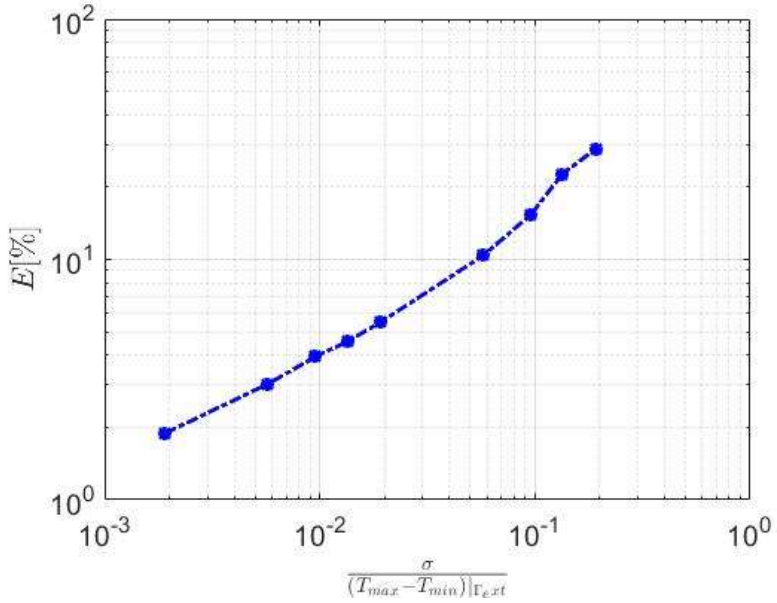

Figure 5.25: Average estimation error as function of the dimensionless noise level

Chapter 6

Experimental applications

The experimental applications here considered are relate to both parameter and function estimation. In particular, four different applications are going to be introduced and analysed:

- inverse estimation of the average performances of a bio-inspired double corrugated tube
- inverse estimation of the local convective heat transfer coefficient in coiled tubes
- inverse estimation of the local convective heat transfer coefficient in straight tubes using insert devices
- inverse estimation of the local convective heat transfer coefficient in straight tubes with cross-helix wall corrugated surface

The above mention applications are analysed using the new estimation methodologies presented in *Chapter 4* and their results are compared with some of the common estimation procedure presented in *Chapter 3*.

The usage of the IHCP for the estimation of the thermal characteristic of the heat exchangers, is going to be a common task in the scientific community, but it still be far away from the industrial application. The aim of the present chapter is the experimental estimation of the thermal performances of the heat exchanger to problems 0D, 1D and 2D with respect to the unknown variable. This type of analysis will allow the researcher to understand the local

phenomena that is driving the heat transfer mechanism as well as the industry to customize their devices for each application (increasing the performances of their products); it will also produce a set of experimental data that the mathematical community could use in order to test new estimation techniques.

6.1 Inverse estimation of the average performances of a bio-inspired double corrugated tube

INTRODUCTION

The 0D inverse problem here addressed, is stated in *Chapter 3* as a parameter estimation procedure, since the number of unknown variables is small. The defined problem, is here specifically applied for the estimation of the thermal performances of a bio-inspired double corrugated tube.

Nature can be an excellent source of inspiration for advanced structures, designs and materials, and the approach is referred to as biomimetic (*Bhushan2009)*. According to Mattheck (*Mattheck1993*), as early as 1893, it was suggested by K. Metzger that trees grow in a way that results in an even stress distribution throughout their structure. For example, the concept of even stress flow in mechanical systems has resulted in numerical models that can explain how trees grow and adapt to their unique loading case, including how root systems grow. Flies, beetles, spiders and geckos have specialized attachment geometries on their skin that allow them to climb up smooth vertical surfaces (*Artz2003*). Sharks have small riblets on their skin that reduce drag (*Dean2010*). In this article, we look to nature for examples of advanced heat exchanger designs, although there are relatively few examples of biological systems that require high heat transfer performance.

Many examples of complex thermal insulation techniques can be found in nature, but cases where high heat transfer is required are less common. Examples of insulation techniques include the fur of arctic animals or the insulating blubber layer found on seals and whales (*Scholander1950*). Some examples of high heat transfer performance in nature include the feet of some birds that have a counter-flow heat exchanger composed of blood vessels entering and exiting the feet (*Johansen1983*). This heat exchanger allows the feet to operate at a lower temperature than the rest of the bird's body and thus eliminates the need for insulation, in the form of feathers, on the feet. The counter-flow vascular heat exchanger at the core of several fish species, such as lamnid sharks and tuna (*Dickson2004*), while opahs

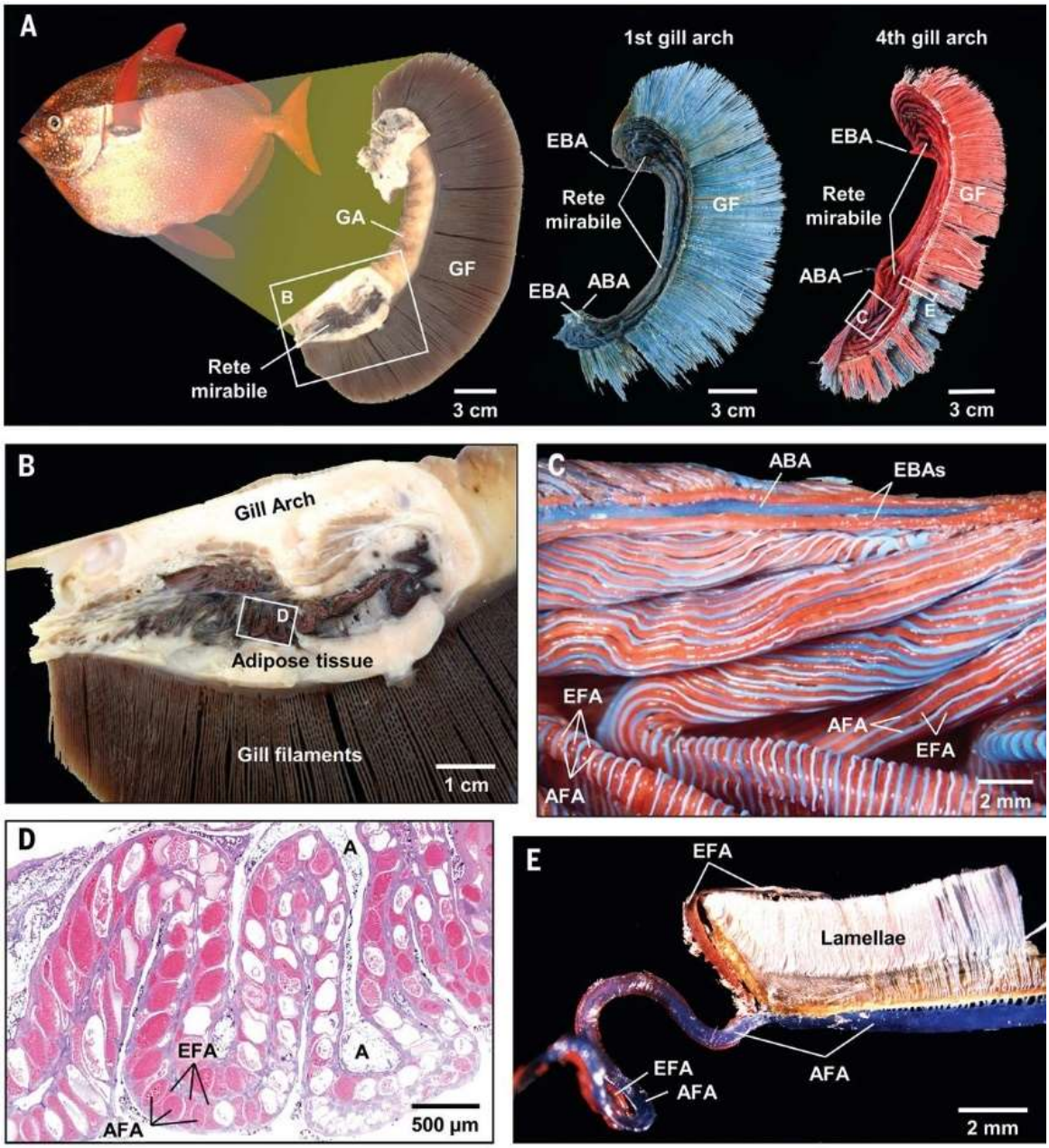

Figure 6.1: Photo of blood vessels in the rete mirabile, which is located in the gill of the opah. Reproduced from a figure from Wegner (*Wegner2015*)

(*Wegner2015)* represents a compact, high performance heat exchanger. This heat exchanger recovers heat generated in the fish's muscles that is carried in the blood before it is pumped to the gills where the heat is rejected to the surroundings, giving these fish the unique ability to maintain a body temperature that is significantly higher than their surroundings. This heat recovery technique allows them to hunt in waters with lower temperatures than fish without the regenerative heat exchanger. For example, the heat exchanger section of a 1.9 kg skipjack tuna was found to have over 250,000 blood flow passages with two distinct diameters of approximately 0.036 mm and 0.084 mm (*Stevens1974*).

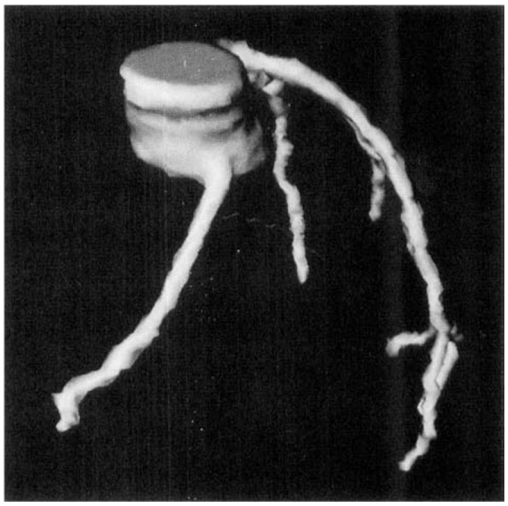

Figure 6.2: 3D magnetic resonance imaging of the opha blood vessels (*Börnert1995*)

In Figure (6.1), it can be seen that some blood vessels are nearly circular, others resemble ellipses, and others are irregular. Cross-sections such as shown in Figure (6.1) only show the geometry at one plane in the heat exchangers, and it is not known how the cross section of these blood vessels behave along the flow direction. To get an idea of how these blood vessels might behave in 3D, we can look at imaging of larger blood vessels. Börnert, (*Börnert1995*) present a 3D image of coronary arteries shown in Figure (6.2) using magnetic resonance imaging.

In the 3D reconstruction, the shape of the arteries seems to fluctuate along the flow path but we assume that the area for flow stays nearly constant to prevent any high flow resistance areas, which would cause stress on the heart. Based on the images in Figure 6.1 and using fish such as the tuna and opah as inspiration, a double corrugated tube geometry for enhanced heat transfer rate was suggested. The considered flow cross-section is elliptical and constantly changes aspect along the flow path while maintaining a constant hydraulic diameter in order to continuously break up the thermal boundary layer that attempts to form in the fluid flow. A similar concept was suggested by Jantsch, (*Jantsch1953*) where a tube was deformed to change the cross sectional shape while maintaining a constant flow area. Jantsch, (*Jantsch1953*) claimed that the geometry gave "an effective kneading of the fluid in the column" that improved contact between the tube wall and fluid.

With growing energy consumptions, the appeal for more efficient techniques to harvest or use the available energy is increasing instantly. Food industry, aerospace, paint production, naval, chemical engineering, and paper manufacturing are only few examples where enhanced heat transfer is on high request (*Rainieri1997, Meng2005, Fan2009, Webb1994, Dong2001, Pethkool2001*). In most applications, laminar flow or viscous fluids are required and that reduces the thermal efficiency of such processes or apparatuses.

EXPERIMENTAL SET-UP

In this experimental study, double corrugated tubes and an equivalent straight tube manufactured using selective laser melting (SLM) technique were investigated in a counter-flow tube-in-shell heat exchanger setup. The concept of the double corrugation is similar to Alternating Elliptical Axis (AEA) tubes. However, the transition in a cross-section is smoother for double corrugated tubes, which would lead to a lower pressure drop. The double corrugated tubes have an elliptical cross section and the D_h is held constant at any point in a flow channel. The walls of double corrugated tubes periodically impinge the fluid flow preventing development of thermal boundary layers and promoting the heat transfer enhancement. The experimental study is carried out at flow with low *Re* using city water, supplied form a district system. The obtained thermal performance results are presented in a form of *Nu* correlations. The pressure drop in the investigated tubes is measured for isothermal flow conditions. The global thermos-hydraulic performance of double corrugated tubes is evaluated at the same pumping power.

The double corrugated tubes and an equivalent straight tube were manufactured using selective laser melting technique in AlSi10Mg powders with a relative density of the alloy after SLM equals to 99.5%, while the thermal properties were described by Mertens (*Mertens2015*). The double corrugated tubes here investigated, are characterized by an elliptical cross section that changes aspect ratio (ξ) in the cross-sectional plane while keeping a constant hydraulic diameter (D_h) along the tube axis. The geometry of the investigated tubes is defined by Equation (6.1):

$$\begin{cases} x = \xi\left(sin\left(\frac{2\pi}{p}z\right)\right) + \frac{R}{2} \\ y = \frac{R}{2}\xi\left(-sin\left(\frac{2\pi}{p}z\right)\right) + \frac{R}{2} \end{cases} \tag{6.1}$$

where x and y are the Cartesian coordinates that define the cross-sectional plane of the tube, while z corresponds to the tube's axis coordinate, R is the radius of an equivalent straight tube, p is a corrugation pitch.

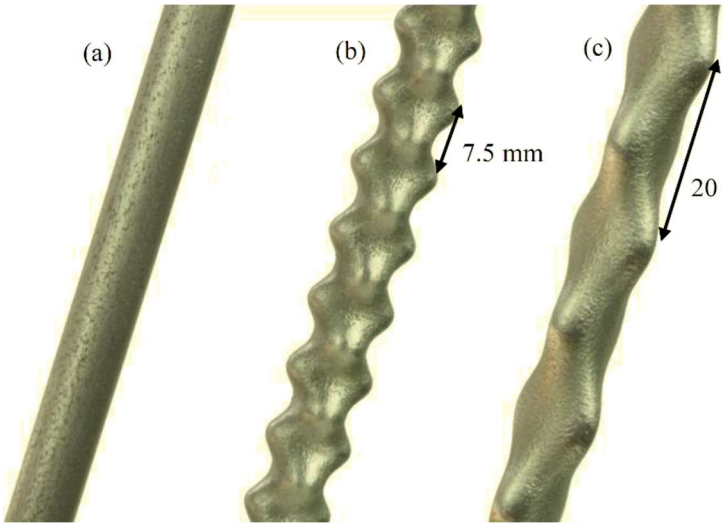

Figure 6.3: 3D printed tubes with the D_h constant (a) the straight reference tube, (b) double corrugated tube with ξ = 2.0 and p = 7.5 mm, (c) double corrugated tube with ξ= 2.2 and p = 20.0 mm.

Therefore, the cross section of the tube at any point in the flow direction is defined as an ellipse with one axis equal to x and the other equal to y, that periodically become equal, forcing the cross-section to be a circle. Parametric equation tool and Lofted Boss/Base feature build in *Solidworks*® environment, was used to approximate the Equation (6.1) with a maximum inaccuracy of ± 3.6 % on the hydraulic diameter D_h. It is noticeable, that inaccuracy decreases with decreasing ξ or increasing p.

The geometrical data and the inaccuracy in D_h of the tested tubes are given in Table (6.1) where $A_{s,i}$ and $A_{s,o}$ are the internal and external heat transfer surface are while δ is the wall thickness of the tubes, respectively.

Table 6.1: Geometrical characteristics of the investigated wavy tubes

Tube name	ξ *(adm)*	p (mm)	l (mm)	$A_{s,i}$ (mm²)	$A_{s,o}$ (mm²)	D_h (mm)	δ (mm)	E_{D_h} (%)
ξ1.6 p7.5	1.6	7.5	250	4195.4	5873.3	5	1	±0.4
ξ2.0 p7.5	2.0	7.5	250	4525.2	6349.8	5	1	±2.8
ξ1.6 p20	1.6	20.0	250	4087.5	5526.9	5	1	±1.8
ξ2.0 p20	2.0	20.0	250	4280.2	5893.9	5	1	±2.9
ξ2.2 p20	2.2	20.0	250	4396.8	6028.2	5	1	±3.6
Straight	-	-	250	3925.0	5495.0	5	1	-

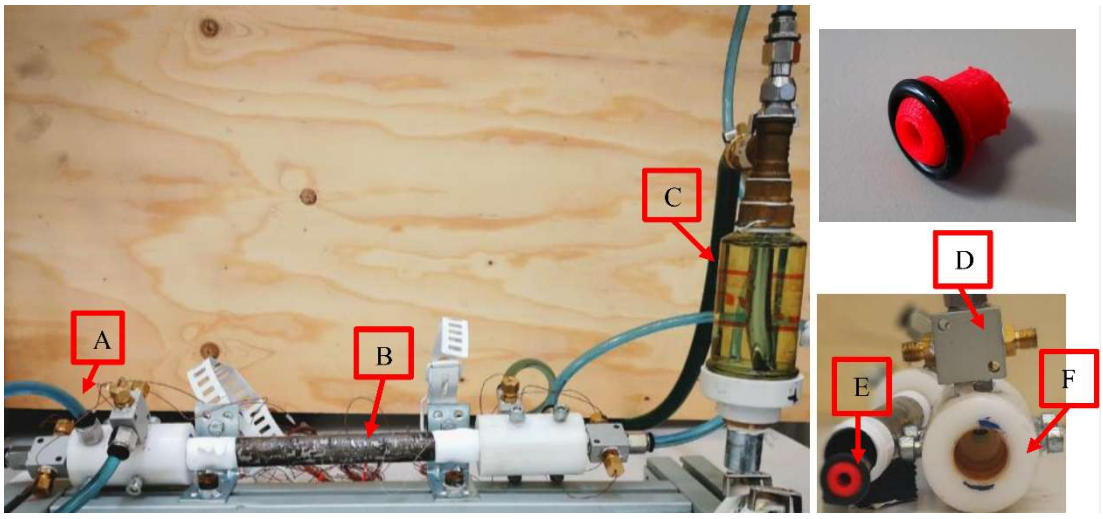

(a)

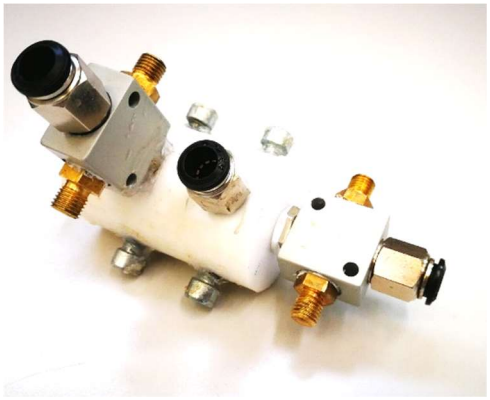

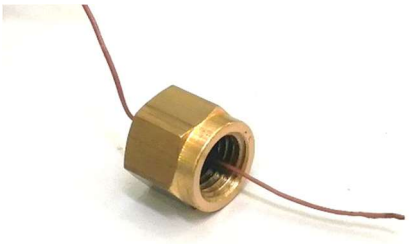

(b) **(c)**

Figure 6.4: (a) Experimental test rig: [A] Pressure drop connector, [B] Shell, [C] air separator, [D] thermocouples holder with water passage, [E] 3D printed connector and [F] turned nylon connector, (b) Head of the shell heat exchanger [F] and (c) installation scheme of the calibrated thermocouple

The double corrugated tube geometry varies in ξ and p. The manufacturing process of the tubes may result in higher inner surface roughness of the tubes. Therefore, surface roughness analysis was carried out using a LEXT OLS4100 3D Measuring Laser Microscope made by Olympus Corporation. A sample for the surface roughness analysis was cut along the flow direction of the straight tube. The surface root square mean roughness, S_q, of a rectangular area 0.62 × 6.56 mm was directly measured according the standard ISO 4287 and found to be 0.013 mm with the maximum difference between the highest and the lowest measured points of 145.6 ± 13 μm.

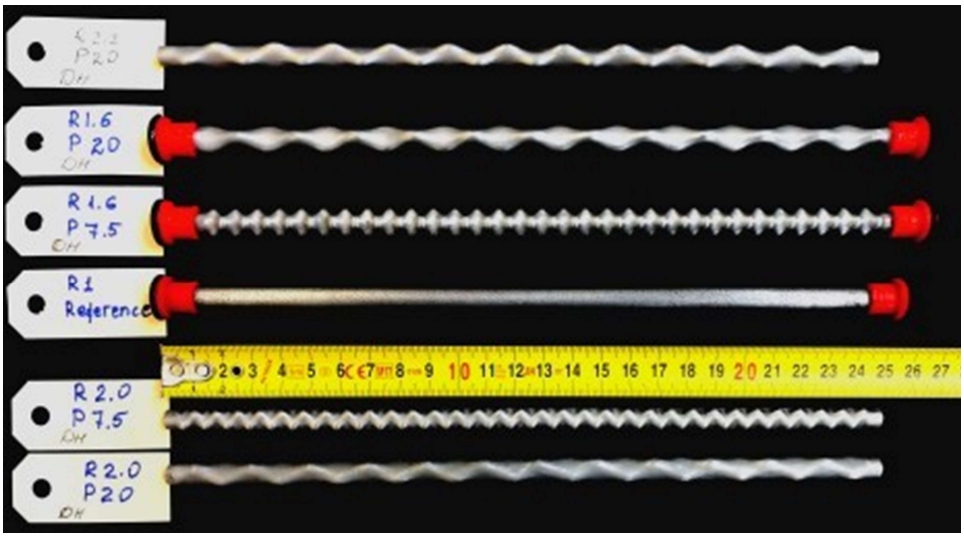

(a)

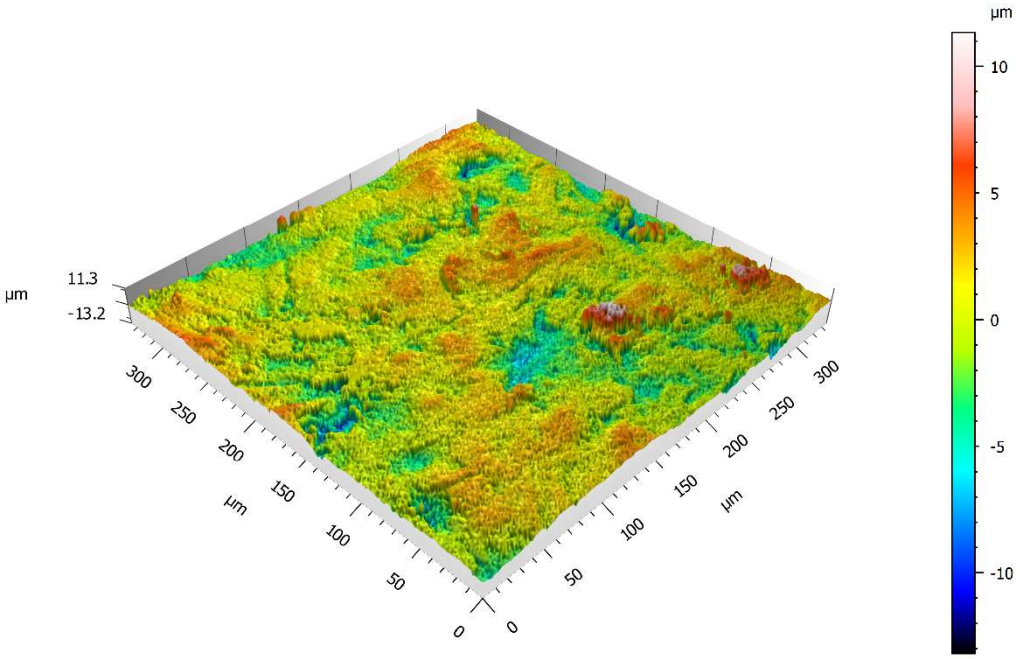

(b)

Figure 6.5: (a) Comparison of all the3D printed tested tubes and (b) measured internal surface roughness

As it is possible to see in Figure (6.5-b) the surface roughness of the 3D printed tube is comparable to the once produced by the standard manufacturing tools, therefore the heat transfer enhancement due to the modification of the solid-fluid interface is negligible if compared to the effect induced by the here adopted wall corrugation profile.

The geometry of double corrugated tubes, shown in Figure (6.3) for three representative test cases, constantly impinges the fluid flow and prevents the development of boundary layers.

The double corrugated tubes were experimentally investigated in a tube-in-tube counter flow heat exchanger shown in Figure (6.4). As it is possible to see, the air contented in the hot water going inside the shell was separated by the air-separator [C].

In order to make a robust temperature measurement, two calibrated T-type thermocouples [D] were used on each of the four sides of the heat exchanger and the average value of each pair were used during the inverse estimation. In order to prevent leakages form the shell to the tube side and vice-versa a 3D printed connector [E] were sealed on the tube, while O-rings were used to prevent leakages between the connector [E] and the shell closer [F].

On this particular customized part [F], were also drilled holes for the pressure drop measurement [A] as well as for the temperature measurements of both the shell and tube side as is possible to see in Figure (6.5). The component [F] were also used in order to seal the shell [B] from the environment.

A schematic representation of the test facility is shown in Figure (6.7).

The water to the test rig was supplied from a district water supply system; in particular, the water flow was separated into two streams by a manifold with giving the possibility to regulate both flows using valves [1].

A cold-water stream was directly connected to the inlet shell side, on which stream two valves [1] were fitted in order to regulate the flow rate, while the outlet went to the drain. The mass flow rate measurement was made by weighting the mass of water contained in a flax coming out from the outlet of the shell in a time period t measured with a chronometer.

The second stream separated from the district water system was connected through a thermal reservoir with a copper coil heat exchanger.

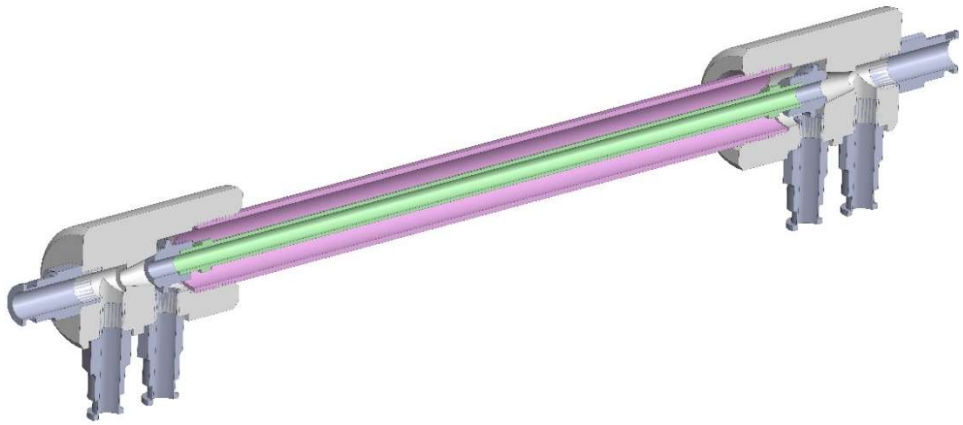

Figure 6.6: 3D CAD model of the here developed shell and tube heat exchanger

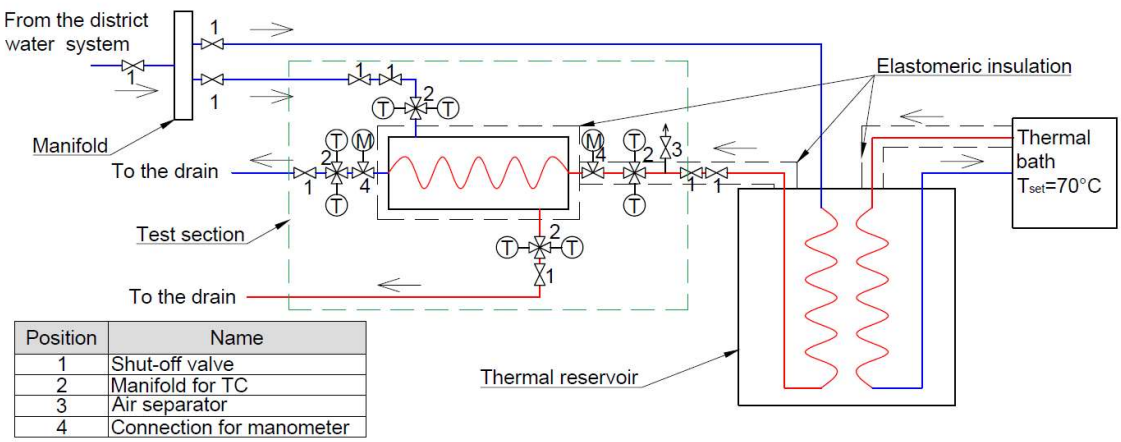

Position	Name
1	Shut-off valve
2	Manifold for TC
3	Air separator
4	Connection for manometer

Figure 6.7: Schematic of the experimental setup

The reservoir was installed in order to increase the thermal inertia of the system compensating the oscillation of the inlet water temperature. The thermal reservoir was maintained at a fixed temperature using a thermal bath with the set point $T_{est} = 70°C$. The heated water flow was regulated using two valves [1] at the inlet of the tube and one valve [1] at the outlet of the tube. The hot water, was then pushed to the air separator [3] before going into the tube under test. This flow regulation technique ensured the air-bubble-free water flow with no temperature stratification at low flow rates.

ESTIMATION PROCEDURE

As already mention in *Chapter 3* the main goal of this kind of heat transfer characterisation is the estimation of the coefficients comparing in the Equation (3.9.1-3.9.2). In order to estimate their values, the IRLS algorithm presented in *Chapter 3* was used, following the methodology presented in *Chapter 4*.

In particular, the inverse problem procedure, requires the estimation of the unknown coefficient α and β related to both the tube and shell side, the correlate the Nusselt to the Reynold number as follows (*Incropera2005, Rainieri2004*):

$$Nu = \alpha \, Re^{\beta} Pr^{0.33} \tag{6.2}$$

The approach is based on the minimisation of the objective function defined as:

$$r = \left\| U_{exp} - U_{pred} \right\|_2 \tag{6.3}$$

where U_{exp} and U_{pred} are respectively the experimental and the simulated global heat transfer coefficient.

For any double flow heat exchanger in a steady state condition, perfectly thermally insulated from the environment in which is negligible the heat conduction in the flow direction, it is possible to determine the average overall heat transfer coefficient U for the inner heat transfer surface area A_i as follows:

$$U = \frac{Q}{A_i \Delta T_{ml}} \tag{6.4}$$

where ΔT_{ml} is the logarithmic mean temperature difference while Q is the exchanged heat flow rate, that could be determined by:

$$Q = \dot{m}^t c_p^t (T_{in}^t - T_{out}^t) = \dot{m}^s c_p^s (T_{in}^s - T_{out}^s) \tag{6.5}$$

where $\dot{m}$ and c_p are the mass flow rate and the specific heat capacity, respectively, while $\cdot^t$ and $\cdot^s$ stay for the tube and the shell side, respectively

Due to the electrical analogy, it is possible to define the overall heat transfer coefficient as a summation of resistance as follows:

$$\frac{1}{UA_i} = \frac{1}{h_i A_i} + R_w + \frac{1}{h_o A_o} \tag{6.6}$$

where h_i and h_o are the internal and external convective heat transfer coefficient respectively, while A_i and A_o are the internal and the external heat exchanger surface areas, respectively.

Due to the quasi-cylindrical configuration characteristic of a tube side heat exchanger, the thermal resistance of the wall R_w could be approximated as:

$$R_w = \frac{\ln\left(\frac{D_o}{D_i}\right)}{2\pi k_w L} \tag{6.7}$$

where D_0 and D_i are the external and internal hydraulic diameter of the tube, respectively, while k_w and L are the thermal conductivity and the length of the tube that is exchanging

heat, respectively. Thus it is possible to assume known the thermal resistance of the wall, for a given heat exchanger configuration, under a given operating condition.
Assuming the internal diameter of the tube, as the characteristic length, it is possible to define the internal Nusselt number coefficient as:

$$Nu_i = \frac{h_i D_i}{k} \tag{6.8}$$

where K is the thermal conductivity of the fluid that is passing inside the tube.
The convective heat transfer coefficients h_o and h_i appearing in the Equation (6.6) are unknown, moreover, its value is difficult to be determined also because it changes for each application. Therefore, they can be estimated, whit a suitable accuracy, by adopting a parameter estimation technique under an inverse problem data processing methodology (*Beck1977*). This implies that the following cost function has to be minimised:

$$r_{(\alpha^t,\beta^t,\alpha^s,\beta^s)} = \sum_{j=1}^{M} \left(U_{exp,j} - U_{pred,j}\right)^2_2 \tag{6.9}$$

where M is the total number of measurements made for a given Reynolds number in the shell side Re^s, varying the Reynolds number Re^t.
It is possible to write the Equation (6.6), highlighting the effect of the unknown parameters:

$$U_{pred} = A_i \left(\frac{D_i}{A_i \lambda^t \alpha^t (Re^t)^{\beta^t} (Pr^t)^{0.33}} + R_w + \frac{D_i}{A_o \lambda^s \alpha^s (Re^s)^{\beta^s} (Pr^s)^{0.33}} \right)^{-1} \tag{6.10}$$

The optimization algorithm will find the best set of unknown parameters that it is able to minimise the cost function defined by the Equation (6.9) giving also their confidence intervals.

RESULTS

The obtained experimental results are presented in terms of both absolute and relative Nusselt number in order to understand quantitatively the heat transfer enhancement and its increment with respect to the straight tube. Moreover, in order to enable a straight forward comparison of the double corrugated tubes when designing heat exchangers with other heat transfer enhancement devices, the presented Nu correlations are obtained using all the geometrical data (such as surface heat transfer area A_s, the cross-section area A_c and hydraulic diameter D_h) of the equivalent straight pipe. Using this approach, the benefits of the enhanced surface area are already included into the comparison. Moreover, Bergles (*Bergles1974*) pointed out that it is more convenient to use nominal geometry for identifying heat transfer augmentation especially if the enhanced tube is used as a direct replacement of an existing straight tube.

The experimental heat transfer results for the straight tube were compared to the correlation developed by Hausen and Sieder both valid for thermal entry region (*Incoprera2002*) in the laminar flow regime but for different thermal boundary condition; in particular, the correlation presented by Hausen is valid for constant surface temperature boundary condition, while the correlation developed by Sieder is valid for constant imposed heat flux boundary condition. Figure (6.8) shows that the obtained results agrees very good with the Hausen correlation within a confidence of 85 % and 95 % with Sieder correlation. These results indicates that the experimental set-up together with the data analysis methodology is reliable.

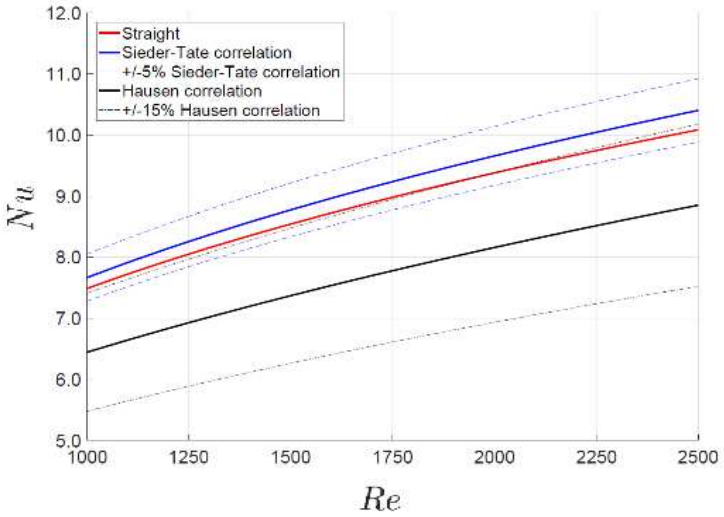

Figure 6.8: Straight pipe: Comparison between the experimental results and the correlations provided by Hausen and Sider (*Incoprera2002)*

The accuracy associated with the estimated values was assigned by the parametric bootstrap method (*Efron1982, Blackwell2010*). In this procedure the term U_{exp} has been substituted by the distribution:

$$U_{exp} = U_{calc} \cdot (1 + \epsilon) \tag{6.11}$$

where U_{calc} was obtained from Equation (6.11) adopting the heat transfer coefficients found by Equation (4.1) while ϵ represents a uniformly distributed random noise with zero mean and variance σ which is assumed to be equal to the uncertainty related to the measured quantity $\Delta T^T = T_{in}^T - T_{out}^T$. In order to find the U_{calc} value, α and β coefficients obtained from the estimation procedure using the experimental measurements, were used.

Considering the overall heat transfer coefficient U_{exp} re-sampled from its probability distribution, as starting value, the unknowns are re-estimated using the same methodology discussed in *Chapter 4*. The re-estimation procedure was repeated many times for different sets of noise sequences, and the results are processed using the standard statistical techniques for evaluating 95% confidence intervals.

The experimental results presented in Figure (6.9) show that the higher Nu values are obtained for double corrugated tubes with shorter corrugation pitch. Moreover, it is possible to see that the thermal performance of the double corrugated tubes strongly depends on the corrugation pitch, while the aspect ratio represents an effect of the second order.

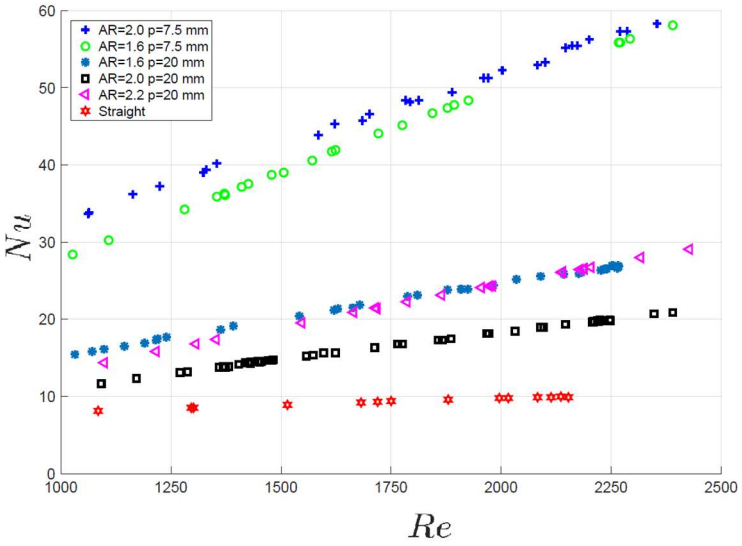

Figure 6.9: Experimental observation at the tube side: Nusselt number distribution as a function of Reynolds number

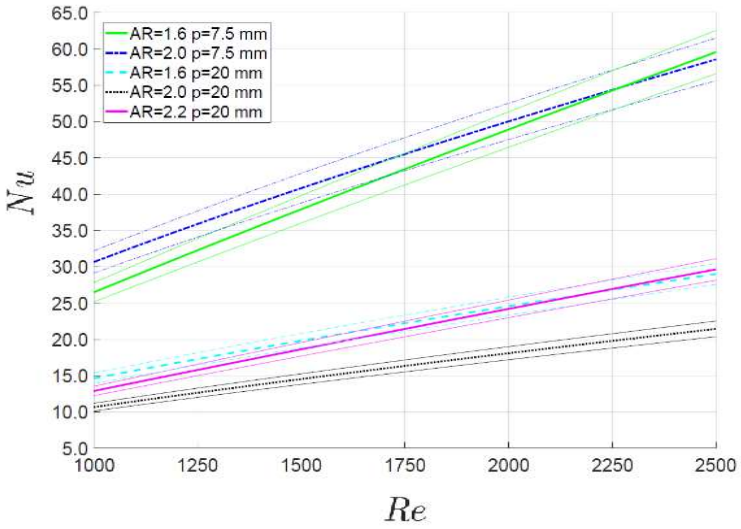

Figure 6.10: Proposed correlation with 95% Confidence Interval at the tube side: Nusselt number distribution as a function of Reynolds number

As it is possible to see, the double corrugated tubes with $p = 7.5mm$ show up to 35 % higher Nu than double corrugated tubes characterized by $p = 20mm$.

It has to be highlighted that the double corrugated tube with $\xi = 1.6$ and $p = 7.5mm$ outperforms the tubes characterized by $\xi = 2.0$ and $p = 7.5mm$ once Re is higher than 2200, approximatively. This suggest that more intense corrugations are more thermally efficient at lower Re than the lower intense corrugation profile.

In order to compare the obtained result, with the once available in literature, the unified correlation derived by Meng (*Meng2005*) for the alternating elliptical axis tubes, valid in the Reynolds number range $500 < Re < 10^4$ was experimentally observed to be:

$$Nu = 0.0615\, Re^{0.76} Pr^{0.33} \left(\frac{Pr_f}{Pr_w}\right)^{0.11} \tag{6.12}$$

where Pr_f and Pr_w are the Prandtl number calculated at the fluid bulk temperature and wall temperature respectively.

The heat transfer enhancement was also compared to one of the common insert devices usually employed as a heat transfer enhancement promoter (*Sivashanmugam2006*) in the Reynolds number range $200 < Re < 3000$:

$$Nu = 0.017\, Re^{0.996} Pr\, \frac{p}{D_{int}} \tag{6.13}$$

where p and D_{int} are the helix pitch and diameter, respectively.

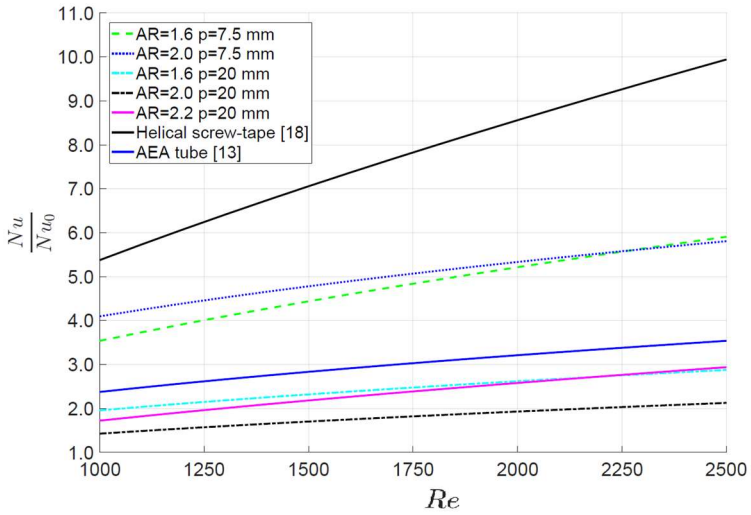

Figure 6.11: Tube side: thermal efficiency

The same consideration could not be extended to the set of tubes characterized by a corrugation pitch of $20mm$ for which the higher thermal performance was obtained for tubes with lower aspect ratios. This phenomena could probably be related to the formation of stagnation point in the valley of the tubes with high aspect ratio that limits the heat transfer capabilities of this kind of geometry. In order to validate this theory, a new experiment has to be performed with higher values of Reynolds number, condition that should ensure the disruption of the stagnation point in tubes with high aspect ratio. Figure (6.11) shows that the double corrugated tubes are up to 500 % (when $p = 7.5mm$) and up to 200 % (when $p = 20mm$) more efficient than an equivalent straight tube. Moreover, it is possible to see that, for the here investigated Reynold number range, the thermal efficiency of the tubes characterized by a pitch of $7.5mm$ is almost twice of the corrugated tubes with $p = 20mm$.

Table 6.2: Correlation coefficients and Nusselt number uncertainties for the tube side

Tube name	α *(adm)*	β *(adm)*	ϵNu
ξ1.6 p7.5	0.039	0.88	±8.0%
ξ2.0 p7.5	0.16	0.77	±8.5%
ξ1.6 p20	0.056	0.75	±9.0%
ξ2.0 p20	0.037	0.76	±11.0%
ξ2.2 p20	0.016	0.91	±9.0%
Straight	0.52	0.33	±14.0%

The experimentally obtained data of thermal performance for the investigated tubes was correlated as given in Equation (4.1) for the tube side, and the obtained correlation coefficients are given in Table (6.2) together with their uncertainties.

The agreement between the experimental data and correlation was checked in terms of overall heat transfer coefficient U. Figure (6.12) shows the comparison between experimental and correlated U values for the double corrugated tube with $\xi = 2.0$ and $p = 7.5mm$ versus Re inside the tube (a) and inside the shell (b).

It is possible to conclude that the methodology presented in *Chapter 4* and validated in *Chapter 5* using synthetic data measurements, was able to estimate the thermal performance of the double corrugated tubes here presented.

The experimental validation of the methodology was performed by testing a straight smooth pipe and compering, with a good agreement between them, the estimated correlation with the equation provided by Hausen and Sider (*Incoprera2002*).

The same estimation procedure, was also applied to the double corrugated tubes showing a high increment of the thermal performances of this new type of passive heat transfer enhancement technique respect to the straight pipe. In particular, the thermal performance of the double corrugated tubes is up to 500 % higher in terms of Nu/Nu_0 for the Reynolds number range here investigated.

An interesting phenomena, probably related to the formation of a stagnation point in the valley of the corrugation, was observed. In particular, higher thermal performances were observed for the smallest aspect ratio of corrugation for the tubes family characterized by the biggest pitch of corrugation; phenomena that is in contrast with what was observed for the family of tubes characterized by the smallest pitch of corrugation in which the stagnation zone is smaller. In order to confirm what it is here supposed to happen, other experiments have to be done extending the Reynolds number range to higher and lower values from the ones here presented.

It is also noticeable that, the corrugation period has higher influence in the thermal performance of double corrugated tubes than its aspect ratio.

It has to be mentioned that the maximum enhancement of the surface area in the investigated double corrugated tube was less than 16%, thus it is of lower importance respect to the thermal enhancement (due to the particular flow motion) that is going to be presented.

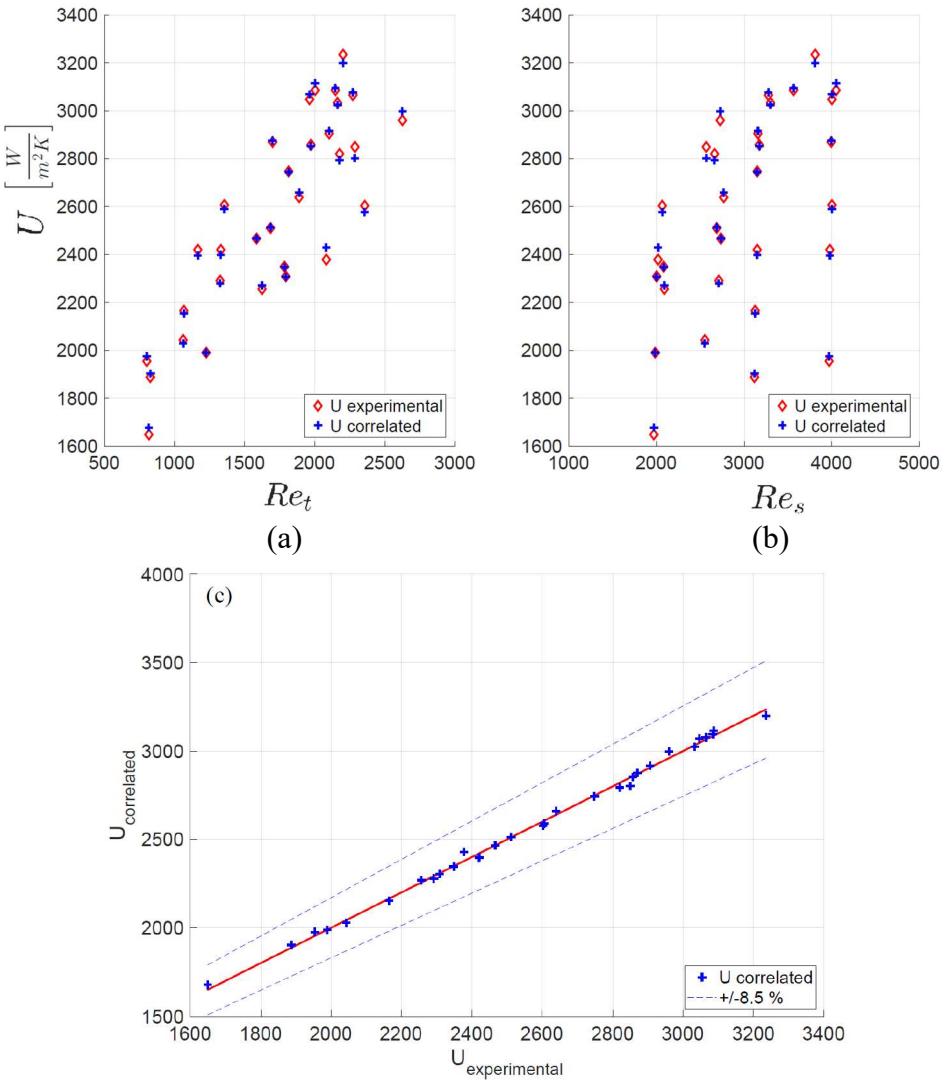

Figure 6.12: Global heat transfer coefficient U for the double corrugated tube with ξ= 2.0 p = 7.5 mm measured experimentally (red '◊') and calculated using the obtained correlations (blue '+') as a function of Re in the tube side (a) in the shell side (b) and correlation graph (c)

Due to the experimental evidence of the good performance of this new type of wall corrugated tubes, it is possible to conclude that they could be used to revamping the existing heat exchanger increasing their thermal efficient as well as to build new compact heat exchanger smaller and cheaper than the one already available on the market.

6.2 Inverse estimation of the local convective heat transfer coefficient in coiled tubes

INTRODUCTION

The 1D inverse problem here addressed, is stated in *Chapter 3* as a function estimation procedure, since the number of unknown variables is bigger than in the previous case. The defined problem, is here specifically applied for the estimation of the local convective heat transfer coefficient in coiled tubes and the estimated results, provided from the new methodologies formulated in *Chapter 4*, are compared with the estimated results coming from some of the common techniques presented in *Chapter 3*.

Coiled tubes have found a lot of applications in industry since they represent a very powerful solution to passive enhance the heat transfer rate. In particular, the curvature of the tubes makes the fluid flowing inside the pipe experiencing the centrifugal force. This force gives rise to secondary flows caused by the particles of the fluid that move with different axial velocity and have the ability to increase the heat exchange. The characteristics of the single-phase heat transfer in tubes was extensively studied by researchers both experimentally and theoretically. As reported by Berger (*Berger1983*) coiled tubes have been investigated since the last years of the nineteenth century and first years of the twentieth (*Thomson1876*; *Grindley1908*). An important observation was firstly made by Williams (*Williams1902*) about the velocity distribution inside curved pipes: they stated that the location of the maximum axial velocity is shifted toward the outer wall of the tube.

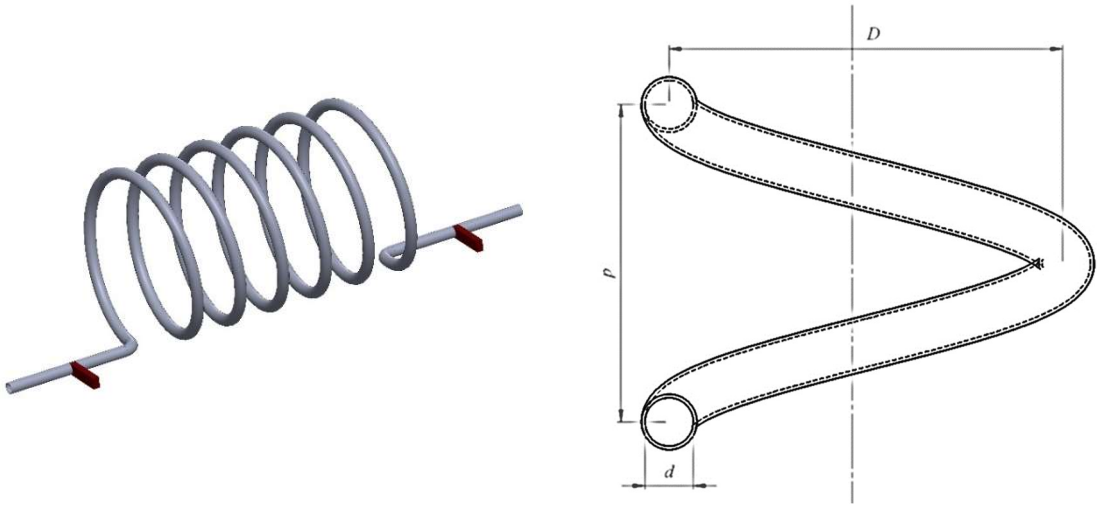

(a) (b)

Figure 6.13: Coiled tube: (a) 3D model and (b) geometrical dimension definition

In 1910 Eustice (*Eustice1910*) demonstrated the presence of a secondary flow by injecting coloured ink inside a water flux in a pipe.

A fundamental step forward in the study of curved tubes is represented by the studies performed by Dean (*Dean1927, Dean1928*). The author analysed the fluid motion inside a toroidal pipe and mathematically described the phenomenon by considering the toroidal geometry. Moreover the author observed that the characteristic length of this kind of heat exchanger is represented by the ratio between the internal radius of the pipe and the radius of curvature of the coil. In particular it is possible to define a new dimensionless parameter called Dean number:

$$De = Re\sqrt{d/D} \tag{6.14}$$

where d and D are the diameter of the pipe and the diameter of the toroid, respectively.

Due to the presence of the centrifugal force that displaces the slower moving fluid close to the wall inward and the fast-moving fluid close to the wall outward, in the stream flow a pair of counter rotating vortices, placed symmetrically with respect to the plane of symmetry appear as shown in Figure (6.14). It is straightforward that as far as the Dean number increases, the centrifugal force increases leading to an increment of the circumferential velocity. It follows that the fluid is pushed toward the outer bend of the coil reducing the boundary layer nearby the wall, while in the inner bend of the coil the boundary layer becomes thicker.

Among all the researcher that investigated this particular passive heat transfer enhancement technique, Berger and McConalogue (*Berger1983, McConalogue1968*) analysed the fluid

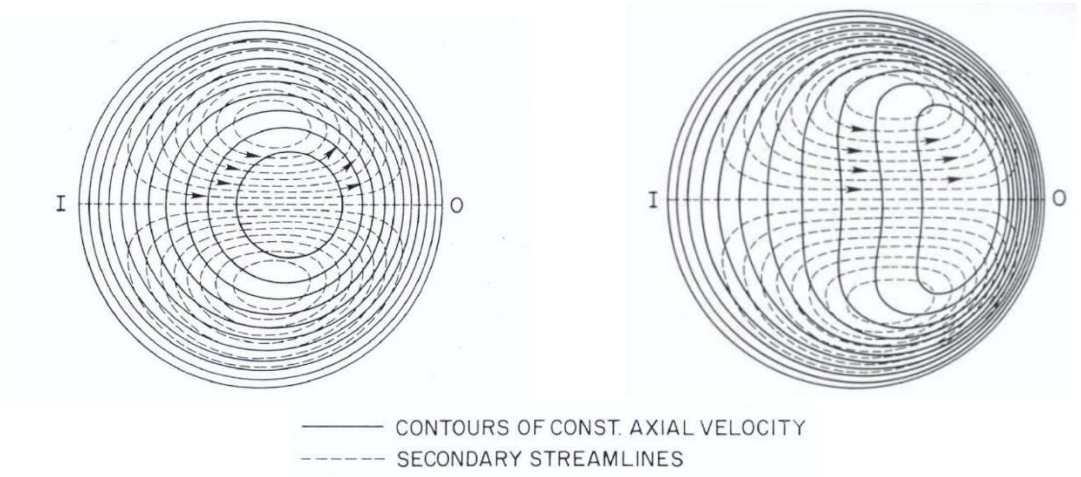

Figure 6.14: Secondary streamlines and axial-velocity contours at low Dean number (I=inner bend, O=outer bend) (*Berger1983, McConalogue1968*)

motion in a curved pipe for a wide Reynolds number range detecting the outward movement of the location of the maximum velocity as it is shown in Figure (6.14).

The analytical formulation of the problem becomes more difficult with the introduction of helically coiled tubes. Two new parameters that characterized the flow are present (*Liu1993*): the torsion τ (6.4) and a modified curvature ratio δ_m (Equation (6.16)):

$$\tau = \frac{\frac{p}{2\pi}}{\left(\frac{D}{2}\right)^2 + \left(\frac{p}{2\pi}\right)^2} \tag{6.15}$$

$$\delta_m = \frac{\frac{D}{2}}{\left(\frac{D}{2}\right)^2 + \left(\frac{p}{2\pi}\right)^2} \tag{6.16}$$

Performing the loose-coiling analysis it is possible to find another dimensionless group that contributes to describe the fluid motion in a coiled pipe, the Germano number:

$$Gn = Re\,\tau = Re\frac{\frac{p}{2\pi}}{\left(\frac{D}{2}\right)^2 + \left(\frac{p}{2\pi}\right)^2} \tag{6.17}$$

The Germano number measures the ratio between the twisting forces and the viscous forces also by taking in account the torsion effect. Truesdell (*Truesdell1970)* suggested the possibility to apply the toroidal model to coiled tube by simply substituting the curvature radius of the toroidal pipe with the helical one. The minor importance of the pitch compared to the torsion, in terms of Nusselt number, were also observed by Murata (*Murata1981*). In particular, the authors confirmed the possibility to use the correlation proposed for the toroidal tube by substituting curvature radius of the toroidal pipe with the helical one; on the other hand their results showed important differences in the local distribution, in particular in the secondary flow pattern.

The effect of the torsion on the laminar convective heat transfer in helically coiled tube was also studied by Yang (*Yang1995*): The results showed that the heat transfer behaviour in a helicoidal pipe is significantly affected by three factors: Dean number, torsion and Prandtl number. The authors, also confirmed that the secondary flow intensity is stronger with the increasing of the Dean number, which effect generates higher temperature gradient close to

the outer wall of the coil. Finally, the authors investigated the effect of the torsion, showing that it significatively affect the temperature field; dependencies that was visible also in terms of the Nusselt number. In particular, Nu decreases ad far as τ increases, while on the other hand it increases as far as De and Pr increase.

A side effect of the wall curvature concern the stabilization of the fluid motion. White (*White1929*) showed that the flow could be maintained laminar for substantially higher Reynolds numbers than it is possible in straight pipes. Sreenivasan (*Sreenivasan1983*) observed that when a flow through a straight tube is passed through a coiled pipe a stabilizing effects appear: in a determinate Reynolds number range the turbulent flow in straight pipes becomes laminar in coiled section and the stabilization effect persisted to a certain degree even after the flow downstream of the coil has been allowed to develop in a long straight section. Moreover, as numerically observed by Di Piazza (*DiPiazza2011*) for the toroidal tubes, the departure from the laminar flow regime is characterized by a complex behaviour: a first transition to a periodic flow followed by a second transition to a quasi periodic flow and then by a transition to a chaotic flow is required before reach the fully turbulent fluid flow regime.

A wide review on helically coiled tubes and other curved pipes was realized by Naphon (*Naphon2006*).

In order to better understand the mechanisms that govern the heat transfer in coiled pipes, the convective heat transfer coefficient distribution along the cross section circumference represents a primary information. The asymmetrical distribution of the velocity field over the cross-section of the tube, that locally increases the temperature gradient at the wall maximising the heat transfer, leads to a significant variation in the convective heat-transfer

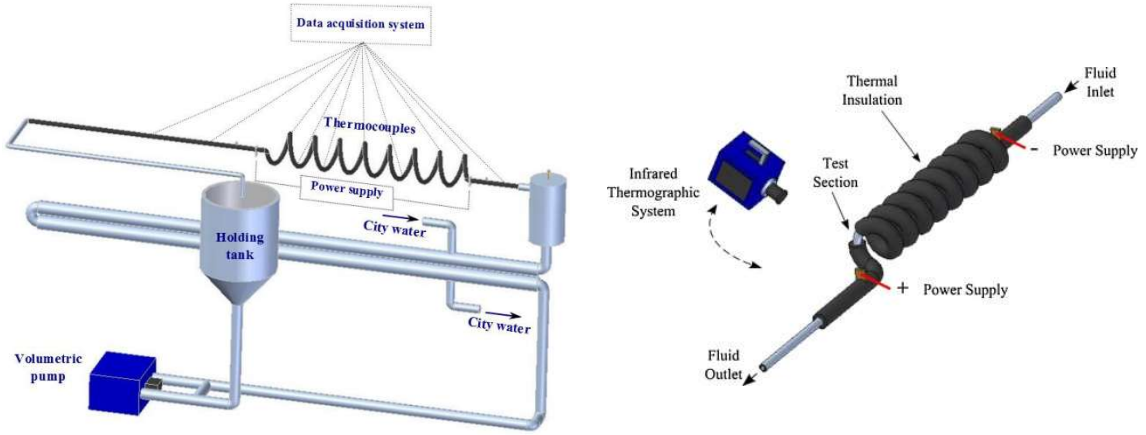

(a) (b)

Figure 6.15: (a) Experimental test rig scheme and (b) experimental data acquisition scheme

coefficient along the circumferential angular coordinate presenting higher values at the outer bend side compared to the inner bend side (*Bai1999*; *Jayakumar2010*).

The irregular temperature distribution may be critical in some industrial applications, such as in those that involve a thermal process. For example, in food industry, the pasteurisation process has to be uniform possibly avoiding local burning (which could damage the food taste) as well as local under-heating (which reduce the bacteria heat-killing).

Although many authors have investigated the forced convective heat transfer in coiled tubes, most of them have presented the average performances while only a few number authors have studied the local phenomenon and most of them have adopted the numerical approach. For this reason, the solution of the ICHP, starting from the temperature distribution acquired on the external wall surface, could give an experimental evidence to the numerical observed non-uniform heat flux distribution at the fluid-solid interface.

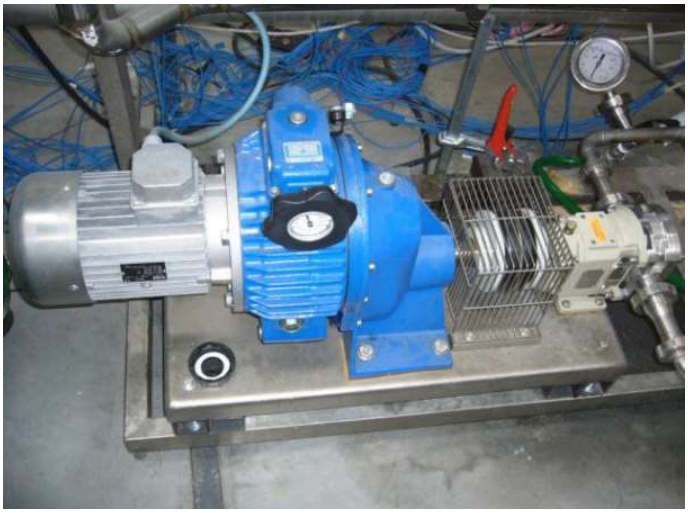

(a)

(b)

Figure 6.16: Experimental apparatus: (a) mechanical reducer and volumetric pump and (b) recirculation circuit

EXPERIMENTAL SET-UP

In order to dealing with this type of problem, the test facility shown in Figure (6.15) was used. The experimental apparatus, essentially composed by an hydraulic circuit coupled with an acquisition data system, was made available by the laboratory of the Industrial Engineering Department of the University of Parma. In this test rig (Figure (6.15-a)) the fluid was heated and later cooled in order to keep the working fluid temperature constant at the inlet tube's section. In this way it was possible to work in a steady state regime, condition that was assumed during the development of the new methodologies shown in *Chapter 4*.

The heating was performed by Joule effect in the solid wall of the tube (Figure (6.15-b)), while the cooling was made by a secondary heat exchanger (Figure (6.17)-a), fed with city water. A holding tank of 30 litres of capacity, made of stainless steel, was used as a reservoir keping the fluid coming from the heated section. The working fluid contained in the tank is pushed by a volumetric pump into a counter flow shell and tube heat exchanger. This type of pump (Figure (6.16-b)), made by CSF (model A1 246300 JABSCO series), guarantees a high stability flowrate, that could be modify by tuning the rotational velocity of the pump using a mechanical reducer made by Motovario S.p.a (type TKR-10) that works between the range 40-200 rpm (Figure (6.16-a)). The maximum flowrate value is determined by the coupling pump-mechanical reducer and it varied between 60 and 200 l/h. The introduction of a recirculating circuit (see the top of Figure (6.16-b)), activated through a manually operated valve, permitted to reduce the flowrate to values lower than 60 l/h. Downstream the heat exchanger a holding section, equipped with a small vent valve on the top of the tank (Figure (6.17-b)) used in order to eliminate the air that accidentally entered the circuit, was installed in order to eliminate entrance effect.

After the holding tank, the fluid pass through the tube under test, which is fixed to the structure by a junction made by Teflon® material (Figure (6.17-b)). It has to be pointed out that the usage of a non-metallic junction is due to the necessity, for safety reason, to electrically insulate the rest of the circuit from the pipe (since it is heated by Joule effect inside the solid wall of the tube). The helical section of the tube is heated by the energy dissipation due to the Joule effect. In particular, the electric current is delivered by a power supply model HP 6671A that work in the range 0-8 V and 0-220 A.

Figure 6.17: (a) Counter current re-conditioning heat exchanger and (b) Electrical insulator

The power supply is connected to the tube by means of electric cables coupled with stainless steel fins of 1 mm thickness directly welded to the tube. It has to be highlighted that this characteristic heating system is necessary to approximate the imposed constant heat flux boundary condition at the fluid-solid interface, keeping the external wall of the tube accessible for the thermographic imaging process. Moreover, it has to be noted that the imposed constant heat flux boundary condition could be approximated only if the axial and peripheral heat conduction effects within the wall can be considered negligible, assumption that could be made since the thermal conductivity and the wall thickness of the tube are small.

The whole length of the heat transfer section was thermally insulated in order to minimize the heat transfer to the environment. The insulation was achieved by superimposing two layers of cellular rubber having a thickness of 9 mm and 32 mm respectively. Both the wall and the inlet and outlet fluid temperature were measured using calibrated T-type thermocouples connected to a multichannel ice-point reference, type KAYE K170-50C. The fluid temperature upstream the starting heating section, was measured by a thermocouple probe placed on the tube's wall. Due the absence of the axial conduction effect within the tube as well as of heating source, the fluid was assumed to be in thermal equilibrium with the tube, therefore the temperature read on the tube external surface is also representative of the bulk temperature of the fluid in the same section. The bulk temperature distribution was assumed to be a linear function of the curvilinear length of the tube; hypothesis that was checked by monitoring the outlet bulk temperature in the same fashion as previously described for the inlet bulk temperature of the fluid. The heat losses towards the environment were estimated in a preliminary calibration of the apparatus in order to estimate the overall thermal resistance between the internal tube wall and the environment: for the estimation,

the temperature difference between the environment and the heated pipe without have fluid flow inside, was measured. The value 6 m·K/W was found for the overall thermal resistance that yielded heat losses of about 1% of the supplied power. The signal coming from the ice point reference was read by high precision multimeter (type HP 3458A) connected to a switch control unit (type HP 3488A) driven by a Personal Computer, while the communication between all the devices, was based on commercial software Labview.

Since the aim of the present work is the local estimation of the circumferential convective heat flux distribution on a cross-section of the tube, a small portion of the external tube wall was made accessible to a thermal imaging camera by removing the thermally insulating layer. In order to precisely acquire the temperature distribution, using a FLIR SC7000 unit, with a 640 x 512 pixel detector array, the external wall surface of the tube were painted with an high emissivity paint. It has to be pointed out that the effective emissivity of the coating was estimated in situ by shooting a target at different known temperatures and the value 0.99 was found, while the thermal sensitivity of the thermographic camera, as reported by the instrument manufacturer, is 20 mK at 303 K, while its accuracy is ±1 K. In order to measure the temperature distribution on the whole test section surface, multiples images were acquired, moving the infrared camera around the section. In particular, the viewing angle was limited to less than ± 30° in order to reduce the distortion due to the perspective (Figure (6.18-d)). The acquired images, thanks to a position reference fixed on the tube wall (Figure (6.18-a)), were conveniently cropped, processed by perspective algorithms (*Cyganek2011*) and merged together in Matlab® environment to obtain continuous temperature functions on the tube wall versus the circumferential angular coordinate (Figure (6.18-c)); at the end of the image processing, the external temperature distribution of the tube, were discretized in 256 angular values over the whole circumferential section.

Like in the previous experiment, the volumetric flow rate was obtained by measuring, at the outlet of the test section, the time required to fill a flask whose mass was weighted by a high precision digital balance (*Tamagnini.srl*). Ethylene Glycol was used as working fluid in the Reynolds number range 70÷1300 which, due to the characteristic dimensions of the coiled tubes under test, corresponded to the Dean number range 12÷290. In the temperature range achieved during the experiments, the Prandtl number of the working fluid varied within the range 125÷280.

The tube under test consists in a stainless steel AISI-304 coiled tube with circular cross-section having an internal radius $r_{int} = 0.007m$ and an external radius $r_{int} = 0.008m$. The thermal conductivity of the pipe $k = 15W/mK$ is assumed constant as well as the

environmental temperature $T_{env} = 296.8K$ and the bulk temperature $T_b = 294.7K$ of the fluid that flows inside the tube. The exterior surface Γ_{ext} of the tube was subjected to an overall convective heat transfer coefficient $h_{env} = 5W/m^2K$ with the environment while the domain Ω, that is assumed to be homogeneous and isotropic, was subjected to an internal heat generation per unit of volume $q_g = 4.8 \cdot 10^6 W/m^3$.

As it is possible to see in Figure (6.18-a), since the temperature gradient along the axis of the tube is almost negligible, the test section can be efficiently modelled as a 2-D solid domain. To evaluate the local value of the convective heat transfer coefficient at the fluid internal wall interface on a given cross section (Figure (6.18-b) - Figure (3.2)), the temperature distribution was acquired on the external wall surface and then the IHCP within the wall domain was solved by considering unknown the convective heat flux distribution on the internal wall surface.

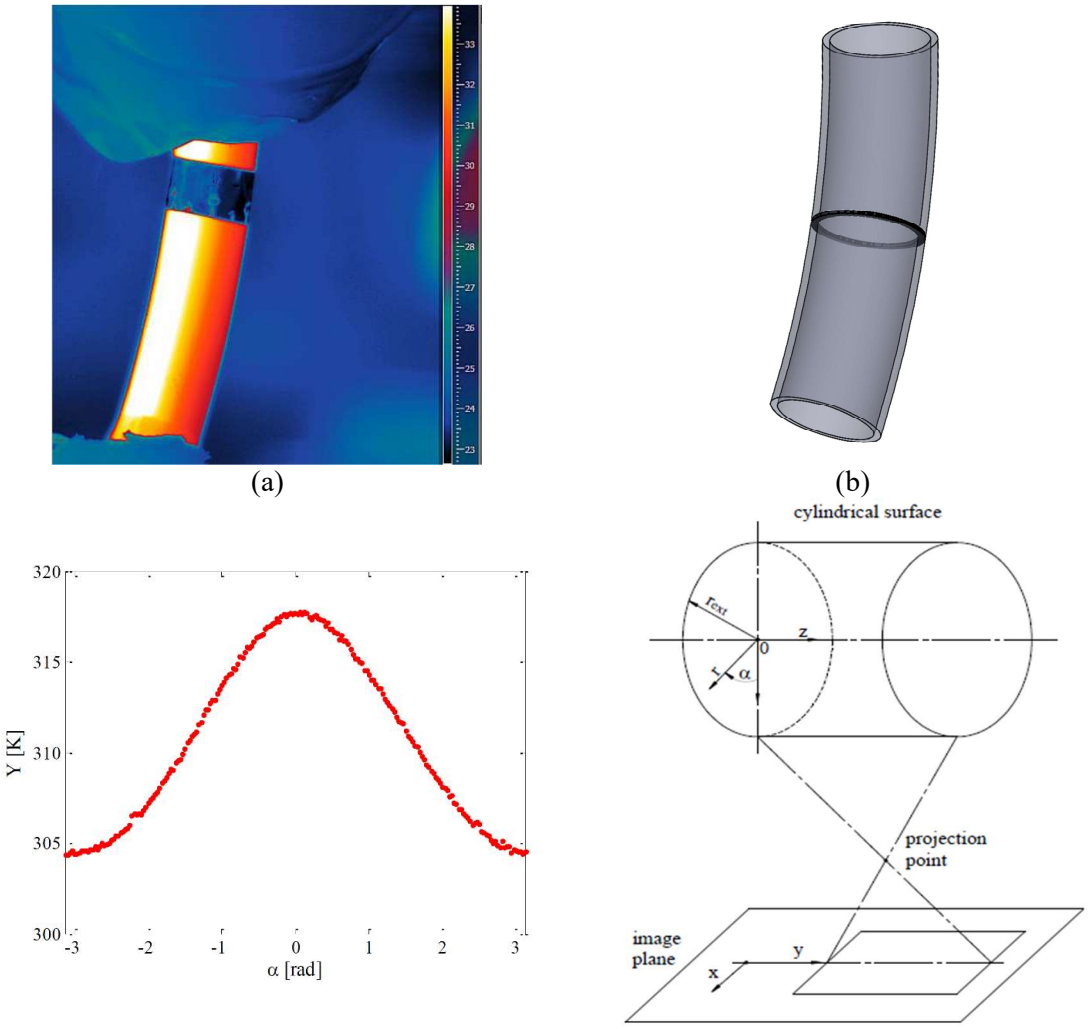

Figure 6.18: (a) Example of a thermographic image (b) 1D temperature acquisition zone (c) acquired temperature around the tube after the unwrapping and cropping procedures and (d) perspective correction and unwrapping scheme

ESTIMATION PROCEDURE

In the fully developed region, the physical system could be modelled as a 2D geometrical domain, in which the temperature and the internal convective heat flux coefficient distribution could be assumed to be a function of the angular coordinate θ. The direct problem presented in *Chapter 3* (Equations (3.22)) could be linearized by writing the internal boundary condition in terms of wall heat flux instead of the convective heat flux coefficient, as follows:

$$\nabla^2 T = -\frac{q_G}{k} \quad \text{in } \Omega \tag{6.18.1}$$

$$-k\frac{\partial T}{\partial \mathbf{n}}\Big|_{\Gamma_{int}} = q(\theta) \quad \text{on } \Gamma_{\text{int}} \tag{6.18.2}$$

$$-k\frac{\partial T}{\partial \mathbf{n}}\Big|_{\Gamma_{ext}} = h_{ext}(Y - T_{env}) \quad \text{on } \Gamma_{\text{ext}} \tag{6.18.3}$$

where Y are some extra temperature measurements taken at the external surface Γ_{ext} by means of the thermographic camera while $q(\theta)$ is the unknown boundary condition that has to be estimated.

In this way, the system of Equation (6.18) becomes linear respect to the imposed heat flux and the convective heat flux distribution could be calculated, once the heat flux estimation is performed, as:

$$h_{int}(\theta) = \frac{q(\theta)}{\left(T_{wall}(\theta)|_{\Gamma_{int}} - T_b\right) A_{int}} \tag{6.19}$$

In order to generalize the results obtained, the heat transfer performances are compared in terms of Nusselt number:

$$Nu_{int}(\theta) = \frac{h_{int}(\theta)\, D_{int}}{k_f} \tag{6.20}$$

Since the absolute value of the Nusselt number depends on the vortex intensity, in order to compare different flow regime, the ratio between the local internal Nusselt number (Eq. (6.20)) and its maximum is presented in Figure (6.27).

For what concerned the estimation based on the calculation of the sensitivity matrix $\boldsymbol{X}$ (e.g. TM, TSVD, GFSVD), it is possible to observe that the system of Equation (6.19) is linear in the unknown variable $\boldsymbol{q}$, therefore it could be written in the discrete domain as follows:

$$\boldsymbol{T} = \boldsymbol{X}\boldsymbol{q} + \boldsymbol{T}_{\boldsymbol{q}=\boldsymbol{0}} \tag{6.21}$$

where $\boldsymbol{T}$ is the estimated temperature on the sampling position (e.g. in all the entire), $\boldsymbol{X}$ is the sensitivity matrix, $\boldsymbol{q}$ is the imposed heat flux distribution and $\boldsymbol{T}_{q=0}$ is the estimated temperature on the sampling position if no heat flux is applied on the boundary at Γ_{int}.
It is possible to demonstrate that, in order to regularize the inversion of the sensitivity matrix, the three methodologies that are going to be compared could be written in terms of filter factor:

$$\begin{aligned} \boldsymbol{q}_{restored} &= \mathbf{X}^{-1}\left(\boldsymbol{Y} - \boldsymbol{T}_{q=0}\right) = \boldsymbol{V}_p\left(\boldsymbol{\Sigma}_{\mathrm{p}}^{-1}\boldsymbol{U}_p^T\,\boldsymbol{Y}\right) \\ &= \sum_{i=1}^{p} \frac{u_i^T}{\sigma_i} v_i\, f_i\, \left(\boldsymbol{Y} - \boldsymbol{T}_{q=0}\right) \end{aligned} \tag{6.22}$$

where $\boldsymbol{U} = [u_1, u_2, \dots, u_n]$ and $\boldsymbol{V} = [v_1, v_2, \dots, v_m]$ are matrices with orthogonal columns that represent a basis in the *data space,* R^n and a basis in the *model space,* R^m respectively, while $\boldsymbol{\Sigma}$ is a diagonal matrix containing the singular values $\boldsymbol{\Sigma} = diag(\sigma_1, \sigma_2, \dots, \sigma_n)$. Those matrices represents the singular value decomposition of the sensitivity matrix $\boldsymbol{X}$ while the filter coefficients f_i are provided by the filter function summarized in Table (4.1).
On the other hands, the estimation procedures that are not based on the sensitivity matrix (e.g. NRF and FRF), require the solution of two auxiliary problems defined by the system of Equations (3.64) and (3.74). Those systems, could be numerically solved for every kind of geometry, but their analytical solution provided by the FRF for the annulus domain, improved the reconstruction quality of the RF method.
It has to be pointed out that for all the estimation procedure used in the present experiment, the unknown heat flux distribution was discretized in 360 values, which was the same number of temperature measurement available at the external surface, after the image processing procedure.

RESULTS

The results are analysed using the new methodologies presented in *Chapter 4*, and the reconstruction provided by those new algorithm are compared with some of the procedure suggested in *Chapter 3*.

In Figure (6.20) it is reported the Nusselt number as a function of the Reynolds number together with the traditional correlation provided by Dittus-Boelter (*Incoprera2002*) for turbulent regime in straight smooth tubes.

These data show a significant increment of the thermal performances compared to the straight smooth wall pipe without inserts, confirming the goodness of this type of devices as convective heat transfer enhancement technique.

A further insight into the phenomena correlated to the heat transfer rate augmentation was found in the analysis of the local heat flux distribution at the internal wall surface. It has to be remarked that the since the IHCP is non-linear in terms of the convective heat transfer coefficient, the problem has to be re-written in terms of heat flux rate. In this way, it is possible to estimate the convective heat flux coefficient after the solution of one direct problem in which the imposed heat flux at the internal boundary, is the one provided by the inverse estimation.

The FRF method is going to be compared with the NRF and the TSVD, since all those three methodologies are based on the ideal low pass filter. As already mention, the solution procedure start with the estimation of the local heat flux distribution, then the local internal temperature distribution could be computed (Figure (6.21)).

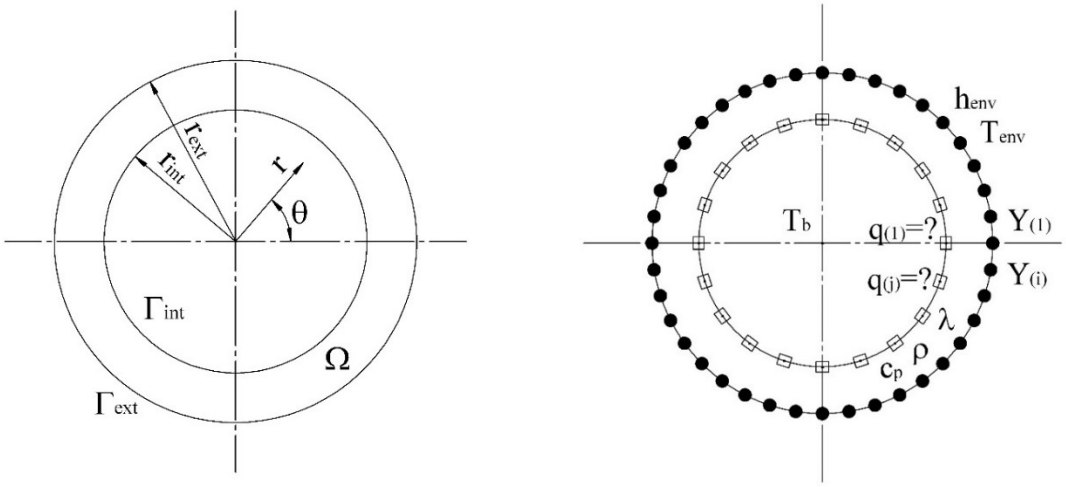

(a) (b)

Figure 6.19: Function estimation: (a) Geometrical domain and (b) inverse problem boundary conditions schemes

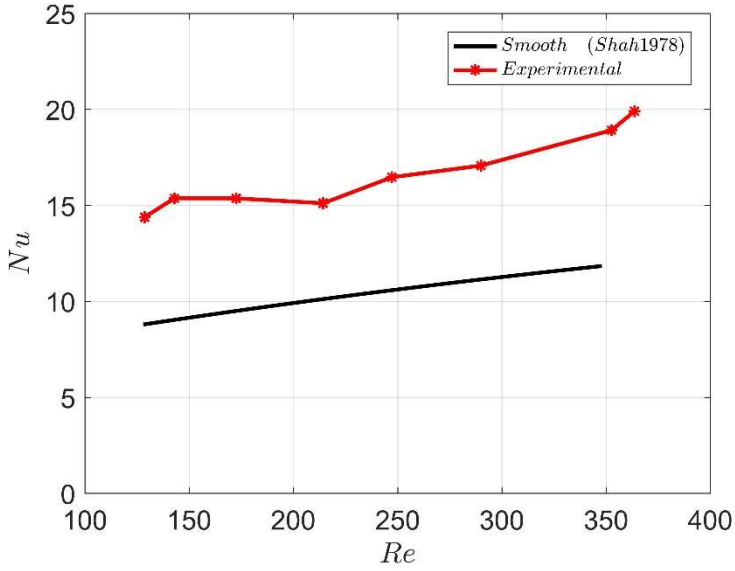

Figure 6.20: Average Nusselt number as a function of the Reynolds number

Finally the results in terms of local convective heat flux coefficient reconstruction are shown in Figure (6.22).

As it is possible to see in Figure (6.22), the reconstruction provided by the FRF and TSVD are almost the same, confirming the robustness of the new approach here presented. It has to be noticed that the NRF reconstruction suffer of ringing artefact, as was shown in the previous chapter using four different test functions.

It has to be pointed out that the Morozov's discrepancy principle was able to estimate the regularization parameter that has to be adopted, for all the three methodologies here presented, as it is possible to see from the random behaviour of the residual between the measured and the estimated external wall temperature profiles showed in Figure (6.23-a).

The application of the discrepancy principle to the three methodologies here analysed is shown in Figure (6.23-b)-(6.23-d). As it is possible to see, the standard deviation of the residuals between the measured and the estimated temperature at the external boundary monotonically decrease as far as the regularization parameter increase.

This behaviour is justified since incrementing the regularization parameter more information about the signal are preserved during the estimation procedure, thus reducing the misfit between the temperature estimation at the external boundary and the measured one.

It has to be pointed out that the standard deviation of the measurement error, which is an input information for the Morozov's discrepancy principle, was estimated by measuring the surface temperature distribution while maintaining the pipe wall under isothermal conditions.

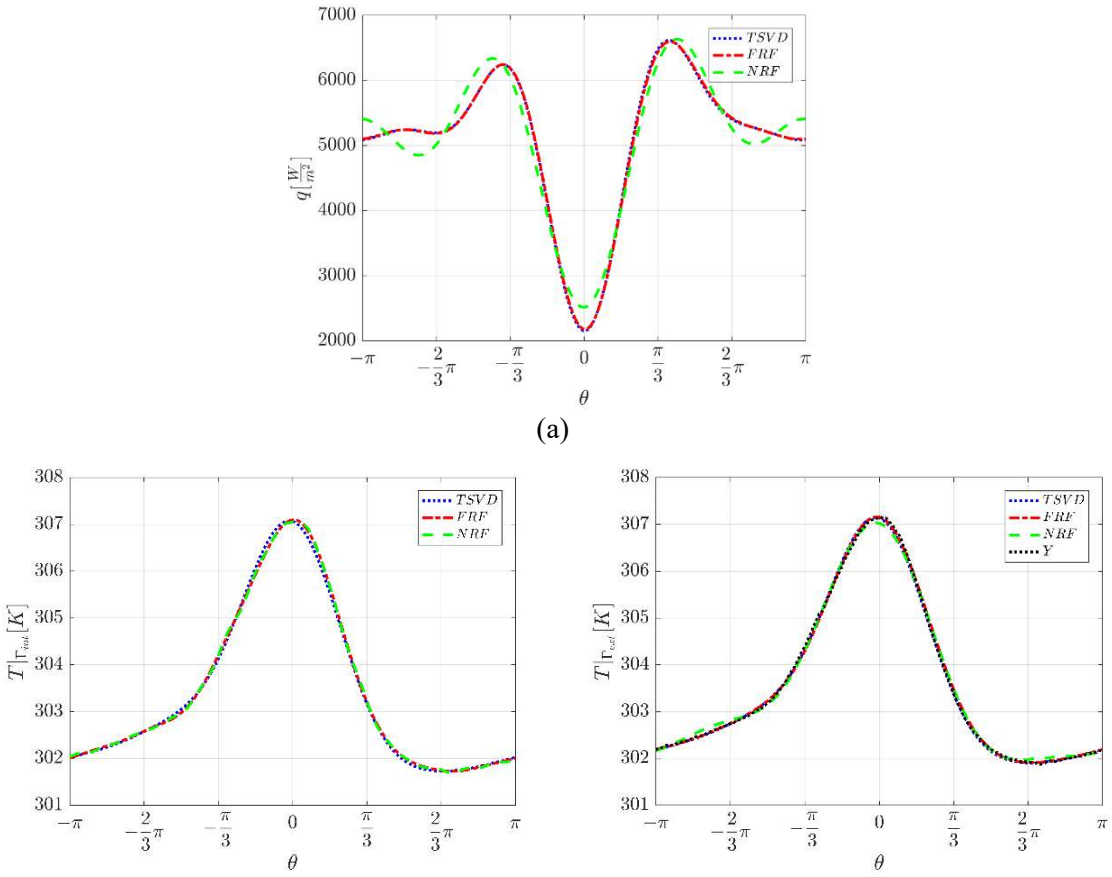

Figure 6.21: Comparison between the truncated reconstruction methodologies proposed in literature and presented in *Chapter 3* (TSVD and NRF) and the new method developed in *Chapter 4* (FRF): (a) heat flux distribution, (b) estimated internal wall temperature distribution and (c) estimated and measured external wall temperature distribution

On the other hand, the continuous behaviour of filter function characteristic of the GFSVD require its comparison with the TM approach.

The estimation procedure is the same already discussed for the truncated reconstruction methodologies. In particular, in Figure (6.24) the estimated heat flux as well as the temperature profiles at the internal and external boundaries are reported.

As it is possible to see, the reconstruction provided by the TSVD methods suffer of ringing artefacts, compared to the reconstruction made by the GFSVD and TM methodologies.

The results in terms of local convective heat flux coefficient reconstruction are shown in Figure (6.25): as it is possible to see, the reconstruction provided by the GFSVD is comparable with the once obtained by the TM confirming the robustness of the new approach here presented.

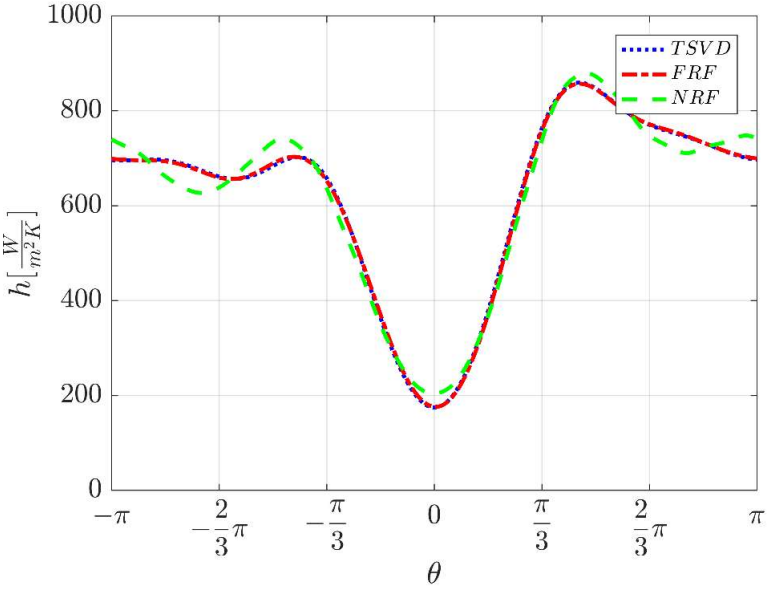

Figure 6.22: Comparison between the truncation reconstruction methodologies proposed in literature and presented in *Chapter 3* (TSVD and NRF) and the new method developed in *Chapter 4* (FRF)

It is also possible to see how the TSVD suffer of ringing artefact compare to the continuous filtering regularization technique. The truncation estimation procedure gives less accurate results, compared to the filtering estimation procedure, even if both the methodologies are based on the regularization principle. The outperform of the truncated estimated solution, compared to the filtered one, is due to the less number of harmonic component comparing in the reconstructed signal.

It has to be pointed out that the Morozov's discrepancy principle was able to estimate the regularization parameter that has to be adopted, for all the three methodologies here presented, as it is possible to see from the random behaviour of the residual between the measured and the estimated external wall temperature profiles showed in Figure (6.26-a).

The application of the discrepancy principle to the three methodologies here analysed is showed in Figure (6.26-b)-(6.26-d).

As it is possible to see, for the TSVD and the GFSVD methodology, the standard deviation of the residuals between the measured and the estimated temperature at the external boundary monotonically decrease as far as the regularization parameter increase.

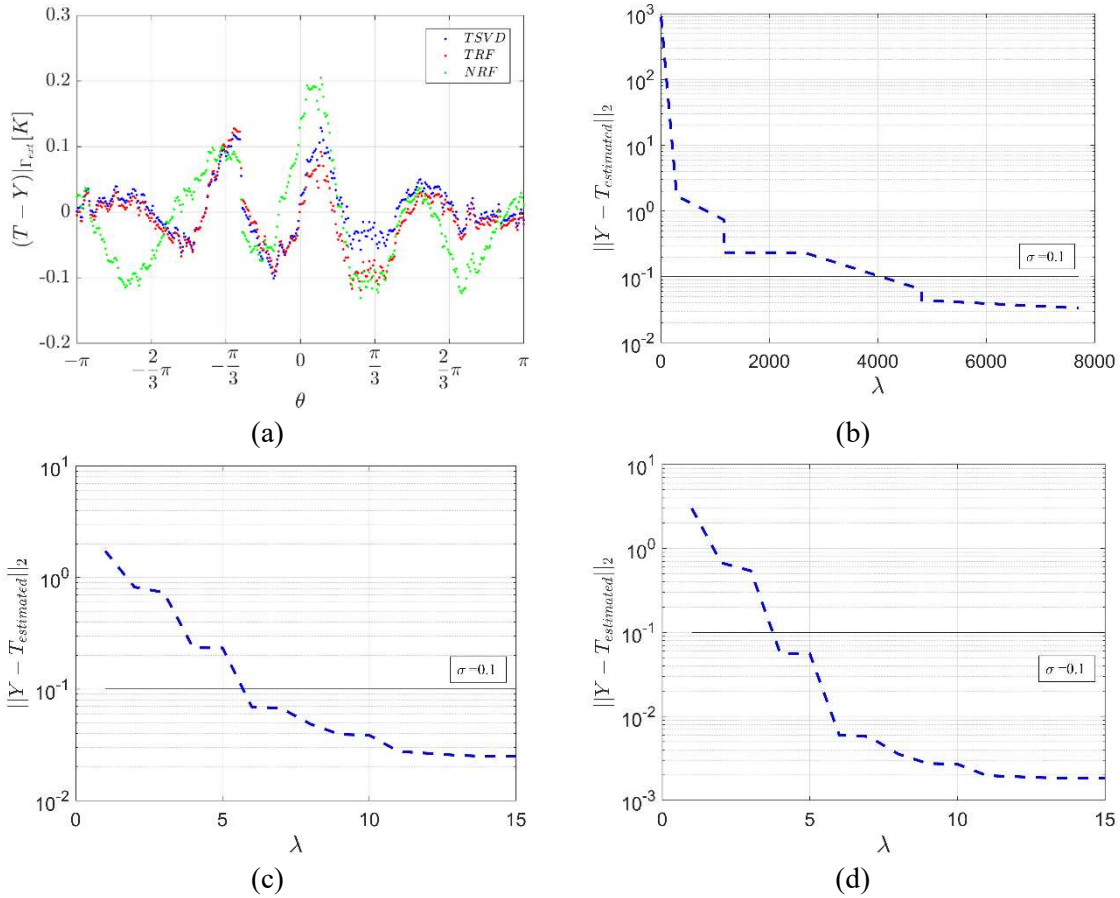

Figure 6.23: (a) Residual between the measured and the estimated external wall temperature, (b) Morozov's discrepancy principle for TSVD method, (c) Morozov's discrepancy principle for FRF method and (d) Morozov's discrepancy principle for NRF method,

This behaviour is justified since incrementing the regularization parameter more information about the signal are preserved during the estimation procedure, thus reducing the misfit between the temperature estimation at the external boundary and the measured one. The opposite observation could be made for the TM method, since in this case the augmentation of the regularization parameter will produce an over-smoothed estimated solution, thus increasing the misfit between the temperature estimation at the external boundary and the measured one.

In Figure (6.20) and Figure (6.23) it is possible to see a great variation between the convective heat transfer coefficient at the outer bend side of the coil and the one at the inner bend side confirming the necessity of taking care about the flow distribution during the design of this type of heat exchanger, especially for all those application in which the homogeneity and the security of the product is necessary.

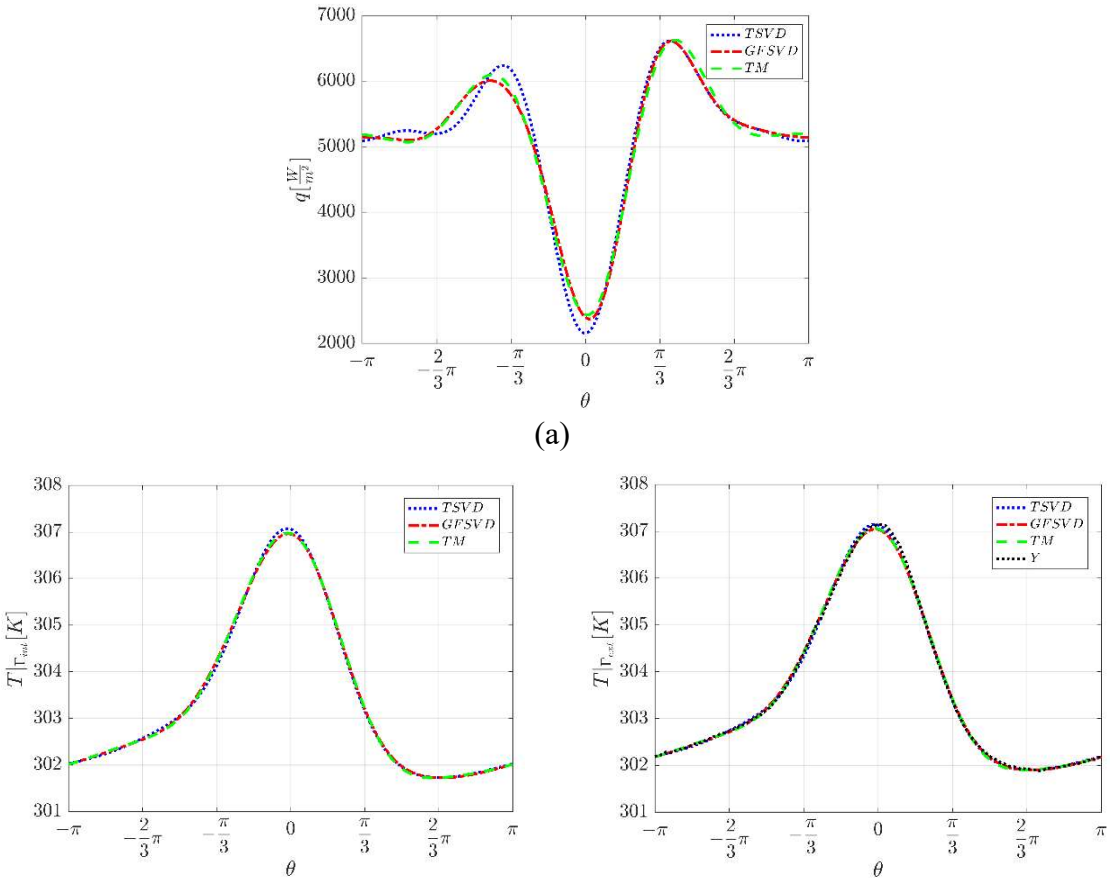

Figure 6.24: Comparison between the filtered reconstruction method proposed in literature and presented in *Chapter 3* (TM) and the new method developed in *Chapter 4* (GFSVD): (a) heat flux distribution, (b) estimated internal wall temperature distribution and (c) estimated and measured external wall temperature distribution

As is possible to see in Figure (6.20) and Figure (6.23), the torsion effect creates a rotation force that affects the flow pattern making the distribution of the convective heat transfer coefficient non-symmetrical, as already observed by Yang (*Yang1995*).

Moreover, it is possible to see that the pattern is particularly steep and Nu/Nu_{max} is above 0.8 for approximately 75% of the circumference.

In order to compare the Nusselt number distribution experimentally reconstructed with the results provided in literature for different working conditions, the Nu/Nu_{max} ratio was determined, as showed in Figure (6.26).

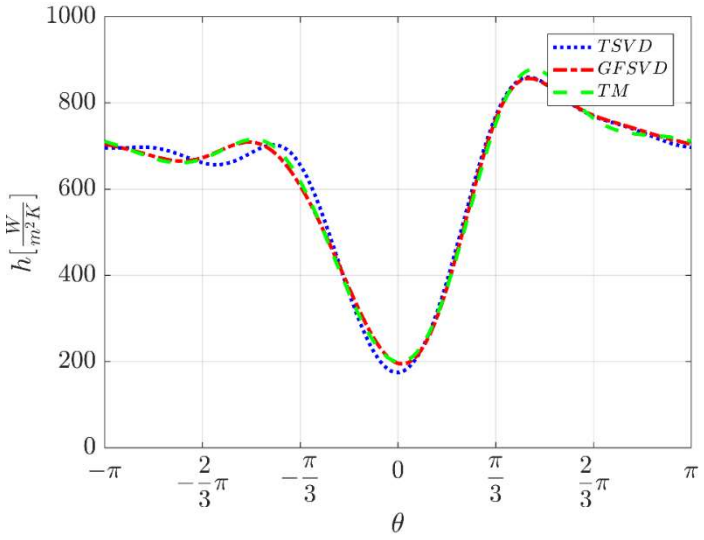

Figure 6.25: Comparison between the filtered reconstruction method proposed in literature and presented in *Chapter 3* (TM) and the new method developed in *Chapter 4* (GFSVD)

As it is possible to see in Figure (6.27), the data provided by Yang (*Yang1995*) match the distribution here reconstructed, even if some discrepancies are registered, especially close to the inner bend side of the coil; this mismatch that could be related to the different working fluid used by Yang ($Pr = 5$).

Given the above consideration, it is possible to conclude that both the new solution methodologies are able to reconstruct the local convective heat flux coefficient, providing results comparable in terms of accuracy, to the common and vastly investigated solution strategies (e.g. TSVD, TM). Moreover, the results obtained are comparable to the ones provided by Yang (*Yang1995*) even if the working fluid employed was different.

The local inverse estimation of the convective heat transfer coefficient here addressed was able to give a better understand on the mechanisms that govern the heat transfer in coiled pipes highlighting the primary role played by the non-uniform flow distribution.

The effectiveness of wall curvature, already discussed in *Chapters 1* and here resume, is due to the centrifugal force acting on the fluid. In particular the coil curvature, generates a velocity field characterized by a local maxima near by the outer bend of the coil that locally increases the temperature gradient at the wall maximising the heat transfer coefficient.

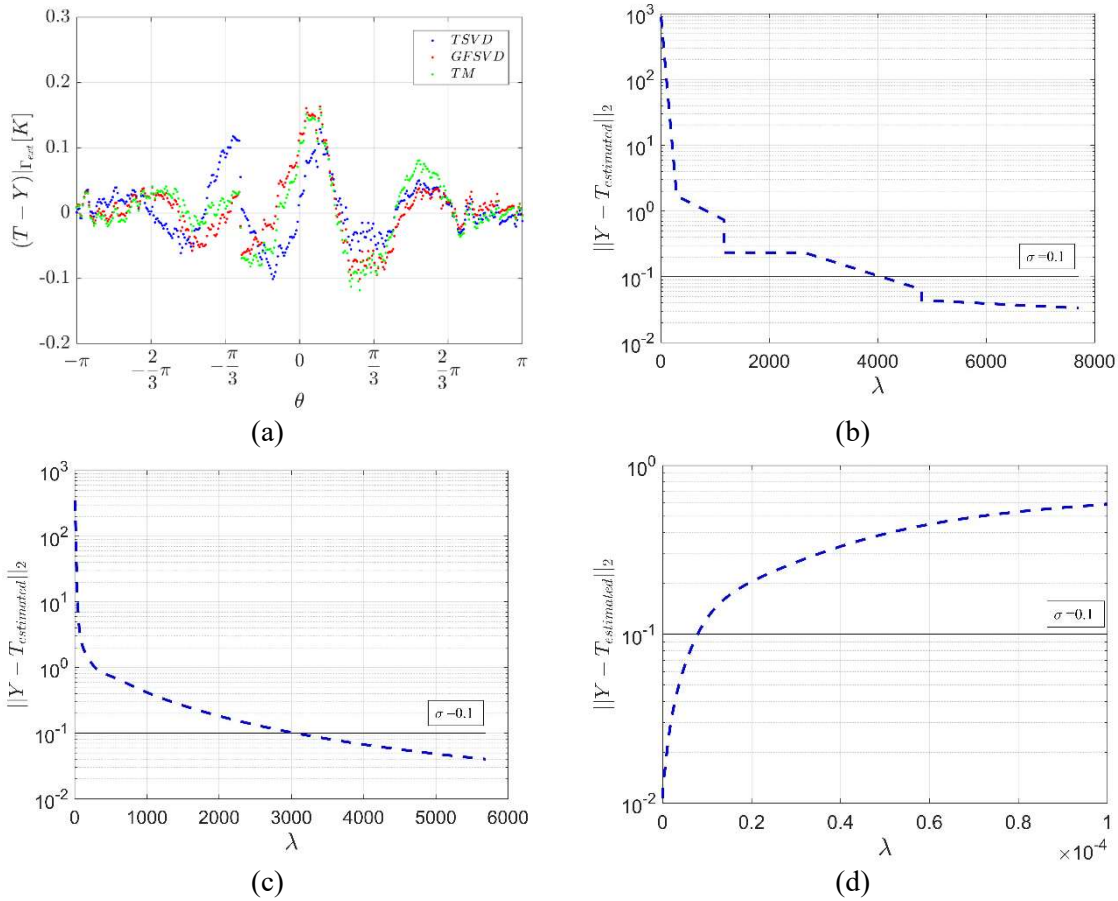

Figure 6.26: (a) Residual between the measured and the estimated external wall temperature, (b) Morozov's discrepancy principle for TSVD method, (c) Morozov's discrepancy principle for GFSVD method and (d) Morozov's discrepancy principle for TM method,

Moreover, the local analysis of the convective heat transfer coefficient, showed a non-asymmetrical distribution of the velocity field over the cross-section of the tube due to the coil pitch.

Finally, it has to be pointed out that the irregular distribution of the heat flux, could be critical in some industrial applications, such as in those that involve a thermal process. For instance, in food pasteurisation, the irregular temperature field induced by the wall curvature could reduce the bacteria heat-killing or could locally overheat the product damaging the taste as well as the organoleptic properties. Therefore, to correctly characterize this type of heat-transfer apparatus, it is necessary to know the local heat transfer coefficient distribution at the fluid-wall interface.

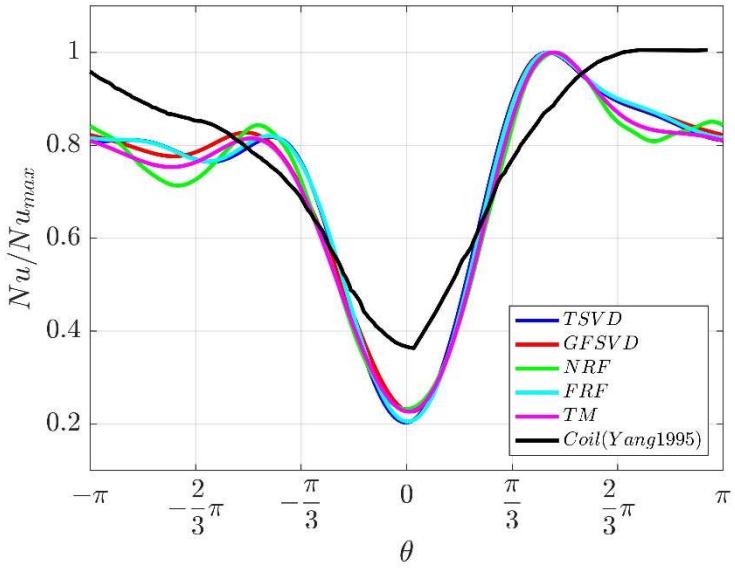

Figure 6.27: Normalized Nusselt number compared with the data by Yang (*Yang1995*)

6.3 Inverse estimation of the local convective heat transfer coefficient in straight tubes using insert devices

INTRODUCTION

The 2D inverse problem here addressed, required the estimation of the local convective heat transfer coefficient in a straight tube fitted with a butterfly shaped turbulator, which represents a new interesting heat transfer enhancement technique. The solution of the IHCP was made by the zero-order Tikhonov regularization method couples with the Morozov's discrepancy principle both described in *Chapter 3*.

The heat transfer enhancement techniques constitute a very interesting research issue in the heat transfer field. In many industrial applications, such as those that involve the food, chemical and pharmaceutical products, engineers have been struggling for techniques generating enhanced heat transfer coefficients, accompanied by reduced pumping power requirement. Today this research topic is attracting a renewed interest in the process industry due to the increase of energy and raw materials cost. The heat transfer enhancement techniques essentially reduce the overall thermal resistance by increasing the heat transfer coefficients. Therefore, it could possible to reduce the size of the heat exchanger as well as to decrease the temperature difference at which they work. Related to this aspect, it has to be highlighted that the reduction of the temperature difference between the heat exchanger and the product, imply the reduction of the thermal stress for the product that yields to a lower damage of the organoleptic properties of the treated food.

The solutions that could be used in order to increase the convective heat transfer can be divided into active techniques, which require mechanical aid or electrostatic fields, and passive techniques that do not require external power (*Bergles1998*). Since the passive techniques do not require a new external power input, they are usually more attractive from the industrial point of view. The passive heat transfer enhancement techniques are based on the changes induced on the fluid flow through a proper conformation of the surface, such as curvature of the walls, surfaces roughness, corrugation, insertion of devices in the main flow directly or by means of additives (*Bergles1998*, *Webb1994*). Since the insert devices could be installed after market, they represent an interesting solution in all those industrial application of plant revamping and renewing. In particular, the inserts are elements that are positioned in the flow passage with the aim of increasing the heat transfer rate. This enhancement technique results particular attractive for the low cost, the rapid installation

and the easy maintenance (*Tu2015*). Within this category of passive heat transfer enhancement techniques, displaced devices, twisted tapes, wire coils are the most commonly adopted. Twisted tapes are metallic or non-metallic strips twisted, with some suitable technique at the desired shape and dimension, which are inserted in the flow with the aim of introducing swirl components into the flow that could disrupt the boundary layer at the pipe fluid surface (*Liu2013*). It is straightforward that the pressure drop inside the tube will increase, after the introduction of the twisted-tape, therefore it could be necessary to change the pump that is installed in the working plant. Twisted-tape inserts have been the object of many research works that analysed the different configurations of this devices studying full-length and short-length twisted tape having constant or variable pitch (*Date1972, Hong1976, Manglik1993*) in order to investigate the optimal design in terms of both thermal and friction loss performances. Hong (*Hong1976*) performed one of the first experimental work on twisted-tape inserts investigating both the pressure drops and the heat transfer enhancement in pipes by using water and ethylene glycol as working fluids. The authors, observed that the insertion of twisted tapes produced an increase of the Nusselt number up to 9 times the one registered by employing a straight empty tube in the same working conditions. Manglik (*Manglik1993*) developed empirical correlations for the Nusselt number and friction factor, identifying a new dimensionless parameter called *swirl number* (which contain the same information provided by the Dean number (*Bozzoli2018a*)). The authors highlighted the crucial role played by this parameter in the description of the heat transfer mechanism and the interaction between viscous, inertia and centrifugal forces, for this particular type of insert devices. Ujhidy (*Ujhidy2003*) investigated laminar flow in coils and tubes containing twisted tapes and helical static elements. These authors highlighted the similarity of the flow pattern characterised by swirl components present in coils and tubes with twisted tapes or helical static elements. Sarma (*Sarma2002*) investigated the turbulent regime in pipes fitted with twisted-tape inserts; these authors suggested a correlation for the Nusselt number as a function of the Reynolds and Prandtl numbers and the twisted tape pitch to tube diameter ratio.

Among all the above mentioned techniques, one of the most promising solution concerned the inserts solution is related to the displacement devices. For this reason, the local estimation of the convective heat transfer coefficient is investigated in order to better understand the heat transfer enhancement mechanism related to those devices.

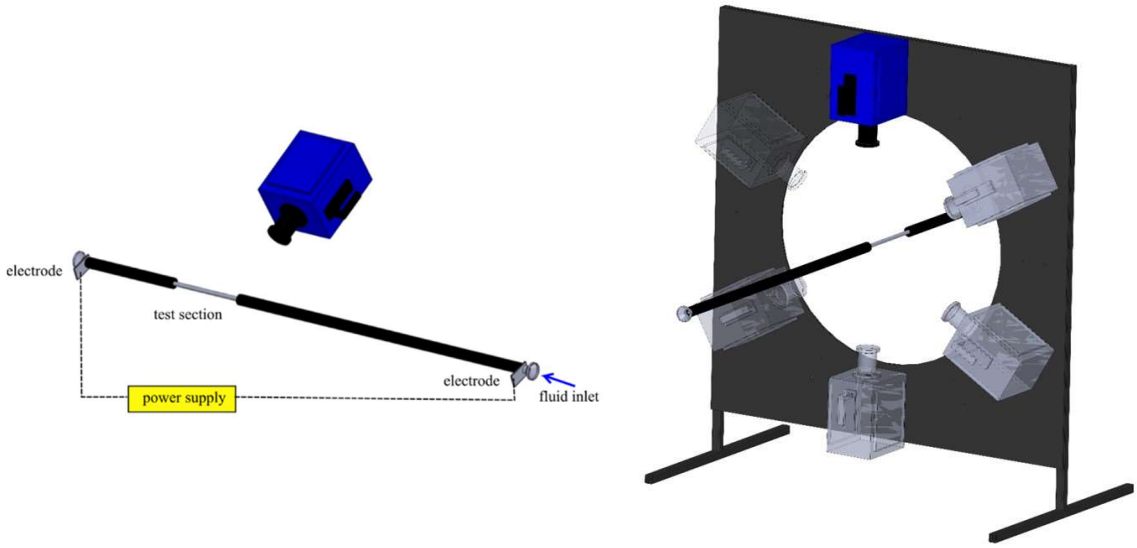

(a) (b)

Figure 6.28: (a) experimental scheme and (b) thermographic camera positions

The displacement devices, are positioned inside straight smooth pipes, with the aim of increasing the heat transfer rate by displacing the hot fluid to the colder regions of the tube and vice versa (*Dewan2004*). This mixing effect, reduce the boundary layer thickness consequently increasing the convective heat transfer coefficient. Many studies were carried out on different types of displacement enhancement devices (e.g., metal grids, disks, cones, static mixers, crowns and balls) (*Dewan2004, Promvonge2007, Promvonge2008c, Jadoaa2011*), but among all, the butterfly shaped turbulator are one of the most remarkable. In many industrial fields, such as in the food, chemical and pharmaceutical industries, engineers have then been striving for techniques producing enhanced heat transfer coefficients, accompanied by reduced pumping power requirements. Displaced enhancement devices are a particular kind of inserts that leaves the heated surface substantially unaltered and changes the fluid flow near the pipe wall increasing the transferred energy. Therefore, this particular type of enhancement technique results attractive for the low cost, rapid installation and easy maintenance.

Displaced enhancement devices has been mainly discussed in literature by considering only the heat transfer performance averaged over the entire tube heat transfer surface area. This approach is acceptable for many applicative cases however the local measuring of the convective heat flux coefficient at the internal wall surface of a pipe could give a better understand on the phenomenon, especially because these inserts usually induce significant spatial variation of local thermal performances.

EXPERIMENTAL SET-UP

The test facilities used for the type of measurements was already described in the previous paragraph, however it has to be pointed out that due the simple external geometry of the tube, a new measurement system was designed as shown in Figure (6.28). The working fluid, water, entered the test section equipped with stainless-steel fin electrodes, which were connected to a power supply. Like in the previous paragraph, it was possible to approximate the constant wall heat flux boundary condition by dissipating energy in the solid domain through the Joule effect. The whole length of the heat transfer section was thermally insulated in order to minimize the heat transfer to the environment. Both the inlet and outlet bulk temperature were measured by placing a thermocouple probe on the tube's wall far away from the heating section. A small portion of the external tube wall, around the position of the insert, was made accessible to a thermal imaging camera by removing the thermally insulating layer, and it was coated with a thin film of high emissivity paint. This thin paint layer changes the surface emissivity without affecting the heat conduction problem in the tube wall. The surface temperature distributions were acquired by means of a FLIR SC7000 unit, with a 640 x 512 pixel detector array. Its thermal sensitivity, as reported by the instrument manufacturer, is 20 mK at 303 K, while its accuracy is ±1 K. A schematic view of the infrared thermographic system arrangement is shown in Figure (6.28).

The tube was fitted with a butterfly-shaped device, as schematically shown in Figure (6.29), and its global and local thermal performances were tested at different fluid flow velocities.

A picture of the considered butterfly-shaped device is reported in Figure (6.29): the device is characterised by two "wings" and two "indentions" having a maximum diameter of 13 mm. The inserts were positioned inside a stainless steel tube having an internal diameter that fits the maximum dimension of the turbulator, and a wall thickness of 1.0 mm. The pipe was three meters long and the butterfly-shaped devices were positioned at a distance of 300 mm one from the other in order to not override the effects of two consequential inserts.

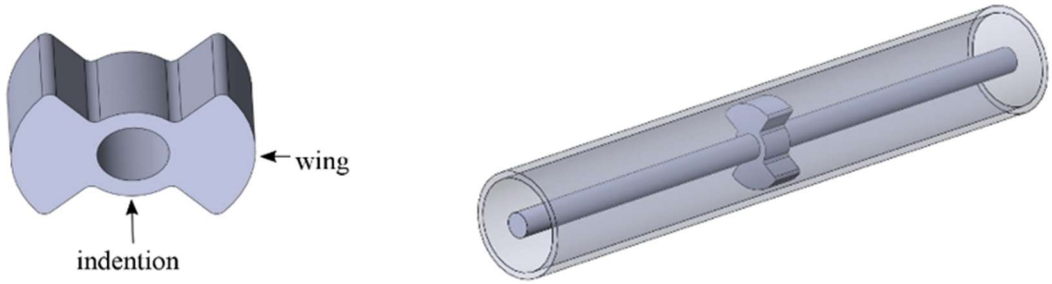

(a) (b)

Figure 6.29: Butterfly shaped turbulator: (a) 3D turbulator's scheme and (b) 3D mounting scheme

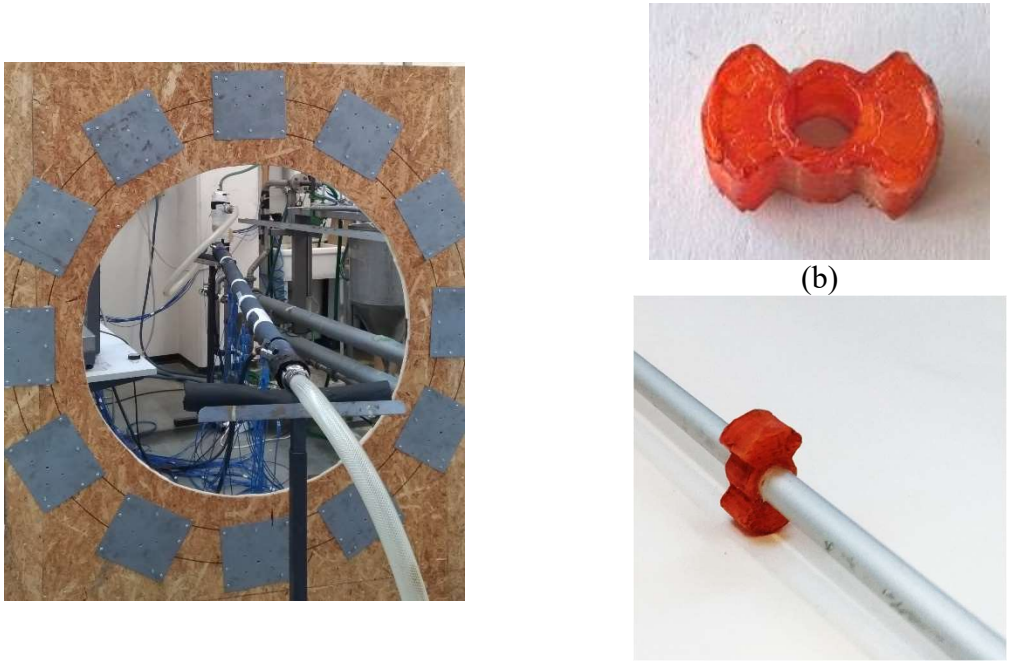

(a) (b) (c)

Figure 6.30: (a) experimental setup (b) 3D printed butterfly shaped turbulator and (c) turbulator mounted on the aluminium rod

Moreover, it has to be highlighted that the turbulators were maintained in a prescribed position thanks to a central aluminium rod, as it is possible to see from Figure (6.30).

To measure the temperature distribution on the whole test section surface, six images were acquired, moving the infrared camera around the tube's axis in different measure station (Figure (6.31)).

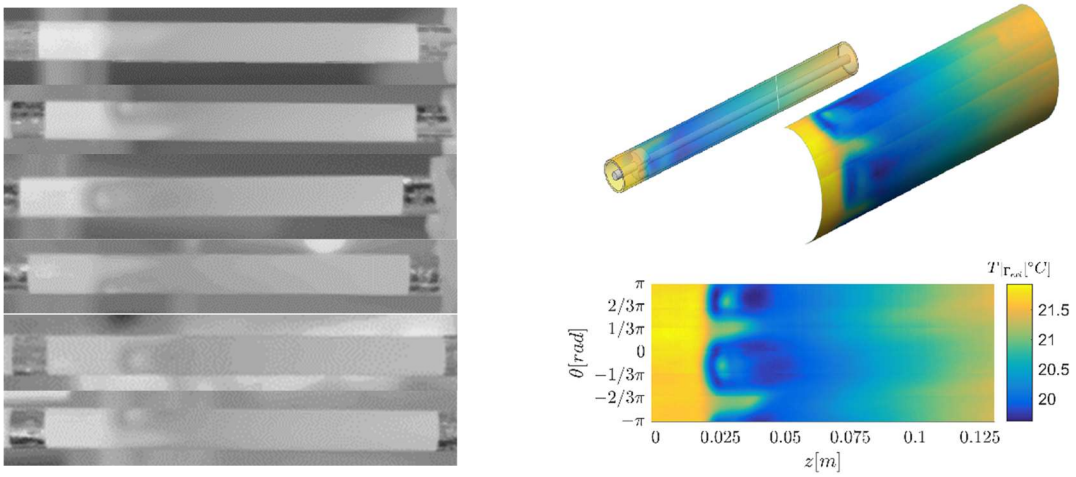

(a) (b)

Figure 6.31: (a) thermographic camera images and (b) image processing scheme

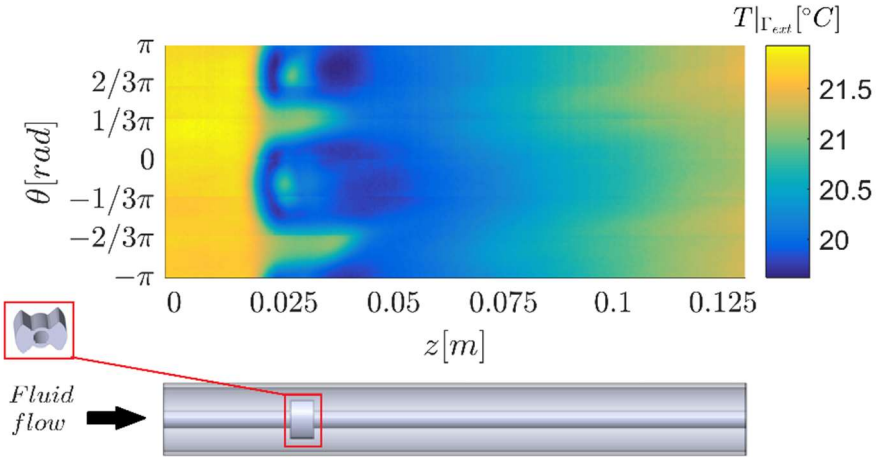

Figure 6.32: Experimental temperature measurements after the image processing ($Re = 7118$)

The camera was conveniently fixed on a support, in order to keep the optical axis normal to the tube axis and minimizing perspective artefacts. Thanks to limiting the viewing angle to less than ± 30°, the surface was considered as a diffuse grey emitter (*Pavelka2013*). The effective emissivity of the coating was estimated in situ by shooting a target at different known temperatures, and the value 0.99 was found.

In Figure (6.32) a representative temperature map of the external surface of the tube, is depicted. It is clearly visible the distortion of the wall temperature distribution caused by the presence of the insert device (which is located at $z \approx 0.03m$).

The image processing procedure was made complex by the non-flat behaviour of the target. In order to overcome this problem, common photo-plans tools based on well-known equations of central projection could be employed but this is not really an easy task when dealing with curved objects (*Pavelka2013*). The image processing procedure adopted, presented by Bozzoli (*Bozzoli2016a*) permitted to rectify optical deformations of the collected images caused by surface curvature, then the acquired images were cropped and merged together to obtain continuous temperature map on the tube wall, thanks to adequate position references fixed on the tube wall. In order to validate the unwrapping algorithm, the typical "chessboard test" was performed: the pattern shown in Figure (6.33) was fixed on the external tube surface and shot by a digital camera, like in the infrared image processing previously used.

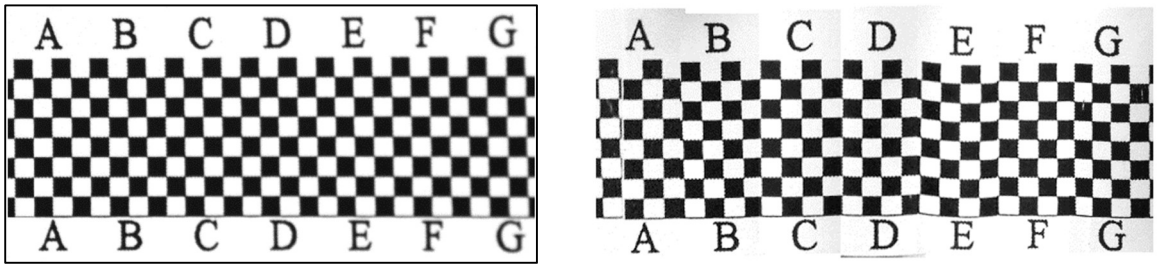

(a) (b)

Figure 6.33: (a) input image (b) unwrapped total image

The obtained pictures were elaborated by a common procedure called "texture unwrapping". The process was made complex by the fact that the observed target surface is not flat: common photo-plans can be produced from images of planar objects by image processing tools based on well-known equations of central projection but this is not really an easy task when dealing with curved objects (*Pavelka2013*). The image processing procedure adopted permits to rectify optical deformations of the collected images caused by surface curvature. Figure (6.33) sketches how a cylindrical surface is projected on a plane when the plane is parallel to the cylinder axis.

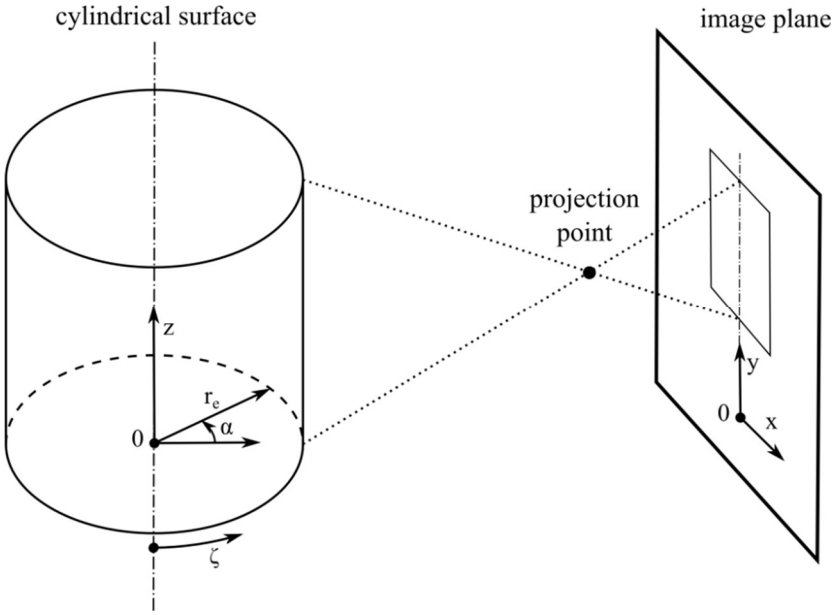

Figure 6.34: Cylindrical surface projection on a plane

Under the assumption that the camera is sufficiently far from the pipe, the planar (x, y) temperature distribution could be mapped into the (α, z) cylindrical as follows:

$$\begin{cases} \alpha = \arctan\left(\frac{x}{\Psi}\right) + \alpha_0 \\ z = \Omega \cdot \mathrm{y} + \mathrm{z}_0 \end{cases}$$

where Ψ, Ω, z0 and α0 are parameters, depending on camera lenses and camera relative position. These parameters can be easily determined by calibrating the acquisition system with a known sample pattern fixed on the tube wall (*Pavelka2013, Cyganek2011*).

In Figure (6.34) the processing steps of a sample image are reported. It is easy to notice from Figure (6.34a) that, for clear geometrical causes, the unwrapping of the image close to the pipe borders is not perfectly achievable and for this reason only the central part of the processed image was considered in the surface reconstruction process. In order to reconstruct the whole image of the test surface, the camera was moved around the section acquiring six different images that were then unwrapped with the procedure discussed above; finally, thanks to the position references (i.e. letters above and below the chessboard pattern) the unwrapped images were merged together to obtain the continuous map on the tube wall (Figure (6.32)). The comparison between the final unwrapped image (Figure (6.32b)) and the original source pattern (Figure (6.32a)) confirms the effectiveness of the procedure.

(a) (b)

Figure 6.35: (a) Example of a camera shot in the visible spectrum (b) Example of the central part of the sample

ESTIMATION PROCEDURE

The direct problem presented in *Chapter 5* (Equations (5.16)) could be linearized by writing the internal boundary condition in terms of wall heat flux instead of the convective heat flux coefficient, as follows:

$$\nabla^2 T = -\frac{q_G}{k} \quad \text{in } \Omega \tag{6.23.1}$$

$$-k\frac{\partial T}{\partial \mathbf{n}}\Big|_{\Gamma_{int}} = q(\theta, z) \quad \text{on } \Gamma_{\text{int}} \tag{6.23.2}$$

$$-k\frac{\partial T}{\partial \mathbf{n}}\Big|_{\Gamma_{ext}} = h_{ext}(Y - T_{env}) \quad \text{on } \Gamma_{\text{ext}} \tag{6.23.3}$$

$$-k\frac{\partial T}{\partial \mathbf{n}}\Big|_{\Gamma_{int}} = 0 \quad \text{on } \Gamma_{top} \tag{6.23.3}$$

$$-k\frac{\partial T}{\partial \mathbf{n}}\Big|_{\Gamma_{int}} = 0 \quad \text{on } \Gamma_{bottom} \tag{6.23.3}$$

where Y are some extra temperature measurements taken at the external surface Γ_{ext} by means of the thermographic camera while $q(\theta)$ is the unknown boundary condition that has to be estimated.

In this way, the system of Equation (6.23) becomes linear respect to the imposed heat flux and the convective heat flux distribution could be calculated, once the heat flux estimation is performed, as:

$$h_{int}(\theta) = \frac{q(\theta)}{\left(T_{wall}(\theta)|_{\Gamma_{int}} - T_b\right) A_{int}} \tag{6.24}$$

Since the inverse problem is linear in the unknown variable $\boldsymbol{q}$, it is possible to write the system of equation in the discrete domain as follows:

$$\boldsymbol{T} = \boldsymbol{X}\boldsymbol{q} + \boldsymbol{T}_{\boldsymbol{q}=\boldsymbol{0}} \tag{6.25}$$

where $\boldsymbol{T}$ is the estimated temperature on the sampling position (e.g. in all the entire), $\boldsymbol{X}$ is the sensitivity matrix, $\boldsymbol{q}$ is the unknown heat flux distribution and $\boldsymbol{T}_{q=0}$ is the estimated temperature on the sampling position if no heat flux is applied on the boundary at Γ_{int}.

The problem could be state, using the Lagrange multipliers in a damped least square problem (*Chapter 3*):

$$\min\left\|\boldsymbol{Y}-\left(\boldsymbol{Xq}+\boldsymbol{T}_{\boldsymbol{q}=\boldsymbol{0}}\right)\right\|_2^2+\lambda^2\|\boldsymbol{qL}\|_2^2 \quad \lambda>0 \tag{6.26}$$

where $\|\cdot\|_2^2$ stands for the square of the two-norm, λ is the unknown regularization parameter and $\boldsymbol{L}$, for the zero order Tikhonov regularization, is the identity matrix:

$$\boldsymbol{L}=\begin{bmatrix}1 & & 0\\ & \ddots & \\ 0 & & 1\end{bmatrix} \tag{6.27}$$

As long as λ is a non-zeros coefficient, the problem defined by the Equation (6.26) could be solved by the method of the normal equations as follows:

$$(\boldsymbol{X}^T\boldsymbol{X}+\lambda^2\boldsymbol{L})\boldsymbol{q}=\boldsymbol{X}^{\boldsymbol{T}}\left(\boldsymbol{Y}-\boldsymbol{T}_{q=0}\right) \quad \lambda>0 \tag{6.28}$$

which yields to the estimated internal wall heat flux:

$$\boldsymbol{q}_\lambda=(\boldsymbol{X}^T\boldsymbol{X}+\lambda^2\boldsymbol{L}^T\boldsymbol{L})^{-1}\boldsymbol{X}^T\left(\boldsymbol{Y}-\boldsymbol{T}_{\boldsymbol{q}=\boldsymbol{0}}\right) \tag{6.29}$$

It has to be pointed out that since the boundary condition adopted on the top and on the bottom of the pipe are not the one that better model the phenomenon, it was necessary to extend the module under investigation two times before and two times after the test section, as shown in Figure (6.36).

It has to be pointed out that, the unknown heat flux distribution was discretized in order to have the same pitch in both the circumferential and axial coordinate: in particular, it was discretised in 360 values along the θ coordinate and 1125 values along the z coordinate.

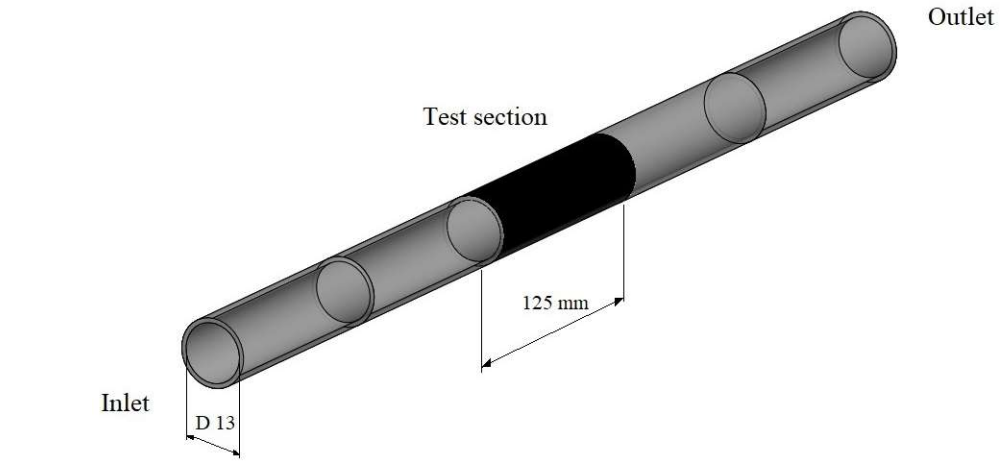

(a)

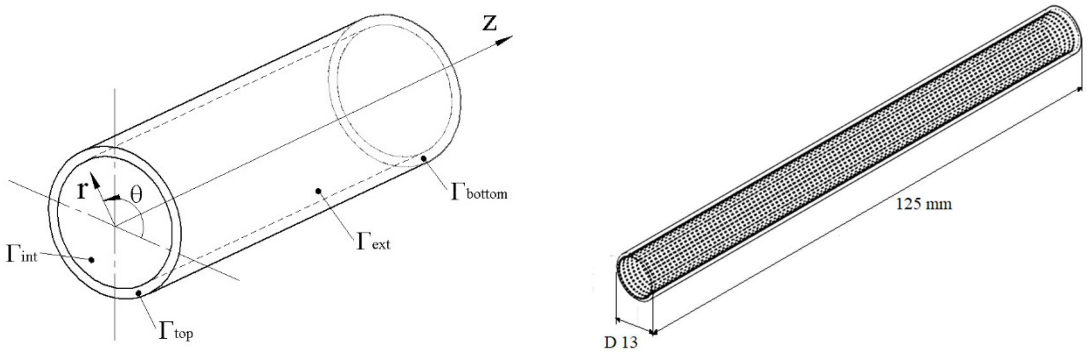

(b)

Figure 6.36: Function estimation: (a) Geometrical domain and (b) inverse problem boundary conditions schemes

This configuration allowed using the same regularization parameter in both the direction, giving the same weight to the filter function. The same discretization was adopted for the temperature measurement available at the external surface, after the image processing procedure.

Finally, in order to generalize the results obtained, the heat transfer performances are compared in terms of average Nusselt number as a function of the Reynolds number:

$$Nu_{int}(\theta) = \frac{h_{int}(\theta)\, D_{int}}{k_f} \tag{6.30}$$

RESULTS

In Figure (6.37) it is reported the Nusselt number as a function of the Reynolds number together with the traditional correlation provided by Dittus-Boelter (*Incoprera2002*) for turbulent regime in straight smooth tubes.

These data show a significant increment of the thermal performances compared to the straight smooth wall pipe without inserts, confirming the goodness of this type of devices as convective heat transfer enhancement technique.

A further insight into the phenomena correlated to the heat transfer rate augmentation was found in the analysis of the local heat flux distribution in correspondence of the insert. It has to be remarked that the since the IHCP is non-linear in terms of the convective heat transfer coefficient, the problem has to be rewritten in terms of heat flux rate. In this way, it is possible to estimate the convective heat flux coefficient after the solution of one direct problem in which the imposed heat flux at the internal boundary, is the one provided by the inverse estimation. In order to understand the thermal efficiency compared to the straight smooth pipe, it is possible to define the local heat flux efficiency η:

$$\eta = \frac{q_{int}}{q_0} \tag{6.31}$$

where q_0 is the internal heat flux for the tube, in the same experimental conditions, without the inserts. The maps of this parameter are fundamental to investigate the effect of the inserts in terms of local peaks, stagnation points and influence lengths.

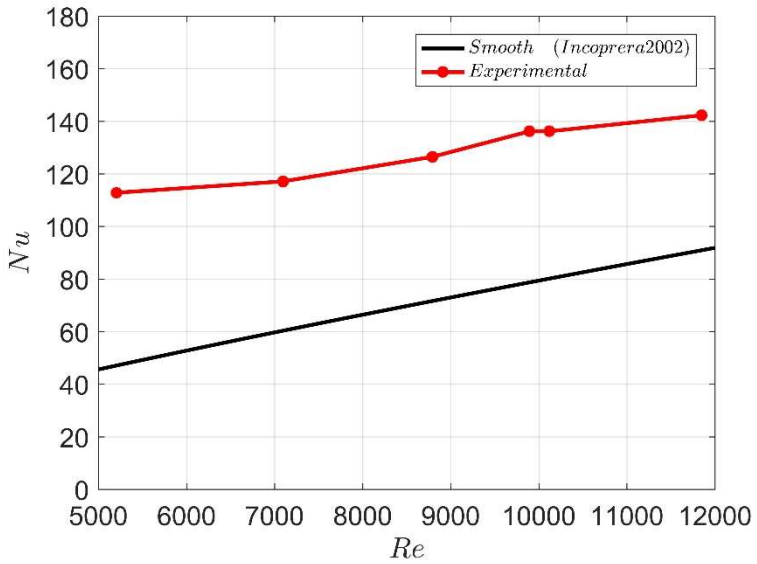

Figure 6.37: Average Nusselt number as a function of the Reynolds number

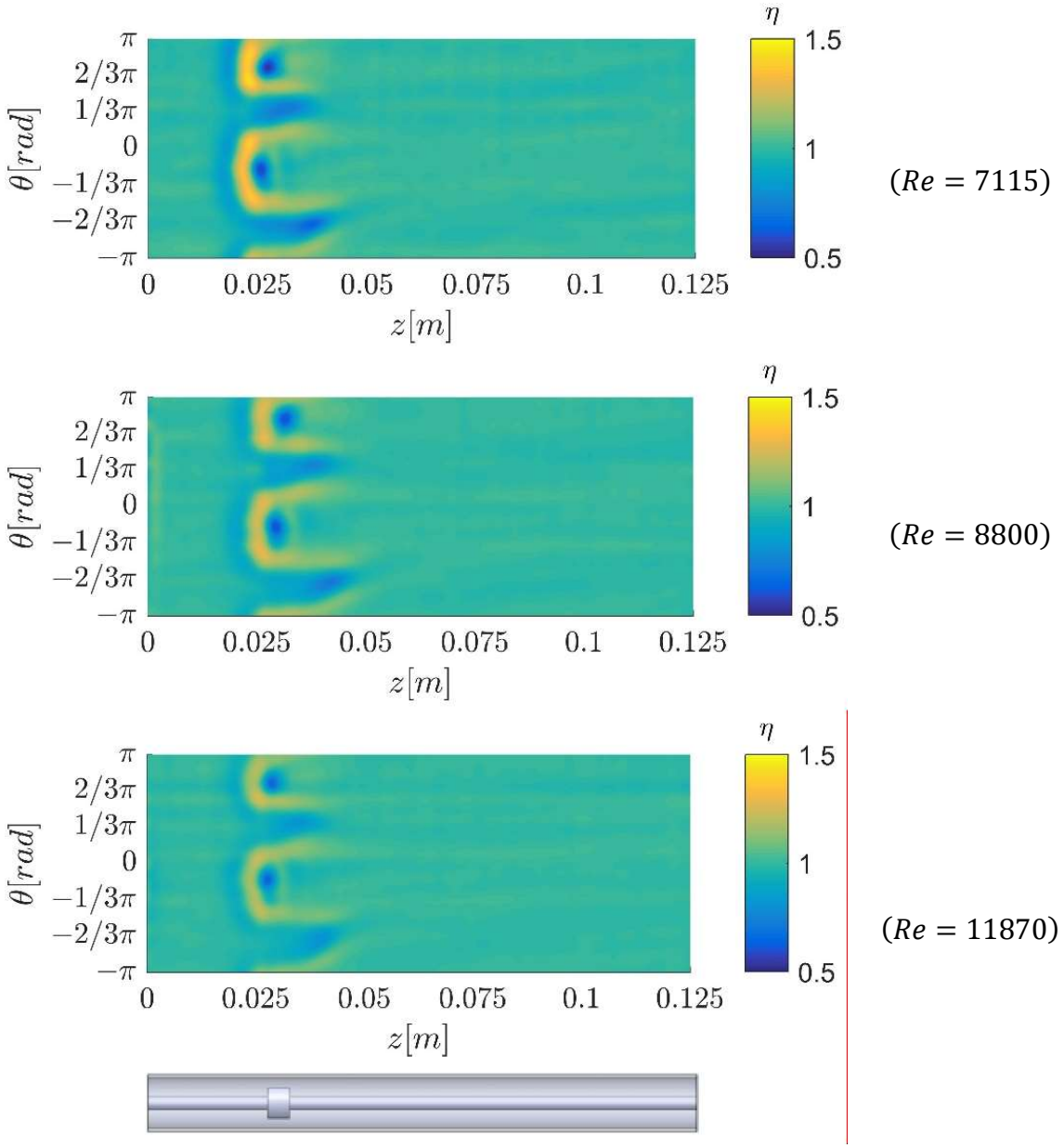

Figure 6.38: Local heat flux efficiency η for three representative Reynolds numbers

The local estimation procedure was repeated for different Reynolds number values in turbulent flow regime in the range 5000 < Re < 12000 in order to investigate the effect of the insert on the heat transfer mechanism.

In Figure (6.38) it is reported the local heat flux efficiency distribution for three different Reynolds number: from these data it is possible to notice that the butterfly-shaped device produces a stagnation point in correspondence of the two extreme parts of the "wings" where the temperature of the fluid reaches the highest values and the heat flux distribution presents its minimum.

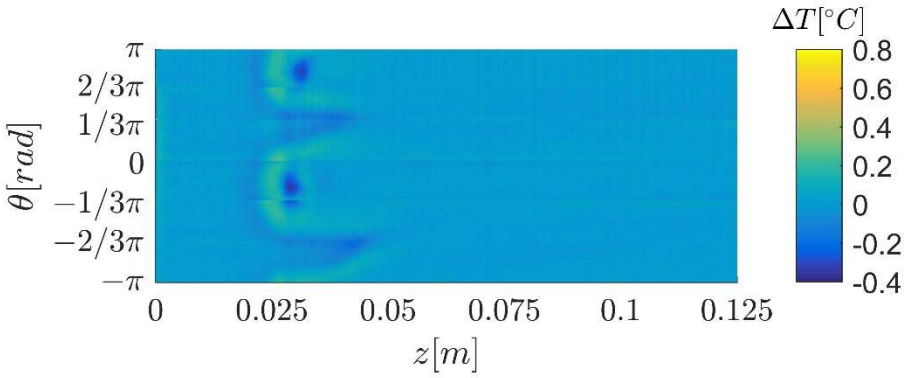

(a)

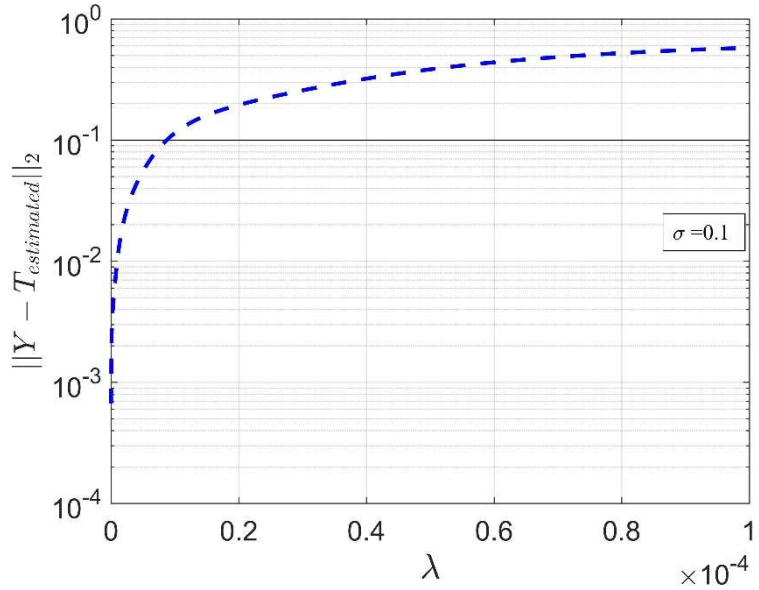

(b)

Figure 6.39: (a) Residual between the measured and the estimated external wall temperature, (b) Morozov's discrepancy principle for a representative case ($Re = 8800$)

It has to be pointed out that the Morozov's discrepancy principle was able to estimate the regularization parameter that has to be adopted, for all the three methodologies here presented, as it is possible to see from the random behaviour of the residual between the measured and the estimated external wall temperature profiles shown in Figure (6.39-a).

The application of the discrepancy principle to the three methodologies here analysed is shown in Figure (6.39-b).

As it is possible to see, the standard deviation of the residuals between the measured and the estimated temperature at the external boundary monotonically decrease as far as the regularization parameter increase. This behaviour is justified since by incrementing the regularization parameter less information about the signal is preserved during the estimation procedure, thus increasing the misfit between the temperature estimation at the external boundary and the measured one producing an over-smoothed estimated solution.

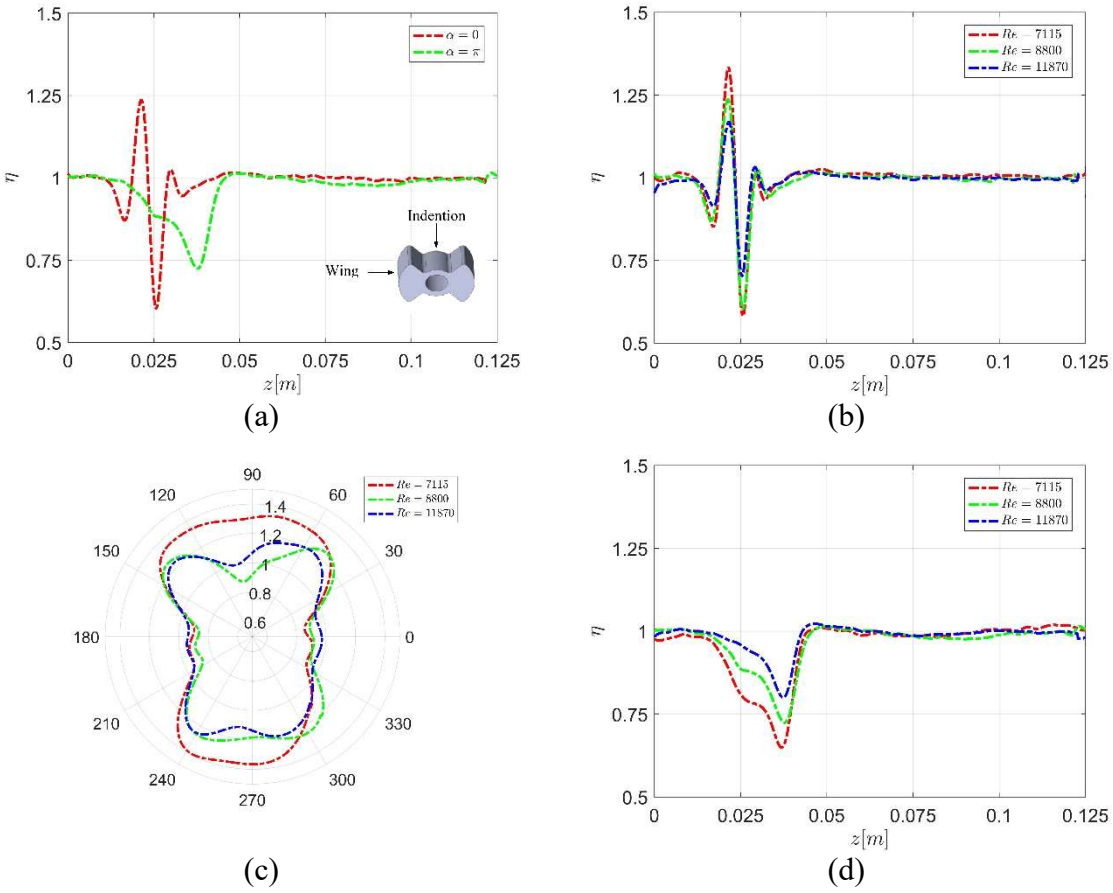

Figure 6.40: Local heat flux efficiency η: (a) axial distribution for different angle ($Re = 8800$) (b) axial distribution at $\alpha = \pi$ for three representative Reynolds numbers, (c) circumferential distribution at $z = 0.03\ m$ for three representative Reynolds numbers and (d) axial distribution at $\alpha = \pi/2$ for three representative Reynolds numbers

The application of the discrepancy principle to the three methodologies here analysed is shown in Figure (6.39-b). As it is possible to see, the standard deviation of the residuals between the measured and the estimated temperature at the external boundary monotonically decrease as far as the regularization parameter increase.

Moreover, it is possible to see that around the stagnation point there is an increase of heat flux and that it is due to the fluid acceleration. Finally, wakes appear in the downstream region. All these behaviours are similar to the ones observed in case of external flow on cross cylinder (*Incoprera2002*). It is also possible to notice that on the wall, by the central part of the indention, there is a local minimum in the heat flux distribution: a further investigation on this unexpected aspect is needed and the introduction of further criteria to valuate local performance should be considered.

In order to better analyse the qualitatively results shown in Figure (6.38), the axial distribution of the local heat flux efficiency η for different values of the angular coordinate α is reported for the representative Reynolds number $Re = 7180$. In particular, there were

considered two different distributions, one in correspondence of a "wing" ($\alpha = 3.14\ rad$) and one in the central zone of the "indention" of the butterfly shaped insert ($\alpha = 1.52\ rad$). In correspondence of the wing ($z = 0.03\ m$) it is evident the peak of minimum heat flux due to the stagnation point preceded by a local maximum due to the fluid acceleration in front and at the side of the wings. The central zone of the indention presents instead a decreasing trend: as first hypothesis, it could be due to a zone of lack of fluid mixing, but further investigations are needed. The same consideration could be extended to the other Reynolds numbers analysed.

For what concerned the circumferential distribution of the local heat flux efficiency η, the results are shown, using polar coordinate, in Figure (6.40-c) for the axial coordinate value $z = 0.03\ m$ (e.g. center of the insert). As it is possible to see for all the Reynolds number investigated, there is a local minima in correspondence of the two extreme parts of the wings (e.g. $\alpha = 0°$ and $\alpha = 180°$) and the two local peaks at the side of each wing.

All the three distribution of the local heat flux efficiency reported present similar trends but some differences in the values of the peaks could be observed. In fact, with the increasing of the Reynolds number the peak value decreases and the minimum value increases. In all probability, as observed by Li (*Li2017*), with increasing of the Reynolds number value, the higher turbulence intensity promotes a more efficient fluid mixing that tends to lessen the difference between the maximum and the minimum values.

The same consideration could be extended to the local convective heat transfer coefficient, since it is derived by the heat flux distribution; therefore, only the local maps of the convective heat transfer coefficients are reported (Figure (6.41)).

Given the above observation it is possible to conclude that the local estimation of the convective heat flux in pipes equipped with butterfly-shaped inserts was necessary to understand the reason of the experimentally measured average heat transfer enhancement. The local investigation was fundamental since it was able to demonstrate the great temperature and heat flux variation nearby the turbulator: characteristic that could be crucial in some practical application such as food and pharmacy industry. It was observed that the butterfly-shaped device produces a stagnation point in correspondence of the two extreme parts of the "wings" where the heat flux distribution presents its minimum. Moreover, it was possible to notice that around the stagnation point there was an increase of the local heat flux probably due to the fluid acceleration. Finally, wakes appear in the downstream region. All these behaviours are similar to the ones observed in case of external flow on cross cylinder.

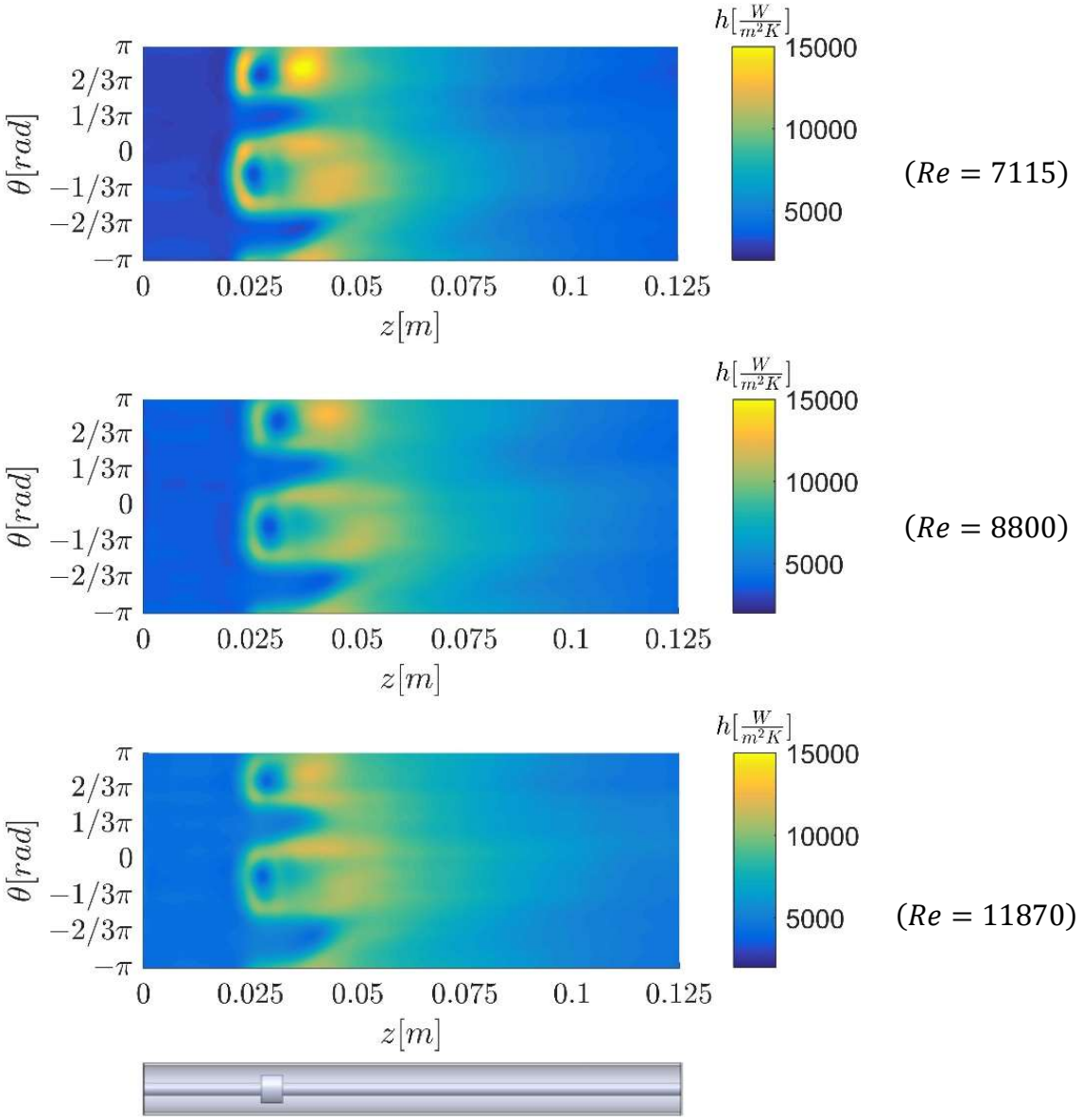

Figure 6.41: Local convective heat transfer coefficient for three representative Reynolds numbers

The experimental results obtained in the present investigation are particularly useful in the design of innovative heat exchangers equipped with these type of devices, as well as in the revamping of already installed smooth tube heat exchanger in order to increase their thermal efficiency.

6.4 Inverse estimation of the local convective heat transfer coefficient in straight tubes with cross-helix wall corrugated surface

INTRODUCTION

The 2D inverse problem here addressed, required the estimation of the local convective heat transfer coefficient in a straight tube characterized by a cross-corrugated wall. The solution of the IHCP was made by the zero-order Tikhonov regularization method couples with the Morozov's discrepancy principle both described in *Chapter 3*.

Such as in the previous paragraph, the local thermal performance is investigated in order to better understand the heat transfer enhancement mechanism related to this particular profile of corrugation.

There are a lot of industrial applications in which the working fluids is thermally treated in laminar flow regime where only low convective heat transfer coefficients could be reached: for example, this situation is encountered for highly viscous Newtonian fluids, like oils and many fluid food products. Therefore, it is straightforward that, in order to increase the thermal heat transfer efficiency of the heat exchanger, it is necessary to apply some techniques for increasing the heat transfer rate.

Among the many different methods which have been considered for enhancing the heat transfer in forced convection (*Webb1994*), the techniques which promote secondary recirculation flows, by inducing non-axial velocity components, appear very interesting in many practical applications. The secondary flow filed could be achieved by employing different methodologies such as spiral fins applied to the heat transfer surface, metallic twisted tape inserted into the tube, spirally roughened walls, etc. Watkinson (*Watkinson1975*) had experimentally investigated the forced convection of oils in straight smooth and internally spiralled fin tubes. The authors observed that for low Reynolds number values, the secondary flow field induced by the presence of the helix in the internal tube wall, cause a significant augmentation in the heat transfer coefficient. In particular, they suggest a correlation which predicts a dependence of the average Nusselt number on the fin pitch concluding that the spiral components produce a stronger effect in laminar than in turbulent flow. Moreover, the authors observed that the secondary swirl flow due to the fins causes instability by inducing an early transition to the turbulent flow, to which a strong heat transfer enhancement is associated. Almost the same dependence on the helix pitch has been

predicted by Ravigururajan (*Ravigururajan1996*) in the fully turbulent flow regime, for small helix angle. The numerical results reported by Date (*Date1974*) show that for highly viscous fluids heat transfer enhancement up to 70% can be obtained by using swirl flow inserts. Manglik (*Manglik1993*) observe the presence of two different flow regimes: for low Reynolds number values, the flow field is characterized by spiral pattern due to the tape's surface; while for high Reynolds number values the centrifugal force due to the rotating components prevails over the spiral pattern producing a secondary flow that mixes the fluid. A significant heat transfer enhancement is associated to both these flow regimes.

The review produced by Garimella (*Garimella1997*) shows that most of the published experimental works are focused on the turbulent flow, also because this type of corrugation produces an early transition to this flow regime: aspect that is of primary importance since the heat transfer rate is higher than in the laminar regime. Related to this aspect, Rainieri (*Rainieri1996*) experimentally observed that the integral inner-fin tubes, for Reynolds number values lower than the critical one usually taken for the smooth wall, a significant enhancement of both the Nusselt number and the friction factor occurs. This behaviour suggests an early transition to the turbulent regime. In the turbulent flow regime in the rage 1000÷15000, Garimella (*Garimella1988*) reported a heat transfer enhancement up to about 500% caused by the onset of swirl components into the main flow that periodically disrupt of the boundary layer. Related to these phenomena Nakayama (*Nakayama1983*) formulate the hypothesis that, according to the angle of the corrugation to the tube axis, different flow regimes can occur: for low helix angles the fluid flows try to follow the corrugation pattern close to the wall, while for high angles the fluid tends to cross the corrugation inducing a periodic separation of the boundary layer which induces important augmentation of the heat transfer coefficient.

The tube here tested was characterised by a cross-corrugation wall surface, which is obtained by the double corrugation of a pipe with two helix having different rotation direction: one clockwise and the other counter-clockwise. This particular type of corrugation produces two different grooves, which meet each other two times per pitch (Figure (6.42)). Due to the complex velocity field caused by the wall corrugation, the local analysis of the thermal performances could give a better understand of the heat transfer mechanism providing a new tool for the design of this type of heat exchanger, customizing the corrugation profile according to the products and production that has to be managed.

EXPERIMENTAL SET-UP

The experimental facility is the same describe in the previous paragraph and schematically shown in Figure (6.28).

The tested tube was made by stainless steel AISI-304. The corrugation profile was characterized by a corrugation pitch of $p = 29\ mm$ and a corrugation depth of $e = 0.6\ mm$ while the tube had an internal diameter, which was assumed as the characteristic length to evaluate both the Reynolds and the Nusselt number, of $D_{env} = 14\ mm$ and a wall thickness of $t = 1\ mm$. The meaning of the parameters used to describe the geometry under investigation are reported in a schematic drawing in Figure (6.42-a), while a picture of the tube tested is shown in Figure (6.42-b).

The tube wall is equipped with stainless steel fin electrodes which are connected to a power supply, type HP 6671A, working in the ranges 0–8 V and 0–220 A. Because of the low thermal conductivity of the wall material, the Joulean dissipation in the tube wall enables to approximate the condition of uniform heat flux at the fluid boundary. The heated section is about 2m long and it is preceded by an unheated development approach section of about 1 m. The whole section is thermally insulated by a 35 mm thick rubber thermal insulator layer, to minimize the heat exchange to the environment. The surface temperature distributions were acquired by means of a FLIR SC7000 unit, with a 640 x 512 pixel detector array. Its thermal sensitivity, as reported by the instrument manufacturer, is 20 mK at 303 K, while its accuracy is ±1 K. In this case, the inlet temperature has been measured by thermocouple probe directly immersed in the fluid upstream and downstream the heated zone. The uncertainties associated to the directly measured quantities have been assumed to be 0.2 C for temperature, and <0.1 C for temperature difference. For what concerns mass–flow rate and wall heat flux a percent uncertainty less than 1% has been estimated. The bulk temperature was assumed to be a linear function of the axial length of the tube, and its values were determined at any location of the heat transfer section starting from the power supplied to the. The data acquisition system consists essentially of a high precision multimeter (type HP 3458A) connected to a switch control unit (type HP 3488A) driven by a Personal Computer.

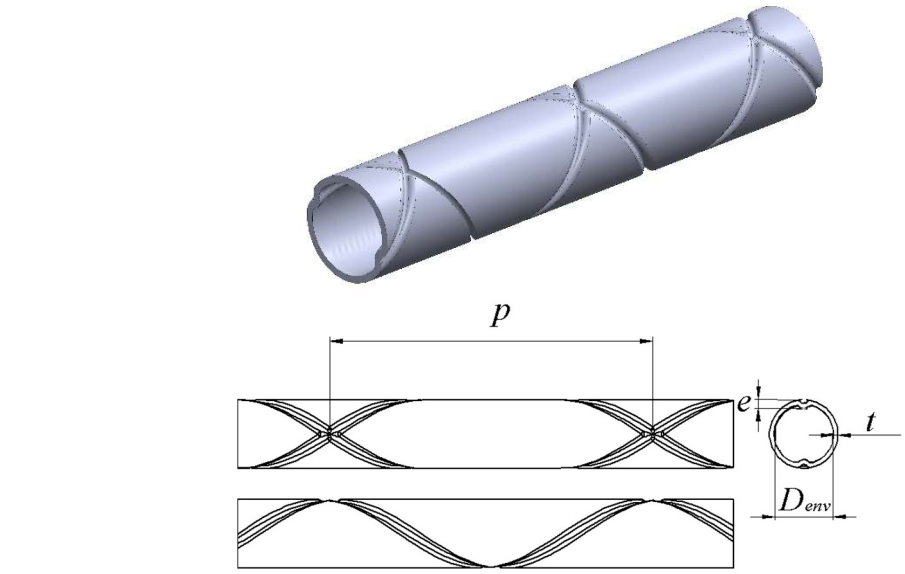

(a)

(b)

Figure 6.42: Tested tube (a) drawing scheme and (b) studied pipe coated with high emissivity paint and fitted with markers for the image cropping process

Flow rates were obtained by measuring the time needed to fill a volumetric flask placed at the outlet of the test section: the time required to fill a flask was measured with a high precision chronometer, while the mass was weighted by a high precision digital balance (*Tamagnini.srl*). Ethylene Glycol characterized by Prandtl number, in the temperature range achieved during the experiments, within the range 125-280 was used as working fluid in the Reynolds number range 365-910.

Since the tested tube is characterized by a rectilinear axis, it was possible to use the same test facility employed in the previous paragraph; therefore, the camera was conveniently fixed on the panel keeping its optical axis normal to the tube axis, minimizing perspective artefacts. Also in his case, the acquired images were trimmed with an angle of view lower than ± 30°, therefore the surface, coated with effective emissivity paint which emissivity was experimentally estimated by shooting a target at different known temperatures, was considered as a diffuse grey emitter (*Pavelka2013*).

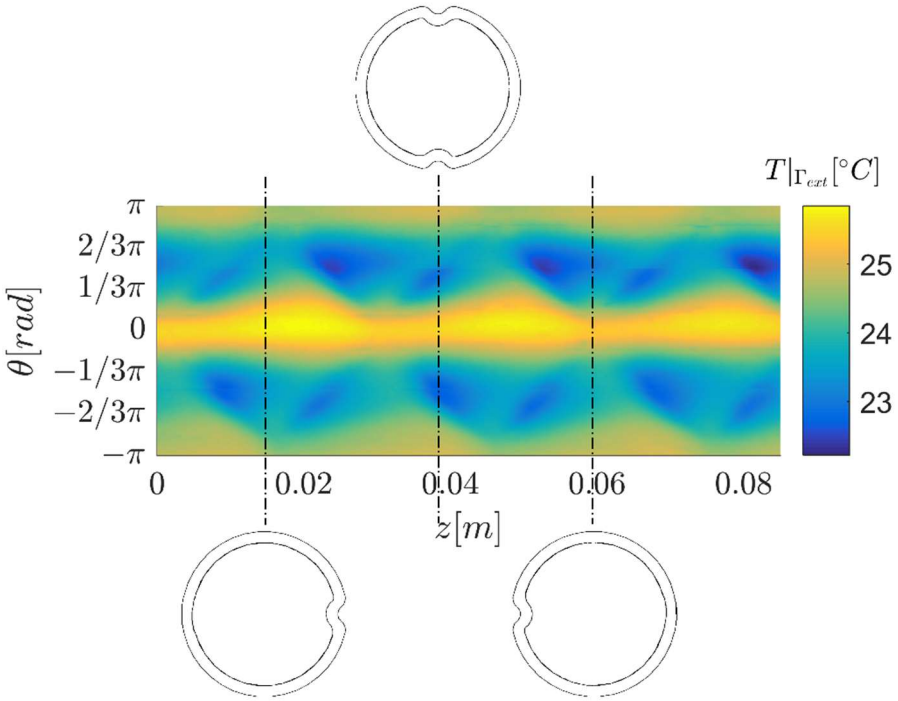

Figure 6.43: Experimental temperature measurements after the image processing (raw data) ($Re = 910$)

The image processing procedure was made complex by the non-planar geometry of the target. In order to partially overcome this problem, common photo-plans tools based on well-known equations of central projection could be employed but this is not really an easy task when dealing with curved objects (*Pavelka2013*). The image processing procedure adopted, presented by Bozzoli (*Bozzoli2016a*) permitted to rectify optical deformations of the collected images caused by surface curvature nevertheless is has to be pointed out that the external wall surface of the tube, was assumed to be cylindrical during the image processing, neglecting the surface deformation of the tube due to the corrugation process. The acquired images were cropped and merged together to obtain continuous temperature map on the tube wall, thanks to adequate position references fixed on the tube wall (Figure (6.42)).

In Figure (6.43) a representative temperature map of the external surface of the tube, is presented. It is clearly visible the distortion of the wall temperature distribution caused by the presence of the helical corrugation.

ESTIMATION PROCEDURE

The same estimation procedure described in the previous paragraph is used for the estimation of the convective heat transfer coefficient in cross-helix wall corrugated tube. In particular, the direct problem presented in *Chapter 5* (Equations (3.22)) could be linearized by writing the internal boundary condition in terms of wall heat flux instead of the convective heat flux coefficient, as follows:

$$\nabla^2 T = -\frac{q_G}{k} \quad \text{in } \Omega \tag{6.32.1}$$

$$-k\frac{\partial T}{\partial \mathbf{n}}\Big|_{\Gamma_{int}} = q(\theta, z) \quad \text{on } \Gamma_{\text{int}} \tag{6.32.2}$$

$$-k\frac{\partial T}{\partial \mathbf{n}}\Big|_{\Gamma_{ext}} = h_{ext}(Y - T_{env}) \quad \text{on } \Gamma_{\text{ext}} \tag{6.32.3}$$

$$-k\frac{\partial T}{\partial \mathbf{n}}\Big|_{\Gamma_{int}} = 0 \quad \text{on } \Gamma_{top} \tag{6.32.3}$$

$$-k\frac{\partial T}{\partial \mathbf{n}}\Big|_{\Gamma_{int}} = 0 \quad \text{on } \Gamma_{bottom} \tag{6.32.3}$$

where Y are some extra temperature measurements taken at the external surface Γ_{ext} by means of the thermographic camera while $\boldsymbol{q}(\theta)$ is the unknown boundary condition that has to be estimated.

In this way, the system of Equation (6.32) becomes linear respect to the imposed heat flux and the convective heat flux distribution could be calculated, once the heat flux estimation is performed.

Since the inverse problem is linear in the unknown variable $\boldsymbol{q}$, the zero order Tikhonov regularization method could be used for the internal wall heat flux estimation:

$$\boldsymbol{q}_\lambda = (\boldsymbol{X}^T\boldsymbol{X} + \lambda^2\boldsymbol{L}^T\boldsymbol{L})^{-1}\boldsymbol{X}^T\left(\boldsymbol{Y} - \boldsymbol{T}_{\boldsymbol{q}=\boldsymbol{0}}\right) \tag{6.33}$$

where $\boldsymbol{T}$ is the estimated temperature on the sampling position (e.g. in all the entire), $\boldsymbol{X}$ is the sensitivity matrix, $\boldsymbol{q}$ is the unknown heat flux distribution, $\boldsymbol{T}_{q=0}$ is the estimated temperature on the sampling position if no heat flux is applied on the boundary at Γ_{int}.and $\boldsymbol{L}$ is the identity matrix.

It has to be pointed out that since the boundary condition adopted on the top and on the bottom of the pipe are not the one that better model the phenomenon, it was necessary to extend the module under investigation two times before and two times after the test section, as shown in Figure (6.44).

It has to be pointed out that, the unknown heat flux distribution was discretized in order to have the same pitch in both the circumferential and axial coordinate: in particular, it was discretised in 360 values along the θ coordinate and 750 values along the z coordinate.

This configuration allowed using the same regularization parameter in both the direction, giving the same weight to the filter function. The same discretization was adopted for the temperature measurement available at the external surface, after the image processing procedure.

Finally, in order to generalize the results obtained, the heat transfer performances are compared in terms of average Nusselt number as a function of the Reynolds number.

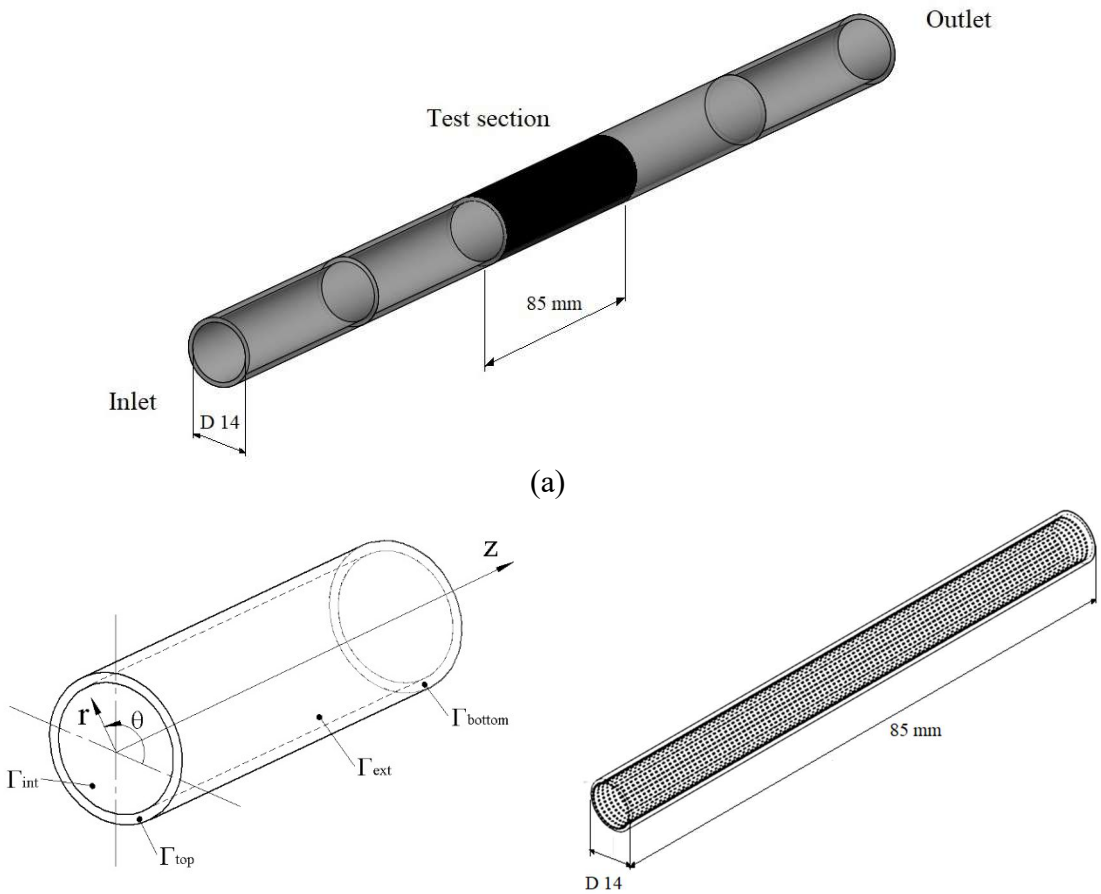

Figure 6.44: Function estimation: (a) Geometrical domain and (b) inverse problem boundary conditions schemes

RESULTS

Before examining the local convective heat transfer characteristics of the cross-helix wall corrugated tubes, it was investigated how these devices impact the overall thermal performance of the pipes under test. The heat transfer performances were dimensionless quantified by means of the Nusselt number in order to generalize the obtained results. The methodology used for the estimation of the average performances was already described in the previews experiment and the results are shown in Figure (6.45) where the Nusselt number if graphed as a function of the Reynolds number together with the traditional correlation provided by Shah (*Shah1978*) for the laminar regime in straight smooth tubes.

These data show a significant increment of the thermal performances compared to the straight smooth wall pipe without inserts, confirming the goodness of this type of devices as convective heat transfer enhancement technique. The local Nusselt number along the dimensionless abscissa, defined in Equation (6.20), is reported in Figure (6.46), for two representative Reynolds number values, together the analytical solution holding for the smooth wall pipe with uniform heat flux boundary condition (*Shah1978*).

$$x^* = \frac{x}{Re\ Pr\ D_{env}} \tag{6.34}$$

where x is the axial coordinate of the tube.

The effect of the corrugation is clearly visible: by increasing the Reynolds number the heat transfer characteristics of the corrugated tube depart from the smooth wall behaviour by providing a significant heat transfer augmentation. For the lowest investigated Reynolds number values, the thermal behaviour is close to smooth wall while for the highest Reynolds number values the heat transfer enhancement due to the wall corrugation appear.

In Figure (6.46) it is also possible to observe that, in agreement with the findings of Rainieri (*Rainieri1996*), in the fully developed region of corrugated pipes the local Nusselt number distribution is not constant but it presents peaks and valleys due to the continuous disruption and formation of the boundary layer caused by the wall corrugation.

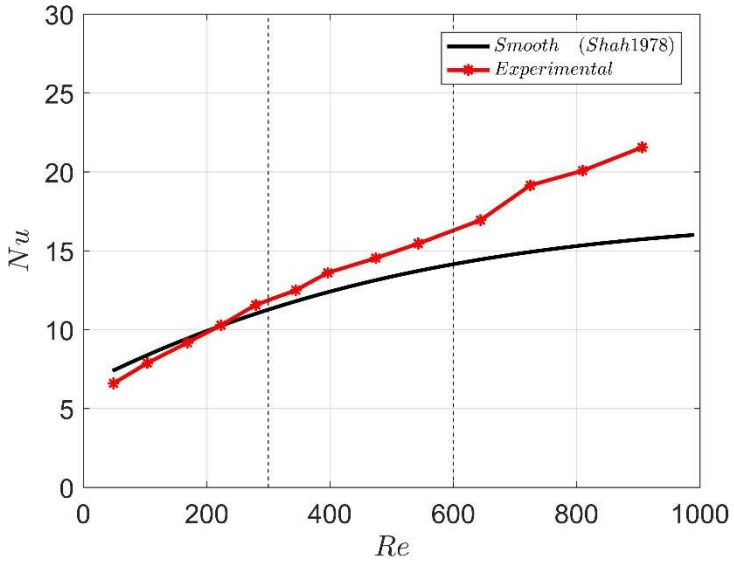

Figure 6.44: Average Nusselt number as a function of the Reynolds number

Moreover, it is possible to notice that one of the main effects of the corrugation is the early transition from the laminar to the unstable flow regime, phenomena that seem occurs through a sequence of intermediate state as found by Guzman (*Guzman1996*). In fact, it is possible to see a first transition to an unstable regime occur around $Re = 300$ while a second transition to the complete unstable regime is visible around $Re = 700$.

A further insight into the heat transfer phenomena was found in the analysis of the local heat transfer performance over the entire surface. It has to be remarked that since the IHCP is non-linear in terms of the convective heat transfer coefficient, the problem has to be re-written in terms of heat flux rate. In this way, it is possible to estimate the convective heat flux coefficient after the solution of one direct problem in which the imposed heat flux at the internal boundary is provided by the inverse estimation.

In order to understand the thermal efficiency compared to the straight smooth pipe, it is possible to define the local heat flux efficiency η:

$$\eta = \frac{q_{int}}{q_0} \tag{6.35}$$

where q_0 is the internal heat flux for the tube, in the same experimental conditions, without the inserts. The maps of this parameter are fundamental in order to investigate the effect of the corrugation in terms of local peaks, stagnation points and influence lengths.

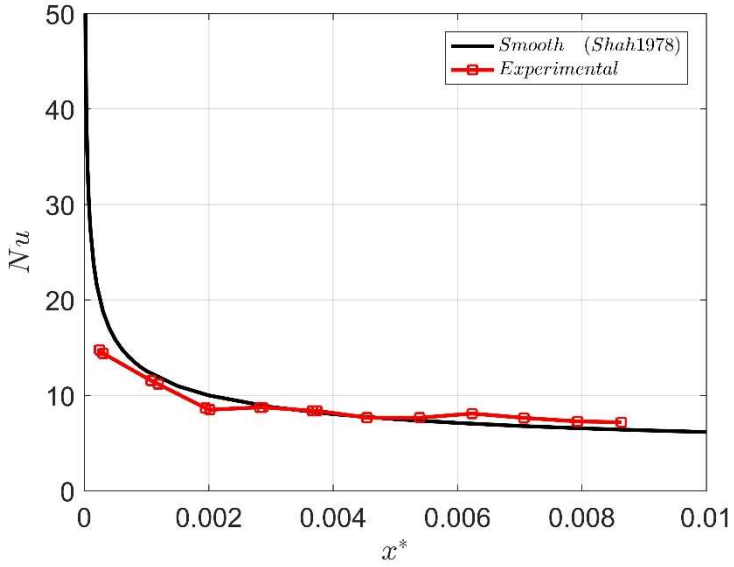

(a)

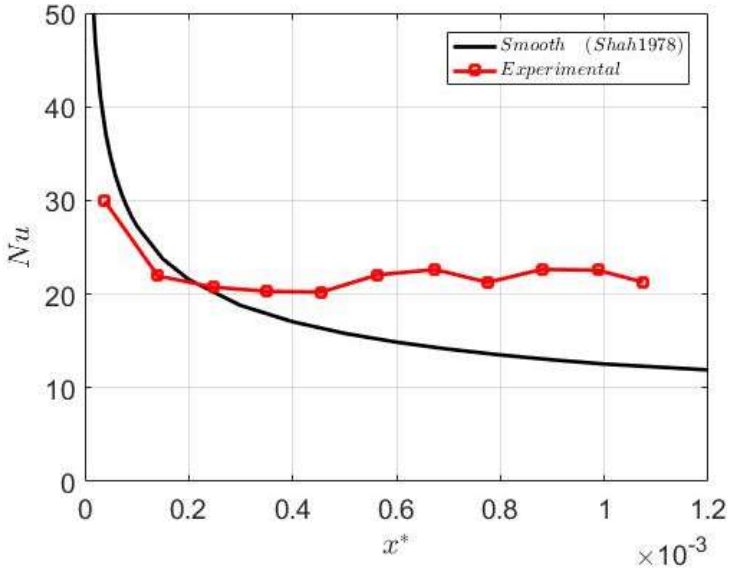

(b)

Figure 6.46: Axial Nusselt number as a function of the dimensionless abscissa for two representative Reynolds number (a) $Re = 100$ and (b) $Re = 909$

The local estimation procedure was repeated for different Reynolds number values in laminar flow regime in the range 100 < Re < 900 in order to investigate the effect of the corrugation on the heat transfer mechanism.

In Figure (6.47) is reported the local heat flux efficiency distribution for three different Reynolds number: from these data it is possible to notice that for all the Reynolds number here investigated, the corrugation profile in not effective where the two helixes meet each other, while the efficiency is higher when they are on the opposite sides of the tube. This phenomena is more visible as far as the Reynolds number increases, according to the observation provided by Nakayama (*Nakayama1983*).

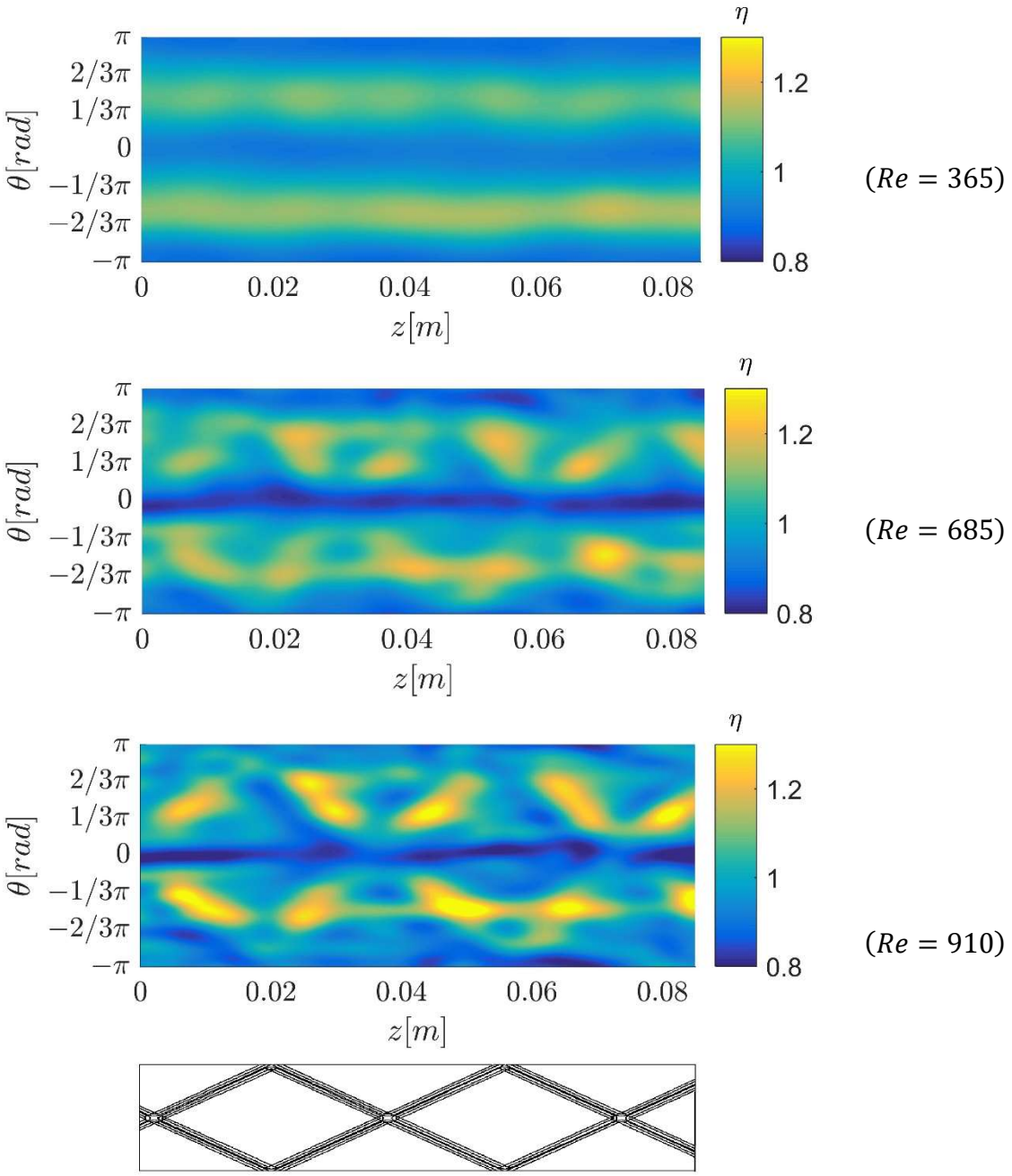

Figure 6.47: Local heat flux efficiency η for three representative Reynolds numbers

It has to be pointed out that in all the cases, the regularization parameter was defined according to the Morozov's discrepancy principle (Figure (6.48)). The application of the discrepancy principle to the three methodologies here analysed is shown in Figure (6.48-b). As it is possible to see, the standard deviation of the residuals between the measured and the estimated temperature at the external boundary monotonically decrease as far as the regularization parameter increases.

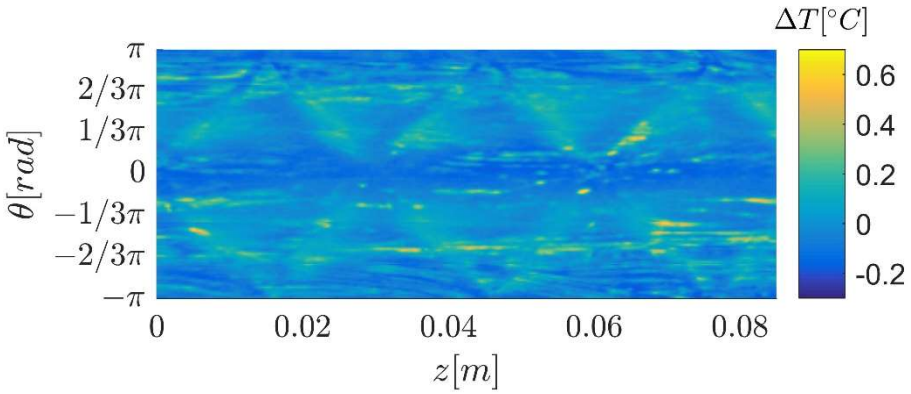

(a)

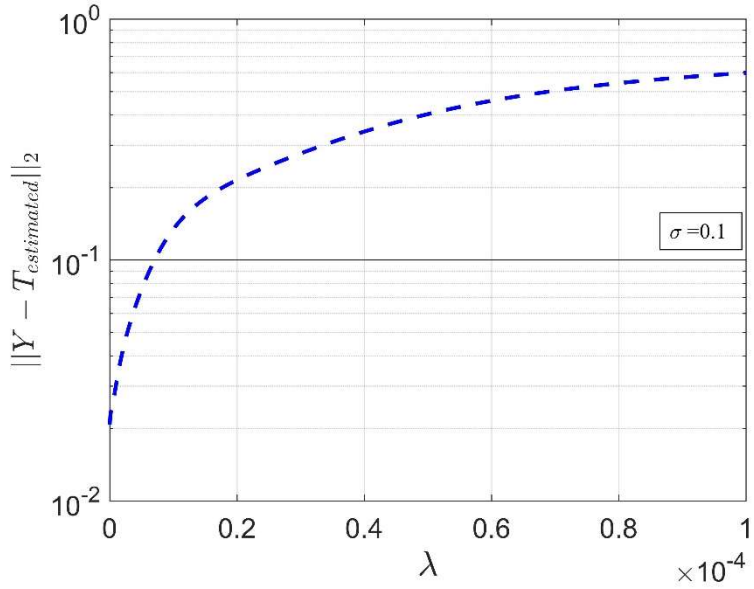

(b)

Figure 6.48: (a) Residual between the measured and the estimated external wall temperature, (b) Morozov's discrepancy principle for a representative case ($Re = 685$)

It is possible to see that in correspondence of the crossing grooves, the heat transfer efficiency is always negligible compared to the straight tube, while in correspondence of opposite grooves the efficiency becomes significant. Finally, it is clearly visible the appearing of a different heat flux efficiency pattern distribution according to the different flow regimes: the pattern is smooth and continuous for low Reynolds number values, it becomes unstable around the transitional regime in which start to appear structures that become clearly distinguishable in the pure turbulent flow regime.

In particular in correspondence of the corrugation crossing, the fluid flow overcomes the corrugation without any perturbation for all the Reynolds number here investigated highlighting the non-effectiveness of the corrugation in this particular position.

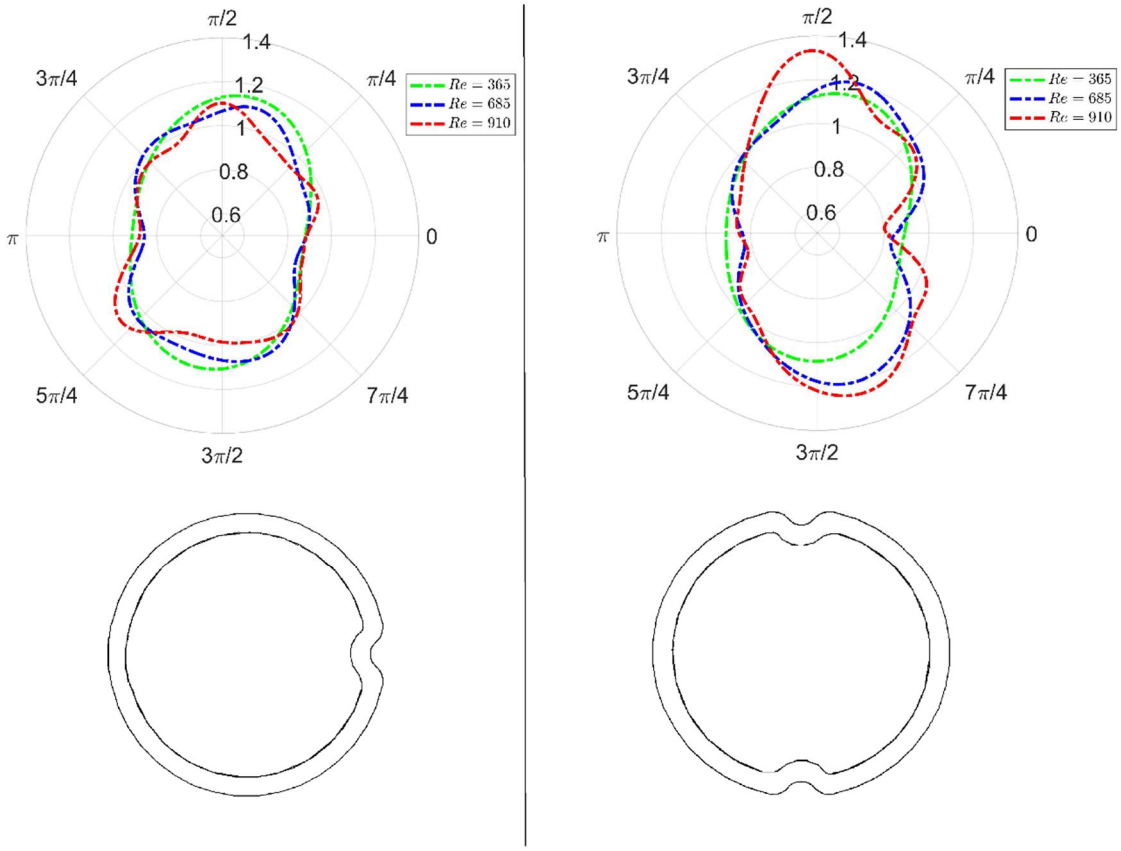

Figure 6.49: Local heat flux efficiency η for three representative Reynolds numbers in two different cross-sections of the pipe

On the other hand, when the corrugation grooves are in opposite positions the efficiency becomes significant for high Reynolds number, while for the lower ones the fluid flow still be able to overcome the corrugation without any significant perturbation.

More details could be catch by analysing the circumferential heat flux efficiency (Figure (6.49)). In particular it is possible to see, that the local efficiency in correspondence of the corrugation crossing is almost negligible, while it becomes significant when the corrugation are opposite. In this configuration is clearly visible the characteristic lobe behaviour assume by the local heat flux efficiency that recall the position of the corrugation groove.

A better understand on the phenomena could be achieved by looking at the local efficiency along two generative of the tube, as shown in Figure (6.50).

Looking at the upper part of Figure (6.49), which represents the heat flux efficiency along the brown line superimposed on the tube scheme depicted below the graph, it is clearly possible to see that for low Reynolds number values, the fluid overcomes the corrugation with small fluctuation that becomes more severe increasing the Reynolds number values.

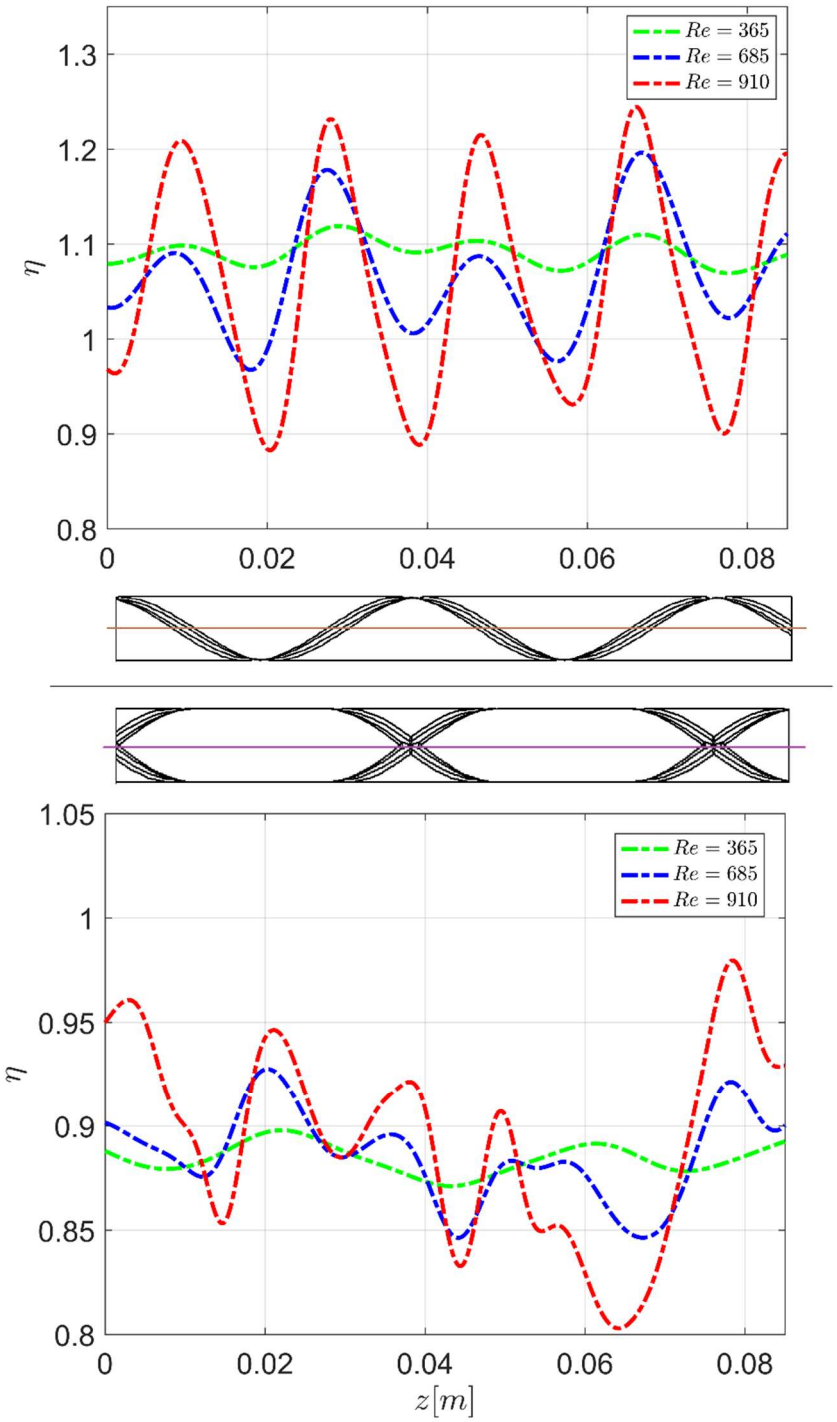

Figure 6.50: Local heat flux efficiency η for three representative Reynolds numbers along two different generative of the pipe

Looking more into detail of this graph, an interesting behaviour that correlate the heat flux efficiency with the corrugation profile comes out. In particular, it is possible to see that, for all the Reynolds numbers here investigated, the heat flux efficiency peaks appear in correspondence of opposite corrugation, while the valleys appear in correspondence of the

corrugation crossing. This aspect confirm what already suggested by Nakayama (*Nakayama1983*) and is in completely agreement with wat was observed in Figure (6.42).
Moreover it is possible to observe the transition from the laminar to the turbulent regime: for the lowest Reynolds numbers reported, the fluid pass over the corrugation in a pretty regular fashion (pure laminar regime), behaviour that is keep also for the highest Reynolds number value (pure turbulent regime) but is lost for the intermediate Reynolds number (transitional regime). This aspect is in completely agreement with the average values reported in Figure (6.44).
For what concerned the lower part of Figure (6.50), which represents the heat flux efficiency along the purple line superimposed on the tube scheme depicted above the second graph it is clearly possible to see that for all the Reynolds number values here investigated, the fluid overcomes the crossing grooves with small random fluctuations in which it is difficult to understand a common scheme like in presence of opposite grooves. This behaviour could be related to the onset of secondary flows caused by the presence of the two helixes that drive the flow form one crossing point to the second one but further investigation are required.
The same consideration could be extended to the local convective heat transfer coefficient, since it is derived by the heat flux distribution; therefore, only the local maps of the convective heat transfer coefficients are reported (Figure (6.51)).
Given the above observation it is possible to conclude that the local estimation of the convective heat flux in wall cross-corrugated pipes was necessary to understand the reason of the experimentally measured average heat transfer enhancement. In fact, the physical phenomena governing the heat transfer enhancement for wall cross-corrugated enhanced tubes have not been wholly understood, despite the fact that many empirical correlations have been suggested for predicting their overall thermal performance.
In terms of average heat transfer enhancement performances the forced convective heat transfer in cross-helix corrugated wall tubes was studied in the Reynolds and Prandtl number ranges 100÷900 and 125÷280 respectively, by adopting ethylene glycol and water-ethylene glycol mixtures as working fluids. The results were expressed in terms of average Nusselt number as well as of local heat flux efficiency and convective heat transfer coefficient. The data show that the corrugation produce an clearly departure from the laminar to the turbulent flow regime, compared to the smooth wall, occurring around $Re = 300$ and a probable second transition is present around $Re = 600$. These data confirm that the transition from laminar to unstable regime can occur through a sequence of intermediate state as observed by Guzman (*Guzman1996*).

The local investigation was fundamental to clearly understand the heat transfer phenomena, since it was able to demonstrate the great non-uniform convective heat flux distribution. In particular, the local inverse estimation procedure, was able to highlight the zone in which the corrugation profile is more effective suggesting the possibility of design of new customized corrugation profile that could enhance the local performances of this type of heat exchanger. Finally, the identification of different heat flux pattern due to different mass flow rate suggest the usage of the local estimation procedure for the identification of different flow regimes.

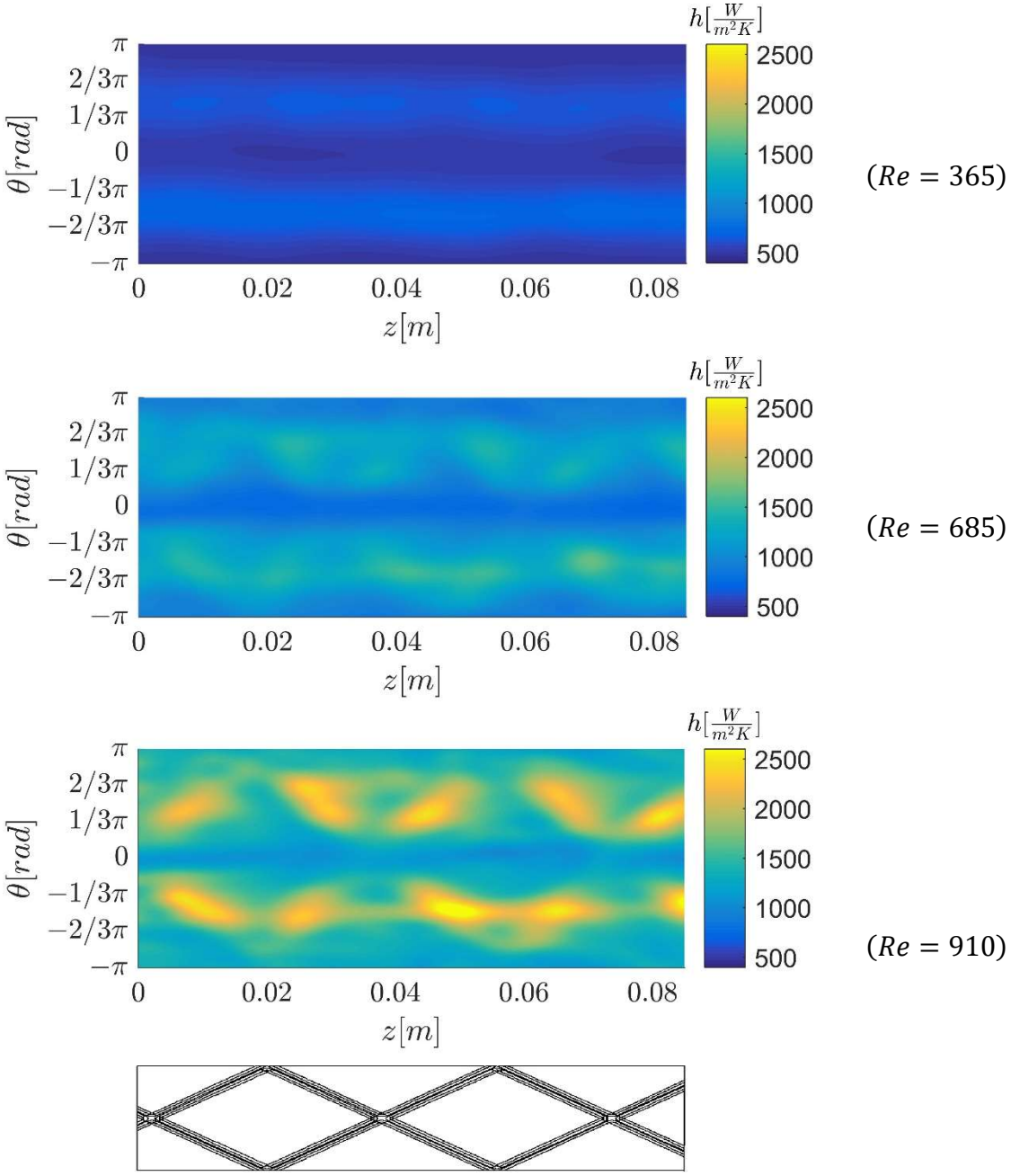

Figure 6.51: Local convective heat transfer coefficient for three representative Reynolds numbers

Conclusion

The aim of this thesis was to develop and test new methodologies able to solve the inverse heat transfer problem, in order to characterize some types of heat transfer devices. First, three new estimation procedures were developed and verified using virtual experiments. After, they were applied to four original experiments built both for industrial and research interest.

The main characteristic of the inverse analysis is to provide information on boundaries that are not directly observable. Therefore, the inverse estimation here addressed allowed to develope new and easy to configure test rigs able to provide useful information related to the non-accessible boundaries although giving valuable information on the physical phenomena occurring inside the pipe. Those information could also be used to optimize the heat transfer device, customizing it for each particular application. It has to be pointed out that even if the experimental setup could be easier, the post processing of the measured data through the inverse estimation could be a more complex task.

Since the inverse estimation is a versatile procedure, all the methodologies proposed could be easily extended to different experimental setup if a proper mathematical description of the physical phenomena is given and the sensitivity analysis is performed. Moreover, the local estimation of thermal performances could also be used in order to validate numerical models comparing the results coming from the simulation with the once experimentally observed.

The computational effort required from the estimation of the solution of the linear inverse problem, here addressed, by means of the Tikhonov regularization and the Singular Value Decomposition are concentrated in the sensitivity matrix calculation. This matrix change each time the physical domain and the boundary condition change requiring its re-calculation. It is straight forward that this problem could be limited if the analytical solution of the direct problem is achievable; it is related to this aspect the proposed improvement of the Reciprocity Functional gap here presented. This original methodology, here named Filtered Reciprocity Functional, require the solution of two auxiliary direct problems that, in this thesis, were analytically solved yielding to the reduction of the disruptive effect of the noise contented in the measurement during the inverse estimation. The beneficial effect introduced by the analytical solution of the auxiliary problems is related to the possibility of separate the signal, which is assumed to be prevalent at the low frequency, from the noise, which is assumed to be uniformly distributed in the frequency domain, by using an ideal low pass filter.

The results showed that the new method outperform the Truncated Singular Value Decomposition and the Numerically integrated Reciprocity Functional, estimating solution with a lower averaged error.

It has to be pointed out that, the above mentioned techniques are characterized by a discontinuous filter function. Related to this aspect, an original improvement of the Truncated Singular Value Decomposition characterized by a continuous filter function, here named Gaussian Filtered Singular Value Decomposition, was proposed. The results showed that the new method outperform the Truncated Singular Value Decomposition providing estimated solution comparable with the one obtained by using the Tikhonov regularization scheme. The improvement in the reconstruction quality of the signal is due to the preservation of some high harmonics order that, even if dumped by the filter function, can give additional information during the inverse estimation.

The experimental application of the inverse analysis allowed to characterize the heat transfer devices considered in the present work. In particular, the new methodology, based on the Iterative Re-weighted Least Square approach, was able to estimate the average thermal performances of a tube in tube heat exchanger, estimating also the confidence interval on each unknown parameter. The inverse estimation were also able to propose useful correlation for the estimation of the average Nusselt number at both the shell and tube sides at different flow regimes. The experimental results demonstrate that the bio-inspired tubes significantly increase the heat transfer performances of the tube, compared to the smooth straight one, in

the tested Reynolds number region. In particular, the thermal performance of the bio-inspired tubes is up to 500 % higher in terms of relative Nusselt number. Moreover, the experimental campaign showed that the bio-inspired tubes with shorted corrugation period are generally more efficient compared to the long period once. It is also noticeable that the corrugation period has higher impact on the thermal performances compared to the aspect ratio.

For what concern the local estimation of the convective heat transfer coefficient in coiled tube, the inverse estimation showed that these devices promote a highly uneven convective heat flux distribution along the circumferential coordinate, impacting on the performances of the thermal treatment: in particular the measurements showed that the convective heat transfer coefficient is lower at the inner bend side than at the outer bend side where its distribution is more flat. These results are representative of a wide range of technical applications and they might be particularly useful in the validation of numerical models or in the design of innovative coiled tube heat exchangers.

Regarding the 3D local estimation of convective heat transfer coefficient in straight tubes fitted with butterfly-shaped insert devices, the inverse analysis showed that even if this kind of insert is very effective, its employment could be critical in some applications due to the presence of great variations in both the temperature and the heat flux distribution. The experimental measurements, pointed out that the butterfly-shaped device promotes a stagnation point in correspondence of the “wings” where the heat flux distribution presents its minimum; it was also possible to notice that around the stagnation point there was an increase of the local heat flux probably due to the fluid acceleration which promotes the presence of wakes in the downstream region. The local estimation of the thermal performances appeared to be particularly useful in the design of innovative heat exchangers equipped with these type of devices especially during the optimization the insert shape.

Finally, the straight cross-helix wall corrugated tubes were analysed. Those devices are employed in a broad variety of industrial applications in order to increase the convective heat transfer by reducing the thickness of the boundary layers. The experimental 3D local estimation of convective heat transfer coefficient of those devices by inverse analysis, allowed to better understand the heat transfer mechanism. In particular, it was possible to observe that the helical corrugation induces significant swirl components for the lower Reynolds number here investigated, while for the higher one, the fluid flow pattern is lost due to the onset of instability introduced by the wall corrugation. Moreover, the local estimation showed the presence of a highly non-uniform heat flux and temperature distribution that could affect the thermal treatment of the fluid that is passing into the tube.

Finally, the inverse estimation allowed identifying of different fluid flow regimes characterized by different fluid flow structure.

Future development could be related to the formulation of new algorithms as well as to the application of the inverse estimation to new experimental setup. For what concern the estimation of the average performances of the tube in tube heat exchanger, it has to be pointed out that the cost function here adopted is based on the residual between the estimated and the measured global convective heat transfer coefficient. Thus, the estimation quality could be probably improved by defining a new cost function based on the observed variable (e.g. the temperature of the fluid) and not on a quantity from it derived (e.g. the global convective heat transfer coefficient). This aspect require a more detail investigation since more the one temperature, as well as combinations of temperatures can be monitored, while the global convective heat transfer coefficient is defined in order to take into account the global performance of the heat exchanger.

For what concern the local estimation of the thermal performances by means of the Filtered Reciprocity Functional, a significant improvement could be achieved if a continuous filter function will be applied.

Finally, all the algorithms here developed were related to the steady state condition, nevertheless their extension to the transitional regime could be achieved by properly tattling the sensitivity matrices, for the sensitivity based solution strategies, and the auxiliary problems, for the reciprocity functional based approach.

Since the inverse estimation is a versatile approach, the new methodologies could be employed for the estimation of the innovative heat transfer devices such as microchannels, heat pipes, thermal energy storage, etc.

Appendix 1

Filtered Reciprocity Functional: mathematical development

A.1 Solve the first auxiliary problem system using the Classical Integral Transform Technique:

The linear system presented in *Chapter 4* (Equation (4.14)) could be solved analytically by using the Classical Integral Transform Technique. The analytical solution of the PDE system avoid the use of numerical method to solve this system making the code computationally fast.

Operate on the physic in θ direction:

Due to physical problem, is possible to write the Laplacian defined in the Equation (4.14.1) using the cylindrical coordinate:

$$\frac{1}{r}\frac{\partial}{\partial r}\left(r\frac{\partial G}{\partial r}\right)+\frac{1}{r^2}\frac{\partial}{\partial \theta}\left(\frac{\partial G}{\partial \theta}\right)=0$$
$$\frac{\partial^2 G}{\partial r^2}+\frac{1}{r}\frac{\partial G}{\partial r}+\frac{1}{r^2}\frac{\partial^2 G}{\partial \theta^2}=0 \quad \text{(A.1)}$$

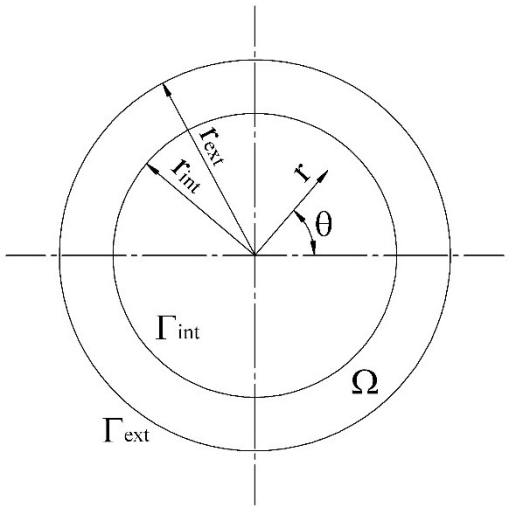

Figure A.1: 2D domain

Defining the integral transform as:

$$\bar{G} = \int_{\theta=0}^{2\pi} G_{(r,\nu,\theta\prime)}\, cos[\nu(\theta - \theta')]\, d\theta' \tag{A.2}$$

and the inversion formula, that could be divided in two part: the first one is a constant term while the second one is function of the number of the harmonics:

$$G = \frac{1}{2\pi}\bar{G}_{(r,\theta,\nu=0)} + \sum_{\nu=1}^{\infty}\frac{1}{\pi}\bar{G}_{(r,\theta,\nu)} \tag{A.3}$$

is possible to re-write the Laplacian in cylindrical coordinate, defined in the Equation (A.1), multiplying times $cos[\nu(\theta - \theta')]$ and integrating it:

$$\int_{\theta\prime=0}^{2\pi}\frac{\partial^2 G}{\partial r^2}\, cos[\nu(\theta - \theta')]\, d\theta' + \int_{\theta\prime=0}^{2\pi}\frac{1}{r}\frac{\partial G}{\partial r}\, cos[\nu(\theta - \theta')]\, d\theta' + \int_{\theta\prime=0}^{2\pi}\frac{1}{r^2}\frac{\partial^2 G}{\partial \theta^2}\, cos[\nu(\theta - \theta')]\, d\theta' = 0$$

$$\frac{\partial^2}{\partial r^2}\int_{\theta\prime=0}^{2\pi} G\, cos[\nu(\theta - \theta')]\, d\theta' + \frac{1}{r}\frac{\partial}{\partial r}\int_{\theta\prime=0}^{2\pi} G\, cos[\nu(\theta - \theta')]\, d\theta' + \frac{1}{r^2}\int_{\theta\prime=0}^{2\pi}\frac{\partial^2 G}{\partial \theta^2}\, cos[\nu(\theta - \theta')]\, d\theta' = 0$$

substituting the definition given in the Equation (A.2) is easy to get:

$$\frac{d^2}{dr^2}\bar{G} + \frac{1}{r}\frac{d}{dr}\bar{G} + \frac{1}{r^2}\int_{\theta\prime=0}^{2\pi} \frac{\partial^2 G}{\partial\theta^2}\ cos[\nu(\theta-\theta')]\, d\theta' = 0 \tag{A.3}$$

the last integral of this equation can be solved integrating by part two times:

$$\int_{\theta\prime=0}^{2\pi} cos[\nu(\theta-\theta')]\frac{\partial^2 G}{\partial\theta^2}d\theta'$$

$$= \left(\frac{\partial G}{\partial\theta}\cos[\ \nu(\theta-\theta')\ ]\right)_{\theta=0}^{2\pi} - \int_{\theta'=0}^{2\pi} -\nu\sin[\nu(\theta-\theta')]\ \frac{\partial G}{\partial\theta}\ d\theta'$$

$$= \left(\frac{\partial G}{\partial\theta}\cos[\ \nu(\theta-\theta')\ ]\right)_{\theta=0}^{2\pi} - (-G\nu\sin[\nu(\theta-\theta')])_{\theta=0}^{2\pi}$$

$$- \int_{\theta'=0}^{2\pi} \nu^2\cos[\nu(\theta-\theta')]\ G\ d\theta' = -\nu^2\bar{G}$$

Substituting this expression in the Equation (A.3) the transformation of the physical problem, become:

$$\frac{d^2}{dr^2}\bar{G} + \frac{1}{r}\frac{d}{dr}\bar{G} + \frac{1}{r^2}\nu^2\bar{G} = 0 \tag{A.4}$$

Operate on the boundary conditions:

The conditions imposed at the internal boundary Γ_{int} (Equation (4.14.2)) is easy transformed by multiplying times $cos[\nu(\theta-\theta')]$ and integrating it to get:

$$\int_{\theta'=0}^{2\pi} \frac{\partial G}{\partial r}\cos[\nu(\theta-\theta')]\, d\theta' = \frac{\partial G}{\partial r}\int_{\theta'=0}^{2\pi} G\cos[\nu(\theta-\theta')]\, d\theta'$$

remembering the definition given in the Equation (A.2) is possible to re-write the last expression to get the transformation of the internal boundary condition:

$$\frac{d\bar{G}}{dr} = 0 \tag{A.5}$$

The conditions imposed at the external boundary Γ_{ext} (Equation (4.14.3)) is easy transformed by multiplying times $cos[\nu(\theta - \theta')]$ and integrating it to get:

$$\int_{\theta'=0}^{2\pi} G \cos[\nu(\theta - \theta')]\, d\theta' = \frac{\partial G}{\partial r} \int_{\theta'=0}^{2\pi} \psi \cos[\nu(\theta - \theta')]\, d\theta'$$

remembering the definition given in the Equation (A.2) is possible to re-write the last expression to get the transformation of the external boundary condition:

$$\bar{G} = \bar{\psi} \tag{A.6}$$

where $\bar{\psi}$ is the transformation of the potential imposed in the first auxiliary problem (Equation (4.14.3)):

$$\bar{\psi} = \int_{\theta'=0}^{2\pi} \psi \cos[\nu(\theta - \theta')]\, d\theta' \tag{A.7}$$

Final system of equation and its solution:

The transformation of the auxiliary problem defined by the Equations (4.14.1)-(4.14.3) is:

$$\begin{aligned} \nabla^2 \bar{G} &= 0 \quad in\ \Omega \\ \left.\frac{d\bar{G}}{dr}\right|_{\Gamma_{int}} &= 0 \quad at\ \Gamma_{int} \\ \bar{G} &= \bar{\psi} \quad at\ \Gamma_{ext} \end{aligned} \tag{A.8}$$

the last system of equations is easy to solve. The solution of the transformed problem is:

$$\bar{G} = \bar{\psi}_{\nu} \cosh\left[\nu\left(\ln\left[\frac{r_{int}}{r}\right]\right)\right] \operatorname{sech}\left[\nu\left(\ln\left[\frac{r_{int}}{r_{ext}}\right]\right)\right] \tag{A.9}$$

In order to obtain the solution of the first auxiliary problem, the last equations has to be inverted using the definition given in the Equation (A.3):

$$G = \frac{1}{2\pi}\bar{\psi}_{\nu=0}\cosh\left[\nu\left(\ln\left[\frac{r_{int}}{r}\right]\right)\right]_{\nu=0}\operatorname{sech}\left[\nu\left(\ln\left[\frac{r_{int}}{r_{ext}}\right]\right)\right]_{\nu=0}$$
$$+\sum_{\nu=1}^{\infty}\frac{1}{\pi}\,\bar{\psi}_{\nu}\cosh\left[\nu\left(\ln\left[\frac{r_{int}}{r}\right]\right)\right]\operatorname{sech}\left[\nu\left(\ln\left[\frac{r_{int}}{r_{ext}}\right]\right)\right] \qquad \text{(A.10)}$$
$$=\frac{1}{2\pi}\bar{\psi}_{\nu=0}+\sum_{\nu=1}^{\infty}\frac{1}{\pi}\,\bar{\psi}_{\nu}\cosh\left[\nu\left(\ln\left[\frac{r_{int}}{r}\right]\right)\right]\operatorname{sech}\left[\nu\left(\ln\left[\frac{r_{int}}{r_{ext}}\right]\right)\right]$$

being $\cosh\left[\nu\left(\ln\left[\frac{r_{int}}{r}\right]\right)\right]_{\nu=0}=1$ and $\operatorname{sech}\left[\nu\left(\ln\left[\frac{r_{int}}{r_{ext}}\right]\right)\right]_{\nu=0}=1$.

A.2 Build the solution of the first auxiliary problem:

According to the definition given in the Equations (4.15.1)-(4.15.3), the solution has to be divided in at least three steps for different values of harmonic frequencies *k* of the orthonormal basis function:

k=1

As defined in the Equation (4.15.1):

$$\psi=\frac{1}{\sqrt{r_{ext}}\sqrt{2\pi}}\quad for\ k=1$$

According to the Equation (A.7):

$$\bar{\psi}_{\nu}=\int_{\theta'=0}^{2\pi}\frac{1}{\sqrt{r_{ext}}\sqrt{2\pi}}\cos[\nu(\theta-\theta')]d\theta'=\frac{1}{\sqrt{r_{ext}}\sqrt{2\pi}}\int_{\theta'=0}^{2\pi}\cos[\nu(\theta-\theta')]d\theta'$$
$$=\frac{1}{\sqrt{r_{ext}}\sqrt{2\pi}}\left(\frac{\sin[\nu\theta]-\sin[\nu\theta-2\pi\nu]}{\nu\theta}\right)_{\theta=0}^{2\pi}=0$$

while:

$$\bar{\psi}_{\nu=0}=\int_{\theta'=0}^{2\pi}\frac{1}{\sqrt{r_{ext}}\sqrt{2\pi}}\cos[\nu(\theta-\theta')]_{\nu=0}d\theta'=\frac{1}{\sqrt{r_{ext}}\sqrt{2\pi}}\int_{\theta'=0}^{2\pi}d\theta'$$
$$=\frac{1}{\sqrt{r_{ext}}\sqrt{2\pi}}2\pi=\sqrt{\frac{2\pi}{r_{ext}}}$$

since $\cos[\nu(\theta-\theta')]_{\nu=0}=1$.

According to Equation (A.10) the auxiliary function is defined as:

$$G_{k=1}=\frac{1}{2\pi}\bar{\psi}_{\nu=0}+\sum_{\nu=1}^{\infty}\frac{1}{\pi}\,\bar{\psi}_{\nu}\cosh\left[\nu\left(\ln\left[\frac{r_{int}}{r}\right]\right)\right]\operatorname{sech}\left[\nu\left(\ln\left[\frac{r_{int}}{r_{ext}}\right]\right)\right]$$

$$=\frac{1}{2\pi}\bar{\psi}_{\nu=0}=\frac{1}{2\pi}\sqrt{\frac{2\pi}{r_{ext}}}=\frac{1}{\sqrt{2\pi\,r_{ext}}}$$

The trace of the auxiliary function at the internal boundary Γ_{int} is:

$$\gamma=G|_{\Gamma_{int}}=\frac{1}{\sqrt{2\pi\,r_{ext}}}$$

The normal derivative of the auxiliary function at the external boundary is:

$$\left.\frac{\partial G}{\partial \boldsymbol{n}}\right|_{\Gamma_{ext}}=0$$

Therefore, the reciprocity functional defined in the Equation (4.16) became:

$$R_G=\int_{\Gamma_{ext}}\left(-\psi\frac{h_{env}(T-T_{env})}{K}-Y\frac{\delta G}{\delta \boldsymbol{n}}\right)d\Gamma_{ext}$$

$$=\int_{\theta'=0}^{2\pi}r_{ext}\left(-\psi\frac{h_{env}(T-T_{env})}{K}-Y\frac{\delta G}{\delta \boldsymbol{n}}\right)d\theta'$$

since the normal derivative of the auxiliary function at the external boundary is null and the temperature profile at the same boundary is supposed to be known and acquired through the thermo-camera imaging, the last equation become:

$$R_G=-r_{ext}\int_{\theta'=0}^{2\pi}\psi\frac{h_{env}(Y-T_{env})}{K}\,d\theta'$$

$$=-r_{ext}\frac{1}{\sqrt{2\pi r_{ext}}}\frac{h_{env}}{K}\left[\int_{\theta'=0}^{2\pi}Y\,d\theta'-\int_{\theta'=0}^{2\pi}T_{env}\,d\theta'\right]$$

Using the Fourier's series expansion, the integral of the measurement at the external boundary Γ_{ext} in the last expression can be re-written as:

$$\begin{aligned}\int_{\theta'=0}^{2\pi} Y\, d\theta' &= \int_{\theta'=0}^{2\pi} \big(a_0 + a_1 \cos[\theta'] + b_1 \sin[\theta'] + \cdots \\ &\quad + a_{k_F} \cos[k_F\theta'] + b_{k_F} \sin[k_F\theta']\big) d\theta' \\ &= \int_{\theta'=0}^{2\pi} a_0 d\theta' + \int_{\theta'=0}^{2\pi} a_1 \cos[\theta']\, d\theta' + \int_{\theta'=0}^{2\pi} b_1 \sin[\theta']\, d\theta' + \cdots \\ &\quad + \int_{\theta'=0}^{2\pi} a_{k_F} \cos[k_F\theta']\, d\theta' + \int_{\theta'=0}^{2\pi} b_{k_F} \sin[k_F\theta']\, d\theta'\end{aligned}$$

where $a_0, a_1, b_1, \ldots, a_{k_F}, b_{k_F}$ are the Fourier's expansion coefficients.

Since the finite integral, from zero to 2π, of both the harmonic function *sine* and *cosine* is null, the last expression becomes:

$$\int_{\theta'=0}^{2\pi} Y\, d\theta' = 2\pi a_0$$

The environmental temperature is supposed to be constant, therefore its integral is:

$$\int_{\theta'=0}^{2\pi} T_{env}\, d\theta' = 2\pi T_{env}$$

Substituting those results, the reciprocity functional becomes:

$$\begin{aligned}R_G &= -r_{ext} \frac{1}{\sqrt{2\pi r_{ext}}} \frac{h_{env}}{K} \left[\int_{\theta'=0}^{2\pi} Y\, d\theta' - \int_{\theta'=0}^{2\pi} T_{env}\, d\theta'\right] \\ &= -r_{ext} \frac{1}{\sqrt{2\pi r_{ext}}} \frac{h_{env}}{K} \left[2\pi a_0 - 2\pi T_{env}\right] \\ &= -\sqrt{2\pi r_{ext}} \frac{h_{env}}{K} \left[a_0 - T_{env}\right]\end{aligned}$$

According to the Equation (4.17) the integral of the internal heat generation is:

$$Q_G = \int_{\Omega'} \left(G\frac{q_g}{K}\right) d\Omega' = \int_{\theta'=0}^{2\pi}\int_{r'=r_{int}}^{r_{ext}} r\frac{q_g}{K}\sqrt{\frac{1}{2\pi\, r_{ext}}}\, dr' d\theta'$$

$$= \frac{q_g}{K}\sqrt{\frac{1}{2\pi\, r_{ext}}}\int_{\theta'=0}^{2\pi}\int_{r'=r_{int}}^{r_{ext}} r\, dr' d\theta' = \frac{q_g}{K}\frac{\pi(r_{ext}^2 - r_{int}^2)}{\sqrt{2\pi r_{ext}}}$$

According to the definition given by the Equation (4.21), the first element of the matrix of the inner product becomes:

$$M = \int_{\Gamma_{\text{int}}} \langle \gamma_v, \gamma_v \rangle \; d\Gamma_{int} = \int_{\theta'=0}^{2\pi} r_{int}\, \langle \gamma_v, \gamma_v \rangle \, d\theta'$$

$$= r_{int}\int_{\theta'=0}^{2\pi}\left(\frac{1}{\sqrt{2\pi r_{ext}}}\frac{1}{\sqrt{2\pi r_{ext}}}\right) d\theta' = \frac{r_{int}}{r_{ext}}$$

<u>k=2,4,6,…,N-1 & k≠2v</u>

As defined in the Equation (4.15.2):

$$\psi = \frac{1}{\sqrt{r_{ext}}\sqrt{\pi}} cos\left[\frac{k}{2}\theta\right] \quad for\ k = 2,4,6, \ldots N-1$$

According to the Equation (a.7):

$$\bar{\psi} = \int_{\theta'=0}^{2\pi} \frac{1}{\sqrt{r_{ext}}\sqrt{\pi}} cos\left[\frac{k}{2}\theta'\right] \cos[v(\theta - \theta')] d\theta'$$

$$= \frac{1}{\sqrt{r_{ext}}\sqrt{\pi}}\int_{\theta'=0}^{2\pi} cos\left[\frac{k}{2}\theta'\right] \cos[v(\theta - \theta')] d\theta' = 0$$

Since the harmonic functions that appear in the inner product have different frequency, their inner product is null. In the same way is possible to calculate the transformation of the basis for the zero harmonic, as follows:

$$\bar{\psi}_{v=0} = \int_{\theta'=0}^{2\pi} \frac{1}{\sqrt{r_{ext}}\sqrt{\pi}} cos\left[\frac{k}{2}\theta'\right] \cos[v(\theta - \theta')]\, d\theta'$$

since $\cos[\nu(\theta-\theta')]_{\nu=0}=1$ the last expression becomes:

$$\bar{\psi}_{\nu=0}=\int_{\theta'=0}^{2\pi}\frac{1}{\sqrt{r_{ext}}\sqrt{\pi}}cos\left[\frac{k}{2}\theta'\right]d\theta'=\frac{1}{\sqrt{r_{ext}}\sqrt{\pi}}\left(\frac{2}{k}\sin\left[\frac{k}{2}\theta\right]\right)_{\theta=0}^{2\pi}=0$$

Considering that $\bar{\psi}$ and $\bar{\psi}_{\nu=0}$ are null, the auxiliary function *G* is null and also all the other result are zeros thus those frequency of the orthonormal basis function doesn't participate in the solution.

k=2,4,6,…,N-1 & k=2v

As defined in the Equation (4.15.2):

$$\psi=\frac{1}{\sqrt{r_{ext}}\sqrt{\pi}}cos\left[\frac{k}{2}\theta\right]\quad for\ k=2,4,6,\dots N-1$$

According to the equation (A.7):

$$\bar{\psi}=\int_{\theta'=0}^{2\pi}\frac{1}{\sqrt{r_{ext}}\sqrt{\pi}}cos\left[\frac{k}{2}\theta'\right]\cos[\nu(\theta-\theta')]d\theta'$$

$$=\frac{1}{\sqrt{r_{ext}}\sqrt{\pi}}\int_{\theta'=0}^{2\pi}cos\left[\frac{2\nu}{2}\theta'\right]\cos[\nu(\theta-\theta')]d\theta'$$

Is possible to re-write the last integral using the subtraction formula for the cosine terms, getting:

$$\int_{\theta'=0}^{2\pi} cos[\nu\theta']\cos[\nu(\theta-\theta')]d\theta' = \int_{\theta'=0}^{2\pi} cos[\nu\theta'](\cos[\nu\theta-\nu\theta'])\,d\theta'$$

$$= \int_{\theta'=0}^{2\pi} cos[\nu\theta'](\cos[\nu\theta]\cos[\nu\theta'] + \sin[\nu\theta]\sin[\nu\theta'])\,d\theta'$$

$$= \int_{\theta'=0}^{2\pi} cos[\nu\theta']\cos[\nu\theta]\cos[\nu\theta']\,d\theta'$$

$$+ \int_{\theta'=0}^{2\pi} cos[\nu\theta']\sin[\nu\theta]\sin[\nu\theta']\,d\theta'$$

$$= \cos[\nu\theta]\int_{\theta'=0}^{2\pi} cos[\nu\theta']\cos[\nu\theta']\,d\theta'$$

$$+ \sin[\nu\theta]\int_{\theta'=0}^{2\pi} cos[\nu\theta']\ \sin[\nu\theta']\,d\theta'$$

since $\int_{\theta'=0}^{2\pi} cos[\nu\theta']\cos[\nu\theta']\,d\theta' = \pi$ and $\int_{\theta'=0}^{2\pi} cos[\nu\theta']\ \sin[\nu\theta']\,d\theta' = 0$ the last expression becomes:

$$\int_{\theta'=0}^{2\pi} cos[\nu\theta']\cos[\nu(\theta-\theta')]d\theta' = \pi\cos[\nu\theta]$$

Then the transformation of the basis becomes:

$$\bar{\psi} = \frac{1}{\sqrt{r_{ext}}\sqrt{\pi}}\int_{\theta'=0}^{2\pi} cos\left[\frac{2\nu}{2}\theta'\right]\cos[\nu(\theta-\theta')]d\theta' = \frac{1}{\sqrt{r_{ext}}\sqrt{\pi}}\cos[\nu\theta]$$

Then the transformation of the basis for $\nu = 0$ is:

$$\bar{\psi}_{\nu=0} = \int_{\theta'=0}^{2\pi} \frac{1}{\sqrt{r_{ext}}\sqrt{\pi}} cos\left[\frac{k}{2}\theta'\right]\cos[\nu(\theta-\theta')]d\theta'$$

since $\cos[\nu(\theta-\theta')]_{\nu=0} = 1$ the last expression become:

$$\bar{\psi}_{\nu=0} = \int_{\theta'=0}^{2\pi} \frac{1}{\sqrt{r_{ext}}\sqrt{\pi}} cos\left[\frac{k}{2}\theta'\right]d\theta' = \frac{1}{\sqrt{r_{ext}}\sqrt{\pi}}\frac{\sin\left[\left(\frac{k}{2}\right)\theta\right]_{\theta=0}^{2\pi}}{\frac{k}{2}} = 0$$

According to the Equation (A.10) the auxiliary function is defined as:

$$G_{k=even} = \frac{1}{2\pi}\bar{\psi}_{(\nu=0)} + \sum_{\nu=1}^{\infty}\frac{1}{\pi}\,\bar{\psi}_{(\nu)}\cosh\left[\nu\left(\ln\left[\frac{r_{int}}{r}\right]\right)\right]\operatorname{sech}\left[\nu\left(\ln\left[\frac{r_{int}}{r_{ext}}\right]\right)\right]$$

$$= \sqrt{\frac{1}{\pi r_{ext}}}\sum_{\nu=1}^{\infty}\cos[\nu\theta]\cosh\left[\nu\,\left(\ln\left[\frac{r_{int}}{r}\right]\right)\right]\operatorname{sech}\left[\nu\,\left(\ln\left[\frac{r_{int}}{r_{ext}}\right]\right)\right]$$

The trace of the auxiliary function at the internal boundary Γ_{int} is:

$$\gamma = G|_{\Gamma_{int}} = \sqrt{\frac{1}{\pi r_{ext}}}\sum_{\nu=1}^{\infty}\cos[\nu\theta]\operatorname{sech}\left[\nu\,\left(\ln\left[\frac{r_{int}}{r_{ext}}\right]\right)\right]$$

The normal derivative of the auxiliary function at the external boundary is:

$$\left.\frac{\partial G}{\partial \boldsymbol{n}}\right|_{\Gamma_{ext}} = -\sqrt{\frac{1}{\pi r_{ext}}}\sum_{\nu=1}^{\infty}\cos[\nu\theta]\operatorname{sech}\left[\nu\,\left(\ln\left[\frac{r_{int}}{r_{ext}}\right]\right)\right]\sinh\left[\nu\,\left(\ln\left[\frac{r_{int}}{r_{ext}}\right]\right)\right]\frac{\nu}{r_{ext}}$$

The reciprocity functional defined in the Equation (4.16) became:

$$R_G = \int_{\Gamma_{ext}} \left(-\psi \frac{h_{env}(Y - T_{env})}{K} - Y \frac{\delta G}{\delta \boldsymbol{n}} \right) d\Gamma_{ext}$$

$$= \int_{\theta'=0}^{2\pi} r_{ext} \left(-\psi \frac{h_{env}(Y - T_{env})}{K} - Y \frac{\delta G}{\delta \boldsymbol{n}} \right) d\theta'$$

$$= -r_{ext} \int_{\theta'=0}^{2\pi} \left(\psi \frac{h_{env}}{K} Y - \psi \frac{h_{env}}{K} T_{env} - Y \frac{\delta G}{\delta \boldsymbol{n}} \right) d\theta'$$

$$= -r_{ext} \int_{\theta'=0}^{2\pi} Y \left(\psi \frac{h_{env}}{K} - \frac{\delta G}{\delta \boldsymbol{n}} \right) d\theta' - r_{ext} \int_{\theta'=0}^{2\pi} \psi \frac{h_{env}}{K} T_{env} \; d\theta'$$

$$= -r_{ext} \int_{\theta'=0}^{2\pi} Y \left(\frac{1}{\sqrt{r_{ext}}\sqrt{\pi}} cos\left[\frac{k}{2} \theta' \right] \frac{h_{env}}{K} \right.$$

$$\left. - \frac{1}{\sqrt{r_{ext}}\sqrt{\pi}} \cos[\nu\theta'] \; \operatorname{sech}\left[\nu \left(\ln\left[\frac{r_{int}}{r_{ext}} \right] \right) \right] \sinh\left[\nu \left(\ln\left[\frac{r_{int}}{r_{ext}} \right] \right) \right] \frac{\nu}{r_{ext}} \right) d\theta'$$

$$- r_{ext} \int_{\theta'=0}^{2\pi} \frac{1}{\sqrt{r_{ext}}\sqrt{\pi}} cos[\nu\theta'] \frac{h_{env}}{K} T_{env} \; d\theta'$$

$$= -r_{ext} \int_{\theta'=0}^{2\pi} Y \left(\frac{1}{\sqrt{r_{ext}}\sqrt{\pi}} cos[\nu\theta'] \frac{h_{env}}{K} \right.$$

$$\left. - \frac{1}{\sqrt{r_{ext}}\sqrt{\pi}} \cos[\nu\theta'] \operatorname{sech}\left[\nu \left(\ln\left[\frac{r_{int}}{r_{ext}} \right] \right) \right] \sinh\left[\nu \left(\ln\left[\frac{r_{int}}{r_{ext}} \right] \right) \right] \frac{\nu}{r_{ext}} \right) d\theta'$$

$$- r_{ext} \frac{1}{\sqrt{r_{ext}}\sqrt{\pi}} \frac{h_{env}}{K} T_{env} \int_{\theta'=0}^{2\pi} cos[\nu\theta'] \; d\theta'$$

since $\int_{\theta'=0}^{2\pi} cos[\nu\theta'] \; d\theta' = 0$ the last expression become:

$$R_G = \int_{\Gamma_{ext}} \left(-\psi \frac{h_{env}(Y - T_{env})}{K} - Y \frac{\delta G}{\delta \boldsymbol{n}} \right) d\Gamma_{ext} =$$

$$= -r_{ext} \int_{\theta'=0}^{2\pi} Y \frac{1}{\sqrt{r_{ext}}\sqrt{\pi}} cos[\nu\theta'] \left(\frac{h_{env}}{K} \right.$$

$$\left. - \operatorname{sech}\left[\nu \left(\ln\left[\frac{r_{int}}{r_{ext}} \right] \right) \right] \sinh\left[\nu \left(\ln\left[\frac{r_{int}}{r_{ext}} \right] \right) \right] \frac{\nu}{r_{ext}} \right) d\theta'$$

$$= -r_{ext} \frac{1}{\sqrt{r_{ext}}\sqrt{\pi}} \left(\frac{h_{env}}{K} \right.$$

$$\left. - \operatorname{sech}\left[\nu \left(\ln\left[\frac{r_{int}}{r_{ext}} \right] \right) \right] \sinh\left[\nu \left(\ln\left[\frac{r_{int}}{r_{ext}} \right] \right) \right] \frac{\nu}{r_{ext}} \right) \int_{\theta'=0}^{2\pi} Y cos[\nu\theta'] \, d\theta'$$

Using the Fourier's series expansion, the integral of the measurement at the external boundary Γ_{ext} in the last expression can be re-written as:

$$\int_{\theta'=0}^{2\pi} Y\cos[\nu\theta']\,d\theta'$$

$$= \int_{\theta'=0}^{2\pi} \big(a_0\cos[\nu\theta']$$

$$+ a_1\cos[\theta']\cos[\nu\theta'] + b_1\sin[\theta']\cos[\nu\theta'] + \cdots$$

$$+ a_{k_F}\cos[k_F\theta']\cos[\nu\theta'] + b_{k_F}\sin[k_F\theta']\cos[\nu\theta']\big)d\theta'$$

$$= \int_{\theta'=0}^{2\pi} a_0\cos[\nu\theta']\,d\theta' + \int_{\theta'=0}^{2\pi} a_1\cos[\theta']\cos[\nu\theta']\,d\theta'$$

$$+ \int_{\theta'=0}^{2\pi} b_1\sin[\theta']\cos[\nu\theta']\,d\theta' + \cdots$$

$$+ \int_{\theta'=0}^{2\pi} a_{k_F}\cos[k_F\theta']\cos[\nu\theta']\,d\theta'$$

$$+ \int_{\theta'=0}^{2\pi} b_{k_F}\sin[k_F\theta']\cos[\nu\theta']\,d\theta'$$

since $\int_{\theta'=0}^{2\pi} a_0\cos[\nu\theta']\,d\theta' = 0$, $\int_{\theta'=0}^{2\pi} b_{k_F}\sin[k_F\theta']\cos[\nu\theta']\,d\theta' = 0$ for every k_F, and:

$$\int_{\theta'=0}^{2\pi} a_{k_F}\cos[k_F\theta']\cos[\nu\theta']\,d\theta' = \begin{cases} 0 & if\ k_F \neq \nu \\ \pi a_{k_F} & if\ k_F = \nu \end{cases}$$

the integral of the measurement at the external boundary becomes:

$$\int_{\theta'=0}^{2\pi} Y cos[\nu\theta']\,d\theta' = \pi a_\nu$$

and the reciprocity functional becomes:

$$
\begin{aligned}
&R_G \\
&= -r_{ext}\frac{1}{\sqrt{r_{ext}}\sqrt{\pi}}\Bigg(\frac{h_{env}}{K} \\
&- \operatorname{sech}\left[\nu\ \left(\ln\left[\frac{r_{int}}{r_{ext}}\right]\right)\right]\sinh\left[\nu\ \left(\ln\left[\frac{r_{int}}{r_{ext}}\right]\right)\right]\frac{\nu}{r_{ext}}\Bigg)\int_{\theta'=0}^{2\pi} Y cos[\nu\theta']\,d\theta' \\
&= -r_{ext}\frac{\pi a_\nu}{\sqrt{r_{ext}}\sqrt{\pi}}\Bigg(\frac{h_{env}}{K} - \operatorname{sech}\left[\nu\ \left(\ln\left[\frac{r_{int}}{r_{ext}}\right]\right)\right]\sinh\left[\nu\ \left(\ln\left[\frac{r_{int}}{r_{ext}}\right]\right)\right]\frac{\nu}{r_{ext}}\Bigg) \\
&= -a_\nu\sqrt{\pi r_{ext}}\Bigg(\frac{h_{env}}{K} - \tanh\left[\nu\ \left(\ln\left[\frac{r_{int}}{r_{ext}}\right]\right)\right]\frac{\nu}{r_{ext}}\Bigg)
\end{aligned}
$$

According to the Equation (4.17) the integral of the internal heat generation is:

$$
\begin{aligned}
&Q_G = \int_{\Omega'}\left(G\frac{q_g}{K}\right)d\Omega' \\
&= \int_{\theta'=0}^{2\pi}\int_{r'=r_{int}}^{r_{ext}} r\frac{q_g}{K}\sqrt{\frac{1}{\pi r_{ext}}}\sum_{\nu=1}^{\infty}\cos[\nu\theta]\cosh\left[\nu\ \left(\ln\left[\frac{r_{int}}{r}\right]\right)\right]\operatorname{sech}\left[\nu\ \left(\ln\left[\frac{r_{int}}{r_{ext}}\right]\right)\right]dr'd\theta \\
&= \frac{q_g}{K}\sqrt{\frac{1}{\pi\, r_{ext}}}\operatorname{sech}\left[\nu\ \left(\ln\left[\frac{r_{int}}{r_{ext}}\right]\right)\right]\int_{\theta'=0}^{2\pi}\int_{r'=r_{int}}^{r_{ext}} r\cos[\nu\theta]\cosh\left[\nu\ \left(\ln\left[\frac{r_{int}}{r}\right]\right)\right]dr'd\theta' \\
&= \frac{q_g}{K}\sqrt{\frac{1}{\pi\, r_{ext}}}\operatorname{sech}\left[\nu\ \left(\ln\left[\frac{r_{int}}{r_{ext}}\right]\right)\right]\int_{\theta'=0}^{2\pi}\cos[\nu\theta]\,d\theta'\int_{r'=r_{int}}^{r_{ext}} r'\cosh\left[\nu\ \left(\ln\left[\frac{r_{int}}{r'}\right]\right)\right]dr'
\end{aligned}
$$

since $\int_{\theta'=0}^{2\pi} cos[\nu\theta']\ d\theta' = 0$ the heat generation terms is null.

The even elements of the diagonal matrix of the inner product becomes:

$$
\begin{aligned}
&M = \int_{\Gamma_{\text{int}}}\langle\gamma_\nu,\gamma_\nu\rangle\ d\Gamma_{int} = \int_{\theta'=0}^{2\pi} r_{int}\,\langle\gamma_\nu,\gamma_\nu\rangle\,d\theta' \\
&= r_{int}\int_{\theta'=0}^{2\pi}\left(\sqrt{\frac{1}{\pi r_{ext}}}\cos[\nu\theta]\ \operatorname{sech}\left[\nu\ \left(\ln\left[\frac{r_{int}}{r_{ext}}\right]\right)\right]\sqrt{\frac{1}{\pi r_{ext}}}\cos[\nu\theta]\ \operatorname{sech}\left[\nu\ \left(\ln\left[\frac{r_{int}}{r_{ext}}\right]\right)\right]\right)d\theta' \\
&= \frac{r_{int}}{\pi r_{ext}}\operatorname{sech}^2\left[\nu\ \left(\ln\left[\frac{r_{int}}{r_{ext}}\right]\right)\right]\int_{\theta'=0}^{2\pi}\cos^2[\nu\theta]\ d\theta'
\end{aligned}
$$

since $\int_{\theta'=0}^{2\pi}\cos^2[\nu\theta]\ d\theta' = \pi$ the last expression becomes:

$$M = \int_{\Gamma_{\text{int}}} \langle \gamma_\nu, \gamma_\nu \rangle \, d\Gamma_{int} = \frac{r_{int}}{r_{ext}} \operatorname{sech}^2 \left[\nu \left(\ln \left[\frac{r_{int}}{r_{ext}} \right] \right) \right]$$

k=3,5,7,…,N & k≠2v+1

As defined in the Equation (4.15.3):

$$\psi = \frac{1}{\sqrt{r_{ext}}\sqrt{\pi}} sin \left[\frac{k-1}{2} \theta \right] \quad for\ k = 2,4,6, \ldots N-1$$

According to the Equation (A.7):

$$\bar{\psi} = \int_{\theta'=0}^{2\pi} \frac{1}{\sqrt{r_{ext}}\sqrt{\pi}} sin \left[\frac{k-1}{2} \theta' \right] \cos[\nu(\theta - \theta')] d\theta'$$

$$= \frac{1}{\sqrt{r_{ext}}\sqrt{\pi}} \int_{\theta'=0}^{2\pi} sin \left[\frac{k-1}{2} \theta' \right] \cos[\nu(\theta - \theta')] d\theta' = 0$$

Since the harmonic functions that appear in the inner product have different frequency, their inner product is null.

In the same way is possible to calculate the transformation of the basis for the zero harmonic, as follows:

$$\bar{\psi}_{\nu=0} = \int_{\theta'=0}^{2\pi} \frac{1}{\sqrt{r_{ext}}\sqrt{\pi}} sin \left[\frac{k-1}{2} \theta' \right] \cos[\nu(\theta - \theta')] \, d\theta'$$

since $\cos[\nu(\theta - \theta')]_{\nu=0} = 1$ the last expression becomes:

$$\bar{\psi}_{\nu=0} = \int_{\theta'=0}^{2\pi} \frac{1}{\sqrt{r_{ext}}\sqrt{\pi}} sin \left[\frac{k-1}{2} \theta' \right] d\theta' = \frac{1}{\sqrt{r_{ext}}\sqrt{\pi}} \left(2 \cos \frac{\left[\frac{k-1}{2} \theta \right]}{k-1} \right)_{\theta=0}^{2\pi}$$

$$= 0$$

Considering that $\bar{\psi}$ and $\bar{\psi}_{\nu=0}$ are null, the auxiliary function G is null and also all the other result are zero thus those frequency of the orthonormal basis function does not participate in the solution.

k=3,5,7,…,N & k=2v+1

As defined in the Equation (4.15.3):

$$\psi = \frac{1}{\sqrt{r_{ext}}\sqrt{\pi}} sin\left[\frac{k-1}{2}\theta\right] \quad for\ k = 2,4,6,\dots N-1$$

According to the Equation (A.7):

$$\bar{\psi} = \int_{\theta'=0}^{2\pi} \frac{1}{\sqrt{r_{ext}}\sqrt{\pi}} sin\left[\frac{k-1}{2}\theta'\right] \cos[v(\theta-\theta')]d\theta'$$

$$= \frac{1}{\sqrt{r_{ext}}\sqrt{\pi}} \int_{\theta'=0}^{2\pi} sin\left[\frac{(2v+1)-1}{2}\theta'\right] \cos[v(\theta-\theta')]d\theta'$$

is possible to re-write the last integral using the subtraction formula the for cosine terms, getting:

$$\int_{\theta'=0}^{2\pi} sin[v\theta']\cos[v(\theta-\theta')]d\theta' = \int_{\theta'=0}^{2\pi} sin[v\theta'](\cos[v\theta - v\theta'])\, d\theta'$$

$$= \int_{\theta'=0}^{2\pi} sin[v\theta'](\cos[v\theta]\cos[v\theta'] + \sin[v\theta]\sin[v\theta'])\, d\theta'$$

$$= \int_{\theta'=0}^{2\pi} sin[v\theta']\cos[v\theta]\cos[v\theta']\, d\theta'$$

$$+ \int_{\theta'=0}^{2\pi} sin[v\theta']\sin[v\theta]\sin[v\theta']\, d\theta'$$

$$= \cos[v\theta] \int_{\theta'=0}^{2\pi} sin[v\theta']\cos[v\theta']\, d\theta'$$

$$+ \sin[v\theta] \int_{\theta'=0}^{2\pi} sin[v\theta']\ \sin[v\theta']\, d\theta'$$

since $\int_{\theta'=0}^{2\pi} sin[v\theta']\cos[v\theta']\, d\theta' = 0$ and $\int_{\theta'=0}^{2\pi} sin[v\theta']\ \sin[v\theta']\, d\theta' = \pi$ the last expression becomes:

$$\int_{\theta'=0}^{2\pi} sin[v\theta']\cos[v(\theta-\theta')]d\theta' = \pi \sin[v\theta]$$

Then the transformation of the basis becomes:

$$\bar{\psi} = \int_{\theta'=0}^{2\pi} \frac{1}{\sqrt{r_{ext}}\sqrt{\pi}} sin\left[\frac{k-1}{2}\theta'\right] \cos[\nu(\theta-\theta')] d\theta' = \sqrt{\frac{\pi}{r_{ext}}} \sin[\nu\phi]$$

The transformation of the basis for $\nu = 0$ is:

$$\bar{\psi}_{\nu=0} = \int_{\theta'=0}^{2\pi} \frac{1}{\sqrt{r_{ext}}\sqrt{\pi}} sin\left[\frac{k-1}{2}\theta'\right] \cos[\nu(\theta-\theta')] d\theta'$$

since $\cos[\nu(\theta-\theta')]_{\nu=0} = 1$ the last expression becomes:

$$\bar{\psi}_{\nu=0} = \int_{\theta'=0}^{2\pi} \frac{1}{\sqrt{r_{ext}}\sqrt{\pi}} sin\left[\frac{k-1}{2}\theta'\right] d\theta' = \frac{1}{\sqrt{r_{ext}}\sqrt{\pi}} \frac{\cos\left[\left(\frac{k-1}{2}\right)\theta\right]_{\theta=0}^{2\pi}}{\left(\frac{k-1}{2}\right)} = 0$$

According to the Equation (A.10) the auxiliary function is defined as:

$$G_{k=odd} = \frac{1}{2\pi}\bar{\psi}_{(\nu=0)} + \sum_{\nu=1}^{\infty} \frac{1}{\pi}\, \bar{\psi}_{(\nu)} \cosh\left[\nu\left(\ln\left[\frac{r_{int}}{r}\right]\right)\right] \operatorname{sech}\left[\nu\left(\ln\left[\frac{r_{int}}{r_{ext}}\right]\right)\right]$$

$$= \sqrt{\frac{1}{\pi r_{ext}}} \sum_{\nu=1}^{\infty} \sin[\nu\theta] \cosh\left[\nu\,\left(\ln\left[\frac{r_{int}}{r}\right]\right)\right] \operatorname{sech}\left[\nu\,\left(\ln\left[\frac{r_{int}}{r_{ext}}\right]\right)\right]$$

The trace of the auxiliary function at the internal boundary Γ_{int} is:

$$\gamma = G|_{\Gamma_{int}} = \sqrt{\frac{1}{\pi r_{ext}}} \sum_{\nu=1}^{\infty} \sin[\nu\theta] \operatorname{sech}\left[\nu\,\left(\ln\left[\frac{r_{int}}{r_{ext}}\right]\right)\right]$$

The normal derivative of the auxiliary function at the external boundary is:

$$\left.\frac{\partial G}{\partial \boldsymbol{n}}\right|_{\Gamma_{ext}} = -\sqrt{\frac{1}{\pi r_{ext}}} \sum_{\nu=1}^{\infty} \sin[\nu\theta] \operatorname{sech}\left[\nu\,\left(\ln\left[\frac{r_{int}}{r_{ext}}\right]\right)\right] \sinh\left[\nu\,\left(\ln\left[\frac{r_{int}}{r_{ext}}\right]\right)\right] \frac{\nu}{r_{ext}}$$

The reciprocity functional defined in the Equation (4.16) became:

$$R_G = \int_{\Gamma_{ext}} \left(-\psi \frac{h_{env}(Y - T_{env})}{K} - Y \frac{\delta G}{\delta \boldsymbol{n}} \right) d\Gamma_{ext}$$

$$= \int_{\theta'=0}^{2\pi} r_{ext} \left(-\psi \frac{h_{env}(Y - T_{env})}{K} - Y \frac{\delta G}{\delta \boldsymbol{n}} \right) d\theta'$$

$$= -r_{ext} \int_{\theta'=0}^{2\pi} \left(\psi \frac{h_{env}}{K} Y - \psi \frac{h_{env}}{K} T_{env} - Y \frac{\delta G}{\delta \boldsymbol{n}} \right) d\theta'$$

$$= -r_{ext} \int_{\theta'=0}^{2\pi} Y \left(\psi \frac{h_{env}}{K} - \frac{\delta G}{\delta \boldsymbol{n}} \right) d\theta' - r_{ext} \int_{\theta'=0}^{2\pi} \psi \frac{h_{env}}{K} T_{env} \; d\theta'$$

$$= -r_{ext} \int_{\theta'=0}^{2\pi} Y \left(\frac{1}{\sqrt{r_{ext}}\sqrt{\pi}} \sinh\left[\frac{k}{2}\theta'\right] \frac{h_{env}}{K} \right.$$

$$\left. - \frac{1}{\sqrt{r_{ext}}\sqrt{\pi}} \sin[\nu\theta'] \; \operatorname{sech}\left[\nu \left(\ln\left[\frac{r_{int}}{r_{ext}}\right]\right)\right] \sinh\left[\nu \left(\ln\left[\frac{r_{int}}{r_{ext}}\right]\right)\right] \frac{\nu}{r_{ext}} \right) d\theta'$$

$$- r_{ext} \int_{\theta'=0}^{2\pi} \frac{1}{\sqrt{r_{ext}}\sqrt{\pi}} sin[\nu\theta'] \frac{h_{env}}{K} T_{env} \; d\theta'$$

$$= -r_{ext} \int_{\theta'=0}^{2\pi} Y \left(\frac{1}{\sqrt{r_{ext}}\sqrt{\pi}} sin[\nu\theta'] \frac{h_{env}}{K} \right.$$

$$\left. - \frac{1}{\sqrt{r_{ext}}\sqrt{\pi}} \sin[\nu\theta'] \operatorname{sech}\left[\nu \left(\ln\left[\frac{r_{int}}{r_{ext}}\right]\right)\right] \sinh\left[\nu \left(\ln\left[\frac{r_{int}}{r_{ext}}\right]\right)\right] \frac{\nu}{r_{ext}} \right) d\theta'$$

$$- r_{ext} \frac{1}{\sqrt{r_{ext}}\sqrt{\pi}} \frac{h_{env}}{K} T_{env} \int_{\theta'=0}^{2\pi} sin[\nu\theta'] \; d\theta'$$

since $\int_{\theta'=0}^{2\pi} sin[\nu\theta'] \; d\theta' = 0$ the last expression become:

$$R_G = \int_{\Gamma_{ext}} \left(-\psi \frac{h_{env}(Y - T_{env})}{K} - Y \frac{\delta G}{\delta \boldsymbol{n}} \right) d\Gamma_{ext} =$$

$$= -r_{ext} \int_{\theta'=0}^{2\pi} Y \frac{1}{\sqrt{r_{ext}}\sqrt{\pi}} sin[\nu\theta'] \left(\frac{h_{env}}{K} \right.$$

$$\left. - \operatorname{sech}\left[\nu \left(\ln\left[\frac{r_{int}}{r_{ext}}\right]\right)\right] \sinh\left[\nu \left(\ln\left[\frac{r_{int}}{r_{ext}}\right]\right)\right] \frac{\nu}{r_{ext}} \right) d\theta'$$

$$= -r_{ext} \frac{1}{\sqrt{r_{ext}}\sqrt{\pi}} \left(\frac{h_{env}}{K} \right.$$

$$\left. - \operatorname{sech}\left[\nu \left(\ln\left[\frac{r_{int}}{r_{ext}}\right]\right)\right] \sinh\left[\nu \left(\ln\left[\frac{r_{int}}{r_{ext}}\right]\right)\right] \frac{\nu}{r_{ext}} \right) \int_{\theta'=0}^{2\pi} Y sin[\nu\theta'] \, d\theta'$$

Using the Fourier's series expansion, the integral of the measurement at the external boundary Γ_{ext} in the last expression can be re-written as:

$$\int_{\theta'=0}^{2\pi} Y \sin[\nu\theta']\, d\theta'$$

$$= \int_{\theta'=0}^{2\pi} \big(a_0 \sin[\nu\theta'] + a_1 \cos[\theta'] \sin[\nu\theta'] + b_1 \sin[\theta'] \sin[\nu\theta']$$

$$+ \cdots + a_{k_F} \cos[k_F\theta'] \sin[\nu\theta'] + b_{k_F} \sin[k_F\theta'] \sin[\nu\theta']\big) d\theta'$$

$$= \int_{\theta'=0}^{2\pi} a_0 \sin[\nu\theta']\, d\theta' + \int_{\theta'=0}^{2\pi} a_1 \cos[\theta'] \sin[\nu\theta']\, d\theta'$$

$$+ \int_{\theta'=0}^{2\pi} b_1 \sin[\theta'] \sin[\nu\theta']\, d\theta' + \cdots$$

$$+ \int_{\theta'=0}^{2\pi} a_{k_F} \cos[k_F\theta'] \sin[\nu\theta']\, d\theta'$$

$$+ \int_{\theta'=0}^{2\pi} b_{k_F} \sin[k_F\theta'] \sin[\nu\theta']\, d\theta'$$

since $\int_{\theta'=0}^{2\pi} a_0 \sin[\nu\theta']\, d\theta' = 0$, $\int_{\theta'=0}^{2\pi} a_{k_F} \cos[k_F\theta'] \sin[\nu\theta']\, d\theta' = 0$ for every k_F, and:

$$\int_{\theta'=0}^{2\pi} b_{k_F} \sin[k_F\theta'] \sin[\nu\theta']\, d\theta' = \begin{cases} 0 & if\ k_F \neq \nu \\ \pi b_{k_F} & if\ k_F = \nu \end{cases}$$

the integral of the measurement at the external boundary becomes:

$$\int_{\theta'=0}^{2\pi} Y \sin[\nu\theta']\, d\theta' = \pi b_\nu$$

and the reciprocity functional becomes:

$$
\begin{aligned}
&R_G \\
&= -r_{ext}\frac{1}{\sqrt{r_{ext}}\sqrt{\pi}}\left(\frac{h_{env}}{K}\right. \\
&\left. - \operatorname{sech}\left[\nu\ \left(\ln\left[\frac{r_{int}}{r_{ext}}\right]\right)\right]\sinh\left[\nu\ \left(\ln\left[\frac{r_{int}}{r_{ext}}\right]\right)\right]\frac{\nu}{r_{ext}}\right)\int_{\theta'=0}^{2\pi} Y sin[\nu\theta']\,d\theta' \\
&= -r_{ext}\frac{\pi b_k}{\sqrt{r_{ext}}\sqrt{\pi}}\left(\frac{h_{env}}{K} - \operatorname{sech}\left[\nu\ \left(\ln\left[\frac{r_{int}}{r_{ext}}\right]\right)\right]\sinh\left[\nu\ \left(\ln\left[\frac{r_{int}}{r_{ext}}\right]\right)\right]\frac{\nu}{r_{ext}}\right) \\
&= -b_k\sqrt{\pi r_{ext}}\left(\frac{h_{env}}{K} - \tanh\left[\nu\ \left(\ln\left[\frac{r_{int}}{r_{ext}}\right]\right)\right]\frac{\nu}{r_{ext}}\right)
\end{aligned}
$$

According to the Equation (4.17) the integral of the internal heat generation is:

$$
\begin{aligned}
&Q_G = \int_{\Omega'}\left(G\frac{q_g}{K}\right)d\Omega' \\
&= \int_{\theta'=0}^{2\pi}\int_{r'=r_{int}}^{r_{ext}} r'\frac{q_g}{K}\sqrt{\frac{1}{\pi r_{ext}}}\sum_{\nu=1}^{\infty}\sin[\nu\theta']\cosh\left[\nu\ \left(\ln\left[\frac{r_{int}}{r'}\right]\right)\right]\operatorname{sech}\left[\nu\ \left(\ln\left[\frac{r_{int}}{r_{ext}}\right]\right)\right]dr'd\theta' \\
&= \frac{q_g}{K}\sqrt{\frac{1}{\pi\, r_{ext}}}\operatorname{sech}\left[\nu\ \left(\ln\left[\frac{r_{int}}{r_{ext}}\right]\right)\right]\int_{\theta'=0}^{2\pi}\int_{r'=r_{int}}^{r_{ext}} r'\sin[\nu\theta']\cosh\left[\nu\ \left(\ln\left[\frac{r_{int}}{r'}\right]\right)\right]dr'd\theta' \\
&= \frac{q_g}{K}\sqrt{\frac{1}{\pi\, r_{ext}}}\operatorname{sech}\left[\nu\ \left(\ln\left[\frac{r_{int}}{r_{ext}}\right]\right)\right]\int_{\theta'=0}^{2\pi}\sin[\nu\theta']\,d\theta'\int_{r'=r_{int}}^{r_{ext}} r'\cosh\left[\nu\ \left(\ln\left[\frac{r_{int}}{r'}\right]\right)\right]dr' \\
&= 0
\end{aligned}
$$

since $\int_{\theta'=0}^{2\pi} sin[\nu\theta']\ d\theta' = 0$ the heat generation terms is null.

The odd elements of the diagonal matrix of the inner product becomes:

$$
\begin{aligned}
&M = \int_{\Gamma_{\text{int}}}\langle\gamma_\nu,\gamma_\nu\rangle\ d\Gamma_{int} = \int_{\theta'=0}^{2\pi} r_{int}\,\langle\gamma_\nu,\gamma_\nu\rangle\,d\theta' \\
&= r_{int}\int_{\theta'=0}^{2\pi}\left(\sqrt{\frac{1}{\pi r_{ext}}}\sin[\nu\theta]\ \operatorname{sech}\left[\nu\ \left(\ln\left[\frac{r_{int}}{r_{ext}}\right]\right)\right]\sqrt{\frac{1}{\pi r_{ext}}}\sin[\nu\theta]\ \operatorname{sech}\left[\nu\ \left(\ln\left[\frac{r_{int}}{r_{ext}}\right]\right)\right]\right)d\theta' \\
&= \frac{r_{int}}{\pi r_{ext}}\operatorname{sech}^2\left[\nu\ \left(\ln\left[\frac{r_{int}}{r_{ext}}\right]\right)\right]\int_{\theta'=0}^{2\pi}\sin^2[\nu\theta]\ d\theta'
\end{aligned}
$$

since $\int_{\theta'=0}^{2\pi} \sin^2[\nu\theta]\ d\theta' = \pi$ the last expression becomes:

$$M = \int_{\Gamma_{\text{int}}} \langle \gamma_\nu, \gamma_\nu \rangle\ d\Gamma_{int} = \frac{r_{int}}{r_{ext}} \operatorname{sech}^2 \left[\nu \left(\ln \left[\frac{r_{int}}{r_{ext}} \right] \right) \right]$$

A.3 Heat flux estimation:

The solution of the first auxiliary problem is easy to get by simply solving the linear system defined in the Equation (4.23). Once the α coefficients are determined, is possible estimating the internal heat flux according to the Equation (4.20).
The results obtained are here summarized:

$$R_G = -\sqrt{\pi r_{ext}} \begin{bmatrix} \sqrt{2}\dfrac{h_{env}}{K}(a_0 - T_{env}) & \\ \left(\dfrac{h_{env}}{K} - \tanh\left[\ln\left[\dfrac{r_{int}}{r_{ext}}\right]\right]\dfrac{1}{r_{ext}}\right) & a_1 \\ \left(\dfrac{h_{env}}{K} - \tanh\left[\ln\left[\dfrac{r_{int}}{r_{ext}}\right]\right]\dfrac{1}{r_{ext}}\right) & b_1 \\ \left(\dfrac{h_{env}}{K} - \tanh\left[2\ \ln\left[\dfrac{r_{int}}{r_{ext}}\right]\right]\dfrac{2}{r_{ext}}\right) & a_2 \\ \left(\dfrac{h_{env}}{K} - \tanh\left[2\ \ln\left[\dfrac{r_{int}}{r_{ext}}\right]\right]\dfrac{2}{r_{ext}}\right) & b_2 \\ \vdots & \\ \left(\dfrac{h_{env}}{K} - \tanh\left[\nu\ \ln\left[\dfrac{r_{int}}{r_{ext}}\right]\right]\dfrac{\nu}{r_{ext}}\right) & a_\nu \\ \left(\dfrac{h_{env}}{K} - \tanh\left[\nu\ \ln\left[\dfrac{r_{int}}{r_{ext}}\right]\right]\dfrac{\nu}{r_{ext}}\right) & b_\nu \end{bmatrix} \qquad \alpha = \begin{bmatrix} \alpha_{\nu=1} \\ \alpha_{\nu=2} \\ \vdots \\ \alpha_{\nu=\nu} \end{bmatrix}$$

$$Q_G = \begin{bmatrix} \dfrac{q_g}{K}\sqrt{\dfrac{\pi}{2r_{ext}}}(r_{ext}^2 - r_{int}^2) \\ 0 \\ \vdots \\ 0 \end{bmatrix}$$

$$M = \frac{r_{int}}{r_{ext}} \begin{bmatrix} 1 & & & & & & & & 0 \\ & \operatorname{sech}^2\left[1 \ln\left[\frac{r_{int}}{r_{ext}}\right]\right] & & & & & & & \\ & & \operatorname{sech}^2\left[1 \ln\left[\frac{r_{int}}{r_{ext}}\right]\right] & & & & & & \\ & & & \operatorname{sech}^2\left[2 \ln\left[\frac{r_{int}}{r_{ext}}\right]\right] & & & & & \\ & & & & \operatorname{sech}^2\left[2 \ln\left[\frac{r_{int}}{r_{ext}}\right]\right] & & & & \\ & & & & & \ddots & & & \\ & & & & & & \operatorname{sech}^2\left[\nu \ln\left[\frac{r_{int}}{r_{ext}}\right]\right] & & \\ 0 & & & & & & & & \operatorname{sech}^2\left[\nu \ln\left[\frac{r_{int}}{r_{ext}}\right]\right] \end{bmatrix}$$

$$\gamma = \frac{1}{\sqrt{\pi r_{ext}}} \begin{bmatrix} 1 & \cdots & 1 & \cdots & 1 \\ \cos[1\ 0] \operatorname{sech}\left[1 \ln\left[\frac{r_{ext}}{r_{int}}\right]\right] & \cdots & \cos[1\ \theta] \operatorname{sech}\left[1 \ln\left[\frac{r_{ext}}{r_{int}}\right]\right] & \cdots & \cos[1\ 2\pi] \operatorname{sech}\left[1 \ln\left[\frac{r_{ext}}{r_{int}}\right]\right] \\ \sin[1\ 0] \operatorname{sech}\left[1 \ln\left[\frac{r_{ext}}{r_{int}}\right]\right] & \cdots & \sin[1\ \theta] \operatorname{sech}\left[1 \ln\left[\frac{r_{ext}}{r_{int}}\right]\right] & \cdots & \cos[1\ 2\pi] \operatorname{sech}\left[1 \ln\left[\frac{r_{ext}}{r_{int}}\right]\right] \\ \cos[2\ 0] \operatorname{sech}\left[2 \ln\left[\frac{r_{ext}}{r_{int}}\right]\right] & \cdots & \cos[2\ \theta] \operatorname{sech}\left[2 \ln\left[\frac{r_{ext}}{r_{int}}\right]\right] & \cdots & \cos[2\ 2\pi] \operatorname{sech}\left[2 \ln\left[\frac{r_{ext}}{r_{int}}\right]\right] \\ \sin[2\ 0] \operatorname{sech}\left[2 \ln\left[\frac{r_{ext}}{r_{int}}\right]\right] & \cdots & \sin[2\ \theta] \operatorname{sech}\left[2 \ln\left[\frac{r_{ext}}{r_{int}}\right]\right] & \cdots & \cos[2\ 2\pi] \operatorname{sech}\left[2 \ln\left[\frac{r_{ext}}{r_{int}}\right]\right] \\ \vdots & & \vdots & & \vdots \\ \cos[\nu\ 0] \operatorname{sech}\left[\nu \ln\left[\frac{r_{ext}}{r_{int}}\right]\right] & \cdots & \cos[\nu\ \theta] \operatorname{sech}\left[\nu \ln\left[\frac{r_{ext}}{r_{int}}\right]\right] & \cdots & \cos[\nu\ 2\pi] \operatorname{sech}\left[\nu \ln\left[\frac{r_{ext}}{r_{int}}\right]\right] \\ \sin[\nu\ 0] \operatorname{sech}\left[\nu \ln\left[\frac{r_{ext}}{r_{int}}\right]\right] & \cdots & \sin[\nu\ \theta] \operatorname{sech}\left[\nu \ln\left[\frac{r_{ext}}{r_{int}}\right]\right] & \cdots & \cos[\nu\ 2\pi] \operatorname{sech}\left[\nu \ln\left[\frac{r_{ext}}{r_{int}}\right]\right] \end{bmatrix}$$

It is worth noting that the M matrix of the inner product is diagonal thus its determinant is given by the product of the its diagonal terms. Since the M matrix as to be inverted, its determinant has to be strictly close to one in order to increase its well conditioning; for this reason, the tube has to be as thin as possible as shown in Figure (A.2.a). This observation is physically justified since as much as the thickness of the tube is small, the easier is to estimate the properties at the inner surface Γ_{int}. This consideration is in contrast with the sensitivity of the transformation of the internal heat generation Q_G (Figure (A.2.b)), but, from the experimental point of view, this problem could be avoided by increasing the internal heat generation q_g or increasing the external radius of the tube (Figure (A.2.b)). Related to aspect, it has to be pointed out that increasing the external radius, will also increase the element of the diagonal matrix M (Figure (A.2.c)) thus increasing its determinant and its capability to be inverted.

As shown in Figure (A.3.a) increasing the numbers of the harmonics, the M matrix becomes ill-conditioned making the solution unstable. For this reason, the solution has to be filtered. The filter here applied require the truncation of the element of the M as far as the noise contented in the measurement increase, according to the Morozov's discrepancy principle.

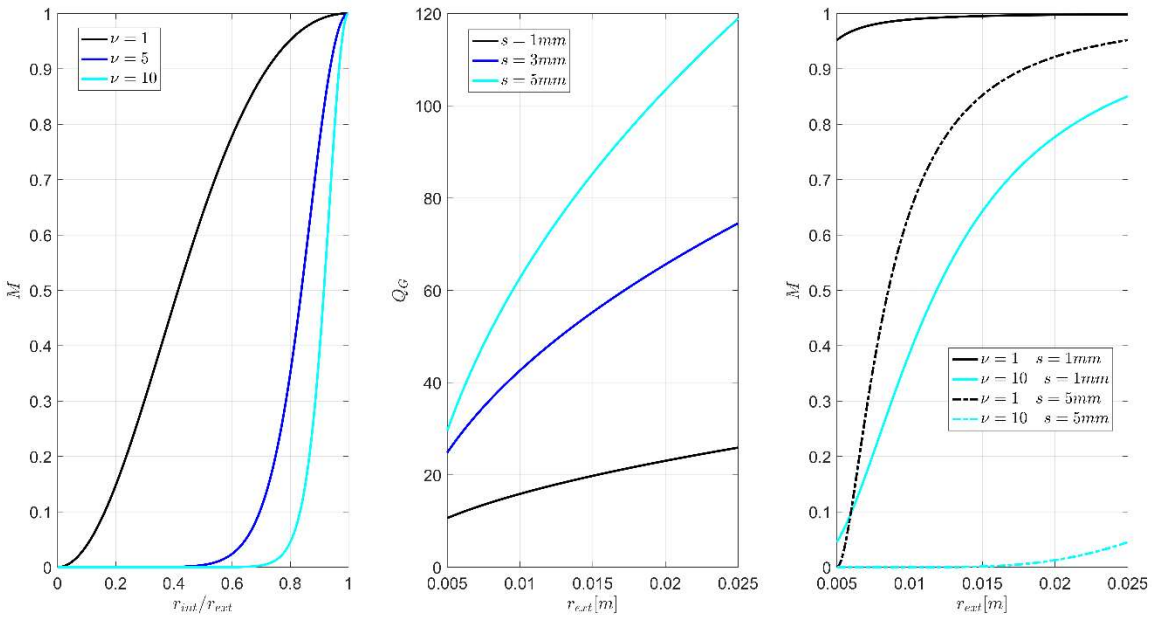

(a) (b) (c)

Figure A.2: (a) effect of the tube thickness on the M matrix, (b) effect of the external dimension of the tube for three different thickness on the Q_G term and (c) effect of the external dimension of the tube for two different thickness and harmonic frequencies on the M matrix

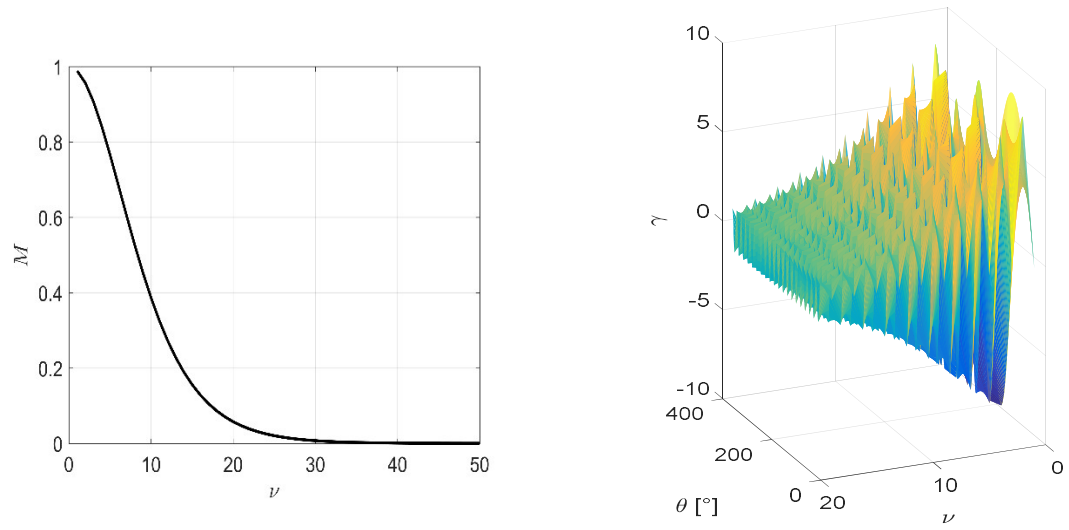

(a) (b)

Figure A.3: (a) effect of the numbers of harmonics on the M for a representative value $r_{int}/r_{ext} = 0.9$ and (b) γ basis

A.4 Solve the second auxiliary problem system using the Classical Integral Transform Technique:

The linear system presented in *Chapter 4* (Equation (4.41)) could be solved analytically by using the Classical Integral Transform Technique. The analytical solution of the PDE system avoid the use of numerical method to solve this system making the code computationally fast.

Operate on the physic in θ direction:

Due to physical problem, is possible to write the Laplacian defined in the Equation (4.41.1) using the cylindrical coordinate:

$$\frac{1}{r}\frac{\partial}{\partial r}\left(r\frac{\partial F}{\partial r}\right)+\frac{1}{r^2}\frac{\partial}{\partial \theta}\left(\frac{\partial F}{\partial \theta}\right)=0$$

$$\frac{\partial^2 F}{\partial r^2}+\frac{1}{r}\frac{\partial F}{\partial r}+\frac{1}{r^2}\frac{\partial^2 F}{\partial \theta^2}=0 \tag{A.11}$$

Defining the integral transform as:

$$\bar{F}=\int_{\theta=0}^{2\pi} F_{(r,\nu,\theta\prime)}\, cos[\nu(\theta-\theta')]\, d\theta' \tag{A.12}$$

and the inversion formula, that could be divided in two part: the first one is a constant term while the second one is function of the number of the harmonics:

$$F = \frac{1}{2\pi}\bar{F}_{(r,\theta,\nu=0)} + \sum_{\nu=1}^{\infty}\frac{1}{\pi}\bar{F}_{(r,\theta,\nu)} \tag{A.13}$$

is possible to re-write the Laplacian in cylindrical coordinate defined in the Equation (A.11) multiplying times $cos[\nu(\theta-\theta')]$ and integrating it:

$$\int_{\theta\prime=0}^{2\pi}\frac{\partial^2 F}{\partial r^2}\,cos[\nu(\theta-\theta')]\,d\theta' + \int_{\theta\prime=0}^{2\pi}\frac{1}{r}\frac{\partial F}{\partial r}\,cos[\nu(\theta-\theta')]\,d\theta' + \int_{\theta\prime=0}^{2\pi}\frac{1}{r^2}\frac{\partial^2 F}{\partial\theta^2}\,cos[\nu(\theta-\theta')]\,d\theta' = 0$$

$$\frac{\partial^2}{\partial r^2}\int_{\theta\prime=0}^{2\pi}F\,cos[\nu(\theta-\theta')]\,d\theta' + \frac{1}{r}\frac{\partial}{\partial r}\int_{\theta\prime=0}^{2\pi}F\,cos[\nu(\theta-\theta')]\,d\theta' + \frac{1}{r^2}\int_{\theta\prime=0}^{2\pi}\frac{\partial^2 F}{\partial\theta^2}\,cos[\nu(\theta-\theta')]\,d\theta' = 0$$

substituting the definition given in the Equation (A.12) is easy to get:

$$\frac{d^2}{dr^2}\bar{F} + \frac{1}{r}\frac{d}{dr}\bar{F} + \frac{1}{r^2}\int_{\theta\prime=0}^{2\pi}\frac{\partial^2 F}{\partial\theta^2}\,cos[\nu(\theta-\theta')]\,d\theta' = 0 \tag{A.14}$$

the last integral of this equation can be solved integrating by part two times:

$$\begin{aligned}\int_{\theta\prime=0}^{2\pi} cos[\nu(\theta-\theta')]\frac{\partial^2 F}{\partial\theta^2}d\theta' &= \left(\frac{\partial F}{\partial\theta}\cos[\,\nu(\theta-\theta')\,]\right)_{\theta=0}^{2\pi} - \int_{\theta'=0}^{2\pi} -\nu\sin[\nu(\theta-\theta')]\,\frac{\partial F}{\partial\theta}\,d\theta' \\ &= \left(\frac{\partial F}{\partial\theta}\cos[\,\nu(\theta-\theta')\,]\right)_{\theta=0}^{2\pi} - (-F\nu\sin[\nu(\theta-\theta')])_{\theta=0}^{2\pi} \\ &\quad - \int_{\theta'=0}^{2\pi}\nu^2\cos[\nu(\theta-\theta')]\;F\,d\theta' = -\nu^2\bar{F}\end{aligned}$$

Substituting this expression in the Equation (A.14) the transformation of the physical problem, become:

$$\frac{d^2}{dr^2}\bar{F} + \frac{1}{r}\frac{d}{dr}\bar{F} + \frac{1}{r^2}\nu^2\bar{F} = 0 \tag{A.15}$$

Operate on the boundary conditions:

The conditions imposed at the internal boundary Γ_{int} (Equation (4.41.2)) is easy transformed by multiplying times $cos[\nu(\theta - \theta')]$:

$$\bar{F} = \int_{\theta'=0}^{2\pi} F \cos[\nu(\theta - \theta')]\, d\theta'$$

remembering the definition given in the Equation (4.41.2) is possible to re-write the last expression to get the transformation of the internal boundary condition:

$$\bar{F} = 0$$

The conditions imposed at the external boundary Γ_{ext} (Equation (4.41.3)) is easy transformed by multiplying times $cos[\nu(\theta - \theta')]$:

$$\bar{F} = \int_{\theta'=0}^{2\pi} \psi \cos[\nu(\theta - \theta')]\, d\theta'$$

remembering the definition given in the Equation (4.41.3) is possible to re-write the last expression to get the transformation of the external boundary condition:

$$\bar{F} = \bar{\psi} \tag{A.16}$$

where $\bar{\psi}$ is the transformation of the potential imposed in the second auxiliary problem (Equation (4.41.3)):

$$\bar{\psi} = \int_{\theta'=0}^{2\pi} \psi \cos[\nu(\theta - \theta')]\, d\theta' \tag{A.17}$$

Final system of equation and its solution:

The transformation of the auxiliary problem defined by the Equations (4.41.1)-(4.41.3) is:

$$\begin{aligned} &\nabla^2 \bar{F} = 0 \quad in\ \Omega \\ &\bar{F} = 0 \quad at\ \Gamma_{int} \\ &\bar{F} = \bar{\psi} \quad at\ \Gamma_{ext} \end{aligned} \tag{A.18}$$

the last system of equations is easy to solve. The solution of the transformed problem is:

$$\bar{F} = \bar{\psi}_\nu \sinh\left[\nu\left(\ln\left[\frac{r_{int}}{r}\right]\right)\right] \operatorname{csch}\left[\nu\left(\ln\left[\frac{r_{int}}{r_{ext}}\right]\right)\right] \tag{A.19}$$

In order to obtain the solution of the second auxiliary problem, the last equations has to be inverted using the definition given in the Equation (A.13):

$$\begin{aligned} F = \frac{1}{2\pi}\bar{\psi}_{\nu=0} \sinh\left[\nu\left(\ln\left[\frac{r_{int}}{r}\right]\right)\right]_{\nu=0} \operatorname{csch}\left[\nu\left(\ln\left[\frac{r_{int}}{r_{ext}}\right]\right)\right]_{\nu=0} \\ + \sum_{\nu=1}^{\infty} \frac{1}{\pi}\, \bar{\psi}_\nu \sinh\left[\nu\left(\ln\left[\frac{r_{int}}{r}\right]\right)\right] \operatorname{csch}\left[\nu\left(\ln\left[\frac{r_{int}}{r_{ext}}\right]\right)\right] \end{aligned} \tag{A.20}$$

The first term on the right hand side of the last equation can be re-written as:

$$\begin{aligned} &\frac{1}{2\pi}\bar{\psi}_{\nu=0} \sinh\left[\nu\left(\ln\left[\frac{r_{int}}{r}\right]\right)\right]_{\nu=0} \operatorname{csch}\left[\nu\left(\ln\left[\frac{r_{int}}{r_{ext}}\right]\right)\right]_{\nu=0} \\ &= \frac{1}{2\pi}\bar{\psi}_{\nu=0} \frac{\sinh\left[\nu\left(\ln\left[\frac{r_{int}}{r}\right]\right)\right]_{\nu=0}}{\sinh\left[\nu\left(\ln\left[\frac{r_{int}}{r}\right]\right)\right]_{\nu=0}} = \frac{0}{0} \end{aligned}$$

then using the L'Hopital rule:

$$\frac{1}{2\pi}\bar{\psi}_{\nu=0}\ \sinh\left[\nu\left(\ln\left[\frac{r_{int}}{r}\right]\right)\right]_{\nu=0}\operatorname{csch}\left[\nu\left(\ln\left[\frac{r_{int}}{r_{ext}}\right]\right)\right]_{\nu=0}$$

$$= \frac{1}{2\pi}\bar{\psi}_{\nu=0}\ \frac{\sinh\left[\nu\left(\ln\left[\frac{r_{int}}{r}\right]\right)\right]_{\nu=0}}{\sinh\left[\nu\left(\ln\left[\frac{r_{int}}{r_{ext}}\right]\right)\right]_{\nu=0}}$$

$$= \frac{1}{2\pi}\bar{\psi}_{\nu=0}\ \frac{\frac{\partial}{\partial\nu}\sinh\left[\nu\left(\ln\left[\frac{r_{int}}{r}\right]\right)\right]_{\nu=0}}{\frac{\partial}{\partial\nu}\sinh\left[\nu\left(\ln\left[\frac{r_{int}}{r_{ext}}\right]\right)\right]_{\nu=0}}$$

$$= \frac{1}{2\pi}\bar{\psi}_{\nu=0}\ \frac{\ln\left[\frac{r_{int}}{r}\right]\cosh\left[\nu\, ln\left[\frac{r_{int}}{r}\right]\right]_{\nu=0}}{\ln\left[\frac{r_{int}}{r_{ext}}\right]\cosh\left[\nu\, ln\left[\frac{r_{int}}{r_{ext}}\right]\right]_{\nu=0}} = \frac{1}{2\pi}\bar{\psi}_{\nu=0}\ \frac{\ln\left[\frac{r_{int}}{r}\right]}{\ln\left[\frac{r_{int}}{r_{ext}}\right]}$$

Finally, the Equation (A.19) became:

$$\begin{aligned} F = {} & \frac{1}{2\pi}\bar{\psi}_{\nu=0}\sinh\left[\nu\left(\ln\left[\frac{r_{int}}{r}\right]\right)\right]_{\nu=0}\operatorname{csch}\left[\nu\left(\ln\left[\frac{r_{int}}{r_{ext}}\right]\right)\right]_{\nu=0} \\ & + \sum_{\nu=1}^{\infty}\frac{1}{\pi}\ \bar{\psi}_{\nu}\sinh\left[\nu\left(\ln\left[\frac{r_{int}}{r}\right]\right)\right]\operatorname{csch}\left[\nu\left(\ln\left[\frac{r_{int}}{r_{ext}}\right]\right)\right] \\ & = \frac{1}{2\pi}\bar{\psi}_{\nu=0}\ \frac{\ln\left[\frac{r_{int}}{r}\right]}{\ln\left[\frac{r_{int}}{r_{ext}}\right]} \\ & + \sum_{\nu=1}^{\infty}\frac{1}{\pi}\ \bar{\psi}_{\nu}\sinh\left[\nu\left(\ln\left[\frac{r_{int}}{r}\right]\right)\right]\operatorname{csch}\left[\nu\left(\ln\left[\frac{r_{int}}{r_{ext}}\right]\right)\right] \end{aligned} \tag{A.21}$$

A.5 Build the solution of the first auxiliary problem:

According to the definition given in the Equations (4.15.1)-(4.15.3), the solution has to be divided in at least three steps for different values of harmonic frequencies k of the orthonormal basis function:

k=1

As defined in the Equation (4.15.1):

$$\psi = \frac{1}{\sqrt{r_{ext}}\sqrt{2\pi}} \quad for\ k = 1$$

According to the Equation (A.17):

$$\bar{\psi}_{\nu} = \int_{\theta'=0}^{2\pi} \frac{1}{\sqrt{r_{ext}}\sqrt{2\pi}} \cos[\nu(\theta-\theta')] d\theta' = \frac{1}{\sqrt{r_{ext}}\sqrt{2\pi}} \int_{\theta'=0}^{2\pi} \cos[\nu(\theta-\theta')] d\theta'$$

$$= \frac{1}{\sqrt{r_{ext}}\sqrt{2\pi}} \left(\frac{\sin[\nu\theta] - \sin[\nu\theta - 2\pi\nu]}{\nu\theta} \right)_{\theta=0}^{2\pi} = 0$$

while:

$$\bar{\psi}_{\nu=0} = \int_{\theta'=0}^{2\pi} \frac{1}{\sqrt{r_{ext}}\sqrt{2\pi}} \cos[\nu(\theta-\theta')]_{\nu=0} d\theta' = \frac{1}{\sqrt{r_{ext}}\sqrt{2\pi}} \int_{\theta'=0}^{2\pi} d\theta'$$

$$= \frac{1}{\sqrt{r_{ext}}\sqrt{2\pi}} 2\pi = \sqrt{\frac{2\pi}{r_{ext}}}$$

since $\cos[\nu(\theta-\theta')]_{\nu=0} = 1$.

According to the Equation (A.21) the auxiliary function is defined as:

$$F_{k=1} = \frac{1}{2\pi} \bar{\psi}_{\nu=0} \frac{\ln\left[\frac{r_{int}}{r}\right]}{\ln\left[\frac{r_{int}}{r_{ext}}\right]} + \sum_{\nu=1}^{\infty} \frac{1}{\pi} \bar{\psi}_{\nu} \sinh\left[\nu\left(\ln\left[\frac{r_{int}}{r}\right]\right)\right] \operatorname{csch}\left[\nu\left(\ln\left[\frac{r_{int}}{r_{ext}}\right]\right)\right]$$

$$= \frac{1}{2\pi} \bar{\psi}_{\nu=0} \frac{\ln\left[\frac{r_{int}}{r}\right]}{\ln\left[\frac{r_{int}}{r_{ext}}\right]} = \frac{1}{2\pi} \sqrt{\frac{2\pi}{r_{ext}}} \frac{\ln\left[\frac{r_{int}}{r}\right]}{\ln\left[\frac{r_{int}}{r_{ext}}\right]} = \frac{1}{\sqrt{2\pi\, r_{ext}}} \frac{\ln\left[\frac{r_{int}}{r}\right]}{\ln\left[\frac{r_{int}}{r_{ext}}\right]}$$

The trace of the auxiliary function at the internal boundary Γ_{int} is:

$$\xi_{int} = \left.\frac{\partial \mathrm{F}_{(\psi)}}{\partial \mathbf{n}}\right|_{\Gamma_{int}} = -\frac{1}{\sqrt{2\pi\, r_{ext}}} \frac{1}{\ln\left[\frac{r_{int}}{r_{ext}}\right] r_{int}}$$

The normal derivative of the auxiliary function at the external boundary is:

$$\left.\frac{\partial F}{\partial \boldsymbol{n}}\right|_{\Gamma_{ext}} = -\frac{1}{\sqrt{2\pi\, r_{ext}}} \frac{1}{\ln\left[\frac{r_{int}}{r_{ext}}\right] r_{ext}}$$

The reciprocity functional defined in the Equation (4.42) became:

$$R_F = \int_{\Gamma_{ext}} \left(-\psi \frac{h_{env}(T - T_{env})}{K} - Y \frac{\delta F}{\delta \boldsymbol{n}} \right) d\Gamma_{ext}$$
$$= \int_{\theta'=0}^{2\pi} r_{ext} \left(-\psi \frac{h_{env}(T - T_{env})}{K} - Y \frac{\delta F}{\delta \boldsymbol{n}} \right) d\theta'$$

since the temperature profile at the external boundary is supposed to be known and acquired through the thermo-camera imaging, the last equation become:

$$R_F = \int_{\Gamma_{ext}} \left(-\psi \frac{h_{env}(T - T_{env})}{K} - Y \frac{\delta F}{\delta \boldsymbol{n}} \right) d\Gamma_{ext}$$
$$= \int_{\theta'=0}^{2\pi} r_{ext} \left(-\psi \frac{h_{env}(Y - T_{env})}{K} - Y \frac{\delta F}{\delta \boldsymbol{n}} \right) d\theta'$$
$$= -r_{ext} \int_{\theta'=0}^{2\pi} \left(\psi \frac{h_{env}(Y - T_{env})}{K} + Y \frac{\delta F}{\delta \boldsymbol{n}} \right) d\theta'$$
$$= -r_{ext} \int_{\theta'=0}^{2\pi} \left(\frac{1}{\sqrt{2\pi\, r_{ext}}} \frac{h_{env}(Y - T_{env})}{K} \right.$$
$$\left. - Y \frac{1}{\sqrt{2\pi\, r_{ext}}} \frac{1}{\ln\left[\frac{r_{int}}{r_{ext}}\right] r_{ext}} \right) d\theta'$$
$$= \frac{-r_{ext}}{\sqrt{2\pi\, r_{ext}}} \int_{\theta'=0}^{2\pi} \left(\frac{h_{env}(Y - T_{env})}{K} - Y \frac{1}{\ln\left[\frac{r_{int}}{r_{ext}}\right] r_{ext}} \right) d\theta'$$
$$= \frac{-r_{ext}}{\sqrt{2\pi\, r_{ext}}} \left(\int_{\theta'=0}^{2\pi} Y \left(\frac{h_{env}}{K} - \frac{1}{\ln\left[\frac{r_{int}}{r_{ext}}\right] r_{ext}} \right) d\theta' \right.$$
$$\left. - \frac{h_{env}}{K} \int_{\theta'=0}^{2\pi} T_{env}\, d\theta' \right)$$
$$= \frac{-r_{ext}}{\sqrt{2\pi\, r_{ext}}} \left(\left(\frac{h_{env}}{K} - \frac{1}{\ln\left[\frac{r_{int}}{r_{ext}}\right] r_{ext}} \right) \int_{\theta'=0}^{2\pi} Y\, d\theta' \right.$$
$$\left. - \frac{h_{env}}{K} \int_{\theta'=0}^{2\pi} T_{env}\, d\theta' \right)$$

Using the Fourier's series expansion, the integral of the measurement at the external boundary Γ_{ext} in the last expression can be re-written as:

$$\begin{aligned}\int_{\theta'=0}^{2\pi} Y\, d\theta' &= \int_{\theta'=0}^{2\pi} \big(a_0 + a_1\cos[\theta'] + b_1\sin[\theta'] + \cdots \\ &\quad + a_{k_F}\cos[k_F\theta'] + b_{k_F}\sin[k_F\theta']\big)d\theta' \\ &= \int_{\theta'=0}^{2\pi} a_0 d\theta' + \int_{\theta'=0}^{2\pi} a_1\cos[\theta']\, d\theta' + \int_{\theta'=0}^{2\pi} b_1\sin[\theta']\, d\theta' + \cdots \\ &\quad + \int_{\theta'=0}^{2\pi} a_{k_F}\cos[k_F\theta']\, d\theta' + \int_{\theta'=0}^{2\pi} b_{k_F}\sin[k_F\theta']\, d\theta'\end{aligned}$$

where $a_0, a_1, b_1, \ldots, a_{k_F}, b_{k_F}$ are the Fourier's expansion coefficients.

Since the finite integral, from zero to 2π, of both the harmonic function *sine* and *cosine* is null, the last expression becomes:

$$\int_{\theta'=0}^{2\pi} Y\, d\theta' = 2\pi a_0$$

Since the environmental temperature is supposed to be constant, its integral is:

$$\int_{\theta'=0}^{2\pi} T_{env}\, d\theta' = 2\pi T_{env}$$

Substituting those results, the reciprocity functional becomes:

$$\begin{aligned}R_F &= \frac{-r_{ext}}{\sqrt{2\pi\, r_{ext}}}\left(\left(\frac{h_{env}}{K} - \frac{1}{\ln\left[\frac{r_{int}}{r_{ext}}\right] r_{ext}}\right)\int_{\theta'=0}^{2\pi} Y\, d\theta' - \frac{h_{env}}{K}\int_{\theta'=0}^{2\pi} T_{env}\, d\theta'\right) = \\ &= \frac{-r_{ext}}{\sqrt{2\pi\, r_{ext}}}\left(\left(\frac{h_{env}}{K} - \frac{1}{\ln\left[\frac{r_{int}}{r_{ext}}\right] r_{ext}}\right)2\pi a_0 - \frac{h_{env}}{K} 2\pi\, T_{env}\right) \\ &= -\sqrt{2\pi r_{ext}}\,\frac{h_{env}}{K}\left(\left(1 - \frac{K}{\ln\left[\frac{r_{int}}{r_{ext}}\right] r_{ext} h_{env}}\right)a_0 - T_{env}\right)\end{aligned}$$

According to the Equation (4.43) the integral of the internal heat generation is:

$$Q_F = \int_{\Omega'} \left(F\frac{q_g}{K}\right) d\Omega' = \int_{\theta'=0}^{2\pi}\int_{r'=r_{int}}^{r_{ext}} r\frac{q_g}{K}\frac{1}{\sqrt{2\pi\, r_{ext}}}\frac{\ln\left[\frac{r_{int}}{r}\right]}{\ln\left[\frac{r_{int}}{r_{ext}}\right]} dr' d\theta'$$

$$= \frac{q_g}{K}\frac{1}{\sqrt{2\pi\, r_{ext}}}\frac{1}{\ln\left[\frac{r_{int}}{r_{ext}}\right]} 2\pi \int_{r'=r_{int}}^{r_{ext}} r\ln\left[\frac{r_{int}}{r}\right] dr'$$

The integral that appear in the last expression can be solved integrating by part:

$$\int_{r'=r_{int}}^{r_{ext}} r\ln\left[\frac{r_{int}}{r}\right] dr' = \left(\ln\left[\frac{r_{int}}{r}\right]\frac{1}{2}r^2\right)_{r=r_{int}}^{r_{ext}} - \int_{r'=r_{int}}^{r_{ext}} \frac{1}{2}r^2\left(-\frac{1}{r}\right) dr'$$

$$= \left(\ln\left[\frac{r_{int}}{r}\right]\frac{1}{2}r^2\right)_{r=r_{int}}^{r_{ext}} + \frac{1}{2}\int_{r'=r_{int}}^{r_{ext}} r\, dr'$$

$$= \left(\ln\left[\frac{r_{int}}{r_{ext}}\right]\frac{1}{2}r_{ext}^2 - \ln\left[\frac{r_{int}}{r_{ext}}\right]\frac{1}{2}r_{int}^2\right) + \frac{1}{4}(r_{ext}^2 - r_{int}^2)$$

$$= \ln\left[\frac{r_{int}}{r_{ext}}\right]\frac{1}{2}r_{ext}^2 + \frac{1}{4}(r_{ext}^2 - r_{int}^2)$$

then the integral of the internal heat generation become:

$$Q_F = \int_{\Omega'} \left(F\frac{q_g}{K}\right) d\Omega' = \frac{q_g}{K}\sqrt{\frac{\pi}{2\, r_{ext}}}\left(r_{ext}^2 + \frac{1}{2}\frac{r_{ext}^2 - r_{int}^2}{\ln\left[\frac{r_{int}}{r_{ext}}\right]}\right)$$

The first element of the matrix of the inner product becomes:

$$N = \int_{\Gamma_{\text{int}}} \langle \xi_v, \xi_v \rangle \, d\Gamma_{int} = \int_{\theta'=0}^{2\pi} r_{int}\, \langle \xi_v, \xi_v \rangle \, d\theta'$$

$$= r_{int}\int_{\theta'=0}^{2\pi}\left(\frac{1}{\sqrt{2\pi\, r_{ext}}}\frac{1}{\ln\left[\frac{r_{int}}{r_{ext}}\right] r_{int}}\frac{1}{\sqrt{2\pi\, r_{ext}}}\frac{1}{\ln\left[\frac{r_{int}}{r_{ext}}\right] r_{int}}\right) d\theta'$$

$$= \frac{1}{\ln^2\left[\frac{r_{int}}{r_{ext}}\right] r_{int} r_{ext}}$$

k=2,4,6,…,N-1 & k≠2v

As defined in the Equation (4.15.2):

$$\psi = \frac{1}{\sqrt{r_{ext}}\sqrt{\pi}} cos\left[\frac{k}{2}\theta\right] \quad for\ k = 2,4,6,\dots N-1$$

According to the Equation (A.17):

$$\bar{\psi} = \int_{\theta'=0}^{2\pi} \frac{1}{\sqrt{r_{ext}}\sqrt{\pi}} cos\left[\frac{k}{2}\theta'\right] \cos[v(\theta-\theta')] d\theta'$$

$$= \frac{1}{\sqrt{r_{ext}}\sqrt{\pi}} \int_{\theta'=0}^{2\pi} cos\left[\frac{k}{2}\theta'\right] \cos[v(\theta-\theta')] d\theta' = 0$$

Since the harmonic function that appear in the inner product have different frequency, their inner product is null. In the same way is possible to calculate the transformation of the basis for the zero harmonic, as follows:

$$\bar{\psi}_{v=0} = \int_{\theta'=0}^{2\pi} \frac{1}{\sqrt{r_{ext}}\sqrt{\pi}} cos\left[\frac{k}{2}\theta'\right] \cos[v(\theta-\theta')]\, d\theta'$$

since $\cos[v(\theta-\theta')]_{v=0} = 1$ the last expression becomes:

$$\bar{\psi}_{v=0} = \int_{\theta'=0}^{2\pi} \frac{1}{\sqrt{r_{ext}}\sqrt{\pi}} cos\left[\frac{k}{2}\theta'\right] d\theta' = \frac{1}{\sqrt{r_{ext}}\sqrt{\pi}} \left(\frac{2}{k}\sin\left[\frac{k}{2}\theta\right]\right)_{\theta=0}^{2\pi} = 0$$

Considering that $\bar{\psi}$ and $\bar{\psi}_{v=0}$ are null, the auxiliary function F is null and also all the other result are zeros thus those frequency of the orthonormal basis function doesn't participate in the solution.

k=2,4,6,…,N-1 & k=2v

As defined in the Equation (4.15.2):

$$\psi = \frac{1}{\sqrt{r_{ext}}\sqrt{\pi}} cos\left[\frac{k}{2}\theta\right] \quad for\ k = 2,4,6,\dots N-1$$

According to the Equation (A.17):

$$\bar{\psi} = \int_{\theta'=0}^{2\pi} \frac{1}{\sqrt{r_{ext}}\sqrt{\pi}} cos\left[\frac{k}{2}\theta'\right] \cos[\nu(\theta-\theta')] d\theta'$$

$$= \frac{1}{\sqrt{r_{ext}}\sqrt{\pi}} \int_{\theta'=0}^{2\pi} cos\left[\frac{2\nu}{2}\theta'\right] \cos[\nu(\theta-\theta')] d\theta'$$

$$= \frac{1}{\sqrt{r_{ext}}\sqrt{\pi}} \frac{4\pi\cos[\nu\theta] + \sin[\nu\theta] - \sin[\nu(\theta-4\pi)]}{4\nu}$$

$$= \frac{1}{\sqrt{r_{ext}}\sqrt{\pi}} \cos[\nu\theta]$$

is possible to re-write the last integral using the subtraction formula the for cosine terms, getting:

$$\int_{\theta'=0}^{2\pi} cos[\nu\theta'] \cos[\nu(\theta-\theta')] d\theta' = \int_{\theta'=0}^{2\pi} cos[\nu\theta'] (\cos[\nu\theta - \nu\theta'])\, d\theta'$$

$$= \int_{\theta'=0}^{2\pi} cos[\nu\theta'] (\cos[\nu\theta]\cos[\nu\theta'] + \sin[\nu\theta]\sin[\nu\theta'])\, d\theta'$$

$$= \int_{\theta'=0}^{2\pi} cos[\nu\theta'] \cos[\nu\theta]\cos[\nu\theta']\, d\theta'$$

$$+ \int_{\theta'=0}^{2\pi} cos[\nu\theta']\sin[\nu\theta]\sin[\nu\theta']\, d\theta'$$

$$= \cos[\nu\theta] \int_{\theta'=0}^{2\pi} cos[\nu\theta']\cos[\nu\theta']\, d\theta'$$

$$+ \sin[\nu\theta] \int_{\theta'=0}^{2\pi} cos[\nu\theta']\ \sin[\nu\theta']\, d\theta'$$

since $\int_{\theta'=0}^{2\pi} cos[\nu\theta']\cos[\nu\theta']\, d\theta' = \pi$ and $\int_{\theta'=0}^{2\pi} cos[\nu\theta']\ \sin[\nu\theta']\, d\theta' = 0$ the last expression becomes:

$$\int_{\theta'=0}^{2\pi} cos[\nu\theta'] \cos[\nu(\theta-\theta')] d\theta' = \pi\cos[\nu\theta]$$

Then the transformation of the basis becomes:

$$\bar{\psi} = \frac{1}{\sqrt{r_{ext}}\sqrt{\pi}} \int_{\theta'=0}^{2\pi} cos\left[\frac{2\nu}{2}\theta'\right] \cos[\nu(\theta-\theta')] d\theta' = \sqrt{\frac{\pi}{r_{ext}}} \cos[\nu\phi]$$

Then the transformation of the basis for $\nu = 0$ is:

$$\bar{\psi}_{\nu=0} = \int_{\theta'=0}^{2\pi} \frac{1}{\sqrt{r_{ext}}\sqrt{\pi}} cos\left[\frac{k}{2}\theta'\right] \cos[\nu(\theta-\theta')] d\theta'$$

since $\cos[\nu(\theta-\theta')]_{\nu=0} = 1$ the last expression become:

$$\bar{\psi}_{\nu=0} = \int_{\theta'=0}^{2\pi} \frac{1}{\sqrt{r_{ext}}\sqrt{\pi}} cos\left[\frac{k}{2}\theta'\right] d\theta' = \frac{1}{\sqrt{r_{ext}}\sqrt{\pi}} \frac{\sin\left[\left(\frac{k}{2}\right)\theta\right]_{\theta=0}^{2\pi}}{\frac{k}{2}} = 0$$

According to the Equation (A.21) the auxiliary function is defined as:

$$F = \frac{1}{2\pi}\bar{\psi}_{\nu=0} \frac{\ln\left[\frac{r_{int}}{r}\right]}{\ln\left[\frac{r_{int}}{r_{ext}}\right]} + \sum_{\nu=1}^{\infty} \frac{1}{\pi} \bar{\psi}_{\nu} \sinh\left[\nu\left(\ln\left[\frac{r_{int}}{r}\right]\right)\right] \operatorname{csch}\left[\nu\left(\ln\left[\frac{r_{int}}{r_{ext}}\right]\right)\right]$$

$$= \sum_{\nu=1}^{\infty} \frac{1}{\pi} \sqrt{\frac{\pi}{r_{ext}}} \cos[\nu\phi] \sinh\left[\nu\left(\ln\left[\frac{r_{int}}{r}\right]\right)\right] \operatorname{csch}\left[\nu\left(\ln\left[\frac{r_{int}}{r_{ext}}\right]\right)\right]$$

The normal derivative of the auxiliary function at the external boundary is:

$$\left.\frac{\partial F}{\partial \boldsymbol{n}}\right|_{\Gamma_{ext}} = -\sqrt{\frac{1}{\pi r_{ext}}} \sum_{\nu=1}^{\infty} \cos[\nu\theta] \operatorname{csch}\left[\nu\left(\ln\left[\frac{r_{int}}{r_{ext}}\right]\right)\right] \cosh\left[\nu\left(\ln\left[\frac{r_{int}}{r_{ext}}\right]\right)\right] \frac{\nu}{r_{ext}}$$

The trace of the auxiliary function at the internal boundary Γ_{int} is:

$$\xi = \left(\frac{\partial F}{\partial \boldsymbol{n}}\right)\Big|_{\Gamma_{int}} = -\sqrt{\frac{1}{\pi r_{ext}}} \sum_{\nu=1}^{\infty} \cos[\nu\theta] \operatorname{csch}\left[\nu\left(\ln\left[\frac{r_{int}}{r_{ext}}\right]\right)\right] \frac{\nu}{r_{int}}$$

The reciprocity functional defined in the Equation (4.42) became:

$$R_F = \int_{\Gamma_{ext}} \left(-\psi \frac{h_{env}(Y - T_{env})}{K} - Y \frac{\delta F}{\delta \boldsymbol{n}} \right) d\Gamma_{ext}$$

$$= \int_{\theta'=0}^{2\pi} r_{ext} \left(-\psi \frac{h_{env}(Y - T_{env})}{K} - Y \frac{\delta F}{\delta \boldsymbol{n}} \right) d\theta'$$

$$= -r_{ext} \int_{\theta'=0}^{2\pi} \left(\psi \frac{h_{env}}{K} Y + \psi \frac{h_{env}}{K} T_{env} + Y \frac{\delta F}{\delta \boldsymbol{n}} \right) d\theta'$$

$$= -r_{ext} \int_{\theta'=0}^{2\pi} Y \left(\psi \frac{h_{env}}{K} - \frac{\delta F}{\delta \boldsymbol{n}} \right) d\theta' - r_{ext} \int_{\theta'=0}^{2\pi} \psi \frac{h_{env}}{K} T_{env} \; d\theta'$$

$$= -r_{ext} \int_{\theta'=0}^{2\pi} Y \left(\frac{1}{\sqrt{r_{ext}}\sqrt{\pi}} cos\left[\frac{k}{2} \theta' \right] \frac{h_{env}}{K} \right.$$

$$\left. - \frac{1}{\sqrt{r_{ext}}\sqrt{\pi}} \cos[\nu\theta'] \; \operatorname{csch}\left[\nu \left(\ln\left[\frac{r_{int}}{r_{ext}} \right] \right) \right] \cosh\left[\nu \left(\ln\left[\frac{r_{int}}{r_{ext}} \right] \right) \right] \frac{\nu}{r_{ext}} \right) d\theta'$$

$$- r_{ext} \int_{\theta'=0}^{2\pi} \frac{1}{\sqrt{r_{ext}}\sqrt{\pi}} cos[\nu\theta'] \frac{h_{env}}{K} T_{env} \; d\theta'$$

$$= -r_{ext} \int_{\theta'=0}^{2\pi} Y \left(\frac{1}{\sqrt{r_{ext}}\sqrt{\pi}} cos[\nu\theta'] \frac{h_{env}}{K} \right.$$

$$\left. - \frac{1}{\sqrt{r_{ext}}\sqrt{\pi}} \cos[\nu\theta'] \operatorname{sech}\left[\nu \left(\ln\left[\frac{r_{int}}{r_{ext}} \right] \right) \right] \sinh\left[\nu \left(\ln\left[\frac{r_{int}}{r_{ext}} \right] \right) \right] \frac{\nu}{r_{ext}} \right) d\theta'$$

$$- r_{ext} \frac{1}{\sqrt{r_{ext}}\sqrt{\pi}} \frac{h_{env}}{K} T_{env} \int_{\theta'=0}^{2\pi} cos[\nu\theta'] \; d\theta'$$

since $\int_{\theta'=0}^{2\pi} cos[\nu\theta'] \; d\theta' = 0$ the last expression become:

$$R_F = \int_{\Gamma_{ext}} \left(-\psi \frac{h_{env}(Y - T_{env})}{K} - Y \frac{\delta F}{\delta \boldsymbol{n}} \right) d\Gamma_{ext} =$$

$$= -r_{ext} \int_{\theta'=0}^{2\pi} Y \frac{1}{\sqrt{r_{ext}}\sqrt{\pi}} cos[\nu\theta'] \left(\frac{h_{env}}{K} \right.$$

$$\left. - \operatorname{csch}\left[\nu \left(\ln\left[\frac{r_{int}}{r_{ext}} \right] \right) \right] \cosh\left[\nu \left(\ln\left[\frac{r_{int}}{r_{ext}} \right] \right) \right] \frac{\nu}{r_{ext}} \right) d\theta'$$

$$= -r_{ext} \frac{1}{\sqrt{r_{ext}}\sqrt{\pi}} \left(\frac{h_{env}}{K} \right.$$

$$\left. - \operatorname{csch}\left[\nu \left(\ln\left[\frac{r_{int}}{r_{ext}} \right] \right) \right] \cosh\left[\nu \left(\ln\left[\frac{r_{int}}{r_{ext}} \right] \right) \right] \frac{\nu}{r_{ext}} \right) \int_{\theta'=0}^{2\pi} Y cos[\nu\theta'] \, d\theta'$$

Using the Fourier's series expansion, the integral of the measurement at the external boundary Γ_{ext} in the last expression can be re-written as:

$$\int_{\theta'=0}^{2\pi} Y\cos[\nu\theta']\,d\theta'$$

$$= \int_{\theta'=0}^{2\pi} \big(a_0\cos[\nu\theta']$$
$$+ a_1\cos[\theta']\cos[\nu\theta'] + b_1\sin[\theta']\cos[\nu\theta'] + \cdots$$
$$+ a_{k_F}\cos[k_F\theta']\cos[\nu\theta'] + b_{k_F}\sin[k_F\theta']\cos[\nu\theta']\big)d\theta'$$
$$= \int_{\theta'=0}^{2\pi} a_0\cos[\nu\theta']\,d\theta' + \int_{\theta'=0}^{2\pi} a_1\cos[\theta']\cos[\nu\theta']\,d\theta'$$
$$+ \int_{\theta'=0}^{2\pi} b_1\sin[\theta']\cos[\nu\theta']\,d\theta' + \cdots$$
$$+ \int_{\theta'=0}^{2\pi} a_{k_F}\cos[k_F\theta']\cos[\nu\theta']\,d\theta'$$
$$+ \int_{\theta'=0}^{2\pi} b_{k_F}\sin[k_F\theta']\cos[\nu\theta']\,d\theta'$$

since $\int_{\theta'=0}^{2\pi} a_0\cos[\nu\theta']\,d\theta' = 0$, $\int_{\theta'=0}^{2\pi} b_{k_F}\sin[k_F\theta']\cos[\nu\theta']\,d\theta' = 0$ for every k_F, and:

$$\int_{\theta'=0}^{2\pi} a_{k_F}\cos[k_F\theta']\cos[\nu\theta']\,d\theta' = \begin{cases} 0 & if\ k_F \neq \nu \\ \pi a_{k_F} & if\ k_F = \nu \end{cases}$$

the integral of the measurement at the external boundary becomes:

$$\int_{\theta'=0}^{2\pi} Y cos[\nu\theta']\,d\theta' = \pi a_\nu$$

and the reciprocity functional becomes:

$$
\begin{aligned}
&R_F \\
&= -r_{ext}\frac{1}{\sqrt{r_{ext}}\sqrt{\pi}}\left(\frac{h_{env}}{K}\right. \\
&\left. - \operatorname{csch}\left[\nu\ \left(\ln\left[\frac{r_{int}}{r_{ext}}\right]\right)\right]\cosh\left[\nu\ \left(\ln\left[\frac{r_{int}}{r_{ext}}\right]\right)\right]\frac{\nu}{r_{ext}}\right)\int_{\theta'=0}^{2\pi} Ycos[\nu\theta']\,d\theta' \\
&= -r_{ext}\frac{\pi a_\nu}{\sqrt{r_{ext}}\sqrt{\pi}}\left(\frac{h_{env}}{K} - \operatorname{csch}\left[\nu\ \left(\ln\left[\frac{r_{int}}{r_{ext}}\right]\right)\right]\cosh\left[\nu\ \left(\ln\left[\frac{r_{int}}{r_{ext}}\right]\right)\right]\frac{\nu}{r_{ext}}\right) \\
&= -a_\nu\sqrt{\pi r_{ext}}\left(\frac{h_{env}}{K} - \coth\left[\nu\ \left(\ln\left[\frac{r_{int}}{r_{ext}}\right]\right)\right]\frac{\nu}{r_{ext}}\right)
\end{aligned}
$$

According to the Equation (4.43) the integral of the internal heat generation is:

$$
\begin{aligned}
&Q_F = \int_{\Omega'}\left(F\frac{q_g}{K}\right)d\Omega' \\
&= \int_{\theta'=0}^{2\pi}\int_{r'=r_{int}}^{r_{ext}} r\frac{q_g}{K}\sqrt{\frac{1}{\pi r_{ext}}}\sum_{\nu=1}^{\infty}\cos[\nu\theta]\sinh\left[\nu\ \left(\ln\left[\frac{r_{int}}{r}\right]\right)\right]\operatorname{csch}\left[\nu\ \left(\ln\left[\frac{r_{int}}{r_{ext}}\right]\right)\right]dr'd\theta' \\
&= \frac{q_g}{K}\sqrt{\frac{1}{\pi\, r_{ext}}}\operatorname{csch}\left[\nu\ \left(\ln\left[\frac{r_{int}}{r_{ext}}\right]\right)\right]\int_{\theta'=0}^{2\pi}\int_{r'=r_{int}}^{r_{ext}} r\cos[\nu\theta]\sinh\left[\nu\ \left(\ln\left[\frac{r_{int}}{r}\right]\right)\right]dr'd\theta' \\
&= \frac{q_g}{K}\sqrt{\frac{1}{\pi\, r_{ext}}}\operatorname{csch}\left[\nu\ \left(\ln\left[\frac{r_{int}}{r_{ext}}\right]\right)\right]\int_{\theta'=0}^{2\pi}\cos[\nu\theta']\,d\theta'\int_{r'=r_{int}}^{r_{ext}} r'\sinh\left[\nu\ \left(\ln\left[\frac{r_{int}}{r'}\right]\right)\right]dr'
\end{aligned}
$$

since $\int_{\theta'=0}^{2\pi} cos[\nu\theta']\ d\theta' = 0$ the heat generation terms is null.

The even elements of the matrix of the inner product becomes:

$$
\begin{aligned}
&N = \int_{\Gamma_{\text{int}}}\langle\xi_\nu,\xi_\nu\rangle\ d\Gamma_{int} = \int_{\theta'=0}^{2\pi} r_{int}\,\langle\xi_\nu,\xi_\nu\rangle\,d\theta' \\
&= r_{int}\int_{\theta'=0}^{2\pi}\left(\sqrt{\frac{1}{\pi r_{ext}}}\cos[\nu\theta]\ \operatorname{csch}\left[\nu\ \left(\ln\left[\frac{r_{int}}{r_{ext}}\right]\right)\right]\frac{\nu}{r_{int}}\sqrt{\frac{1}{\pi r_{ext}}}\cos[\nu\theta]\ \operatorname{csch}\left[\nu\ \left(\ln\left[\frac{r_{int}}{r_{ext}}\right]\right)\right]\frac{\nu}{r_{int}}\right)d\theta' \\
&= \frac{r_{int}}{\pi r_{ext}}\operatorname{csch}^2\left[\nu\ \left(\ln\left[\frac{r_{int}}{r_{ext}}\right]\right)\right]\frac{\nu^2}{r_{int}^2}\int_{\theta'=0}^{2\pi}\cos^2[\nu\theta]\ d\theta'
\end{aligned}
$$

since $\int_{\theta'=0}^{2\pi} \cos^2[\nu\theta]\ d\theta' = \pi$ the last expression becomes:

$$N = \int_{\Gamma_{\text{int}}} \langle \xi_\nu, \xi_\nu \rangle\ d\Gamma_{int} = \frac{\nu^2}{r_{ext} r_{int}} \text{csch}^2 \left[\nu \left(\ln \left[\frac{r_{int}}{r_{ext}} \right] \right) \right]$$

k=3,5,7,…,N & k≠2v+1

As defined in the Equation (4.15.3):

$$\psi = \frac{1}{\sqrt{r_{ext}}\sqrt{\pi}} sin \left[\frac{k-1}{2} \theta \right] \quad for\ k = 2,4,6, \dots N-1$$

According to the Equation (A.7):

$$\bar{\psi} = \int_{\theta'=0}^{2\pi} \frac{1}{\sqrt{r_{ext}}\sqrt{\pi}} sin \left[\frac{k-1}{2} \theta' \right] \cos[\nu(\theta - \theta')] d\theta'$$

$$= \frac{1}{\sqrt{r_{ext}}\sqrt{\pi}} \int_{\theta'=0}^{2\pi} sin \left[\frac{k-1}{2} \theta' \right] \cos[\nu(\theta - \theta')] d\theta' = 0$$

Since the harmonic function that appear in the inner product have different frequency, their inner product is null. In the same way is possible to calculate the transformation of the basis for the zero harmonic, as follows:

$$\bar{\psi}_{\nu=0} = \int_{\theta'=0}^{2\pi} \frac{1}{\sqrt{r_{ext}}\sqrt{\pi}} sin \left[\frac{k-1}{2} \theta' \right] \cos[\nu(\theta - \theta')]\ d\theta'$$

since $\cos[\nu(\theta - \theta')]_{\nu=0} = 1$ the last expression becomes:

$$\bar{\psi}_{\nu=0} = \int_{\theta'=0}^{2\pi} \frac{1}{\sqrt{r_{ext}}\sqrt{\pi}} sin \left[\frac{k-1}{2} \theta' \right] d\theta' = \frac{1}{\sqrt{r_{ext}}\sqrt{\pi}} \left(2 \cos \frac{\left[\frac{k-1}{2} \theta \right]}{k-1} \right)_{\theta=0}^{2\pi}$$

$$= 0$$

Considering that $\bar{\psi}$ and $\bar{\psi}_{v=0}$ are null, the auxiliary function G is null and also all the other result are zero thus those frequency of the orthonormal basis function doesn't participate in the solution.

k=3,5,7,…,N & k=2v+1

As defined in the Equation (4.41.3):

$$\psi = \frac{1}{\sqrt{r_{ext}}\sqrt{\pi}} sin\left[\frac{k-1}{2}\theta\right] \quad for\ k = 2,4,6,\dots N-1$$

According to the Equation (A.7):

$$\bar{\psi} = \int_{\theta'=0}^{2\pi} \frac{1}{\sqrt{r_{ext}}\sqrt{\pi}} sin\left[\frac{k-1}{2}\theta'\right] \cos[v(\theta-\theta')]d\theta'$$

$$= \frac{1}{\sqrt{r_{ext}}\sqrt{\pi}} \int_{\theta'=0}^{2\pi} sin\left[\frac{(2v+1)-1}{2}\theta'\right] \cos[v(\theta-\theta')]d\theta'$$

is possible to re-write the last integral using the subtraction formula the for cosine terms, getting:

$$\int_{\theta'=0}^{2\pi} sin[v\theta']\cos[v(\theta-\theta')]d\theta' = \int_{\theta'=0}^{2\pi} sin[v\theta'](\cos[v\theta - v\theta'])\, d\theta'$$

$$= \int_{\theta'=0}^{2\pi} sin[v\theta'](\cos[v\theta]\cos[v\theta'] + \sin[v\theta]\sin[v\theta'])\, d\theta'$$

$$= \int_{\theta'=0}^{2\pi} sin[v\theta']\cos[v\theta]\cos[v\theta']\, d\theta'$$

$$+ \int_{\theta'=0}^{2\pi} sin[v\theta']\sin[v\theta]\sin[v\theta']\, d\theta'$$

$$= \cos[v\theta] \int_{\theta'=0}^{2\pi} sin[v\theta']\cos[v\theta']\, d\theta'$$

$$+ \sin[v\theta] \int_{\theta'=0}^{2\pi} sin[v\theta']\ \sin[v\theta']\, d\theta'$$

since $\int_{\theta'=0}^{2\pi} sin[v\theta']\cos[v\theta']\, d\theta' = 0$ and $\int_{\theta'=0}^{2\pi} sin[v\theta']\ \sin[v\theta']\, d\theta' = \pi$ the last expression becomes:

$$\int_{\theta'=0}^{2\pi} sin[\nu\theta']\cos[\nu(\theta-\theta')]d\theta' = \pi \sin[\nu\theta]$$

Then the transformation of the basis becomes:

$$\bar{\psi} = \int_{\theta'=0}^{2\pi} \frac{1}{\sqrt{r_{ext}}\sqrt{\pi}} sin\left[\frac{k-1}{2}\theta'\right]\cos[\nu(\theta-\theta')]d\theta' = \sqrt{\frac{\pi}{r_{ext}}}\sin[\nu\phi]$$

Then the transformation of the basis for $\nu = 0$ is:

$$\bar{\psi}_{\nu=0} = \int_{\theta'=0}^{2\pi} \frac{1}{\sqrt{r_{ext}}\sqrt{\pi}} sin\left[\frac{k-1}{2}\theta'\right]\cos[\nu(\theta-\theta')]d\theta'$$

since $\cos[\nu(\theta-\theta')]_{\nu=0} = 1$ the last expression becomes:

$$\bar{\psi}_{\nu=0} = \int_{\theta'=0}^{2\pi} \frac{1}{\sqrt{r_{ext}}\sqrt{\pi}} sin\left[\frac{k-1}{2}\theta'\right] d\theta' = \frac{1}{\sqrt{r_{ext}}\sqrt{\pi}} \frac{\cos\left[\left(\frac{k-1}{2}\right)\theta\right]_{\theta=0}^{2\pi}}{\left(\frac{k-1}{2}\right)} = 0$$

According to the Equation (A.21) the auxiliary function is defined as:

$$F = \frac{1}{2\pi}\bar{\psi}_{\nu=0}\frac{\ln\left[\frac{r_{int}}{r}\right]}{\ln\left[\frac{r_{int}}{r_{ext}}\right]} + \sum_{\nu=1}^{\infty}\frac{1}{\pi}\bar{\psi}_{\nu}\sinh\left[\nu\left(\ln\left[\frac{r_{int}}{r}\right]\right)\right]\operatorname{csch}\left[\nu\left(\ln\left[\frac{r_{int}}{r_{ext}}\right]\right)\right]$$

$$= \sum_{\nu=1}^{\infty}\frac{1}{\pi}\sqrt{\frac{\pi}{r_{ext}}}\sin[\nu\phi]\sinh\left[\nu\left(\ln\left[\frac{r_{int}}{r}\right]\right)\right]\operatorname{csch}\left[\nu\left(\ln\left[\frac{r_{int}}{r_{ext}}\right]\right)\right]$$

The normal derivative of the auxiliary function at the external boundary is:

$$\left.\frac{\partial F}{\partial \boldsymbol{n}}\right|_{\Gamma_{ext}} = -\sqrt{\frac{1}{\pi r_{ext}}}\sum_{\nu=1}^{\infty}\sin[\nu\theta]\operatorname{csch}\left[\nu\left(\ln\left[\frac{r_{int}}{r_{ext}}\right]\right)\right]\cosh\left[\nu\left(\ln\left[\frac{r_{int}}{r_{ext}}\right]\right)\right]\frac{\nu}{r_{ext}}$$

The trace of the auxiliary function at the internal boundary Γ_{int} is:

$$\xi = \left(\frac{\partial F}{\partial \boldsymbol{n}}\right)\Big|_{\Gamma_{int}} = -\sqrt{\frac{1}{\pi r_{ext}}}\sum_{\nu=1}^{\infty}\sin[\nu\theta]\operatorname{csch}\left[\nu\left(\ln\left[\frac{r_{int}}{r_{ext}}\right]\right)\right]\frac{\nu}{r_{int}}$$

The reciprocity functional defined in the Equation (4.42) became:

$$R_F = \int_{\Gamma_{ext}} \left(-\psi \frac{h_{env}(Y - T_{env})}{K} - Y \frac{\delta F}{\delta \boldsymbol{n}} \right) d\Gamma_{ext}$$

$$= \int_{\theta'=0}^{2\pi} r_{ext} \left(-\psi \frac{h_{env}(Y - T_{env})}{K} - Y \frac{\delta F}{\delta \boldsymbol{n}} \right) d\theta'$$

$$= -r_{ext} \int_{\theta'=0}^{2\pi} \left(\psi \frac{h_{env}}{K} Y - \psi \frac{h_{env}}{K} T_{env} - Y \frac{\delta F}{\delta \boldsymbol{n}} \right) d\theta'$$

$$= -r_{ext} \int_{\theta'=0}^{2\pi} Y \left(\psi \frac{h_{env}}{K} - \frac{\delta F}{\delta \boldsymbol{n}} \right) d\theta' - r_{ext} \int_{\theta'=0}^{2\pi} \psi \frac{h_{env}}{K} T_{env} \; d\theta'$$

$$= -r_{ext} \int_{\theta'=0}^{2\pi} Y \left(\frac{1}{\sqrt{r_{ext}}\sqrt{\pi}} \sin\left[\frac{k}{2}\theta'\right] \frac{h_{env}}{K} \right.$$

$$\left. - \frac{1}{\sqrt{r_{ext}}\sqrt{\pi}} \sin[\nu\theta'] \; \operatorname{csch}\left[\nu \left(\ln\left[\frac{r_{int}}{r_{ext}}\right]\right)\right] \cosh\left[\nu \left(\ln\left[\frac{r_{int}}{r_{ext}}\right]\right)\right] \frac{\nu}{r_{ext}} \right) d\theta'$$

$$- r_{ext} \int_{\theta'=0}^{2\pi} \frac{1}{\sqrt{r_{ext}}\sqrt{\pi}} sin[\nu\theta'] \frac{h_{env}}{K} T_{env} \; d\theta'$$

$$= -r_{ext} \int_{\theta'=0}^{2\pi} Y \left(\frac{1}{\sqrt{r_{ext}}\sqrt{\pi}} sin[\nu\theta'] \frac{h_{env}}{K} \right.$$

$$\left. - \frac{1}{\sqrt{r_{ext}}\sqrt{\pi}} \sin[\nu\theta'] \operatorname{csch}\left[\nu \left(\ln\left[\frac{r_{int}}{r_{ext}}\right]\right)\right] \cosh\left[\nu \left(\ln\left[\frac{r_{int}}{r_{ext}}\right]\right)\right] \frac{\nu}{r_{ext}} \right) d\theta'$$

$$- r_{ext} \frac{1}{\sqrt{r_{ext}}\sqrt{\pi}} \frac{h_{env}}{K} T_{env} \int_{\theta'=0}^{2\pi} sin[\nu\theta'] \; d\theta'$$

since $\int_{\theta'=0}^{2\pi} sin[\nu\theta'] \; d\theta' = 0$ the last expression become:

$$R_F = \int_{\Gamma_{ext}} \left(-\psi \frac{h_{env}(Y - T_{env})}{K} - Y \frac{\delta F}{\delta \boldsymbol{n}} \right) d\Gamma_{ext} =$$

$$= -r_{ext} \int_{\theta'=0}^{2\pi} Y \frac{1}{\sqrt{r_{ext}}\sqrt{\pi}} sin[\nu\theta'] \left(\frac{h_{env}}{K} \right.$$

$$\left. - \operatorname{csch}\left[\nu \left(\ln\left[\frac{r_{int}}{r_{ext}}\right]\right)\right] \cosh\left[\nu \left(\ln\left[\frac{r_{int}}{r_{ext}}\right]\right)\right] \frac{\nu}{r_{ext}} \right) d\theta'$$

$$= -r_{ext} \frac{1}{\sqrt{r_{ext}}\sqrt{\pi}} \left(\frac{h_{env}}{K} \right.$$

$$\left. - \operatorname{sech}\left[\nu \left(\ln\left[\frac{r_{int}}{r_{ext}}\right]\right)\right] \sinh\left[\nu \left(\ln\left[\frac{r_{int}}{r_{ext}}\right]\right)\right] \frac{\nu}{r_{ext}} \right) \int_{\theta'=0}^{2\pi} Y sin[\nu\theta'] \, d\theta'$$

Using the Fourier's series expansion, the integral of the measurement at the external boundary Γ_{ext} in the last expression can be re-written as:

$$\int_{\theta'=0}^{2\pi} Y \sin[\nu\theta']\, d\theta'$$

$$= \int_{\theta'=0}^{2\pi} \big(a_0 \sin[\nu\theta'] + a_1 \cos[\theta'] \sin[\nu\theta'] + b_1 \sin[\theta'] \sin[\nu\theta']$$

$$+ \cdots + a_{k_F} \cos[k_F\theta'] \sin[\nu\theta'] + b_{k_F} \sin[k_F\theta'] \sin[\nu\theta']\big) d\theta'$$

$$= \int_{\theta'=0}^{2\pi} a_0 \sin[\nu\theta']\, d\theta' + \int_{\theta'=0}^{2\pi} a_1 \cos[\theta'] \sin[\nu\theta']\, d\theta'$$

$$+ \int_{\theta'=0}^{2\pi} b_1 \sin[\theta'] \sin[\nu\theta']\, d\theta' + \cdots$$

$$+ \int_{\theta'=0}^{2\pi} a_{k_F} \cos[k_F\theta'] \sin[\nu\theta']\, d\theta'$$

$$+ \int_{\theta'=0}^{2\pi} b_{k_F} \sin[k_F\theta'] \sin[\nu\theta']\, d\theta'$$

since $\int_{\theta'=0}^{2\pi} a_0 \sin[\nu\theta']\, d\theta' = 0$, $\int_{\theta'=0}^{2\pi} a_{k_F} \cos[k_F\theta'] \sin[\nu\theta']\, d\theta' = 0$ for every k_F, and:

$$\int_{\theta'=0}^{2\pi} b_{k_F} \sin[k_F\theta'] \sin[\nu\theta']\, d\theta' = \begin{cases} 0 & if\ k_F \neq \nu \\ \pi b_{k_F} & if\ k_F = \nu \end{cases}$$

the integral of the measurement at the external boundary becomes:

$$\int_{\theta'=0}^{2\pi} Y \sin[\nu\theta']\, d\theta' = \pi b_\nu$$

and the reciprocity functional becomes:

$$
\begin{aligned}
&R_F \\
&= -r_{ext}\frac{1}{\sqrt{r_{ext}}\sqrt{\pi}}\Big(\frac{h_{env}}{K} \\
&- \operatorname{csch}\left[\nu\ \left(\ln\left[\frac{r_{int}}{r_{ext}}\right]\right)\right]\cosh\left[\nu\ \left(\ln\left[\frac{r_{int}}{r_{ext}}\right]\right)\right]\frac{\nu}{r_{ext}}\Big)\int_{\theta'=0}^{2\pi} Ysin[\nu\theta']\,d\theta' \\
&= -r_{ext}\frac{\pi b_k}{\sqrt{r_{ext}}\sqrt{\pi}}\Big(\frac{h_{env}}{K} - \operatorname{csch}\left[\nu\ \left(\ln\left[\frac{r_{int}}{r_{ext}}\right]\right)\right]\cosh\left[\nu\ \left(\ln\left[\frac{r_{int}}{r_{ext}}\right]\right)\right]\frac{\nu}{r_{ext}}\Big) \\
&= -b_k\sqrt{\pi r_{ext}}\Big(\frac{h_{env}}{K} - \coth\left[\nu\ \left(\ln\left[\frac{r_{int}}{r_{ext}}\right]\right)\right]\frac{\nu}{r_{ext}}\Big)
\end{aligned}
$$

According to the Equation (4.43) the integral of the internal heat generation is:

$$
\begin{aligned}
&Q_F = \int_{\Omega'}\left(F\frac{q_g}{K}\right)d\Omega' \\
&= \int_{\theta'=0}^{2\pi}\int_{r'=r_{int}}^{r_{ext}} r'\frac{q_g}{K}\sqrt{\frac{1}{\pi r_{ext}}}\sum_{\nu=1}^{\infty}\sin[\nu\theta']\sinh\left[\nu\ \left(\ln\left[\frac{r_{int}}{r'}\right]\right)\right]\operatorname{csch}\left[\nu\ \left(\ln\left[\frac{r_{int}}{r_{ext}}\right]\right)\right]dr'd\theta' \\
&= \frac{q_g}{K}\sqrt{\frac{1}{\pi\, r_{ext}}}\operatorname{csch}\left[\nu\ \left(\ln\left[\frac{r_{int}}{r_{ext}}\right]\right)\right]\int_{\theta'=0}^{2\pi}\int_{r'=r_{int}}^{r_{ext}} r'\sin[\nu\theta']\sinh\left[\nu\ \left(\ln\left[\frac{r_{int}}{r'}\right]\right)\right]dr'd\theta' \\
&= \frac{q_g}{K}\sqrt{\frac{1}{\pi\, r_{ext}}}\operatorname{csch}\left[\nu\ \left(\ln\left[\frac{r_{int}}{r_{ext}}\right]\right)\right]\int_{\theta'=0}^{2\pi}\sin[\nu\theta']\,d\theta'\int_{r'=r_{int}}^{r_{ext}} r'\sinh\left[\nu\ \left(\ln\left[\frac{r_{int}}{r'}\right]\right)\right]dr' \\
&= 0
\end{aligned}
$$

since $\int_{\theta'=0}^{2\pi} sin[\nu\theta']\ d\theta' = 0$ the heat generation terms is null.

The odd element of the diagonal matrix of the inner product becomes:

$$
\begin{aligned}
&N = \int_{\Gamma_{\text{int}}}\langle\xi_\nu,\xi_\nu\rangle\ d\Gamma_{int} = \int_{\theta'=0}^{2\pi} r_{int}\,\langle\xi_\nu,\xi_\nu\rangle\,d\theta' \\
&= r_{int}\int_{\theta'=0}^{2\pi}\left(\sqrt{\frac{1}{\pi r_{ext}}}\sin[\nu\theta]\ \operatorname{csch}\left[\nu\ \left(\ln\left[\frac{r_{int}}{r_{ext}}\right]\right)\right]\frac{\nu}{r_{int}}\sqrt{\frac{1}{\pi r_{ext}}}\sin[\nu\theta]\ \operatorname{csch}\left[\nu\ \left(\ln\left[\frac{r_{int}}{r_{ext}}\right]\right)\right]\frac{\nu}{r_{int}}\right)d\theta' \\
&= \frac{r_{int}}{\pi r_{ext}}\operatorname{csch}^2\left[\nu\ \left(\ln\left[\frac{r_{int}}{r_{ext}}\right]\right)\right]\frac{\nu^2}{r_{int}^2}\int_{\theta'=0}^{2\pi}\sin^2[\nu\theta]\ d\theta'
\end{aligned}
$$

since $\int_{\theta'=0}^{2\pi}\sin^2[\nu\theta]\ d\theta' = \pi$ the last expression becomes:

$$N = \int_{\Gamma_{\text{int}}} \langle \xi_\nu, \xi_\nu \rangle \, d\Gamma_{int} = \frac{\nu}{r_{int} r_{ext}} \operatorname{csch}^2 \left[\nu \left(\ln \left[\frac{r_{int}}{r_{ext}} \right] \right) \right]$$

A.6 Solve the second auxiliary problem:

The solution of the first auxiliary problem is easy to get by simply solving the linear system defined in the Equation (4.48). Once the β coefficients are determined, is possible estimating the internal heat flux by those coefficients according to the Equation (4.46).
The results obtained are here summarized:

$$R_F = -\sqrt{\pi r_{ext}} \begin{bmatrix} \sqrt{2} \frac{h_{env}}{K} \left(\left(1 - \frac{K}{h_{env} r_{ext} \ln \left(\frac{r_{int}}{r_{ext}} \right)} \right) a_0 - T_{env} \right) \\ \left(\frac{h_{env}}{K} - \coth \left[\ln \left[\frac{r_{int}}{r_{ext}} \right] \right] \frac{1}{r_{ext}} \right) \quad a_1 \\ \left(\frac{h_{env}}{K} - \coth \left[\ln \left[\frac{r_{int}}{r_{ext}} \right] \right] \frac{1}{r_{ext}} \right) \quad b_1 \\ \left(\frac{h_{env}}{K} - \coth \left[2 \ln \left[\frac{r_{int}}{r_{ext}} \right] \right] \frac{2}{r_{ext}} \right) \quad a_2 \\ \left(\frac{h_{env}}{K} - \coth \left[2 \ln \left[\frac{r_{int}}{r_{ext}} \right] \right] \frac{2}{r_{ext}} \right) \quad b_2 \\ \vdots \\ \left(\frac{h_{env}}{K} - \coth \left[\nu \ln \left[\frac{r_{int}}{r_{ext}} \right] \right] \frac{\nu}{r_{ext}} \right) \quad a_\nu \\ \left(\frac{h_{env}}{K} - \coth \left[\nu \ln \left[\frac{r_{int}}{r_{ext}} \right] \right] \frac{\nu}{r_{ext}} \right) \quad b_\nu \end{bmatrix}$$

$$Q_G = \begin{bmatrix} \frac{q_g}{K} \sqrt{\frac{\pi}{2 r_{ext}}} \left(r_{ext}^2 + \frac{1}{2} \frac{(r_{ext}^2 - r_{int}^2)}{\ln \left[\frac{r_{int}}{r_{ext}} \right]} \right) \\ 0 \\ \vdots \\ 0 \end{bmatrix} \qquad \beta = \begin{bmatrix} \beta_{\nu=1} \\ \beta_{\nu=2} \\ \vdots \\ \beta_{\nu=\nu} \end{bmatrix}$$

$$N = \frac{1}{r_{int} r_{ext}} \begin{bmatrix} \frac{1}{\ln^2\left[\frac{r_{int}}{r_{ext}}\right]} & & & & & & & 0 \\ & \operatorname{csch}^2\left[1 \ln\left[\frac{r_{int}}{r_{ext}}\right]\right] & & & & & & \\ & & \operatorname{csch}^2\left[1 \ln\left[\frac{r_{int}}{r_{ext}}\right]\right] & & & & & \\ & & & 2^2 \operatorname{csch}^2\left[2 \ln\left[\frac{r_{int}}{r_{ext}}\right]\right] & & & & \\ & & & & 2^2 \operatorname{csch}^2\left[2 \ln\left[\frac{r_{int}}{r_{ext}}\right]\right] & & & \\ & & & & & \ddots & & \\ & & & & & & \nu^2 \operatorname{csch}^2\left[\nu \ln\left[\frac{r_{int}}{r_{ext}}\right]\right] & \\ 0 & & & & & & & \nu^2 \operatorname{csch}^2\left[\nu \ln\left[\frac{r_{int}}{r_{ext}}\right]\right] \end{bmatrix}$$

$$\xi = \frac{1}{\sqrt{\pi r_{ext}}} \begin{bmatrix} 1 & \cdots & 1 & \cdots & 1 \\ \cos[1\ 0] \operatorname{sech}\left[1 \ln\left[\frac{r_{ext}}{r_{int}}\right]\right] & \cdots & \cos[1\ \theta] \operatorname{sech}\left[1 \ln\left[\frac{r_{ext}}{r_{int}}\right]\right] & \cdots & \cos[1\ 2\pi] \operatorname{csch}\left[1 \ln\left[\frac{r_{ext}}{r_{int}}\right]\right] \\ \sin[1\ 0] \operatorname{sech}\left[1 \ln\left[\frac{r_{ext}}{r_{int}}\right]\right] & \cdots & \sin[1\ \theta] \operatorname{sech}\left[1 \ln\left[\frac{r_{ext}}{r_{int}}\right]\right] & \cdots & \sin[1\ 2\pi] \operatorname{csch}\left[1 \ln\left[\frac{r_{ext}}{r_{int}}\right]\right] \\ \cos[2\ 0] \operatorname{sech}\left[2 \ln\left[\frac{r_{ext}}{r_{int}}\right]\right] & \cdots & \cos[2\ \theta] \operatorname{sech}\left[2 \ln\left[\frac{r_{ext}}{r_{int}}\right]\right] & \cdots & \cos[2\ 2\pi] \operatorname{csch}\left[2 \ln\left[\frac{r_{ext}}{r_{int}}\right]\right] \\ \sin[2\ 0] \operatorname{sech}\left[2 \ln\left[\frac{r_{ext}}{r_{int}}\right]\right] & \cdots & \sin[2\ \theta] \operatorname{sech}\left[2 \ln\left[\frac{r_{ext}}{r_{int}}\right]\right] & \cdots & \sin[2\ 2\pi] \operatorname{csch}\left[2 \ln\left[\frac{r_{ext}}{r_{int}}\right]\right] \\ \vdots & & \vdots & & \vdots \\ \cos[\nu\ 0] \operatorname{sech}\left[\nu \ln\left[\frac{r_{ext}}{r_{int}}\right]\right] & \cdots & \cos[\nu\ \theta] \operatorname{sech}\left[\nu \ln\left[\frac{r_{ext}}{r_{int}}\right]\right] & \cdots & \cos[\nu\ 2\pi] \operatorname{csch}\left[\nu \ln\left[\frac{r_{ext}}{r_{int}}\right]\right] \\ \sin[\nu\ 0] \operatorname{sech}\left[\nu \ln\left[\frac{r_{ext}}{r_{int}}\right]\right] & \cdots & \sin[\nu\ \theta] \operatorname{sech}\left[\nu \ln\left[\frac{r_{ext}}{r_{int}}\right]\right] & \cdots & \sin[\nu\ 2\pi] \operatorname{csch}\left[\nu \ln\left[\frac{r_{ext}}{r_{int}}\right]\right] \end{bmatrix}$$

As it is possible to see in Figure (A.2.a), the element of the matrix of the inner product of the second auxiliary problem increase as far as the tube becomes thin. It has to be pointed out that in this case the elements appearing on the diagonal of the *N* matrix, could become very large highlighting the less ill-posedness of the problem respect to the heat flux estimation.

Like in the previous case, as far as the tube becomes thinner, the sensitivity to the heat generation parameter become smaller, therefore it is necessary to increase the heat generation due to the Joule effect in the tube, or increase its the external diameter (Figure (A.2.b)). The increment of the external diameter has also a beneficial effect on the matrix of the inner products (Figure (A.2.c)), since its diagonal elements increase as far as the external diameter becomes bigger.

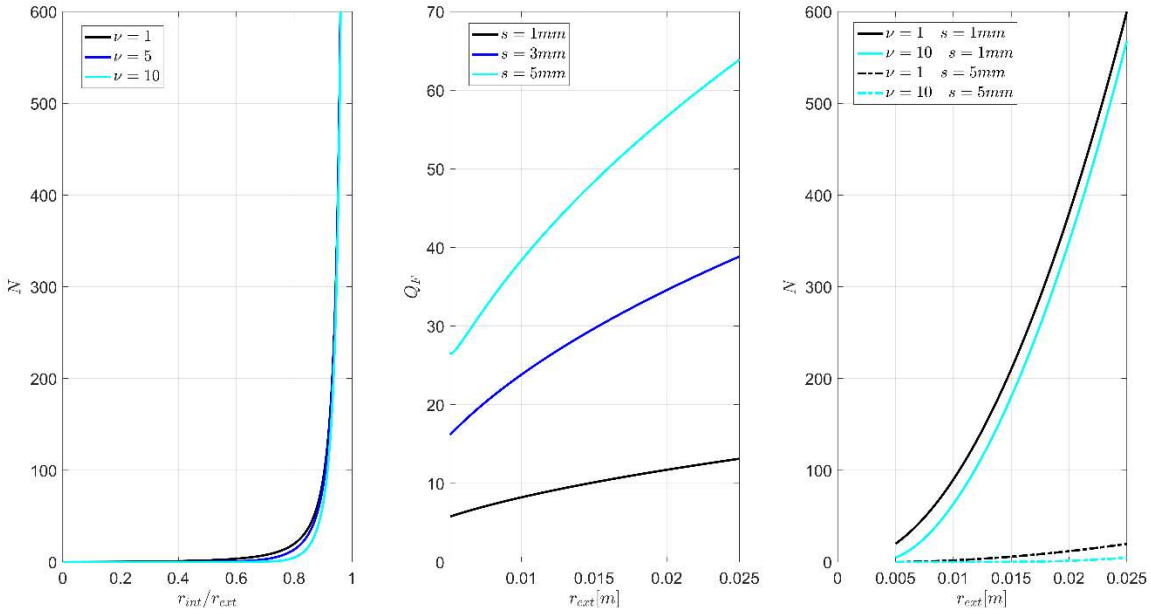

(a) (b) (c)

Figure A.4: (a) effect of the tube thickness on the *N* matrix, (b) effect of the external dimension of the tube for three different thickness on the Q_F term and (c) effect of the external dimension of the tube for two different thickness and harmonic frequencies on the *N* matrix

As shown in Figure (A.3.a) increasing the numbers of the harmonics, the matrix of the inner product becomes ill-conditioned making the solution unstable. For this reason, the solution has to be filtered. The filter here applied require the truncation of the element of the *M* as far as the noise contented in the measurement increase. In particular the same number of harmonic used during the estimation of the heat flux was assumed.

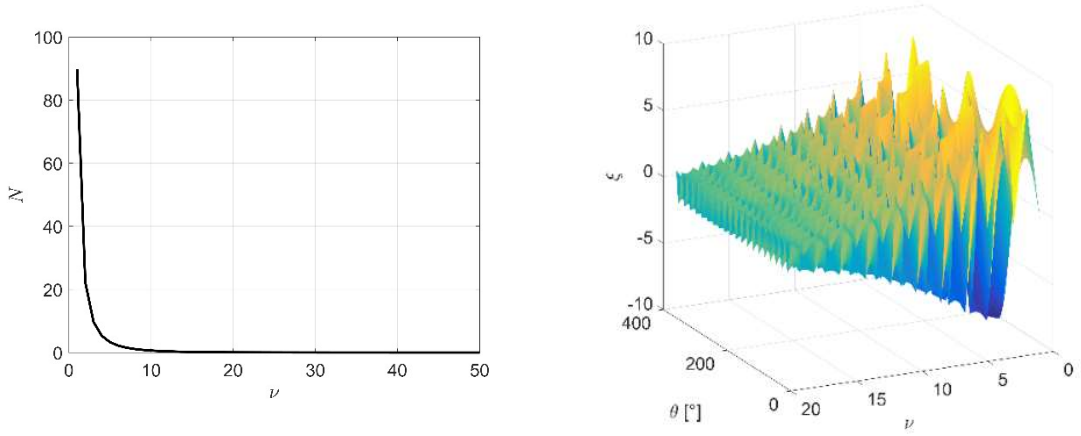

(a) (b)

Figure A.5: (a) effect of the numbers of harmonics on the N for a representative value $r_{int}/r_{ext} = 0.9$ and (b) ξ basis

A.7. Filtering requirement

As far as the harmonic order increase, the diagonal elements of the matrices of the inner product become smaller and smaller. This behaviour require the filtering of the harmonic number used to reconstruct the signal. In fact, since the matrices of the inner product has to be inverted in order the estimate the internal boundary condition values, small diagonal elements will produce extremely high diagonal element in the inverted matrices, making the solutions unstable. It is straightforward that as far as the noise contained in the measurement increase, the number of harmonic used to reconstruct the signal has to decrease in order to keep the solution stable. Moreover, that the reduction of the number of harmonic used to reconstruct the signal will reduce its quality especially if it is characterized by a sharp behaviour.

As already shown in *Chapter 3*, due to the linearization of the problem, all the methodologies based on the sensitivity matrix, require the inverse estimation of the internal wall heat flux before the estimation of the internal convective heat transfer coefficient. Therefore, the core of the inverse problem is the estimation of the heat flux distribution, being the convective heat flux coefficient derived from it. The Reciprocity Functional approach is not based on the sensitivity matrix, moreover the two auxiliary problem are not linked together. Nevertheless, the same pattern could be recognised since the critical point of this estimation procedure is the assessment of the internal wall heat flux: behaviour due to the elements of the diagonal matrix *M* that go to zero faster than the elements of the *N* matrix.

Lemma 1:

If the harmonic order increase, the diagonal elements of the *M* matrix go to zero.

Proof 1:

$$\lim_{\nu\to\infty} diag(M) = \lim_{\nu\to\infty} \operatorname{sech}^2\left(\nu \log\left(\frac{r_{int}}{r_{ext}}\right)\right) = 0$$

Lemma 2:

If the harmonic order increase, the diagonal elements of the *N* matrix go to zero.

Proof 2:

$$\lim_{\nu\to\infty} diag(N) = \lim_{\nu\to\infty} \nu^2 \operatorname{csch}^2\left(\nu \log\left(\frac{r_{int}}{r_{ext}}\right)\right) = \lim_{\nu\to\infty} \nu^2 \frac{1}{\sinh^2\left(\nu \log\left(\frac{r_{int}}{r_{ext}}\right)\right)} = \frac{\infty}{\infty}$$

The application for two times of the l'Hopital rule is needed:

$$\lim_{\nu\to\infty} diag(N) = \lim_{\nu\to\infty} 2\nu \frac{1}{\ln\left(\frac{r_{int}}{r_{ext}}\right) 2\sinh\left(\nu \log\left(\frac{r_{int}}{r_{ext}}\right)\right)\cosh\left(\nu \log\left(\frac{r_{int}}{r_{ext}}\right)\right)} = 0$$

Lemma 3:

If the harmonic order increase, the ratio between the elements of *M* and *N* goes to zero.

Proof 3:

$$\lim_{\nu\to\infty} \frac{diag(M)}{diag(N)} = \lim_{\nu\to\infty} \frac{1}{\nu^2} \frac{\operatorname{sech}^2\left(\nu \log\left(\frac{r_{int}}{r_{ext}}\right)\right)}{\operatorname{csch}^2\left(\nu \log\left(\frac{r_{int}}{r_{ext}}\right)\right)} = \lim_{\nu\to\infty} \frac{1}{\nu^2} \tanh\left(\nu \log\left(\frac{r_{int}}{r_{ext}}\right)\right) = 0$$

A.8. Reciprocity functional analysis

The information contained in the measurement is passed to the inverse problems through the reciprocity functionals. Even if the functional gaps are related to two different problems, they share the same set of data; therefore, as far as the harmonic order increase, they tend to the same value.

Lemma 4:

If the harmonic order increase, the ratio between the elements of R_G and R_F goes to one.

Proof 4:

$$\lim_{\nu\to\infty}\frac{R_G}{R_F}=\lim_{\nu\to\infty}\frac{\left(\frac{h_{env}}{K}-\frac{\nu}{r_{ext}}\tanh\left[\nu\ \ln\left[\frac{r_{int}}{r_{ext}}\right]\right]\right)\quad c_F}{\left(\frac{h_{env}}{K}-\frac{\nu}{r_{ext}}\coth\left[\nu\ \ln\left[\frac{r_{int}}{r_{ext}}\right]\right]\right)\quad c_F}$$

$$=\lim_{\nu\to\infty}\frac{\frac{h_{env}}{K}-\frac{\nu}{r_{ext}}\tanh\left[\nu\ \ln\left[\frac{r_{int}}{r_{ext}}\right]\right]}{\frac{h_{env}}{K}-\frac{\nu}{r_{ext}}\coth\left[\nu\ \ln\left[\frac{r_{int}}{r_{ext}}\right]\right]}$$

$$=\lim_{\nu\to\infty}\frac{\frac{\nu}{r_{ext}}\frac{h_{env}}{K}\frac{r_{ext}}{\nu}-\tanh\left[\nu\ \ln\left[\frac{r_{int}}{r_{ext}}\right]\right]}{\frac{\nu}{r_{ext}}\frac{h_{env}}{K}\frac{r_{ext}}{\nu}-\coth\left[\nu\ \ln\left[\frac{r_{int}}{r_{ext}}\right]\right]}=1$$

where c_F is a general coefficient of the Fourier's series expansion.

Bibliography

Abichandani1987	*Abichandani H., Sarma S. C., 'Hydrodynamics and heat transfer in liquid full scraper surface heat exchanger - a review', Food Process Engineering, 9 121-141, 1987*
Acikalin2004	*Acikalin T., Wait S., Garimella S., Raman A., 'Experimental investigation of the thermal performance of piezoelectric fans', Heat Transfer Engineering, 25 (1) 4–14, 2004*
Ali 2001	*Ali S., Pressure drop correlations for flow through regular helical coil tubes, Fluid Dynamic Research, 28 295-310, 2001*
Alifanov1974	*Alifanov, O.M., 'Solution of an inverse problem of heat conduction by iterative methods', J. Eng. Phys, **26**(4), 471-476, 1974*
Alifanov1977	*Alifanov, O.M., 'Determination of the heat loads from a solution of the nonlinear inverse problem', High Temperature, **15**(3), 498-504,1977*
Alifanov1978a	*Alifanov, O.M. and Mikhailov, V.V., 'Solution of the nonlinear inverse thermal conductivity problem by the iteration method', J. Eng. Phys., **35**(1501-1506, 1978*
Alifanov1978b	*Alifanov, O.M. and Rumyantsev, S.V., 'One method of solving incorrectly stated problems', J. Eng. Phys., **34**(2), 223-226, 1978*
Alifanov1979	*Alifanov, O.M. and Rumyantsev, S.V., 'On the stability of iterative methos for the solution of the ill-posed problem', Soviet Math. Dokl., **20**(5), 1133-1136, 1979*
Alifanov1980	*Alifanov, O.M. and Rumyantsev, S.V., 'Regularizing gradient algorithm for inverse thermal-conduction problem', J. Eng. Phys., **39**(2), 858-861,1980*
Alifanov1981	*Alifanov, O.M. and Kerov, N.V., 'Determination of external thermal load parameters by solving the two dimensional inverse heat conduction problem', J. Eng., Phys., **41**(4), 1049-1053, 1981*
Alifanov1983	*Alifanov, O.M. and Mikhailov, V.V., 'Determining thermal loads from the data of themperature measurements in a solid', High Temperature, **21**(5), 724-730, 1983*

Alifanov1985a	*Alifanov, O.M. and Klibanov, M.V., 'Uniqueness conditions and methods of solutionof the coefficient inverse problem in thermal conductivity', J. Eng. Phys., **48**(6), 730-735, 1985*
Alifanov1985b	*Alifanov, O.M. and Klibanov, M.V., 'Solution of the overdetermined inverse problem of thermal conductivity involving inaccurate data', **21**(1), 112-117, 1985*
Alifanov1985c	*Alifanov, O.M. and Tryanin, A.P., 'Determination of the coefficient of internal heat exchange and the effective thermal conductivity of a porous solid on basis of nonstationary experiment', J. Eng. Phys., **48**(3), 356-365, 1985*
Alifanov1994	*Alifanov, O.M., 'Inverse heat transfer problem',Springer-Verlag, New York, 1994*
Alifanov1995	*Alifanov, O.M., Artyukhin, E. and Rumyantsev, A., 'Exterme method for solving ill-posed problems with application to inverse heat transfer problem', Begell House, New York, 1995*
Amato1991	*Amato U. and Hughes W., 'Maximum-Entropy regularization of Fredholm integral-equation of the 1st kind', inverse Problem 7, 793-808, 1991*
Andrieux1993	*Andrieux S. and Abda A.B.,'The reciprocity gap: A general concept for flaws identification problems', Mechanics Research Communications, Vol. 20, pp. 415-420, 1993*
Andrieux1996	*Andrieux S. and Abda A. B., 'Identification of planar cracks by complete overdetermined data: inversion formulae', Inverse problems, v. 12, pp. 553-563, 1996.*
Armijo1966	*Armijo L., 'Minimization of functions having Lipschitz continuous first partial derivatives'. Pacific J. Math. 16 (1): 1–3, 1966*
Artz2003	*Arzt E., Gorb S. and Spolenak R., 'From micro to nano contacts in biological attachment devices', Proc. Natl. Acad. Sci. 100 (2003) 10603–10606.*
Aster2005	*Aster R.C., Borchers B., Thurber C.H., 'Parameter estimation and inverse problems', Elsevier Academic Press, 2005*
Bai1999	*Bai B., Guo L., Feng Z., Chen X., 'Turbulent Heat Transfer in a Horizontal Helically Coiled Tube', Heat Transfer-Asian Research, 28 (5) 395-403, 1999*
Banks1990	*Banks H.T., Kojima F. Winfree W.P., 'Boundary estimation problems arising in thermal tomography', Inverse problem, 6, 897-921, 1990*
Bard1974	*Bard Y.B., 'Non-linear parameter estimation', Acad. Pres New York, 1974*
Bazàn2009	*Bazàn F.S.V. and J.B. Francisco, 'An improved fixed-point algorithm for determining a Tikhonov regularization parameter', Inverse Problem, 25-045007, 2009*
Bazàn2012	*Fermín S.V. Bazán, J.B. Francisco, Koung Hee Leem, G. Pelekanos, 'A maximum product criterion as a Tikhonov parameter choice rule for Kirsch's factorization method', J. Comput. Appl. Math. 236, 4264–4275, 2012*
Beck1962	*Beck, J.V., 'Calculation of the surface heat flux from an internal temperature history', ASME paper 62-HT-46, 1962*
Beck1977	*Beck, J.V. and Arnold, K.J., 'Parameter estimation in engineering and science', New York, 1977*

Beck1979 — *Beck J. V., 'Criteria of comparison of methods of solution of inverse heat conduction problem', Nucl. Eng. Design, **53**,11-22,1979*

Beck1984 — *Beck J.V. and Murio D., ' Combined function specification – regularization procedure for solution of inverse heat conduction problem', AIAA Paper No. AIAA-84-0491, 1984*

Beck1985 — *Beck, J.V., Blackwell, B. and St.Clair, C.R., 'Inverse heat conduction: ill-posed problem', Wiley Interscience, New York, 1985*

Bejan1993 — *Bejan A., 'Heat Transfer', John Wiley & Sons, Inc New York (1993).*

Berger1983 — *Berger S.A., Talbot L., Yao L.S., 'Flow in curved pipes', Annual Review of Fluid Mechanics, 15 461-512, 1983*

Bergles1974 — *Bergles A.E., Blumenkrantz A.R. and Taborek J., 'Performance evaluation criteria for enhanced heat transfer surfaces', in: Proc. Fifth Int. Heat Transf. Conf., Tokyo, Japan, 1974*

Bergles1998 — *Bergles A.E., 'Handbook of heat transfer-Chapter 11: techniques to enhance heat transfer', McGraw-Hill, 1998*

Blackwell2010 — *Blackwell B. and Beck J. V., 'A technique for uncertainty analysis for inverse heat conduction problems', Int. J. Heat Mass Transf. 53 753–759, 2010*

Börnert1995 — *Börnert P. and Jensen D., 'Coronary artery imaging at 0.5 t using segmented 3d echo planar imaging', Magn. Reson. Med. 34 (1995) 779–785*

Bozzoli2011 — *Bozzoli F. and Rainieri S., 'Comparative application of CGM and Wiener filtering techniques for the estimation of the heat flux distribution', Inverse Problems in Science and Engineering, 19 551-571, 2011*

Bozzoli2013 — *Bozzoli F., Pagliarini G., Rainieri S., 'Experimental validation of the filtering technique approach applied to the restoration of the heat source field', Experimental Thermal and Fluid Science, **44** 858–867, 2013*

Bozzoli2014a — *Bozzoli F., Cattani L., Rainieri S., Pagliarini G., 'Estimation of local heat transfer coefficient in coiled tubes under inverse heat conduction problem approach', Experimental Thermal and Fluid Science, **59** 246–251, 2014*

Bozzoli2014b — *Bozzoli F., Cattani L., Corradi C., Mordacci M., Rainieri S. 'Inverse estimation of the local heat transfer coefficient in curved tubes: a numerical validation', Journal of Physics: Conference Series, 501, 2014*

Bozzoli2016 — *Bozzoli F., Cattani L., Mocerino A., Rainieri S., 'Experimental estimation of the local heat-transfer coefficient in coiled tubes in turbulent flow regime', Journal of Physics: Conference Series 745 (3), 032034*

Bozzoli2016a — *Bozzoli, F., Cattani, L. and Rainieri, S., 'Effect of wall corrugation on local convective heat transfer in coiled tubes', International Journal of Heat and Mass Transfer, Vol. 101; 76–90, 2016*

Bozzoli2017a — *Bozzoli F., Cattani L., Mocerino A., Rainieri S., 'Turbulent flow regime in coiled tubes: local heat-transfer coefficient', Heat and Mass Transfer, 1-11*

Bozzoli2017b — *Bozzoli F., Cattani L., Mocerino A., Rainieri S., Bazàn F.S.V., 'A novel method for estimating the distribution of convective heat flux*

in ducts: Gaussian Filtered Singular Value Decomposition', ICIPE2017

Bozzoli2018 *Bozzoli F. Mocerino A., Rainieri S., Vocale P., 'Inverse heat transfer modeling applied to the estimation of the apparent thermal conductivity of an intumescent fire retardant paint', Experimental Thermal and Fluid Science 90, 143-152*

Bozzoli2018a *Bozzoli F., Cattani L., Mocerino A., Rainieri S., 'Experimental investigation on the convective heat transfer enhancement in tubes with twisted-tape inserts', UIT conference 2018*

Bozzoli2018b *Bozzoli F., Cattani L., Mocerino A., Rainieri S., 'A novel method for estimating the distribution of convective heat flux in ducts: Gaussian Filtered Singular Value Decomposition', Inverse problems in science & engineering*

Brizaut1993 *Brizaut J.S:, Delaunay D., Garnier B. and Jarny Y., ' Implemantation of an inverse method for identification or reticulation kinetics from temperature measurements on a thick sample', Journal of Heat and Mass Transfer, 36, 4039-4047, 1993*

Broyden1967 *Broyden C.G., 'Quasi-Newton methods and their application to function minimizations', Math. Comp., vol. 21, pp. 368-380, 1967*

Bhushan2009 *Bhushan B., 'Biomimetics: lessons from nature-an overview', Philos. Trans. R. Soc. A Math. Phys. Eng. Sci. 367 (2009) 1445–1486.*

Cattani2010 *Cattani L., Bozzoli F., Rainieri S. and Pagliarini G., 'Experimental investigation on the convective heat transfer enhancement in tubes with cross-helix profile wall corrugation', UIT conference 2010*

Cheng2003 *Cheng C.H. and Chang M.H., 'A simplified conjugate gradient method for shape identification based on thermal data', Numerical heattransfer, 43, 489-507, 2003*

Cocchi1990 *Cocchi A.,'Termofisica per ingegneri', Libreria editoriale petroni, (1994).*

Colaço2003a *Colaço M.J., Dulikravich G.S. and Martin T. J., , 'Optimization of Wall Electrodes for Electro-Hydrodynamic Control of Natural Convection Effects During Solidification', In: ASME International Mechanical Engineering Congress & Exposition, 2003a*

Colaço2003b *Colaço M.J., Dulikravich G.S. and Martin T.J., 'Reducing Convection Effects in Solidification by Appling Magnetic Fields Having Optimized Intensity Distribution', ASME Summer Heat Transfer Conference, 2003b*

Colaço2003c *Colaço M.J., Orlande H.R.B., Dulikravich G.S. and Rodrigues F. A., 'A Comparison of Two Solution Techniques for the Inverse Problem of Simultaneously Estimating the Spatial Variations of Diffusion', ASME International Mechanical Engineering Congress & Exposition, 2003c*

Colaço2004 *Colaço M.J., Dulikravich G.S. and Martin T. J., 'Optimization of Wall Electrodes for Electro-Hydrodynamic Control of Natural Convection Effects During Solidification', Materials and Manufacturing Processes, Vol. 19, No. 4, pp. 719-736, 2004*

Colaço2006 *Colaço M.J., Dulikravich G.S., Martin T.J., 'Optimization of wall electrodes for electro-hydrodynamic control of natural convection during solidification', Taylor and Francis, vol.19, 2004*

Colaço2013 — *Colaço M.J., Alves C.J.S., 'A fast non-intrusive method for estimating spatial thermal contact conductance by means of the reciprocity functional approach and the method of fundamental solutions', Int. J. Heat Mass Transf. 60, 653–663, 2013*

Colaço2015 — *Colaço M.J., Alves C.J., Bozzoli F., 'The reciprocity function approach applied to the non-intrusive estimation of spatially varying internal heat transfer coefficients in ducts: numerical and experimental results', Int. J. Heat Mass Transf. 90, 1221–1231, 2015*

Colaço2015a — *Colaço M.J., Alves C.J.S. and Orlande H.R., 'Transient non-intrusive method for estimating spatial thermal contact conductance by means of the reciprocity functional approach and the method of fundamental solutions', Inverse Prob. Sci. Eng. 23 (4), 688–717, 2015a*

Colaço2006 — *Colaço M.J., Orlande H.R.B. and Dulikravich G.S., 'Inverse and Optimization Problems in Heat Transfer', J. of the Braz. Soc. of Mec. Sci. & Eng., 2006*

Corana1987 — *Corana, A., Marchesi, M., Martini, C. and Ridella, S., 'Minimizing Multimodal Functions of Continuous Variables with the 'Simulated Annealing Algorithm', ACM Transactions on Mathematical Software, vol. 13, pp. 262-280, 1987*

Cyganek2011 — *Cyganek B., Siebert J.P., 'An Introduction to 3D Computer Vision Techniques and Algorithms', Wiley, New York, 2011*

Dahl2010 — *J. Dahl, P. C. Hansen, S. H. Jensen, and T. L. Jensen, 'Algorithms and software for total variation image reconstruction via first-order methods', Numer. Algo., 53, pp. 67–92, 2010*

Dantas1996 — *Dantas L. and Orlande H.R.B., 'A function estimation approach for determining temperature-dependent thermophysical properties', Inverse Problem in engineering', **3**, 261-279, 1996*

Date1972 — *Date A.W. and Singham J.R., 'Numerical prediction of friction and heat transfer characteristic of fully developed laminar flow in tubes containing twisted tapes', ASME Journal of Heat Transfer, 17, 1972*

Date1974 — *Date A.W., 'Prediction of fully-developed flow in a tube containing a twisted-tape', Int. J. Heat Mass Transfer 17 845–859, 1974*

Davies1972 — *Davies, M. and Whitting, I. J., A Modified Form of Leoenberg's Correction. Numerical Methodrfor Non-Linear Optimisation, eds F. A. Lootsma. Academic Press, London, 1972, pp. 191-201.*

Dean1927 — *Dean, W. R., 'Note on the motion of fluid in a curved pipe', The London, Edinburgh, and Dublin Philosophical Magazine and Journal of Science, 4 208-223, 1927*

Dean1928 — *Dean, W. R.., 'The stream-line motion of fluid in a curved pipe', The London, Edinburgh, and Dublin Philosophical Magazine and Journal of Science, 5 673-695, 1928*

Dean2010 — *Dean B. and. Bhushan B, 'Shark-skin surfaces for fluid-drag reduction in turbulent flow: a review', Philos. Trans. R. Soc. A Math. Phys. Eng. Sci. 368, 5737–5737, 2010*

Deb2002 — *Deb K., 'Multi-Objective Optimization Using Evolutionary Algorithms', John Wiley & Sons, 2002*

Delbary2008 — *Delbary F., Aramini R., Bozza G., Brignone M., Piana M., 'On the use of the reciprocity gap functional in inverse scattering with*

near-field data: an application to mammography', J. Phys. Conf. Ser. 135, 2008

Dennis2013 — *B.H. Dennis, G.S. Dulikravich, 'Inverse determination of unsteady temperatures and heat fluxes on inaccessible boundaries', J. Inverse Ill-posed Probl. 20 (5–6) (2013) 791–803*

Dewan2004 — *Dewan A., Mahanta1 P., Sumithra Raju K. and Suresh Kumar P., Review of passive heat transfer augmentation techniques, Proceedings of the Institution of Mechanical Engineers, 218 A: Journal of Power and Energy, 2004*

Dickson2004 — *Dickson K.A. and Graham J.B., 'Evolution and Consequences of Endothermy in Fishes', Physiol. Biochem. Zool. 77 (2004) 998–1018*

DiPiazza2011 — *Di Piazza I. and Ciofalo M., 'Transition to turbulence in toroidal pipes', Journal of Fluid Mechanics, 687 72-117, 2011*

Dong2001 — *Dong Y., Huixiong L. and Tingkuan C., 'Pressure drop, heat transfer and performance of single-phase turbulent flow in spirally corrugated tubes', Exp. Therm. Fluid Sci. 24 (2001) 131–138*

Dorigo2004 — *Dorigo, M. and Stützle, T., 'Ant Colony Optimization', MIT Press., 2004*

Dulikravich1996 — *Dulikravich, G.S. and Martin, T.J., 'Inverse Shape and Boundary Condition Problems and Optimization in Heat Conduction', Chapter 10 in Advances in Numerical Heat Transfer, 1 381-426, Minkowycz, W. J. And Sparrow, E. M. (eds.), Taylor and Francis, (1996).*

Dulikravich2003a — *Dulikravich G.S., Colaço M.J., Martin T.J. and Lee S., 'Magnetized Fiber Orientation and Concentration Control in Solidifying Composites", In: Symposium on Materials Processing Under the Influence of Electrical and Magnetical Fields, 2003a*

Dulikravich2003b — *Dulikravich G.S., Colaço M.J., Martin T.J. and Lee S., 'An Inverse Method Allowing User-Specified Layout of Magnetized Micro-Fibers in Solidifying Composites', Journal of Composite Materials, vol. 37, no. 15, pp. 1351-1365, 2003b*

Dulikravich2003c — *Dulikravich G.S., Colaço M.J., Dennis B.H., Martin T.J. and Lee S., 'Optimization of Intensities, and Orientations of Magnets Controlling Melt Flow During Solidification', In: Symposium on Materials Processing Under the Influence of Electrical and Magnetical Fields, 2003c*

Dulikravich2004 — *Dulikravich G.S., Colaço M.J., Dennis B.H., Martin T.J. and Lee, S., 'Optimization of Intensities, and Orientations of Magnets Controlling Melt Flow During Solidification', Materials and Manufacturing Processes, vol. 19, iss. 4, pp. 695-718, 2004*

Eberhart2001 — *Eberhart R., Shi Y. and Kennedy J., 'Swarm Intelligence', Morgan Kaufmann, 2001*

Eiamsa-ard2010 — *Eiamsa-ard S. and Promvonge P., 'Thermal characterization of turbulent tube flows over diamond shaped elements in tandem', International Journal of Thermal Sciences, 49 1051-1062, 2010*

Eustice1910 — *Eustice J., 'Flow of water in curved pipes', Proceedings of the Royal Society of London Series A, 84 107-118, 1910*

Fan2009 — *Fan J.F., Ding W.K., Zhang J.F., He Y.L. and Tao W.Q., 'A performance evaluation plot of enhanced heat transfer techniques*

oriented for energy-saving', Int. J. Heat Mass Transf. 52 (2009) 33–44

Fand1961 — *Fand R.M. and Kaye J., The influence of sound on free convection from a horizontal cylinder, Journal of Heat Transfer, 83(2) 133-143, 1961*

Fletcher1963 — *Fletcher R. and Powel M.J.D., 'A rapidly convergent descent method for minimization' Computer J., vol.6, pp.163-168, 1963*

Fletcher1964 — *Fletcher R. and Reeves R.M., 'Function minimization by conjugate gradients', The Computer Journal 7,149-154, 1964*

Fletcher2000 — *Fletcher R., 'Practical method of optimization', John Wiley and Sons, 2000*

Garcia2007 — *Garcia A., Solano J.P., Vicente P.G., Viedma A., 'Flow pattern assessment in tubes with wire coil inserts in laminar and transition regimes', International Journal of Heat and Fluid Flow, 28 516–525, 2007*

Garimella1988 — *Garimella S., Chandrachood V., Christensen R.N., Richards D.E., 'Investigation of heat transfer and pressure drop augmentation for turbulent flow in spirally enhanced tubes', ASHRAE Trans. 94 (2), 1988*

Garimella1997 — *Garimella S., Christensen R.N., 'Performance evaluation of spirally fluted annuli: geometry and flow regime effects', Heat Transfer Eng. 18 (1) 34–46, 1997*

Genetti1973 — *Genetti W.E. and Priebe J.S., 'Heat transfer with a static mixer', AIChE, (1973).*

Giedt1955 — *Giedt, W.H., 'The determination of transient temperatures and heat transfer at a gas-metal interface applied to a 40mm gun barrel', Jet Propulsion, **25**, 158-162, 1955*

Goffe1994 — *Goffe, W.L., Ferrier, G.D. and Rogers, J., 'Global Optimization of Statistical Function with Simulated Annealing', Journal of Econometrics, vol. 60, pp. 65-99, 1994*

Goldberg1989 — *Goldberg, D.E., 'Genetic Algorithms in Search, Optimization, and Machine Learning', Addison-Wesley Pub Co., 1989*

Goldstein1962 — *Goldstein A.A., 'Cauchy's method of minimization', Numer. Math. 4, 146–150, 1962*

Goldstein1965 — *Goldstein A.A., 'On steepest descent', SIAM J. Control, 3, 147–151, 1965*

Goldstein1967 — *Goldstein A.A., 'An effective algorithm for minimization', Numer. Math., 10, 184–189, 1967*

Gose1957 — *Gose E.E., Peterson E.E., Arcivos A., 'On the rate of heat transfer in liquids with gas injection through the boundary layer', Journal of Applied Physics, 28 (1957).*

Grindley1908 — *Grindley J.H. and Gibson A.H., 'On the frictional resistance to the flow of air through a pipe', Proceedings of the Royal Society of London Series A, 80 114-139, 1908*

Gubbins2004 — *Gubbins D., 'Time Series Analysis and Inverse Theory for Geophysicists'. Cambridge University Press, Cambridge, U.K., 2004.*

Guzman1996 — *Guzman A. M. and Amon C. H., 'Dynamic flow characterization of transitional and chaotic regimes in converging-diverging channels' ,J. Fluid Mech. 321 25, 1996*

Hadamard1923 — *Hadamard, J., 'Lecture on Cauchy's problem in linear differential equations', Yale University Press, New Haven, CT, 1923*

Hansen2008 — *Hansen P.C., 'Regularization tools: a matlab package for analysis and solution of discrete ill-posed problem'*

Hansen1992 — *Hansen P.C., 'Analysis of discrete ill-posed problems by means of the L-curve', 1992*

Hansen1993 — *Hansen P.C., 'The use of the L-curve in the regularization of discrete ill-posed problems', 1993*

Hansen1999 — *Hansen P.C., 'The L-curve and its use in the numerical treatment of inverse problems', 1999*

Härröd1986 — *Härröd M., 'Hydrodynamics Scraped Surface Heat Exchangers', Food Process Engineering, 9 1-62, 1986*

Hong1976 — *Hong S.W., Bergles A.E., Augmentation of laminar flow heat transfer in tubes by means of twisted-tape inserts, Journal of Heat Transfer, 98 251-256, 1976*

Hsu2000 — *Hsu P.T., Wang S.G., Li T.Y., 'An inverse problem approach for estimating the wall heat flux in filmwise condensation on a vertical surface with variable heat flux and body force convection', Applied mathematical modelling, 24, 235-245, 2000*

Huang1992 — *Huang C.H., Ozisik M.N., and Sawaf B., 'Conjugate Gradient Method for Determining Unknown Contact Conductance During Metal Casting', International Journal of Heat and Mass Transfer,* ***35*** *1779-1789 (1992).*

Huang2005 — *Huang C-H. and Tsai Y-L., 'A transient 3-D inverse problem in imaging the time-dependent local heat transfer coefficient for plate fin', Applied Thermal Engineering 25 2478-2495, 2005*

Kak2001 — *Kak A.C. and Slaney M.., 'Principles of ComputerizedTomographic Imaging'. SIAM, Philadelphia, 2001.*

Kennedy1995 — *Kennedy, J. and Eberhart, R.C., 'Particle Swarm Optimization', Proceedings of the 1995 IEEE International Conference on Neural Networks, vol. 4, pp. 1942-1948, 1995*

Kennedy1999 — *Kennedy, J., 'Small Worlds and Mega-Minds: Effects of Neighborhood Topology on Particle Swarm Performance', Proceedings of the 1999 Congress of Evolutionary Computation, IEEE Press, vol. 3, pp. 1931-1938, 1999*

Kudirka1965 — *Kudirka A.A., 'Two-phase heat transfer with gas injection through a porous boundary surface', ASME, paper 65-HT-47, 1965*

Kuppan2000 — *Kuppan T., 'Heat Exchanger Design Handbook', CRC Press, 2000*

Efron1982 — *Efron B., 'The jackknife, the bootstrap and other resampling plans', Society for Industrial and Applied Mathematics, 1982.*

Ekstrom1974 — *Ekstrom, M. P., & Rhoads, R. L. 'On the application of eigenvector expansions to numerical deconvolution', Journal of Computational Physics, 14(4), 319-340, 1974*

Incoprera2002 — *Incoprera F.P., De Witt D.P., 'Fundamentals of Heat and Mass Transfer', John Wiley & Sons, Inc. New York (2002).*

Jadoaa2011 — *Jadooa A.A., 'Experimental Investigations Heat Transfer and Pressure Drop Characteristics of Flow Through Circular Tube Fitted With Drilled Cut-Conical Rings', Journal of Engineering and Technology, 29 No.3, 2011*

Jantsch1953 — *Jantsch E., 'Turbular heat transfer aparatus', US Patent number 2,663,321, 1953.*

Jayakumar2010 — *Jayakumar J.S., Mahajani S.M., Mandal J.C.,. Iyer K.N, Vijayan P.K., 'CFD analysis of singlephase flows inside helically coiled tubes', Computers & chemical engineering, 34 430-446, 2010*

Jha2016 — *Jha R., Dulikravich G.S., Chakraborti N., Fan M., Schwartz J., Koch C.C., Colaço M.J., Poloni C., Egorov I.N., 'Algorithms for design optimization of chemistry of hard magnetic alloys using experimental data', Journal of alloys and compounds, 682, 454-467, 2016*

Johansen1983 — *Johansen K. and. Bech C, 'Heat conservation during cold exposure in birds (vasomotor and respiratory implications)', Polar Res. 1 (1983) 259–268.*

Jurkowsky1996 — *Jurkowsky T., Jarny Y. and Delaunay D., 'Estimation of thermal conductivity of thermoplastic under molding conditions: an apparatus and an inverse algorithm', Int. J. Heat Mass Transfer, **40**, 4169-4181*

Lamm1999 — *Lamm P.K., personal communication March 1999,*

Lawson1995 — *Lawson C.L. and Hanson R.J., 'Solving Least Squares Problems', SIAM, Philadelphia, 1995*

Leal2013 — *Léal L., Miscevic M., Lavieille P., Amokrane M., Pigache F., Topin F., Nogarède c B., Tadrist L., 'An overview of heat transfer enhancement methods and new perspectives: Focus on active methods using electroactive materials', International Journal of Heat and Mass Transfer, 61 505–524, 2013*

Levenberg1944 — *Levenberg, K., A method for the solution of certain nonlinear problems in least squares. Quarterly of Applied Mathematics, 1944,2, 164-168.*

Levesey1987 — *Levesey A.K. and Brochon J.C., 'Analysing the distribution of decay constant in pulse-fuorometry using the maximum-entropy method', Biophy J. 52, 693-706, 1987*

Li2017 — *Li P., Liu P., Liu Z., Liu W., 'Experimental and numerical study on the heat transfer and flow performance for the circular tube fitted with drainage inserts', International Journal of Heat and Mass Transfer 107; 686-696, 2017*

Li1994 — *Li, H. Y. and Ozisik, M. N., "Identification of the Temperature Profile in an Absorbing, Emitting, and Isotropically Scattering Medium by Inverse Analysis", J. Heat Transfer, 114, 1060- 1063, 1992.*

Liu1993 — *Liu S., Masliyah J. H., 'Axially invariant laminar flow in helical pipes with a finite pitch', Journal of Fluid Mechanics, 251 315-353, 1993*

Liu2013 — *Liu S. and Sakr M., 'A comprehensive review on passive heat transfer enhancements in pipe exchangers Renew'. Sust. Energ. Rev. 19 64-81, 2013*

Manglik1993 — *Manglik R.M., A.E.Bergles, Heat transfer and pressure drop correlations for twisted tape inserts in isothermal tubes , Journal of Heat Transfer, 115 890-896, 1993*

Marquardt1963 — *Marquardt, D., An algorithm for least squares estimation of nonlinear parameters. Journal of the Society of Industrial and Applied Mathematics, 1963,11(2), 43lH41.*

Mertens — *Mertens A., Dedry O., Reuter D., Rigo O. and Lecomte-Beckers J., 'Thermal treatments of alsi10mg processed by laser beam melting'*

Mattheck1993	*Mattheck C., Bethge K. and Schäfer J., 'Safety factors in trees', J. Theor. Biol. 165 (1993) 185–189.*
McConalogue1968	*McConalogue D. J., and Srivastava R.S., 'Motion of a fluid in a curved tube', Proceedings of the Royal Society of London. Series A. Mathematical and Physical Sciences, 307 37-53, 1968*
McElhincy1977	*McElhiney J.E., Preckshot G.W., 'Heat transfer in the entrance length of a horizontal rotating tube', International Journal of Heat and Mass transfer, 20 847–854, 1977*
Meng2005	*Meng J.A., Liang X.G., Chen Z.J. and Li Z.X., 'Experimental study on convective heat transfer in alternating elliptical axis tubes', Exp. Therm. Fluid Sci. 29 (2005) 457–465*
Mertens2015	*Mertens A., Dedry O., Reuter D., Rigo O., Lecomte-Beckers J., 'Thermal treatments of alsi10mg processed by laser beam melting', 2015*
Miyazaki1971	*Miyazaki H., 'Combined free and forced convective heat transfer and fluid flow in a rotating curved circular tube', International Journal of Heat and Mass transfer, 14 1295–1309,1971*
Moore1920	*Moore E.H., 'On the reciprocal of the general algebraic matrix', Bulletin of the American Mathematical Society, 26:394–395, 1920.*
Mocerino2018	*Mocerino, A., Colaço, M., Bozzoli, F., 'Filtered reciprocity functional approach to estimate internal heat transfer coefficients in 2D cylindrical domains using infrared thermography', International Journal of Heat and Mass Transfer 125, 1181-1195*
Mori1967	*Mori Y., Nakayama W., 'Forced convection heat transfer in a straight pipe rotating around a parallel axis', International Journal of Heat and Mass transfer, 10 1179–1194 (1967).*
Morozov1984	*Morozov V.A., 'Methods for Solving Incorrectly Posed Problems', Springer-Verlag, New York (1984).*
Murio1993	*Murio, D.A.,'The Mollification Method and the Numerical Solution of Ill-Posed Problems', John Wiley and Sons, New York*
Naka2001	*Naka S., Yura T.G. and Fukuyama T., 'Practical Distribution State Estimation using Hybrid Particle Swarm Optimization', Proceedings IEEE Power Engineering Society, 2001*
Nakayama1983	*Nakayama W., Takahashi K. and Daikoku T., 'Spiral ribbing to enhance single-phase heat transfer inside tubes', Proceedings of the ASME–JSME Thermal Engineering Joint Conference, Honolulu, 1983.*
Naphon2006	*Naphon P., S.Wongwises, 'A review of flow and heat transfer characteristics in curved tubes', Renewable and sustainable energy reviews, 10 463–490, 2004*
Newton1977	*Newton D.C., Allen P.H.G., 'Senftleben effect in insulating oil under uniform electric stress', Letters in Heat and Mass Transfer, 4 9–16 (1977).*
Orlande1993	*Orlande, H. R. B. and zisik M.N, 'Inverse Problem of Estimating Interface ConductanceBetween Periodically Contacting Surfaces', Journal of Thermophysics and Heat Transfer, 7 319-325 (1993).*
Olande1994	*Orlande H.R.B. and Ozisik M.N., 'Determination of the Reaction Function in a Reaction-Diffusion Parabolic Problem', Journal of heat transfer, 116, 1041-1044, 1994*

Orlande2011 — *Orlande H.R.B, Fundym O., Maillet D., Cotta R.M., 'Thermal measurements and inverse techniques', CRC press, Taylor and Francis group, 2011*

Ozisik1993 — *Ozisik M.N., 'Heat Conduction', 2nd ed., Jhon Wiley & sons, Inc., 1993*

Park1999 — *Park H.H, Yoon T.Y., 'Solution of the inverse radiation problem using a conjugate gradient method', International journal of heat and mass transfer, **43**, 1767-1776,2000*

Pavelka2013 — *Pavelka K., Ruzicka S. and Bila Z., 'Photo-Plan Creation of Cylindrical Objects', ISPRS Annals of the Photogrammetry, Remote Sensing and Spatial Information Sciences, Volume II-5/W1; 2013.*

Peltier1834 — *Peltier J.C.A., Ann.Chim.Phys., 56:371,470*

Penrose1955 — *R. Penrose. 'A generalized inverse for matrices', Proceedings of the Cambridge Philosophical Society, 51:406–413, 1955*

Pethkool2001 — *Pethkool S., Eiamsa-ard S., Kwankaomeng S. and Promvonge P., 'Turbulent heat transfer enhancement in a heat exchanger using helically corrugated tube', Int. Commun. Heat Mass Transf. 38 (2011) 340–347*

Polak1971 — *Polak E., 'Computational methods in optimization', Academic Press, New York, 1971*

Powell1977 — *Powell M.J.D.,' Restart procedure for the conjugate gradient method', Mathematical programming, vol.12, pp.241-254, 1977*

Promvonge2007 — *Promvonge P., Eiamsa-ard S., 'Heat transfer in a circular tube fitted with free-spacing snail entry and conical-nozzle turbulators', International Communications in Heat and Mass Transfer, 34 838–848, 2007*

Promvonge2008a — *Promvonge P., Thermal augmentation in circular tube with twisted tape and wire coil turbulators, Energy Conversion and Management, 49 2949–2955, 2008a*

Promvonge2008b — *Promvonge P., 'Thermal augmentation in circular tube with twisted tape and wire coil turbulators', Energy Conversion and Management, 49 2949–2955, 2008b*

Promvonge2008c — *Promvonge, P., 'Heat transfer behaviors in round tubes with conical ring inserts', Energy Conversion and Management, Vol. 49; 8-15, 2008*

Rainieri1996 — *Rainieri S., Farina A. and Pagliarini G., 'Experimental investigation of heat transfer and pressure drop augmentation for laminar flow in spirally enhanced tubes', Proceedings 2nd European Thermal-Sciences and 14th UIT National Heat Transfer Conference, 203-209, 1996*

Rainieri1997 — *Rainieri S. and Pagliarini G., 'Convective heat transfer to orange juice in smooth and corrugated tubes', Int. J. Heat Technol. 15 (1997) 69–75*

Rainieri2002 — *Rainieri S. and Pagliarini G., 'Convective heat transfer to temperature dependent property fluids in the entry region of corrugated tubes', International Journal of Heat and Mass Transfer, 45 4525-4536, 2002*

Rainieri2004 — *Rainieri S., Bozzoli F., Cattani L., Vocale P., 'Parameter estimation applied to the heat transfer characterization of Scraped*

Surface Heat Exchangers for food applications', Journal of Food Engineering, 125 147–156, 2014

Rainieri2009 — *Rainieri S., Bozzoli F. and Pagliarini G., 'Effect of a hydrophobic coating on the local heat transfer coefficient in forced convection under wet conditions', Experimental Heat Transfer, 22 163-177, 2009*

Rainieri2011 — *Rainieri S., Bozzoli F., Schiavi L. and Pagliarini G., 'Numerical analysis of convective heat transfer enhancement in swirl tubes', International Journal of Numerical Methods for Heat and Fluid Flow, 21 (5) 559-571, 2011*

Rainieri2014 — *Rainieri S., Bozzoli F., Cattani L. and Vocale P., 'Parameter estimation applied to the heat transfer characterisation of Scraped Surface Heat Exchangers for food applications', Journal of food engineering, 125, 147-156, 2014*

Ravigururajan1996 — *Ravigururajan T.S., Bergles A.E., 'Development and verification of general correlations for pressure drop and heat transfer in single-phase turbulent flow in enhanced tubes', Exper. Ther. Fluid Sci. 13 55–70, 1996*

Reddy2002 — *Reddy J., 'Energy Principles and Variational Methods in Applied Mechanics', John Wiley & Sons, Inc, 2002.*

Sarma2002 — *Sarma P. K., Subramanyam T., Kishorea P.S., Rao D. V. and Kakac S., 'A new method to predictconvective heat transfer in a tube with twisted tape inserts for turbulent flow', Int. J. Therm. Sci. 41 955–960, 2002*

Scholander1950 — *Scholander P.F., Walters V., Hock R. and. Irving L, 'Body insulation of some arctic and tropical mammals and birds', Biol. Bull. 99 (1950) 225–236*

Seebeck1823 — *Seebeck T.J., 'MAgnetisch polarisation der metalle und erze durch temperature-differenz', Abh. K. Akad. Wiss, Berlin, 265:289-346*

Shah1978 — *Shah R. K. and London A. L., 'Laminar Flow Forced Convection in Ducts', New York: Academic Press, 1978*

Shah1981 — *Shah, R. K.,Kakaç S., Bergles A.E. and Mayinger F., 'Classification of heat exchangers, in Heat Exchangers: Thermal-Hydraulic Fundamentals and Design', Hemisphere Publishing, Washington, DC, pp. 9–46, 1981*

Shah2003 — *Shah R., K. and Sekulic D.P., 'Fundamentals of heat exchanger design', Jhon Wiley & Sons, 2003*

Shifrin2010 — *Shifrin E.I. and Shushpannikov P.S., 'Identification of a spheroidal defect in an elastic solid using a reciprocity gap functional', Inverse Prob. 26 (5), 055001.2010*

Sivashanmungan2006 — *Sivashanmugam P., Suresh S., 'Experimental studies on heat transfer and friction factor characteristics of laminar flow through a circular tube fitted with helical screw-tape inserts', Applied Thermal Engineering, 26 1990-1997, 2006*

Skelland1958 — *Skelland, A.H.P., Correlation of scraped-film heat transfer in the votator, Chemical Engineering Science, 7 166-175, 1958*

Skilling1984 — *Skilling J. and Bryan R.K., 'Maximum-Entropy image-restoration-general algorithm', Monthly notice R.Arstron. Soc. 211, 111-124, 1984*

Sreenivasan1983 — *Sreenivasan K.R. and Strykowski P.J., 'Stabilization Effects in Flow Through Helically Coiled Pipes', Experiments in Fluids I 31-36,1983*

Stark1995 — *Stark P.B. and Parker R.L.,'Bounded-variable least-squares: An algorithm and applications', Computational Statistics, 10(2):129–141, 1995*

Stevens1974 — *Stevens E.D., Lam H.M. and Kendall J., 'Vascular Anatomy of the Counter-Current Heat Exchanger of Skipjack Tuna', J. Exp. Biol. 61 (1974) 145–153*

Stolz1960 — *Stolz, G., 'Numerical solution to an inverse problem of heat conduction form simple shape', ASME J. Heat Trasnfer, **82**, 20-26,1960*

Storn1996 — *Storn, R. and Price, K.V., 'Minimizing the Real Function of the ICEC'96 Contest by Differential Evolution', IEEE Conf. on Evolutionary Computation, pp. 842-844, 1996*

Sununu1970 — *Sununu J.H., 'Heat transfer with static mixer system', Keniks Corp. Tech. Rep 1002, 1970*

Tamari1976 — *Tamari M., Nishikawa K., 'The stirring effect of bubbles upon the heat transfer to liquid', Heat Transfer Jpn. Res, (5/2), 1976*

Thomson1848 — *Thomson W., 'On absolute thermometric scale founded on Carnot's theory of the motive power of heat and calculated from Regnault's observation', Philos.Mag., 33:313-317*

Thomson1876 — *Thomson J., 'On the origin of windings of rivers in alluvial plants with remarks on the flow of water round bends of pipes', Proceedings of the Royal Society of London Series A, 26 356-57, 1876*

Tikhonov1963 — *Tikhonov, A.N., 'Solution of incorrectly formulated problem and the regularization method', Soviet Math Dokl, **4**(4), 1035-1038,1963*

Tikhonov1975 — *Tikhonov, A.N., 'Inverse problem in heat conduction', J. Eng.Phys., **29**(1), 816-820,1975*

Tikhonov1977 — *Tikhonov, A.N. and Arsenin, V.Y., 'Solution of ill-posed problems', Winston and Sons, Washington DC, 1977*

Truesdell1970 — *Truesdell L.C., Adler R.J., 'Numerical treatment of fully developed laminar flow in helically coiled tubes', AICHE Journal, 16 1010-1015, 1970*

Tu2015 — *Tu W., Tang Y., Hu J., Wang Q. and Lu L., 'Heat transfer and friction characteristics of laminar flow through a circular tube with small pipe inserts', Int. J. Therm. Sci. 96 94-101, 2015*

Twomey1963 — *Twomey S., 'On the numerical solution of the Fredholm integral equation of the first kind by inversion of the linear system produced by Quadrature', J. Assoc. Comp. Mach. **10**, 97-101, 1963*

Ujhidy2003 — *Ujhidy A., Nemeth J. and Szepvolgyi J., 'Fluid flow in tubes with helical elements', Chem. Eng and Processing 42 1–7, 2003*

VanDerMeer1978 — *Van Der Meer T.H., Hoogendoorn C.J., 'Heat transfer coefficients for viscous fluids in a static mixer', Chemical Engineering Science 33 1277-1282, 1978*

Vogel2002 — *Vogel C. R., 'Computational Methods for Inverse Problems', SIAM, Philadelphia, 2002.*

Walker1990 — *Walker, G., 1990, 'Industrial Heat Exchangers: A Basic Guide', 2nd ed., Hemisphere Publishing, Washington, DC.*

Watkins1976 — *Watkins R.W., Robertson C.R., Acrivos A., 'Entrance Region Heat Transfer in Flowing Suspensions', International Journal of Heat and Mass Transfer, 19 693–695, 1976*

Watkinson1975 — *Watkinson A.P., Miletti D.L. and Kubanek G.R., 'Heat Transfer and Pressure Drop of Internally Finned Tubes in Laminar Oil Flow', Proceedings of the AICHE-ASME Heat Transfer Conference, ASME, (75) HT-41, 1–9, 1975*

Webb1994 — *Webb R.L., 'Principles of enhanced heat transfer', John Wiley & Sons, Inc New York (1994).*

Wegner2015 — *Wegner N.C., Snodgrass O.E., Dewar H. and Hyde J.R., 'Whole-body endothermy in a mesopelagic fish, the opah, Lampris guttatus', Science (80-.). 348 (2015) 786–789*

Weigand2011 — *Weigand, B., & Spring, S., 'Multiple Jet Impingement− A Review', Heat Transfer Research, 42(2), 2011*

White1929 — *White C.M., 'Streamline flow through curved pipes', Proceedings of the Royal Society of London. Series A, 645-663, 1929*

Williams1902 — *Williams G.S., Hubbel C.W., Femkell G.H., 'Experiments at Detroit, Michigan, on the effect of curvature upon the flow of water in pipes', Trans. ASCE, 47 1-196, 1902*

Woodbury2003 — *Woodbury K.A., 'Inverse engineering handbook', New York, CRC press, 2003*

Wolfe1969 — *Wolfe P., 'Convergence Conditions for Ascent Methods', SIAM Review. 11 (2): 226–000, 1969*

Wolfe1971 — *Wolfe P., 'Convergence condition for ascent methods II: some corrections', SIAM Rev., 13, 185–188, 1971*

Yang1995 — *Yang G, Dong F, Ebadian M.A., 'Laminar forced convection in a helicoidal pipe with finite pitch', International journal of heat and mass transfer, 5 853-862, 1995*

Ylmaz2001 — *Yilmaz M., Sara O.N., Karsli S.,' Performance evaluation criteria for heat exchangers based on second law analysis', Exergy, an International Journal, 1(4) 278-294, 2001*

Zabras1988 — *Zabras N., Mukherjee S. and Richmond O., 'An Analysis of Inverse Heat Transfer Problems With Phase Changes Using an Integral Method' J. Heat Transfer, 110, 554-561,1988*

Zabras1995 — *Zabras, N. and Ngugen, T. H., 'Control of the Freezing Interface Morphology in Solidification Processes in the Presence of Natural Convection', International Journal for Numerical Methods in Engineering, 38 1555-1578, 1995*

Zimparov2001 — Zimparov V., '*Extended performance evaluation criteria for enhanced heat transfer surfaces: heat transfer through ducts with constant heat flux', International Journal of Heat and Mass Transfer, 44(1) 169-180, 2001*

Zimparov2002 — *Zimparov V., 'Enhancement of heat transfer by a combination of a single-start spirally corrugated tubes with a twisted tape', Experimental Thermal and Fluid Science, 25 535-546, 2002*

Acknowledgment

First of all, I would like to thank my Advisors Prof. Sara Rainieri and all my co-advisors Prof. Carlos J.S. Alves, Prof. Fabio Bozzoli and Prof. Marcelo J. Colaço for the great help provided during the last three years. They contributed to grow my knowledge, and I am sorry if I was not able to learn more from them. They also gave me sincere advice for helping me with the all-day problems. I would also like to thank Professor Pagliarini and Professor Farina, for their help and experience. Thank you for everything.

A special thanks go to my co-advisor Prof. Fabio Bozzoli, since with help, experience and patient introduced me to the inverse problem driving me all along my PhD. He also gave me the opportunity to travel abroad with the Overworld program, a co-founded European program for the student mobility: with this grant I spent four months in Brazil working with Prof. Marcelo Colaço from the Federal University of Rio de Janeiro, and in him I found more than the teacher that with motivation, enthusiasm, and knowledge helped me during my stay in Brazil. I will be eternally grateful to him for the occasions that gave me and for the opportunities, support, help and friendship that is still giving me. Thank to Prof. Bozzoli and the good friendship with Prof. Colaço I was able to travel to Brazil other two times, founded by the Erasmus KA107 program. Related to this topic, I would like to thanks Angelina Mannon for the support gave me in the burocratic procedures. When I was in Brazil, I had the opportunity to meet Prof. Helcio Orlande: it is following his courses, together with the ones provided by Prof. Colaço, that I really understood what the inverse problem is. I am grateful to his advice and experience.

During my stay in Brazil I found a lot of friends, in particular I would like to thank Cesar, Massoud and all the guys of the laboratory that helped me during my stay in Brazil.
During my Ph.D. I had also the opportunity to spend four months in Lisbon, working with Prof. Carlos Alves from the Technical University of Lisbon. I will miss the conversations during the lunch and also after lunch, sometimes with a fresh bear. I am grateful to him also for helped me during my stay in Lisbon and in Caldas da Rainha.
A special thank goes to Kristina Navickatè from the Danish Technical University that provide the bio-inspired tube for one of the experimental part of this thesis and to Inoussa Tougri from the Federal University of Rio de Janeiro for the help gave me during the experimental measurements. Related to this topic I have to thanks Chiara Freddi (‘The queen of the Lab’) for spending with me a lot of time working on the experimental apparatuses.
Thanks to all my colleges for the help and friendship provided during my Ph.D. Carlotta, Milena, Carlo, Enrico and Massimiliano. A special thanks goes to Pamela and Luca, for the grateful help that they gave me during the last three years.
Finally, I want to sincerely thank my parents, my family, Chiara and her family for the daily enormous support and for the patience shown during all these years.

Ringraziamenti

La vita deve essere vissuta guardando in avanti, ma può essere capita solo guardandosi indietro. Per questo arrivati alla fine del percorso bisogna sempre ricordare da dove si è partiti. Voglio quindi ringraziare in modo particolare i miei genitori per avermi reso quello che sono e per avermi sempre guidato ed aiutato.

Uno speciale ringraziamento va a Chiara con la quale ho condiviso tutti i momenti difficili degli ultimi anni e con la quale spero di condividere gli anni futuri, magari con meno problemi e più spensieratezza.

Come il vino e l'oro, gli amici migliori sono i più antichi. Per questo voglio ringraziare Albert, Canta, Gara e Pella per essermi sempre stati vicini, anche se il tempo ci ha allontanati. Con loro voglio ringraziare tutti gli amici che mi hanno sempre aiutato.

Infine, ma non per importanza, voglio ringraziare i fisici: Deny, Fabi, Baldo e Marco per avermi adottato. Siete veramente delle persone speciali!

Grazie di cuore a tutti!

ad meliora et maiora semper

Parma,
31/08/2018